

AFIT/DS/ENY/99-01

**Flow Separation Prevention on a Turbine  
Blade in Cascade at Low Reynolds Number**

**DISSERTATION**

**James P. Lake, B.S., M.S.  
Captain, USAF**

**AFIT/DS/ENY/99-01**

Approved for public release; distribution unlimited

DTIC QUALITY INSPECTED 1

19990616 027

## **Disclaimer**

The views expressed in this dissertation are those of the author and do not reflect the official policy or position of the United States Air Force, the Department of Defense, or the United States Government.

AFIT/DS/ENY/99-01

**Flow Separation Prevention on a Turbine Blade in  
Cascade at Low Reynolds Number**

**DISSERTATION**

Presented to the Faculty of the Graduate School of Engineering of the Air Force Institute of  
Technology Air University In Partial Fulfillment for the Degree of

**Doctor of Philosophy**

**James P. Lake, B.S., M.S.**

**Captain, USAF**

Air Force Institute of Technology

Wright-Patterson AFB, Ohio

June, 1999

Sponsored in part by Wright Laboratory

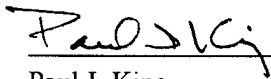
Approved for public release; distribution unlimited

# Flow Separation Prevention on a Turbine Blade in Cascade at Low Reynolds Number

**James P. Lake, B.S., M.S.**

**Captain, USAF**

Approved:

  
\_\_\_\_\_

Paul I. King  
Committee Chairman

3 Jun 99

Date

  
\_\_\_\_\_

Jeffery K. Little, Lt. Col. USAF  
Committee member

3 Jun 99

Date

  
\_\_\_\_\_

Glen P. Perram, Lt. Col. USAF  
Committee member

3 Jun 99

Date

  
\_\_\_\_\_

Thomas C. Hartrum  
Dean's Representative

3 Jun 99

Date

Accepted:

  
\_\_\_\_\_

Robert A. Calico, Jr.  
Dean, School of Engineering

## **Dedication**

I dedicate this work to my wife and family who have supported me while I've been away from home and in the lab.

## Acknowledgments

I wish to acknowledge the efforts of everyone involved with this project. The contributions from the AFIT shop employees, including Russ Hastings, Jan LeValley, and Condie Inman were exemplary in their detail and expedience in the construction of the tunnel and support equipment. Greg Cala provided the initial traverse mechanism with his control software for it. David Pestian helped significantly by spending his time designing and ordering the active turbulence control equipment I needed. Chris Murawski contributed to my basic understanding of experimental procedure, while Alex Giese helped me to calculate the turbulent length scales using his software. Karsten Lipiec provided many good ideas for improving the tunnel, not to mention doing a lot of the dirty work. Thanks to Paige in building 435 who helped me make sense of the acquisition process. Steve Pennington in building 5 provided desperate support in last minute needed machining of the blade cassette holder. Charles Stevens also helped with measuring the inlet flow angles and sealing up the cracks. This dissertation was written using Scientific Workplace version 2.5. Using this word processor was made easier with the help and advice of Captain Robert Latin, Captain Clarence Chenault, Major Joel Schubbe and Major Nate Titus.

Dr. Rolf Sondergaard deserves mention for designing the entire tunnel on Pro-engineer and for giving me the instructions to perform the computational simulations. Dr. Sondergaard also assisted with the excaberating process of taking the boundary layer profile data, not to mention answering every stupid question I had. William Nilson helped me install and make sense of the maze of wires, transducers, scanivalves and thermocouples that are used in the collection of data from the tunnel. Captain Jeff Bons procured a working 3-axis traverse mechanism and taught me how to use the LabView software package that did everything but write this for me. I owe the greatest debt of

gratitude to Dr. Richard Rivir and Dr. Paul King, who provided the ideas, funding, and support to complete this project.

# Table Of Contents

	Page
Dedication .....	iv
Acknowledgments .....	v
Table Of Contents .....	vii
List of Figures .....	xvi
List of Tables .....	xxvi
List of Symbols .....	xxvii
Abstract .....	xxxvi
Chapter 1. INTRODUCTION .....	1
1.1 Low Pressure Turbine .....	1
1.2 Previous Low Pressure Turbine Experiments .....	3
1.3 Current Research Focus .....	4
1.4 Determination of Improved Performance .....	5
1.4.1 Comparison of Experimental Loss Coefficients .....	12
1.5 Chapter Summary .....	13
Chapter 2. BACKGROUND AND THEORY .....	15
2.1 Overview of Turbine Blade Boundary Layer Aerodynamics .....	15
2.2 Experimental and Numerical Studies of Turbine Boundary Layers .....	15

2.2.1	Experimental Determination of Laminar-to-Turbulent Transition Modes .....	16
2.2.2	Limitations of Numerical Code LPT Modelling .....	18
2.3	Separation Control Using Passive Methods .....	19
Chapter 3.	TUNNEL AND CASCADE CHARACTERISTICS .....	23
3.1	Data Collection Locations .....	23
3.2	Flow Incidence Angle Measurements .....	25
3.3	Periodicity and Uniformity Measurements .....	26
3.4	Test Section Inlet Turbulence Scale Measurements .....	33
Chapter 4.	DATA COLLECTION INSTRUMENTS .....	36
4.1	Velocity Measurements Using TSI 1210-T1.5 Hot Wire .....	36
4.2	Boundary Layer Velocity Measurements Using TSI 1279S-10A Miniature Hot Film Probe .....	37
4.3	Temperature Measurements Using J-Type Thermocouples .....	39
4.4	Pressure Measurements .....	40
4.4.1	Blade Surface Static Pressure Measurements .....	41
4.4.2	Exit Total Pressure Measurements .....	42
Chapter 5.	NUMERICAL SIMULATION OF TURBINE CASCADE .....	44
5.1	Overview of Allison Software code .....	44
5.2	Grid Generation Around Pak-B Airfoil .....	44
5.3	VBI Computational Method .....	44

5.4	Two-Dimensional Software Results . . . . .	45
5.4.1	VBI 2-D Code Results For Reynolds Number = 50k . . . . .	46
5.4.2	VBI 2-D Code Results For Reynolds Number = 100k . . . . .	47
Chapter 6.	BASELINE LPT BLADE PERFORMANCE . . . . .	49
6.1	Baseline Pak-B Overview . . . . .	49
6.2	Experimental and Simulated Surface Static Pressures . . . . .	49
6.2.1	Cp Curves for Re = 50k . . . . .	50
6.2.2	Cp Curves for Re = 100k . . . . .	50
6.2.3	Cp Curves for Re = 200k . . . . .	52
6.2.4	Uncertainty in Cp Measurements . . . . .	56
6.3	Boundary Layer Velocity and Turbulence Profiles . . . . .	56
6.3.1	Boundary Layer Measurements at Re = 50k . . . . .	56
6.3.2	Boundary Layer Measurements at Re = 100k . . . . .	58
6.3.3	Uncertainty in Boundary Layer Measurements . . . . .	63
6.4	Exit Velocity Wake Profiles . . . . .	63
6.4.1	Exit Velocity Wake Data . . . . .	63
6.4.2	Exit Momentum Deficit Calculations . . . . .	66
6.4.3	Uncertainty in Wake Momentum Deficit Measurements . . . . .	66
6.5	2-D Profile Loss Coefficient Measurements . . . . .	67
6.5.1	Exit Pressure Data . . . . .	67

6.5.2	Baseline Performance Loss Coefficients .....	68
6.5.3	Uncertainty in Loss Coefficient Measurements .....	70
Chapter 7.	<b>PERFORMANCE OF PAK-B BLADE WITH BOUNDARY LAYER TRIP AT 35% CHORD .....</b>	<b>71</b>
7.1	Trip Configurations Tested .....	71
7.2	Boundary Layer Profiles Using Large Trip Wire .....	78
7.3	Exit Velocity Wake Measurements Using Large Trip Wire .....	78
7.4	Loss Coefficient Measurements Using Large Trip Wire .....	78
Chapter 8.	<b>LOSS REDUCTION USING DIMPLES .....</b>	<b>87</b>
8.1	Background and Separation Control Methodology .....	87
8.2	Previous Studies Using Recessed Dimples .....	89
8.3	Dimple Variations Previously Tested .....	89
8.4	Experiment Test Article .....	90
8.5	Boundary Layer Velocity and Turbulence Measurements Downstream of Dimples .....	91
8.5.1	Boundary Layer Measurements at $Re = 50k$ for Dimples at 50%, 55% and 65% axial chord .....	92
8.5.2	Boundary Layer Measurements at $Re = 100k$ for Dimples at 50%, 55% and 65% axial chord .....	97
8.6	Exit Velocity Wake Profiles For Dimpled Blade .....	101
8.6.1	Exit Momentum Deficit Calculations .....	101
8.7	Loss Coefficient Reduction Using Dimples .....	106

8.7.1	Exit Pressure Data For $Tu = 1\%$ .....	106
8.7.2	Exit Pressure Data for $Tu = 4\%$ .....	109
8.7.3	Loss Coefficient for Dimpled Blade .....	109
Chapter 9.	<b>LOSS REDUCTION USING V-GROOVES</b> .....	113
9.1	Background and Previous Studies .....	113
9.2	V-Groove Experiment Test Article .....	114
9.3	Boundary Layer Velocity and Turbulence Measurements with V-Grooves at 55% and 60% Chord for $Re = 50k$ .....	114
9.4	Boundary Layer Velocity and Turbulence Measurements with V-Grooves at 55% and 60% Chord for $Re = 100k$ .....	117
9.5	Turbulent Boundary Layer Measurements with V-Grooves at 55% and 60% Chord .....	117
9.6	Exit Velocity Wake Profiles for V-Grooves .....	117
9.7	Exit Momentum Deficit Calculations for V-Grooves .....	122
9.8	Loss Coefficient Measurement for V-Grooves .....	122
Chapter 10.	<b>SUMMARY AND CONCLUSIONS</b> .....	135
References	.....	143
Appendix A.	<b>BOUNDARY LAYER MEASUREMENTS FOR BLADE WITH DIMPLES</b> .....	148
A.1	Velocity and Turbulence Measurements at $Re = 50k$ and $Re = 100k$ .....	148
Appendix B.	<b>BOUNDARY LAYER MEASUREMENTS FOR BLADE WITH V-GROOVES</b> .....	166
B.1	Velocity and Turbulence Measurements at $Re = 50k$ and $Re = 100k$ .....	166

Appendix C. ADJUSTABLE LINEAR CASCADE EXPERIMENTAL FACILITY .....	178
C.1    Baseline Wind Tunnel Design .....	178
C.2    Active/Passive Turbulence Generator .....	180
C.2.1    Active Turbulence Generation .....	182
C.3    Adjustable Inlet and Exit Angle Cascade Test Section .....	182
C.4    Removable Blade Cassette .....	187
C.4.1    Testing Other Blade Shapes .....	188
Appendix D. EXPERIMENTAL DATA COLLECTION SOFTWARE .....	189
D.1    Overview of Software and Equipment .....	189
D.2    Hot Wire Calibration .....	189
D.3    Current Tunnel Conditions .....	190
D.4    Velocity Profiles Across The Blade Cassette Inlet and Exit .....	194
D.4.1    Blade Cassette Velocity Profile Inputs .....	195
D.4.2    Blade Cassette Velocity Profile Outputs .....	196
D.5    Pressure Transducer Calibration .....	198
D.6    Wake Traverse Velocity and Pressure Data Collection .....	199
D.6.1    Wake Traverse Data Collection Inputs .....	199
D.6.2    Wake Traverse Data Collection Outputs .....	200
D.7    Surface Pressure Coefficient Determination .....	200
D.7.1    Surface Pressure Coefficient Inputs .....	200

D.7.2	Surface Pressure Coefficient Outputs . . . . .	202
D.8	Boundary Layer Velocity and Turbulence Measurements . . . . .	203
D.8.1	Boundary Layer Traverse Inputs . . . . .	205
D.8.2	Boundary Layer Traverse Outputs . . . . .	205
D.9	Turbulent Length Scale Determination Using Hot Wire . . . . .	205
D.9.1	Required Data Inputs for Length Scale Software . . . . .	206
D.9.2	Calculation Process of Length Scale Software . . . . .	206
D.9.3	Turbulence Intensity Verification Using Power Spectrum Curve . . . . .	208
D.9.4	Integral Length Scale Determination and Program Outputs . . . . .	208
Appendix E. 2-D VANE BLADE INTERACTION CODE . . . . .		212
E.1	VBI Software Inputs . . . . .	212
E.2	The $k - \epsilon$ Two-Equation Model for Turbulent Viscosity . . . . .	212
Appendix F. BASELINE PERFORMANCE LOSS COEFFICIENT ESTIMATION . . . . .		214
F.1	Extrapolation of Losses from Previous Experiments . . . . .	214
F.2	Estimation of Losses Using Curve Fits . . . . .	214
Appendix G. BLADE SURFACE CURVATURE DISTRIBUTION . . . . .		217
Appendix H. HOT WIRE CONTROL EQUATIONS . . . . .		219
H.1	Hot Wire Physical Characteristics . . . . .	219
H.2	Velocity Determination Equations . . . . .	219
H.2.1	Atmospheric Molecular Weight . . . . .	219

H.2.2	Atmospheric Constants . . . . .	220
H.2.3	Atmospheric Properties . . . . .	221
H.2.4	Velocity Determination Using Atmospheric Properties and Hot Wire Voltage . . . . .	223
H.3	Turbulence Determination Equations . . . . .	224
<b>Appendix I. UNCERTAINTY ANALYSIS . . . . .</b>		<b>226</b>
I.1	Surface Static Pressure $C_p$ Measurements . . . . .	226
I.2	Loss Coefficient Measurements . . . . .	227
I.3	Velocity Measurements . . . . .	228
I.4	Wake Momentum Deficit Measurements . . . . .	228
<b>Appendix J. REJECTED SEPARATION CONTROL METHODS . . . . .</b>		<b>230</b>
J.1	Separation Control Methods Unsuitable for LPT Use . . . . .	230
J.1.1	Triangular Plow Vortex Generator Device . . . . .	230
J.1.2	Semi-Circle Vortex Generator Device . . . . .	231
J.1.3	Simple Vane Vortex Generator Device . . . . .	231
J.1.4	Passive Cavity Using Adverse Pressure Gradient . . . . .	231
J.1.5	Passive Injection Using Adverse Pressure Gradient . . . . .	232
J.1.6	$\pm 45^\circ$ Small-Scale Riblets Located On the Suction Surface . . . . .	232
J.1.7	Leading Edge Vane Vortex Generators . . . . .	233
J.1.8	Wheeler Channel Groove Cut Into Surface . . . . .	233
J.1.9	Afterbody Groove Cut Into Surface . . . . .	233

J.1.10	Small-Scale V-Groove Riblets .....	235
J.1.11	Triangular Ramp Vortex Generator .....	237
J.1.12	Parallel Concave Slat Vortex Generators .....	238
J.1.13	Wheeler Vortex Generators .....	238
J.1.14	Ogee Submerged Vortex Generators .....	239
J.1.15	Small-Scale Square Ribs .....	239
J.1.16	Large-Scale Vortex Generators .....	240
J.1.17	Transverse Grooves Placed at Baseline Separation Point .....	241
J.1.18	Increased Surface Roughness Over Surface of Pak-B Blade .....	242
Appendix K. LIMITATIONS OF LPT COMPUTATIONAL MODELLING .....		245
K.1	Research Conducted by Halstead et al. [23] .....	245
Vita	.....	247

## List of Figures

		Page
Figure 1.	Unsteady wake passing over Pak-B blade surface (mounting pin locations also shown). . . . .	2
Figure 2.	Brayton cycle for an ideal gas jet engine. . . . .	7
Figure 3.	T-S diagram of a typical low pressure turbine stage. . . . .	9
Figure 4.	T-S diagram showing improvement possible with decrease in pressure drop. . . . .	11
Figure 5.	Trend of increasing stage efficiency with reduction in loss coefficient. . . . .	11
Figure 6.	Station numbers and T-S/R diagram for exit nozzle. . . . .	13
Figure 7.	Laminar separation transition to turbulent flow. . . . .	17
Figure 8.	Measurement collection locations for the adjustable test section. . . . .	23
Figure 9.	Three hole wedge probe used in inlet angle measurements. . . . .	25
Figure 10.	Measured inlet and exit flow angles. . . . .	27
Figure 11.	Traverse movement pattern to verify 2-D flow with a hot wire probe. . . . .	28
Figure 12.	Inlet velocity traverse for slot #1 at +10 cm , + 5 cm, 0 cm, -5 cm, -10 cm, and Tu = 1%. . . . .	29
Figure 13.	Inlet velocity traverse for slot #1 at +10 cm , + 5 cm, 0 cm, -5 cm, -10 cm, and Tu = 4%. . . . .	30
Figure 14.	Exit velocity traverse for slot #3 at +10 cm , + 5 cm, 0 cm, -5 cm, -10 cm, and Tu = 1%. . . . .	31
Figure 15.	Exit velocity traverse for slot #3 at +10 cm , + 5 cm, 0 cm, -5 cm, -10 cm, and Tu = 4%. . . . .	32

	Page
Figure 16. Power spectrum of inlet flowfield for $Tu = 1\%$ . . . . .	35
Figure 17. Power spectrum of inlet flowfield for $Tu = 4\%$ . . . . .	35
Figure 18. Hot wire data collection diagram. . . . .	37
Figure 19. TSI 1279S-10A subminiature boundary layer probe (not to scale). . . . .	38
Figure 20. Locations of boundary layer measurements over the suction surface. . . . .	39
Figure 21. Surface static pressure port locations molded within blades #4 and #6. . . . .	42
Figure 22. Blade surface pressure data collection diagram. . . . .	43
Figure 23. O-H grid surrounding Pak-B airfoil . . . . .	45
Figure 24. Two dimensional VBI code surface pressure coefficient results. . . . .	46
Figure 25. 2-D VBI code simulations of boundary layer velocity. . . . .	48
Figure 26. Experimental and simulated $C_p$ curves for $Re = 50k$ and $Tu = 1\%$ . . . . .	51
Figure 27. Experimental and simulated $C_p$ curves for $Re = 50k$ and $Tu = 4\%$ . . . . .	51
Figure 28. Experimental and simulated $C_p$ curves for $Re = 100k$ and $Tu = 1\%$ . . . . .	52
Figure 29. Experimental and simulated $C_p$ curves for $Re = 100k$ and $Tu = 4\%$ . . . . .	53
Figure 30. Experimental and simulated VBI-2D $C_p$ curves for $Re = 200k$ . . . . .	53
Figure 31. Experimental and simulated $C_p$ curves for $Re = 200k$ and $Tu = 4\%$ . . . . .	54
Figure 32. Variation of separation start with Reynolds number and turbulence intensity. . . . .	55
Figure 33. Baseline velocity and turbulence profiles over the suction surface. . . . .	59
Figure 34. Baseline velocity and turbulence profiles with increased freestream turbulence. . . . .	60

	Page
Figure 35. Baseline velocity and turbulence profiles for $Re = 100k$ .	61
Figure 36. Baseline velocity and turbulence profiles with moderate freestream turbulence.	62
Figure 37. Baseline Pak-B exit velocity profiles for $Tu = 1\%$ .	64
Figure 38. Baseline Pak-B exit velocity profiles at $Tu = 4\%$ .	65
Figure 39. Baseline Pak-B blade momentum deficit measurements.	66
Figure 40. Baseline Pak-B exit stagnation pressure loss at $Tu = 1\%$ .	68
Figure 41. Baseline Pak-B exit stagnation pressure loss at $Tu = 4\%$ .	69
Figure 42. Baseline Pak-B exit loss coefficients.	70
Figure 43. Boundary layer trip attempts measured at 67.2% axial chord for $Re = 50k$ .	73
Figure 44. Boundary layer profiles measured at 67% chord with trip wire at 10% axial chord.	74
Figure 45. Boundary layer profiles measured at 84.8% chord with trip wire at 10% axial chord.	75
Figure 46. Boundary layer profiles measured at 67% chord with trip wire at 20% axial chord.	76
Figure 47. Boundary layer profiles measured at 84.8% chord with trip wire at 20% axial chord.	77
Figure 48. Measured velocity and turbulence profiles for baseline blade with trip at 35%.	79
Figure 49. Measured velocity and turbulence profiles for baseline blade with trip at 35%.	80
Figure 50. Measured velocity and turbulence profiles for baseline blade with trip at 35% with $Tu = 4\%$ .	81

	Page
Figure 51. Measured velocity and turbulence profiles for baseline blade with trip at 35% with $Tu = 4\%$ . . . . .	82
Figure 52. Exit velocities for baseline blade with trip at 35%. . . . .	83
Figure 53. Stagnation pressure loss for baseline blade with trip wire at 35% axial chord. . . . .	85
Figure 54. Wake velocity and total pressure loss coefficients for baseline blade with trip wire at 35%. . . . .	86
Figure 55. Diagram of considered separation control methods. . . . .	87
Figure 56. Dimples milled into the suction surface of the blade at three different locations. . . . .	91
Figure 57. Detail of ten downstream measurement locations for dimples (not to scale). . . . .	92
Figure 58. Measured velocity and turbulence profiles behind a dimple at 50%. . . . .	94
Figure 59. Measured velocity and turbulence profiles behind a dimple at 55%. . . . .	95
Figure 60. Measured velocity and turbulence profiles behind a dimple at 65%. . . . .	96
Figure 61. Measured velocity and turbulence profiles behind a dimple at 50%. . . . .	98
Figure 62. Measured velocity and turbulence profiles behind a dimple at 55%. . . . .	99
Figure 63. Measured velocity and turbulence profiles behind a dimple at 65%. . . . .	100
Figure 64. Exit velocity profiles for Dimples at 50% chord. . . . .	102
Figure 65. Exit velocity profiles for Dimples at 55% chord. . . . .	103
Figure 66. Exit velocity profiles for Dimples at 65% chord. . . . .	104
Figure 67. Wake momentum values for baseline blade, and dimples at 50%, 55%, and 65% chord. . . . .	105

	Page
Figure 68. Exit stagnation pressure loss for dimples at 50% . . . . .	107
Figure 69. Exit stagnation pressure loss for dimples at 55% . . . . .	107
Figure 70. Exit stagnation pressure loss for dimples at 65% . . . . .	108
Figure 71. Exit stagnation pressure loss for dimples at 50% with $Tu = 4\%$ . . . . .	109
Figure 72. Exit stagnation pressure loss for dimples at 55% with $Tu = 4\%$ . . . . .	110
Figure 73. Exit stagnation pressure loss for dimples at 65% with $Tu = 4\%$ . . . . .	110
Figure 74. Loss coefficient for baseline blade and dimples located at 50%, 55%, and 65% axial chord. . . . .	112
Figure 75. Large scale V-groove separation control design. . . . .	113
Figure 76. Measured velocity and turbulence profiles between V-grooves starting at 55%. . . . .	115
Figure 77. Measured velocity and turbulence profiles between V-grooves starting at 60%. . . . .	116
Figure 78. Measured velocity and turbulence profiles between V-grooves starting at 55%. . . . .	118
Figure 79. Measured velocity and turbulence profiles between V-grooves starting at 60%. . . . .	119
Figure 80. Tripped boundary layer profiles at 67% chord for V-grooves starting at 55%. . . . .	120
Figure 81. Tripped boundary layer profiles at 84.8% chord for V-grooves starting at 55%. . . . .	120
Figure 82. Tripped boundary layer profiles at 67% chord for V-grooves starting at 60%. . . . .	121
Figure 83. Tripped boundary layer profiles at 84.8% chord for V-grooves starting at 60%. . . . .	121

	Page
Figure 84. Exit velocity profiles for V-grooves starting at 55% chord. . . . .	123
Figure 85. Exit velocity profiles for V-grooves starting at 60% chord. . . . .	124
Figure 86. Exit velocity profiles for V-grooves starting at 55% chord with boundary layer trip. . . . .	125
Figure 87. Exit velocity profiles for V-grooves starting at 60% chord with boundary layer trip. . . . .	126
Figure 88. Wake momentum values for baseline blade, and V-grooves starting at 55% and 60% chord. . . . .	127
Figure 89. Exit stagnation pressure loss for V-grooves starting at 55% chord. . . . .	129
Figure 90. Exit stagnation pressure loss for V-grooves starting at 60% chord. . . . .	130
Figure 91. Exit stagnation pressure loss for V-grooves starting at 55% chord with boundary layer trip. . . . .	131
Figure 92. Exit stagnation pressure loss for V-grooves starting at 60% chord with boundary layer trip. . . . .	132
Figure 93. Loss coefficient for baseline blade and V-grooves starting at 55% and 60% chord. . . . .	133
Figure 94. Loss coefficient for baseline blade and V-grooves starting at 55% and 60% chord with boundary layer trip. . . . .	134
Figure 95. Improvement in loss coefficient using dimples at 50%, 55%, and 65% axial chord. . . . .	138
Figure 96. Effect of dimple distance from baseline separation on loss coefficient. . . . .	139
Figure 97. Change in loss coefficient using V-grooves with and without a trip wire. . . . .	142
Figure 98. Measured velocity and turbulence profiles between dimples at 50%. . . . .	148
Figure 99. Measured velocity and turbulence profiles behind a dimple at 50% with $Tu = 4\%$ . . . . .	149

	Page
Figure 100. Measured velocity and turbulence profiles between dimples at 50% with $Tu = 4\%$ . . . . .	150
Figure 101. Measured velocity and turbulence profiles between dimples at 55%. . . . .	151
Figure 102. Measured velocity and turbulence profiles behind a dimple at 55% with $Tu = 4\%$ . . . . .	152
Figure 103. Measured velocity and turbulence profiles between dimples at 55% with $Tu = 4\%$ . . . . .	153
Figure 104. Measured velocity and turbulence profiles between dimples at 65%. . . . .	154
Figure 105. Measured velocity and turbulence profiles behind a dimple at 65% with $Tu = 4\%$ . . . . .	155
Figure 106. Measured velocity and turbulence profiles between dimples at 65% with $Tu = 4\%$ . . . . .	156
Figure 107. Measured velocity and turbulence profiles between dimples at 50%. . . . .	157
Figure 108. Measured velocity and turbulence profiles behind a dimple at 50% with $Tu = 4\%$ . . . . .	158
Figure 109. Measured velocity and turbulence profiles between dimples at 50% with $Tu = 4\%$ . . . . .	159
Figure 110. Measured velocity and turbulence profiles between dimples at 55%. . . . .	160
Figure 111. Measured velocity and turbulence profiles behind a dimple at 55% with $Tu = 4\%$ . . . . .	161
Figure 112. Measured velocity and turbulence profiles between dimples at 55% with $Tu = 4\%$ . . . . .	162
Figure 113. Measured velocity and turbulence profiles between dimples at 65%. . . . .	163
Figure 114. Measured velocity and turbulence profiles behind a dimple at 65% with $Tu = 4\%$ . . . . .	164

	Page
Figure 115. Measured velocity and turbulence profiles between dimples at 65% with $Tu = 4\%$ . . . . .	165
Figure 116. Measured velocity and turbulence profiles inside a V-groove starting at 55%. . . . .	166
Figure 117. Measured velocity and turbulence profiles between V-grooves starting at 55% with $Tu = 4\%$ . . . . .	167
Figure 118. Measured velocity and turbulence profiles inside a V-groove starting at 55% with $Tu = 4\%$ . . . . .	168
Figure 119. Measured velocity and turbulence profiles inside a V-groove starting at 60%. . . . .	169
Figure 120. Measured velocity and turbulence profiles between V-grooves starting at 60% with $Tu = 4\%$ . . . . .	170
Figure 121. Measured velocity and turbulence profiles inside a V-groove starting at 60% with $Tu = 4\%$ . . . . .	171
Figure 122. Measured velocity and turbulence profiles inside a V-groove starting at 55%. . . . .	172
Figure 123. Measured velocity and turbulence profiles between V-grooves starting at 55% with $Tu = 4\%$ . . . . .	173
Figure 124. Measured velocity and turbulence profiles inside a V-groove starting at 55% with $Tu = 4\%$ . . . . .	174
Figure 125. Measured velocity and turbulence profiles inside a V-groove starting at 60%. . . . .	175
Figure 126. Measured velocity and turbulence profiles between V-grooves starting at 60% with $Tu = 4\%$ . . . . .	176
Figure 127. Measured velocity and turbulence profiles inside a V-groove starting at 60% with $Tu = 4\%$ . . . . .	177
Figure 128. Cross-sectional area of wind tunnel. . . . .	178

	Page
Figure 129. Unmodified Aerolab wind tunnel. . . . .	179
Figure 130. Turbulence grid capable of producing high turbulence levels with and without blowing air. . . . .	180
Figure 131. Decay of passive grid turbulence with downstream position. . . . .	181
Figure 132. Turbulence generator placement upstream of straight test section. . . . .	183
Figure 133. Front and top views of the pressure control system for active turbulence generation using blown air. . . . .	184
Figure 134. New linear cascade test section with independently adjustable inlet and exit angle capability. . . . .	186
Figure 135. Side view of blade cassette . . . . .	187
Figure 136. Software used for calibration of the hot wire. . . . .	191
Figure 137. Relationship between tunnel inlet velocity, Reynolds number, and drive motor setting. . . . .	192
Figure 138. Current tunnel conditions determination program. . . . .	193
Figure 139. Tunnel test section 3-axis coordinate system used with the Dantec traverse. . . . .	195
Figure 140. Velocity and turbulence measurements made using 3-axis traverse and hot wire probe program. . . . .	196
Figure 141. Pressure transducer calibration software. . . . .	198
Figure 142. Exit wake total pressure and velocity measurement program. . . . .	199
Figure 143. Blade surface pressure coefficient data collection program. . . . .	201
Figure 144. Boundary layer traverse software. . . . .	204
Figure 145. Turbulent length scale determination software. . . . .	207

	Page
Figure 146. Power spectrum for inlet conditions of $Re = 50k$ and $Tu = 4\%$ . . . . .	210
Figure 147. Normalized auto-correlation function for inlet conditions of $Re = 50k$ and $Tu = 4\%$ . . . . .	211
Figure 148. Radius of curvature plots for Pak-B blade. . . . .	218
Figure 149. Plow, Semi-Circle and Vane concepts eliminated by available data. . . . .	230
Figure 150. Porous suction surface methods. . . . .	232
Figure 151. Rejected methods with difficult application. . . . .	234
Figure 152. Other submerged design modifications considered and rejected. . . . .	236
Figure 153. Large-Scale vortex generator using NACA airfoil. . . . .	241
Figure 154. Transverse groove separation control device. . . . .	242
Figure 155. Surface roughness strip applied to Pak-B airfoil. . . . .	243

## List of Tables

	Page
Table 1. Baseline Pak-B data collected . . . . .	20
Table 2. Flow inlet angles for blade 5 and 2-D VBI software model . . . . .	26
Table 3. Reynolds number conversion . . . . .	197
Table 4. 2-D VBI code aerodynamic inputs . . . . .	212

## List of Symbols

### English Symbols

Symbol	Definition
$a$	Speed of sound (m/s)
$a_{0-4}$	Constants used in data acquisition software
$A_\epsilon$	Vane Blade Interaction code software constant
$A_\mu$	Vane Blade Interaction code software constant
$b$	Space between riblet channels (mm)
$b_{0-3}$	Constants used in data acquisition software
$c$	Axial chord length (cm)
$c$	Specific fuel consumption (kg/N·s)
$c$	Velocity (m/s)
$c_{0-2}$	Constants used in data acquisition software
$c_p$	Specific heat at constant pressure $\left(\frac{J}{kg \cdot K}\right)$
$C_D$	Drag coefficient
$C_D$	Actual to ideal mass flow rate
$C_f$	Skin friction coefficient
$C_{fg}$	Ideal to actual thrust ratio
$C_{int}$	Intercept of hot wire calibration curve
$C_L$	Lift coefficient
$C_p$	Pressure coefficient
$C_V$	Actual to ideal velocity ratio
$C_\mu$	Software constant

D	Diameter (mm)
$d_{0-2}$	Constants used in data acquisition software
$D_{loc}$	Optimal dimple location (% chord)
$D_{slo}$	Slope of hot wire calibration curve
$d_w$	Diameter of hot wire filament (mm)
$e_{0-3}$	Constants used in data acquisition software
e	Energy ( $m^2/s^2$ )
f	Frequency (1/s)
f	Fuel to air ratio
$F_{1-5}$	Variables used in data acquisition software
$F_g$	Thrust (N)
$f_\mu$	Dimensionless software variable
G	Power spectrum
h	Height of surface roughness (mm)
$h^+$	Nondimensional height of surface roughness
$h_v$	Heating value of the fuel
H	Shape factor
HP	Horsepower
$\bar{I}$	Unit tensor
k	Roughness height (mm)
k	Thermal Conductivity ( $\frac{W}{m \cdot K}$ )
k	Turbulent kinetic energy ( $\frac{m^2}{s^2 \cdot kg}$ )
k	Variable used in data acquisition software
l	Length (mm)

$L_I$	Integral length scale (mm)
$\dot{m}$	Mass flow rate (kg/s)
$m_f$	Humidity mass fraction
$M_\infty$	Freestream Mach number
$M_w$	Molecular weight of air
$Mw_{air}$	Molecular weight of dry air
$Mw_{H_2O}$	Molecular weight of water
$n$	Number of data points
$Nu$	Nusselt number
$P$	Pressure $\left(\frac{kg}{cm^2}\right)$
$Pr$	Prandtl number
$\vec{q}$	Heat flux vector
$\dot{Q}$	Rate of heat interaction (J/s)
$R$	Range (m)
$\mathfrak{R}$	Transport variable
$R$	Gas Constant $\left(\frac{J}{kg \cdot K}\right)$
$Re$	Reynolds number based on axial chord length and inlet velocity
$Re_{exp}$	Exponent used in hot wire calibration
$Re_k$	Reynolds number based on roughness height
$Re_T$	Turbulent Reynolds number
$Re_\theta$	Reynolds number based on momentum thickness
$s$	Entropy $\left(\frac{J}{kg \cdot K}\right)$
$s$	Spanwise spacing of surface roughness (mm)
$s$	Blade spacing (cm)

S	Traverse slot number
$s^+$	Nondimensional spanwise spacing of surface roughness
t	Thickness of riblet material (mm)
t	Time (sec)
T	Temperature (Celsius)
$T_D$	Dewpoint (Celsius)
$T_g$	Recovery temperature (Kelvin)
$T_I$	Integral time scale (sec)
$T_K$	Temperature (Kelvin)
$T_m$	Gas temperature (Kelvin)
$T_R$	Overheat ratio exponent for hot wire
Tu	Freestream turbulence level in percent
U	Velocity (m/s)
$u_k$	Velocity at top of roughness elements (m/s)
V	Vee shape formed by two adjoining vortex generators
V	Voltage (volts)
$\vec{V}$	Absolute velocity (m/s)
w	Width of flow modification device (mm)
W	Mass of aircraft (kg)
$\dot{W}$	Work (J/s)
$\vec{W}$	Relative velocity (m/s)
x	Streamwise spatial distance (cm)
X	Mole fraction
y	Spatial distance (m)

$y^+$	Dimensionless wall distance
Z	Variable used in data acquisition software

### Greek Symbols

Symbol	Definition
$\gamma$	Total pressure loss coefficient
$\gamma$	Ratio of specific heats
$\delta_0$	Unmodified boundary layer height at 99% of freestream velocity (mm)
$\delta$	Boundary layer height at 99% of freestream velocity (mm)
$\delta^*$	Displacement thickness
$\varepsilon$	Turbulent dissipation
$\eta$	Efficiency
$\theta$	Momentum thickness
$\Theta$	Momentum wake deficit
$\Lambda$	Sweep angle of flow modification device, degrees
$\mu$	Viscosity $\left(\frac{kg}{m \cdot s}\right)$
$\mu_u$	Variable used in data acquisition software
$\nu$	Kinematic viscosity $\left(\frac{m^2}{s}\right)$
$\vec{\omega}$	Angular velocity (radians/s)
$\rho$	Density $\left(\frac{kg}{m^3}\right)$
$\rho_x$	Normalized auto-correlation curve
$\sigma$	Deviation
$\tau$	Time (sec)
$\tau$	Shearing stress (1/sec)

$\overline{\overline{\tau}}_e$	Viscous stress tensor
$\phi$	Favre average example variable
$\phi_{a,b}$	Variables used in data acquisition software
$\psi_{a,b}$	Variables used in data acquisition software
$\Omega$	Resistance (ohms)

### Subscripts

Symbol	Definition
$\infty$	Freestream condition
$\theta$	Relation using momentum thickness
0	Original unmodified reference value
0	Surface value
0	Total value
0 – 9	Engine station numbers
1	Final value
<i>a</i>	Reference to air
<i>A</i>	Atmospheric reference condition
<i>c</i>	Chord length (mm)
<i>crit</i>	Critical value for roughness
<i>e</i>	Effective
<i>exit</i>	Blade cassette exit plane value
<i>g</i>	Gas value
<i>inlet</i>	Blade cassette inlet plane value
<i>int</i>	Calibration intercept value

<i>k</i>	Roughness value
<i>L</i>	Lift (N)
<i>m</i>	Mean value
<i>max</i>	Maximum
<i>P</i>	Pressure ( $\frac{N}{m^2}$ )
<i>R</i>	Rotor blade value
<i>rms</i>	Root-mean-square
<i>root</i>	Root of airfoil
<i>s</i>	Surface static value
<i>slo</i>	Calibration slope value
<i>static</i>	Static reference value
<i>surface</i>	Blade surface value
<i>t</i>	Turbulent quantity
<i>T</i>	Turbulent
<i>tip</i>	Tip of airfoil
<i>total</i>	Total reference value
<i>x</i>	Surface location number
<i>y</i>	Specific distance location
<i>v</i>	Reference to water
<i>w</i>	Exit velocity magnitude
<i>w</i>	Wire value
<i>wall</i>	Static reading from test section wall surface

## Superscript

Symbol	Definition
—	mean value
/	Fluctuating component
<i>t</i>	Turbulent quantity

## Abbreviations

Abbreviation	Definition
2-D	Two-dimensional
3-D	Three-dimensional
AC	Alternating current
AFIT	Air Force Institute of Technology
AFRL	Air Force Research Laboratory
CFD	Computational Fluid Dynamics
DC	Direct current
Gb	Gigabyte
Hz	Hertz (1/sec)
LES	Large Eddy Simulation
LPT	Low Pressure Turbine
N-S	Navier-Stokes
ODE	Ordinary Differential Equation
SFC	Specific fuel consumption
SR	Sampling Rate
VBI	Vane-Blade Interaction software

VG                    Vortex generator  
VI                    Virtual Instrument software

## Abstract

The problem of flow separation from a low pressure turbine blade was investigated. The operating conditions under which the separation occurred were documented through measurement of surface pressure coefficients, boundary layer velocity and turbulence profiles, total pressure loss coefficient and wake velocity momentum deficit. Three different means for reducing the losses associated with the flow separation were also investigated. A boundary layer trip, dimples, and V-grooves were studied as passive means requiring no additional energy to reduce the separation losses. The boundary layer trip was only successful for an inlet and axial chord Reynolds number of 50k with a reduction in loss coefficient of 58.2%. Three sets of dimples were tested with the placement of each at axial chord locations of 50%, 55%, and 65%. The dimples provided reductions in the loss coefficient for Reynolds numbers of 50k, 100k, and 200k ranging from 5.1% ( $Re = 100k$ , freestream turbulence level of 4%) to 51.7% ( $Re = 50k$ , freestream turbulence level of 4%). Two sets of V-grooves were tested with axial chord start locations of 55% and 60%. The V-grooves provided smaller reductions in loss coefficient than the dimples. Boundary layer profiles, total pressure loss coefficients, and wake velocity momentum deficits are presented for the three passive modifications.

# **Flow Separation Prevention on a Turbine Blade in Cascade at Low Reynolds Number**

## **Chapter 1 - Introduction**

The recent Air Force interest in the use of Unmanned Aerial Vehicles (UAV) for reconnaissance has led to new requirements for turbomachinery engine designers. The low Reynolds number effects of high altitude, low temperatures and sustained low speed cruise velocities for smaller engines has shown inefficiencies due to flow separation losses with the low pressure turbine (LPT). For example, UAV aircraft such as the Teledyne Ryan Tier II+ Global Hawk using the Allison AE3007-H 3-stage low pressure turbine (LPT) suffer from this loss of efficiency (MacArthur [1]) while flying at its operational altitude of 19.812 km (65,000 feet) at a standard cruise velocity of 176.4 m/s (343 Kts TAS). The author proposes that surface modifications to LPT blades can reduce these losses by maintaining attached flow across the surface of the blades. With the blade efficiency increased, loiter time, range, and performance will all improve.

To solve the loss in efficiency problem a technique has been developed that promotes attached flow over the suction surface of the blade at low Reynolds numbers but does not inhibit the already acceptable flow field present with high Reynolds numbers. To accomplish this, passive techniques requiring no additional power from the engine or additional weight have been studied. These passive techniques provide a solution to one of the most recently discovered problems with turbomachinery.

### **1.1 Low Pressure Turbine**

Investigation of LPT efficiency has remained largely neglected until recent years despite the many improvements and research conducted over the last six decades for other turbomachinery components. The compressor has been improved by increasing its efficiency and overall pressure

ratio as well as the individual stage pressure ratios. The high pressure turbine has been improved by increasing its allowable maximum temperature through cooling techniques. The lower temperature characteristics of the low pressure turbine do not require active cooling in modern engines, and hence more focus is given to improving the LPT blades' aerodynamic performance.

Pratt and Whitney introduced the Pak-B blade in an attempt to improve the low Reynolds number efficiency of the LPT. The Pak-B blade shape is a modified version of the commercially used Pak airfoil. The Pak-B airfoil was intentionally designed for lower Mach number operation. While in operation, each of the blades in the low pressure turbine shed wakes which travel downstream. When these wakes come into contact with a blade in the next row, the wake passes over the surface. This region inside the wake has a higher freestream turbulence level than the air upstream and downstream of it. The turbulence level inside the wake may reach up to 20% (Halstead [2,3]). While this higher turbulence level provides a beneficial effect with boundary layer attachment, the duration is only intermittent. Between wakes, the flow over the suction surface of the blade is laminar with separation occurring for the low Reynolds numbers typical of UAV missions. Experiments by Murawski et al. [4] and Qiu and Simon [5] have shown that losses associated with separation decrease the effectiveness of the Pak-B blades (see Figure 1) at low Reynolds numbers.

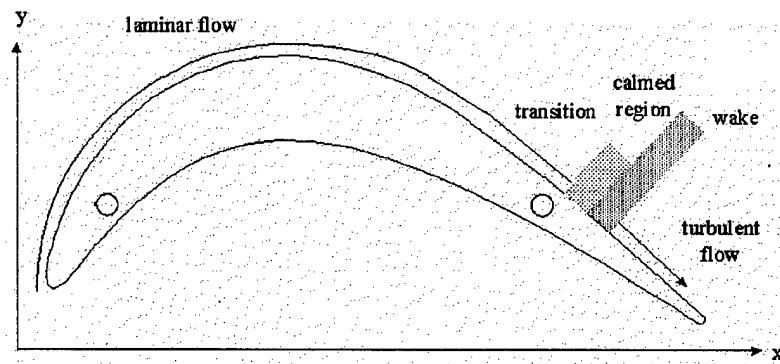


Figure 1. Unsteady wake passing over Pak-B blade surface (mounting pin locations also shown).

In addition to the work of Murawski et al. [4], ongoing efforts by Simon and Volino [6] focusing on the low pressure Pak-B turbine blade have also shown separation losses for applications at high altitudes and low temperatures. These lower Reynolds number effects have been receiving increasing attention and the problem is now understood as one of separation and transition over the suction surface of the blade due to regions of strong pressure gradient and diffusion. Hourmouziadis [7] has shown that for these low Reynolds number environments profile losses rise sharply and efficiency is decreased.

## **1.2 Previous Low Pressure Turbine Experiments**

To document the existing baseline efficiency of the Pak-B blade, linear cascade tunnels have been used to simulate the engine operating environment. A linear cascade tunnel contains blades arranged in a row, as if the low pressure blade spool were cut and unrolled onto a flat surface. Many experimenters have chosen to use linear cascades for their LPT experiments including Rivir [8], Murawski et al. [4], and Qiu and Simon [9]. Murawski et al. [4] and Qiu and Simon [9] have documented the existing separation that exists on the Pak-B LPT blade at low Reynolds numbers. Rivir [8] investigated the effect of turbulent length scale on transition location for the Langston airfoil previously described by Baughn et al. [10]. Murawski et al. [4] and Qiu and Simon [9] verified the basic low Reynolds number separation problem of the Pak-B airfoil with measurements of velocity, surface pressure, separation location, and boundary layer thickness. Murawski et al. [4] found the Pak-B to have suction surface separation extending from the 75% to 90% chord at a low inlet and axial chord Reynolds number of 53,000. Qiu and Simon [9] documented the reattachment of turbulent flow downstream of the 90% chord position. The boundary layer thickness shows a significant increase with flow separation, which decreases overall performance. To better understand the effect of separation bubbles, a brief explanation is given.

Werle [11] classified separation that occurs on turbine blades into four categories that include leading edge bubbles, transonic shock induced separation, pressure side bubbles, and trailing edge wake separation. Recent tests by Murawski et al. [4] and Qiu and Simon [9] have shown that operation at low Reynolds numbers can lead to an additional form of separation where the laminar flow detaches due to the strong streamwise pressure gradient. Once the laminar flow separates from the suction side of the blade, transition can occur. The separated flow transition which occurs on the Pak-B blade is one of three modes of transition that have been defined by Mayle [12] and Halstead [13]. These three modes of boundary layer transition are natural transition, bypass transition and separated-flow transition. The control of this particular form of separated-flow transition and laminar separation over the Pak-B blade is the focus of this research.

Most past experiments have focused on the airflow over blades of existing design, with almost no comparable experiments on slightly modified blades to improve upon the performance. One exception to this is Chen et al. [14] who attempted to decrease separation losses for compressor airfoils using riblets on the suction side of the airfoil - the experiment was unsuccessful. The poor performance of the riblets on convex surfaces excluded their use in this experiment. The modification of turbine blades with passive surface features to reduce separation has never been attempted before. The possibilities for passive surface modifications goes beyond just low pressure turbines. Passive techniques could be used on other aircraft parts such as propellers (Occhipinti [15]) or even automobiles. This research documents successful integration of surface modifications with the Pak-B airfoil which reduced the losses associated with separated flow.

### **1.3 Current Research Focus**

This project focused on the control of low Reynolds number separation effects on low pressure turbine blades of the Pratt and Whitney Pak-B blade design. In particular, measurements of

separation and loss coefficient were made for the unmodified Pak-B blades. Data was taken for freestream turbulence ( $Tu$ ) levels of 1% and 4% to model various engine operating conditions for low inlet Reynolds numbers ( $Re$ ) of 50,000, 100,000 and 200,000. These Reynolds numbers are typical of the conditions a UAV low pressure turbine blade will operate under during a mission. The turbulence intensities are typical of the regions of flow over the blade between wakes.

The modifications to the Pak-B blade included the use of a trip wire, dimples, and longitudinal V-grooves as a means of reducing separation losses. The benefits of dimples in a cylinder was shown by Bearman and Harvey [16, 17], while application of V-grooves to the surface of a convex ramp was tested by Lin et al. [18]. An investigation into the use of a simple wire to trip the boundary layer from a laminar state to a turbulent one was also investigated. More information on the above surface modifications are presented in Chapters 7, 8, and 9. A typical test sequence included blade surface modifications made to an existing central blade of the cascade and subsequent re-examination (varied Reynolds number and turbulence level) for the improvements in reducing separation and improving loss coefficient. The overall purpose of this project was to demonstrate that a turbine blade with separation problems at low Reynolds numbers, if properly modified, will experience reduced flow separation and improved blade performance.

#### **1.4 Determination of Improved Performance**

To better judge the merit of the research a numerical parameter is required for comparison. Improvements to aircraft performance such as range, fuel economy and engine thermal efficiency are factors which can be easily compared to a baseline case. Aircraft range can be estimated from the Breguet range formula (Anderson [19]):

$$R = \frac{\eta_0}{c} \frac{C_L}{C_D} \ln \frac{W_0}{W_1} \quad (1)$$

where  $\eta_0$  is the overall engine efficiency and  $c$  is the specific fuel consumption. Also in equation 1 is the ratio of lift ( $C_L$ ) to drag ( $C_D$ ) coefficients and the ratio of the initial weight ( $W_0$ ) of the aircraft to the final weight ( $W_1$ ). Equation 1 can be re-arranged in terms of the weight of fuel expended:

$$\Delta W_{fuel} = W_1 \left[ \exp \left( \frac{Rc C_D}{\eta_0 C_L} \right) - 1 \right] \quad (2)$$

where  $\Delta W_{fuel} = W_0 - W_1$ . Examination of equation 1 and equation 2 shows two definite advantages to improving the overall engine efficiency - increased range or decreased fuel consumption.

The thermal efficiency is expressed by the increased kinetic energy imparted to the gas per unit of heat energy supplied by the fuel. For a stationary engine (e.g. in a test cell) this simplifies to:

$$\eta_{th} = \frac{\left( \frac{c_9^2}{2} \right)}{f h_v} \quad (3)$$

where  $c_9$  is the nozzle exit velocity,  $f$  is the fuel-air ratio and  $h_v$  is the heating value of the fuel. It will be shown later that reduced total pressure losses result in an increase in  $c_9$  and hence an increase in thermal efficiency.

The engine efficiency can be determined with the aid of a T-S diagram. A T-S diagram depicts the change in entropy with the change in temperature for a given engine cycle. For example, the ideal jet engine can be depicted with the Brayton cycle shown in Figure 2 (Mattingly [20]). Figure 2a depicts the T-S diagram for the components shown in Figure 2b. The compressor increases the pressure of the air from step 2 to 3 without an increase in entropy (isentropically). As seen in Figure 2a, the increase in pressure also increases the temperature of the air. From step 3 to 4 the fuel is burned and heat is added to the system. In the ideal process, the addition of heat to the system is assumed to occur at a constant pressure. The hot air expands from step 4 to 9 as the air exits through the turbine blades and exhaust nozzle. The expansion through the turbine is also assumed to be isentropic. Finally, the heat from the engine is rejected externally through a constant pressure process from step 9 to 0.

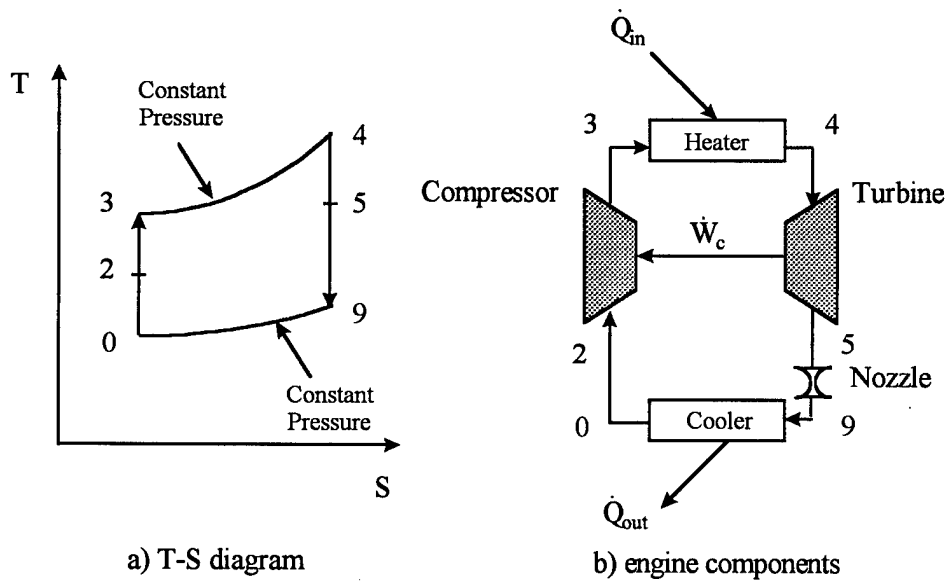


Figure 2. Brayton cycle for an ideal gas jet engine.

The work of each of the components in Figure 2b are depicted as  $\dot{W}$ . The work of the compressor is defined as:

$$\dot{W}_c = \dot{m} c_p (T_{t3} - T_{t2}) \quad (4)$$

where  $\dot{m}$  is the mass flow rate and  $c_p$  is the ratio of specific heats at constant pressure. The change in temperature across the compressor is included as  $T_{t3} - T_{t2}$ . The work of the turbine is equal to the work required by the compressor:

$$\dot{W}_c = \dot{W}_t = \dot{m} c_p (T_{t4} - T_{t5}) \quad (5)$$

where  $\dot{W}_t$  is defined similarly to equation 4 for the turbine. The actual work output of a turbine is less than ideal due to losses. The losses in an engine can be described with a T-S diagram for each part of the jet engine.

Figure 3a shows the station numbers for the stator and rotor blades. The passage between the blades is from station 2 to 2R. The exit passage to the next stage is from station 3R to 3. The work done by the rotor blades occurs from station 2R to 3R. For discussion purposes it will be assumed that the flow in the space between the blade rows is isentropic. The T-S diagram for a typical low pressure turbine stage is illustrated in Figure 3b.

As seen in Figure 3b, the generation of entropy over the rotor decreases the total pressure at station 3R. This decrease in total pressure is carried through to the exit (station 3) of the stage. The greater the drop in stagnation pressure, the lower the efficiency of the stage. The passive techniques tested reduce this pressure loss and therefore increase the stage efficiency of the low pressure turbine.

The results of the experiment discussed in Chapters 6 through 9 showed the potential for reducing the stagnation pressure drop over a set of blades. A reduction in pressure drop increases the efficiency of the low pressure turbine stage and hence engine efficiency overall. The maximum reduction in stagnation pressure drop is depicted in Figure 3b. For zero losses the values at  $t_{3R}$  and  $t_{2R}$  are coincident, and  $P_{t_{3R}}$  (also  $P_{t_{2R}}$ ) are increased to ideal values. For a given temperature drop

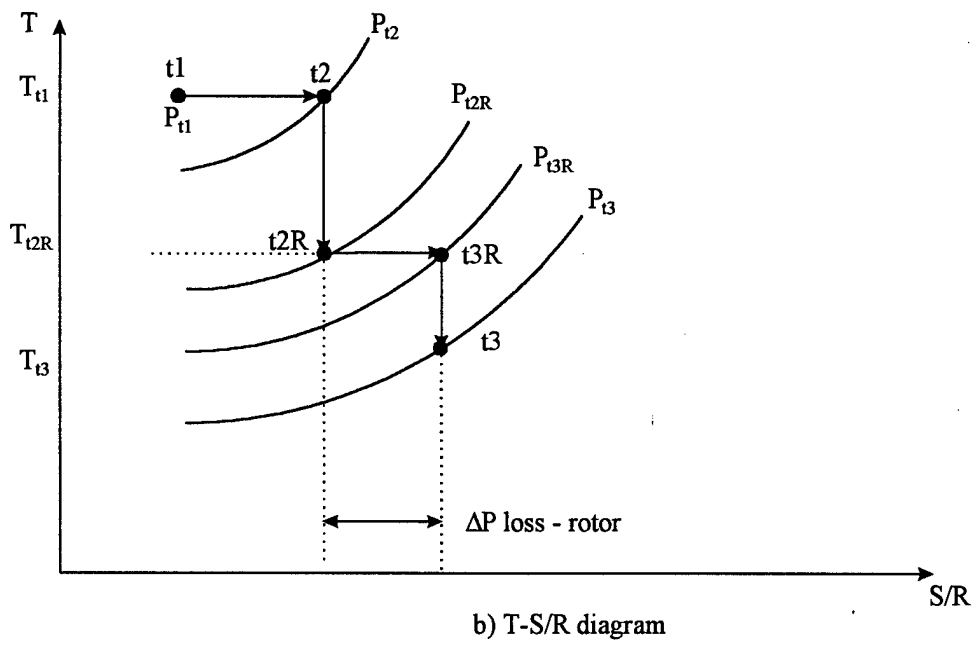
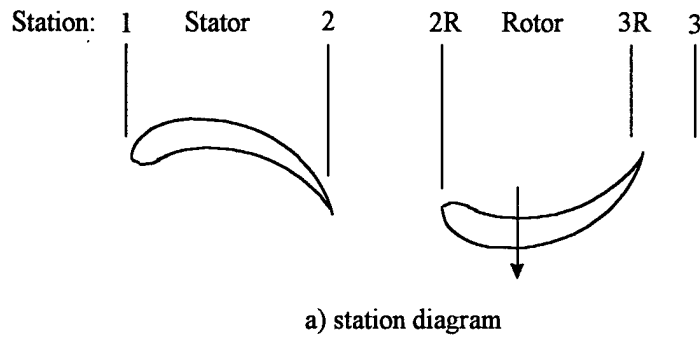


Figure 3. T-S diagram of a typical low pressure turbine stage.

across the LPT stage, a higher exit pressure ( $P_{t3}$ ) for the same inlet pressure ( $P_{t1}$ ) will correlate with a decrease in the production of entropy. This can be represented by the Gibbs equation (Mattingly [20]):

$$ds = c_p \frac{dT}{T} - R \frac{dP_t}{P_t} \quad (6)$$

where  $R$  is the gas constant. For a constant temperature equation 6 reduces to:

$$\frac{ds}{R} = -\frac{dP_t}{P_t} \quad (7)$$

for the case of constant temperature. The relation between pressure drop and efficiency for the turbine stage is represented by (Mattingly [20]):

$$\eta_t = \frac{1 - \tau}{1 - \pi_t^{(\gamma-1)/\gamma}} \quad (8)$$

where  $\tau = T_{t3}/T_{t1}$  and  $\pi_t = P_{t3}/P_{t1}$ . The pressure  $P_{t3}$  is a function of the loss coefficient:

$$P_{t3} = \frac{P_{t2R}}{1 + \gamma_{loss} \left[ 1 - \left( \frac{T_3}{T_{t3R}} \right)^{\gamma/(\gamma-1)} \right]} \left( \frac{T_{t3}}{T_{t3R}} \right)^{\gamma/(\gamma-1)} \quad (9)$$

where  $\gamma_{loss}$  is defined as the loss coefficient and  $\gamma$  is the ratio of specific heats. Equation 8 shows that for a given temperature ratio across the blades, a larger pressure ratio ( $\pi_t$ ) will increase the efficiency,  $\eta$ . The magnitude of typical LPT stage efficiencies can be determined from numbers representative of a jet engine. Assuming initial values of  $\tau = 0.84$ ,  $P_{t3} = 748.1$  kPa,  $P_{t2r} = 1043.0$  kPa,  $T_3 = 1505.5$  K,  $T_{t3R} = 1664.4$  K,  $T_{t3} = 1560.0$  K, and  $\gamma_{loss} = 0.15$  for equations 9 and 8, the baseline loss coefficient is  $\eta_t = 90.87\%$ . As  $\gamma_{loss}$  is reduced  $\pi_t$  increases and improvement in stage efficiency with reduction of loss coefficient can be determined from equations 8 and 9. Figure 5 shows that a 10% reduction in loss coefficient can improve stage efficiency by 0.57%. The resulting linear curve shows that:

$$\frac{\Delta\eta}{\eta} \approx 0.057 \cdot \left( \frac{\Delta\gamma}{\gamma} \right) \quad (10)$$

where  $\frac{\Delta\eta}{\eta}$  is the percent increase in efficiency and  $\frac{\Delta\gamma}{\gamma}$  is the percent reduction in loss coefficient.

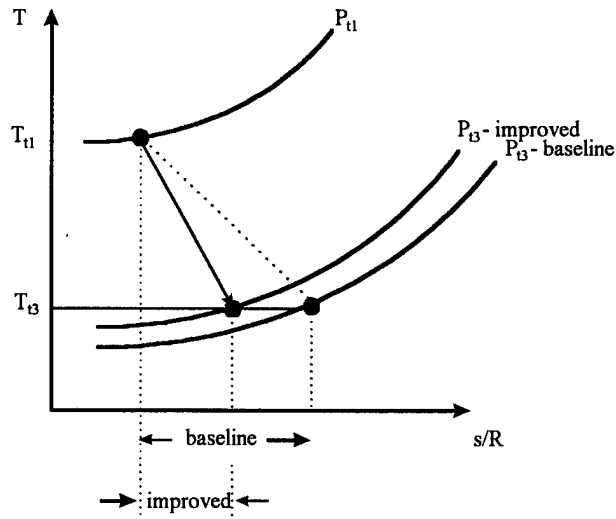


Figure 4. T-S diagram showing improvement possible with decrease in pressure drop.

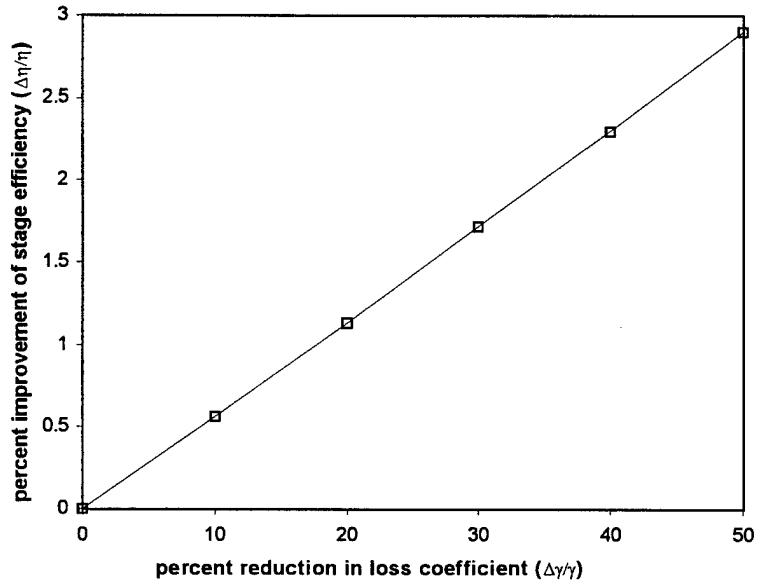


Figure 5. Trend of increasing stage efficiency with reduction in loss coefficient.

### 1.4.1 Comparison of Experimental Loss Coefficients

Installation of a passive separation control method into an existing engine would change the stagnation pressure drop across the modified blades. The change in pressure drop for a variety of passive techniques can be compared using a non-dimensional form. The nondimensional loss coefficient can be defined using the nomenclature of Figure 3:

$$\gamma = \frac{P_{t2R} - P_{t3R}}{\frac{1}{2}\rho U_{3R}^2} \quad (11)$$

where  $P_{t2}$  and  $U_2$  are measured downstream of the blade.

The increase in exit pressure within the engine due to the reduction in separation losses is also a consideration. For ideal operation, the engine exit static pressure,  $P_9$  is equal to the atmospheric pressure,  $P_0$ . Using the station numbers in Figure 6, the ratio of actual thrust ( $F_g$ ) to ideal thrust can be written as:

$$C_{fg} = \frac{F_{g-actual}}{F_{g-ideal}} = C_D C_V \sqrt{\frac{1 - \left(\frac{P_{9i}}{P_{ts}}\right)^{(\gamma-1)/\gamma}}{1 - \left(\frac{P_0}{P_{ts}}\right)^{(\gamma-1)/\gamma}}} \left[ 1 + \frac{\gamma-1}{2\gamma} \frac{1 - \frac{P_0}{P_9}}{\left(\frac{P_{t9}}{P_9}\right)^{(\gamma-1)/\gamma} - 1} \right] \quad (12)$$

where  $C_D$  is the actual to ideal mass flow rate ratio and  $C_V$  is the actual to ideal velocity ratio. Considering the recent works of Murawski et al. [4] and Qiu and Simon [5] which have shown that the pressure losses due to separation within the turbine stages operating at low Reynolds numbers are higher than expected, the pressure ratio  $P_0/P_9$  would no longer equal unity. Equation 12 indicates that with the increased pressure losses engine thrust is decreased for an engine with fixed exit area. The exit area is at station 9 in Figure 6a. For the case of a nozzle correctly expanding the flow, the T-S/R diagram of Figure 6b is useful. The relationship between temperature and pressure is:

$$T_9 = \left(\frac{P_{t9}}{P_9}\right)^{-(\gamma-1)/\gamma} T_{t9} \quad (13)$$

which can be substituted into the energy (assuming no heat addition and a calorically perfect gas) equation:

$$c_p (T_{t9} - T_9) = \frac{u_9^2}{2} \quad (14)$$

to yield:

$$c_p T_{t9} \left( 1 - \left( \frac{P_{t9}}{P_9} \right)^{-\frac{\gamma-1}{\gamma}} \right) = \frac{c_9^2}{2} \quad (15)$$

where an increase in engine pressure will lead to an increase in exit velocity. Since thrust is equal to the mass flow rate times the exit velocity, an increase in exit velocity increases the thrust and thermal efficiency (c.f., equation 3).

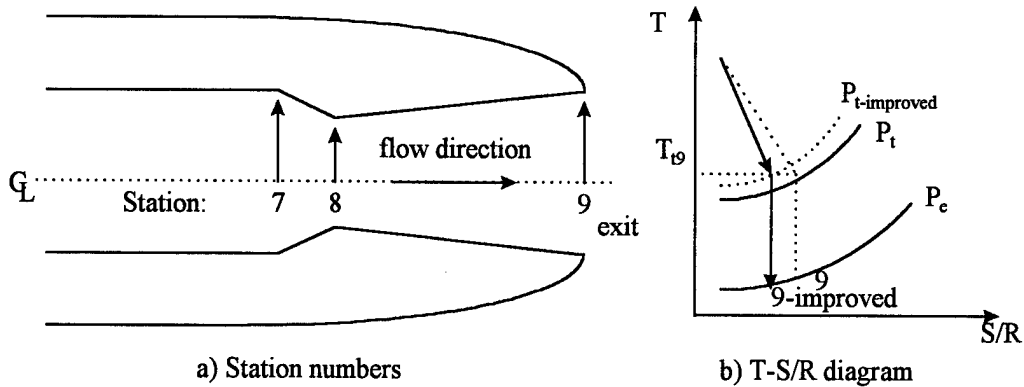


Figure 6. Station numbers and T-S/R diagram for exit nozzle.

## 1.5 Chapter Summary

Chapter 2 includes a discussion on boundary layer development and previously conducted experiments, followed by a description of the wind tunnel used in this research in Chapter 3. Chapter 4 explains the data collection equipment used in the wind tunnel. Simulations for the baseline performance using the 2-D VBI code are shown in Chapter 5. The baseline performance of the Pak-B blades is then discussed in Chapter 6, illustrating the severe losses caused by the flow separation. The results of using a boundary layer trip are presented in Chapter 7. Chapters 8 and 9 discuss the improved performance of the Pak-B blade with the addition of dimples or V-grooves to the surface

of the blade. The conclusions gained from the experiments and simulations are discussed last in Chapter 10.

## **Chapter 2 - Background and Theory**

### **2.1 Overview of Turbine Blade Boundary Layer Aerodynamics**

Low pressure turbine (LPT) blades have been studied more in the last ten years than in all the decades previously. Halstead et al. [2, 3] documented the flow consists of low to medium levels of freestream turbulence (1% to 20%), passing wakes, centrifugal effects and vortices. The unsteady nature of these interactions makes LPT flowfields a difficult problem to examine.

Experimental studies by Werle [11], Mayle [12] and Addison and Hodson [21] of low pressure turbine blades operating at low axial chord Reynolds numbers indicate a gradual transition process from laminar flow to turbulent flow over the suction side of the blade. The approximately steady transition process is interrupted by the time-dependent passing of wakes due to the motion of the rotor relative to the upstream stator. This cyclic influence quickly trips the flow through a fast succession of transitional, turbulent, and back to transitional state for a small region as the wake travels downstream (Halstead et al. [3]). This unsteady phenomena was not examined since the primary goal in this research project was to reduce the flow separation which occurs during non-wake periods. The results gained from the baseline blade experiments are valuable to programmers who need experimental data to increase the accuracy of their numerical models (Domey [22]).

### **2.2 Experimental and Numerical Studies of Turbine Boundary Layers**

Attempts to numerically model the complex effects in the low pressure turbine have met with only limited success due to the lack of experimental data for low Reynolds numbers (Werle [11]). To build better computational transition models for the low Reynolds number boundary layer of a LPT airfoil, detailed boundary layer velocity, turbulence, and pressure measurements are needed for determination of the simulations accuracy. Halstead et al. [2, 23] tested four different numerical models; STANX, KEP, a Navier-Stokes solver, and the Fan-Lakshminarayana code. Each of the

four codes used by Halstead et al. [2,23] have shown less-than-desirable accuracy in the simulation of low Reynolds number characteristics. A code that produces typically good outputs except in a low Reynolds number environment is the 2-D Allison Vane-Blade Interaction (VBI) code. The 2-D VBI code was used in this study to model the baseline Pak-B blade cassette for reasons discussed later. As with other codes the VBI results showed the code's inability to correctly model the region of separated flow. Like most codes, the 2-D VBI code was incapable of simulating the 3-D effects of the passive modifications to the Pak-B blades to improve efficiency. More accurate numerical models were not available for this research. Halstead and Solomon [24] have stated that perhaps only a full Large-Eddy Simulation (LES) code or even a Direct Numerical Simulation (DNS) would provide accurate results for blades with modified three dimensional surface features.

### **2.2.1 Experimental Determination of Laminar-to-Turbulent Transition Modes**

Perhaps the most important goal of examining turbomachinery blades is the determination of the location and length of transition over the blade surface. This goal is difficult due to the different possible causes of flow turbulence. The complexity of the mechanical design and unsteady flowfield are also complicating factors for experimenters.

Detailed experiments by Mayle [12] and Walker [25] showed that flow can enter transition over airfoil surfaces through three basic means depending on the Reynolds number, freestream turbulence and pressure gradients. The three means are natural transition, bypass transition, and separation bubble transition (Walker [25]). For natural transition to occur, the environment must consist of low freestream turbulence levels and no adverse pressure gradients. The first step of natural transition is the formation of 2-D Tollmien-Schlichting waves which amplify instabilities and create 3-D loop vortices and large fluctuations (Mayle [12]). These 3-D disturbances coalesce into turbulent spots which then grow as they travel downstream. Eventually these spots merge together in the cre-

ation of a fully turbulent boundary layer concluding the process identified by Walker [25] as natural transition.

For bypass mode transition to occur, flow conditions with freestream turbulence levels of approximately 20% are necessary. The initially laminar flow over the blade will immediately form turbulent spots (Mayle [12]) under such high turbulence levels. Since in this case the 2-D Tollmien-Schlichting waves are not found the term “bypass mode” is used (Walker [25]). Walker [25] determined that linear stability theory can still be valuable as a guide for bypass mode in the determination of the length of the transitional flow. The value of linear stability theory is due to the fact that although the 2-D Tollmien-Schlichting waves are bypassed in this mode, the disturbances within the boundary layer can still be predicted using linear stability theory (Walker [25]). The application of linear stability theory is, however, limited and unable to provide relevant results for separated flow transition.

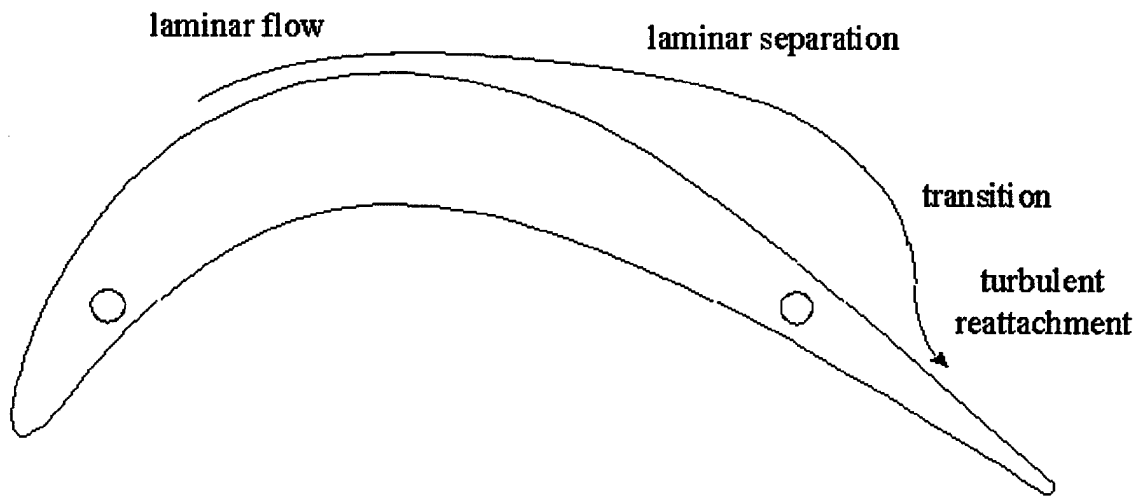


Figure 7. Laminar separation transition to turbulent flow.

For adverse pressure gradients the laminar flow may separate forming a separation bubble (see Figure 7). The fluid undergoes the transitional process, becoming turbulent while separated from the blade surface. Once the separated flow is fully turbulent, Qiu and Simon [9] and Mayle [12] showed the increased energy of the fluid enhances re-attachment of the flow to the surface of the blade. It is this form of laminar flow separation and turbulent flow reattachment that exists over the surface of the Pak-B blade at low Reynolds numbers. This research focused on the prevention of the laminar separation bubble to increase efficiency. The computational modelling of laminar separation is an attempt to identify conditions for bubble transition, but is very difficult.

### **2.2.2 Limitations of Numerical Code LPT Modelling**

The modelling of transition from laminar to turbulent flow is difficult to accomplish accurately. Freestream turbulence level, Reynolds number, and pressure gradient all influence the predicted results. To compare the influence of these different freestream factors, Reed et al. [26] examined many methods of predicting the linear stability of fluid flows. Most methods examined by Reed et al. [26] required some prior knowledge of the flow to predict the desired results. The  $e^N$  method (Reed et al. [26]), for example, requires the initial disturbance amplitude. Sharma et al. [27] determined that part of the reason numerical turbulence models have difficulty in predicting flow behavior is the nonisotropic nature of turbulence within some laminar and transitional boundary layers. Mueller [28] found that the accuracy from some software packages has been so poor that the software results would not only hinder engine design, but decrease engine performance. Much of this inaccuracy is due to the difficult nature of predicting the evolution and location of separation bubbles that form on the suction surface of the blade. These bubbles may completely separate and cause high losses for the blade at low Reynolds numbers (Werle [11] and Mayle [12]). Other codes for predicting the separation losses were investigated by Halstead et al. [23] and are discussed further in Appendix K.

The Allison 2-D Vane Blade Interaction (VBI) code was chosen for use in this research because of its efficient combination of airfoil wrapping O-grids and passage filling H-grids. The combination of the O and H grids in the VBI code provided more accurate results than would otherwise have been possible.

The 2-D VBI code is capable of modelling the flow of a low pressure turbine cascade and was used to provide initial surface pressure coefficient data for inlet chord Reynolds numbers of 50k, 100k, and 200k. While the 2-D VBI code predicted a small separation bubble at a Reynolds number of 50k, the code failed to predict separation bubbles for Reynolds numbers of 100k and 200k. Detailed information for the Allison 2-D VBI code such as user inputs and simulated boundary layer velocity profiles are included in Chapter 5 and Appendix E. The results presented using the 2-D VBI code illustrate the shortcomings even the advanced VBI code has.

Several authors including Rivir [8], Werle [11], and Mayle [12] have expressed the need for more experimental data to fully explain the flowfield within the LPT. The works of Halstead [13] and Addison and Hodson [21] have provided a significant increase in the understanding of unsteady wake phenomena and the existence of large regions of laminar and transitional flow; however much remains to be documented for low Reynolds number flowfields. Additional experimental data of boundary layer growth, turbulence intensities within the boundary layer, and turbulent length scales are all desired (Rivir, [29]) in understanding the problem of laminar separation bubbles.

### **2.3 Separation Control Using Passive Methods**

As shown in many experiments performed by Murawski et al. [4] and Qiu and Simon [9], separation is more apt to occur by decreasing either the axial chord Reynolds number below 300,000 or decreasing the freestream turbulence levels below 10%, conditions under which low pressure turbine blades frequently operate at altitude and cruise conditions. As the Reynolds number is de-

creased, the transition location moves aft towards the trailing edge on the suction surface of the blade. This effect combined with the lower freestream turbulence level (which prevents the flow from transitioning to a turbulent state) can combine to create a laminar separation bubble before transition. The laminar separation bubble creates losses which reduce the engine operating efficiency. Previous work by Murawski et al. [4] and Qiu and Simon [9] with the Pak-B blades have exhibited this laminar separation problem. The Pak-B blades were therefore ideally suited for further in-depth research into the control of separated flow. Reduction of the separation problem over the Pak-B blades provides the community with a better insight into proper blade design and describes methods by which flows can be modified and controlled within the LPT. The experimental work was completed in two parts.

The first goal of this study was to obtain boundary layer velocity and turbulence profiles, surface pressure coefficients, and total pressure loss data for the unmodified Pak-B blade at low Reynolds numbers of 50k, 100k, and 200k and turbulence intensities of 1% and 4%. The experimental boundary layer data was used to determine the location of separation on the suction surface of the Pak-B blade. Attention was given to verify that inlet Mach numbers were appropriate and relevant for the experiments conducted. The total pressure loss coefficient ( $\gamma$ ) and wake momentum deficit ( $\Theta$ ) measurements indicated the efficiency of the baseline Pak-B blade. A listing of the types of experimental data collected for the baseline Pak-B blade is provided in Table 1.

Table 1. Baseline Pak-B data collected

Reynolds number	$C_p$	B.L. Profiles	$\gamma$	$\Theta$
50k	X	X	X	X
100k	X	X	X	X
200k	X		X	X

The second goal of this study was to examine the baseline Pak-B experimental data, including the recorded chordwise locations of separation and reattachment, for possible means of reducing the

losses associated with laminar separation. Study of the Pak-B experimental data and the work of several separation control researchers suggested three passive design modifications to the suction surface likely to have the most beneficial impact. The first modification previously documented by Bearman and Harvey [16, 17] involved the use of dimples recessed into the blade surface. These dimples were placed spanwise over a portion of the blade. As suggested by Bearman and Harvey [16, 17] these dimples create vortices within the boundary layer which energize the flow from a baseline laminar state to a transitional one before separation can occur. This increase in skin friction reduced the 2-D profile losses associated with separation.

The second design modification tested was the placement of streamwise longitudinal V-grooves on the suction surface of the Pak-B blade. Previously test by Lin et al. [18] for separation control over a convex surface in a turbulent boundary layer, these grooves are similar to riblets, but much larger. The increased size of the V-grooves enhanced the formation of vortices extending longitudinally downstream for a turbulent boundary layer and subsequently mixed higher energy flow from the freestream with the lower energy boundary layer to reduce separation (Yurchenko [30]).

The third modification was the placement of a trip wire on the surface of the Pak-B blade at the 35% axial chord position. This trip wire created a state of turbulent flow over the suction side of the blade. Verification was made that the flow remains attached to the suction surface for all Reynolds numbers tested when a trip is used. The loss coefficient was greatly reduced at a Reynolds number of 50k; however, at higher Reynolds numbers of 100k and 200k the loss coefficient for the blade with the wire trip was higher than the baseline blade.

The experiments with the modified blades were done in an adjustable cascade tunnel which was capable of turning the flow through the 95° necessary to simulate the operational environment of the Pak-B blades. The same turbulence levels and Reynolds numbers used in initial tests with an unmodified baseline Pak-B blade were repeated for the three modified blades. The tests included

measurement of the surface pressure coefficient, boundary layer profiles, total pressure loss coefficient ( $\gamma$ ), and the momentum wake deficit ( $\Theta$ ). In summary, these tests show that for a turbine blade with a high degree of turning and low Reynolds number flow separation problems, passive surface modifications will reduce the cascade flow losses.

## Chapter 3 - Tunnel and Cascade Characteristics

### 3.1 Data Collection Locations

The wind tunnel adjustable test section was designed to accommodate several different types of data collection. The tunnel has four thermocouples suspended from the tunnel ceiling for recovery temperature measurement marked T-1 through T-4 (see Figure 8). The first thermocouple is located 100cm (39.4 inches) up from the bottom and 61 cm (24 inches) from the inside wall on the 304.8 cm (120 inch) wide by 266.7 cm (105 inch) high inlet flow straightener screen. The second thermocouple is located 45.7 cm (18 inches) downstream of the turbulence generating grid and 1.45 m (57 inches) upstream of blade #1. Thermocouple #3 is located on the 40% axial chord line of blade #1. The last thermocouple is 76.2 cm (30 inches) downstream of blade #1.

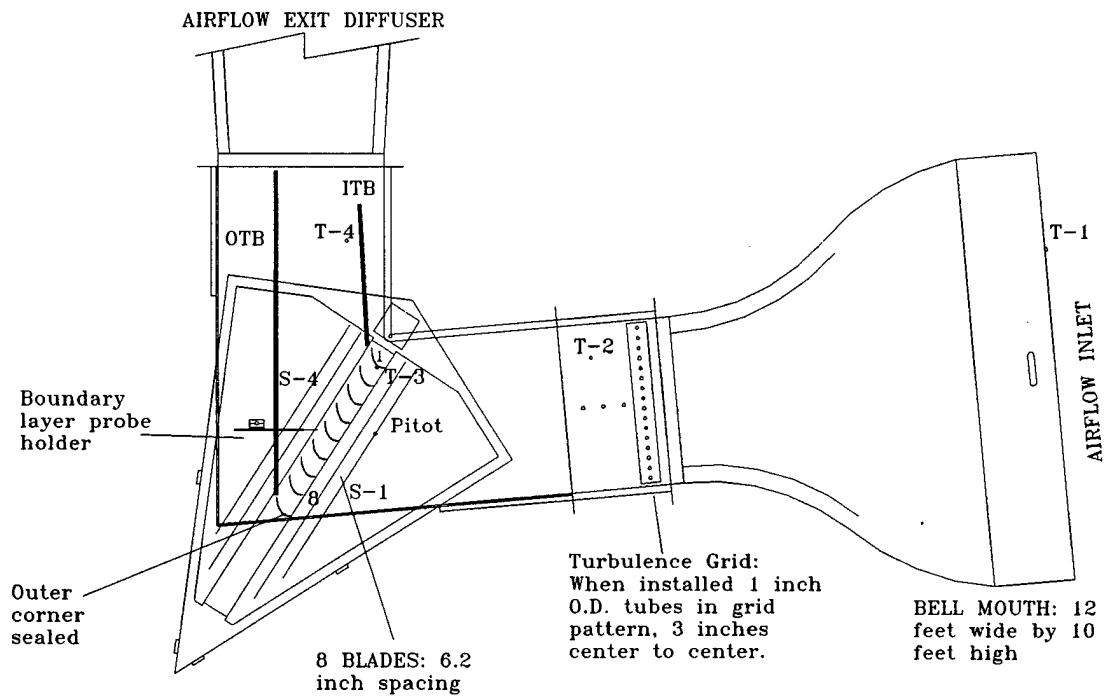


Figure 8. Measurement collection locations for the adjustable test section.

The blade cassette consists of 8 Pak-B blades each approximately seven times engine scale. Each test blade has an axial chord length of 17.78 cm (7 inches) with an axial chord to spacing ratio (solidity) of 1.129. To enhance the approximately 2-D flowfield of the mid-span of the blade, each test blade is stretched in the z-axis to 78.63 cm (34.5 inches) for an aspect ratio of 4.92 to 1. The test blades were molded from Ultralloy 108 white resin and placed inside the test section between traverse slots #2 and #3.

Four traverse slots, S-1 to S-4, are located in the plexiglass top of the test section. The slots are for hot wire and pressure probe access into the test section flowfield. The hot wire and pressure probe were used to record flowfield variations across the pitch of the blades. The first slot is upstream of the blades and marked S-1 in Figure 8. The centerline of the 1.27 cm (0.5 inch) wide slot S-1 is approximately one axial chord length upstream of the blades (19.69 cm) while slot S-2 is approximately  $\frac{1}{2}$  chord length (9.53 cm) upstream of the blades. Slots S-3 and S-4 are downstream of the blade cassette approximately  $\frac{1}{2}$  chord and 1 axial chord length downstream respectively. The precise location of S-3 and S-4 are 10.8 cm (4.25 inches) and 21.34 cm (8.4 inches) downstream, respectively.

A pitot-static probe is located 19.69 cm (7.75 inches) upstream of blade #5 to provide pressure for three different measurements. The pitot-static probe was used to provide inlet total pressure readings when collecting data from the surface pressure taps on blades #4 and #6. The pressure probe also provided an upstream pressure reference for the exit total pressure measurements necessary for calculation of the loss coefficients. Finally, the pressure probe was used to determine the inlet velocity and Reynolds number when the hot wire was being used for velocity and turbulence measurements downstream of the blade cassette. The inlet and exit angle of the flow through the blade cassette was determined through a pressure probe similar to the pitot-static probe.

### 3.2 Flow Incidence Angle Measurements

To ensure proper modelling of the engine environment, the flow inlet and exit angles were measured using a 3-hole wedge probe (see Figure 9). The two side ports on the  $30^\circ$  faces were connected to the two ports of a Dwyer Instruments 5.08 cm (2 inch) inclined manometer. A reading of zero  $\pm 0.005$  inH<sub>2</sub>O on the manometer indicated the probe was facing directly into the flow. The low error in the manometer measurement allowed measurement of the flow angle to within  $\pm 0.25^\circ$ .

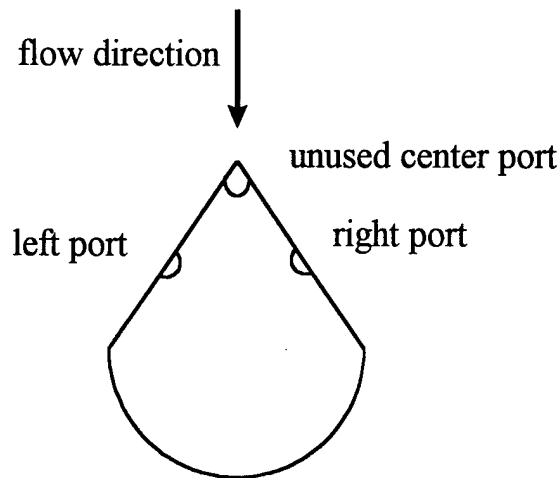


Figure 9. Three hole wedge probe used in inlet angle measurements.

The Pak-B low pressure turbine blade design has a camber angle (angle on centerline between leadline and trailing edges of blade) of  $36^\circ$ , a stagger angle (angle between centerline of blade and axial direction) of  $25^\circ$  and an incidence of  $-1^\circ$  for the 50,000 Reynolds number case. The measured experimental inlet and exit flow angles are both shown in Figure 10. The measured inlet angle values are near the design value of  $35^\circ$ . The exit flow angles are also presented in Figure 10 and are near their design value of  $60^\circ$ . The measured angles for the higher turbulence case of 4% created by the turbulence grid are depicted as solid filled symbols. The traverse distance in centimeters is shown on the lower x-axis of Figure 10. The numbers across the top x-axis of Figure 10 represent

the inlet tangent points of the leading edge blade circle to the inlet plane for each of the eight blades in the cassette. The exit angles in Figure 10 correspond with the trailing edge of the blades labeled across the top of the figure. The Reynolds number case of 50,000 shows a non-uniformity which was necessary to get the  $C_p$  distributions for both blade #4 and #6 close to the desired operational setting. The exit angles for a Reynolds number of 50,000 and freestream turbulence of 1% show a  $\pm 3^\circ$  variation which was indicative of the large separation regions over the suction surface of the blades at this condition. Table 2 provides a comparison of the inlet angles between test blade #5 and the 2-D VBI computational model. The stagger and camber angle are  $25^\circ$  and  $36^\circ$ , respectively, for both the experimental and computational runs.

Table 2. Flow inlet angles for blade 5 and 2-D VBI software model

Reynolds number	Inlet angle - Tunnel	Inlet angle - VBI code
50k	$35.5^\circ$	$36^\circ$
100k	$36.5^\circ$	$35^\circ$

### 3.3 Periodicity and Uniformity Measurements

Air velocity magnitude and turbulence intensity were measured across the blade row inlet and exit with a TSI 1210-T1.5 hot wire probe to ensure periodicity and uniformity. Periodicity is the regularness of the velocity peaks and valleys caused by the air flow moving around objects within the test section. Good periodicity downstream of the blade cassette would have each peak 15.75 cm (6.2 inches) apart corresponding to the distance separating each blade. Uniformity is defined as the consistency of the mean velocity across the tunnel. For good uniformity, each velocity peak would have the same value, and each velocity valley would have a constant and smaller value. The measurements were made across a 60 cm (23.62 inch) span from blade #3 to blade #7. The hot wire probe was moved by a DanTec 3-axis traverse through the traverse slots. To verify 2-D flow across the midspan of the test blades, velocity and turbulence measurements were made at five different

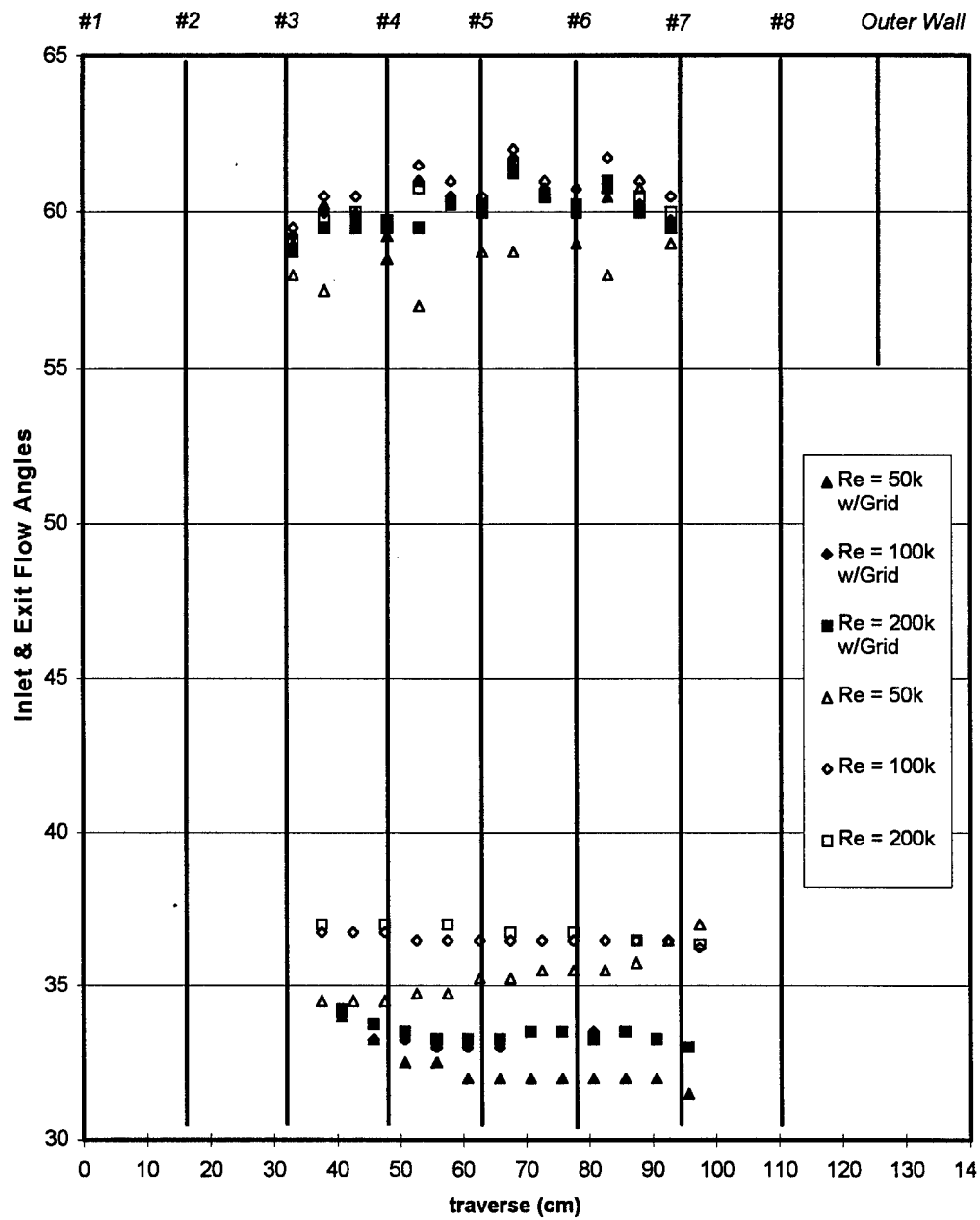


Figure 10. Measured inlet and exit flow angles.

heights within the test section. The hot wire was moved across the blade row inlet and exit 10 cm below the center span, 5 cm below, across the center span, and at +5 and +10 cm above. This method is shown in Figure 11.

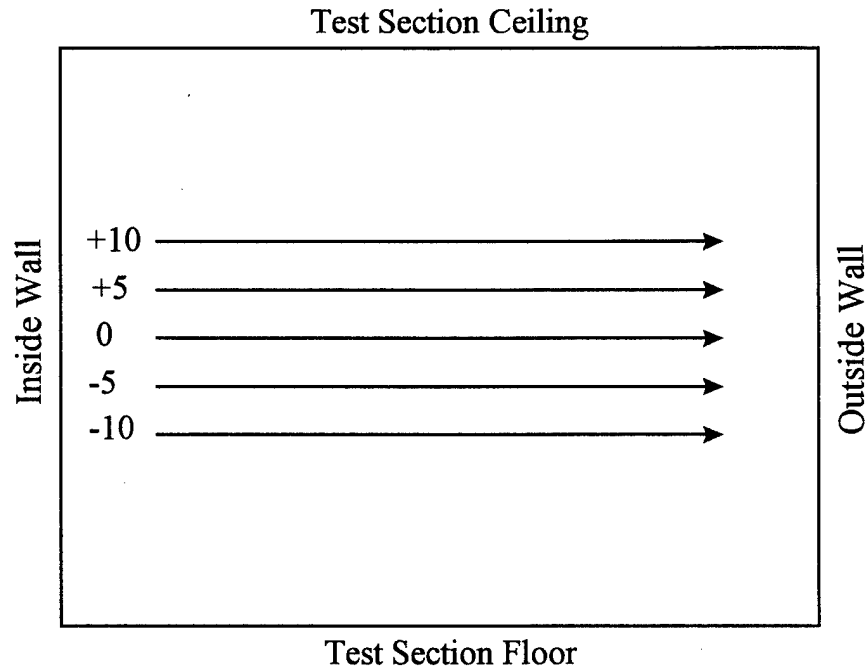


Figure 11. Traverse movement pattern to verify 2-D flow with a hot wire probe.

Each velocity measurement was made three times with the data then ensemble averaged. The averaged measured velocity results are presented in Figures 12 through 15. The figures each contain velocities for all three Reynolds numbers used in this experiment. The velocities shown in Figures 12 through 15 illustrate the periodicity and uniformity of the flow by having no major differences between graphs. The velocity information collected with the hot wire was also used to determine the length scales of the turbulence within the test section inlet.

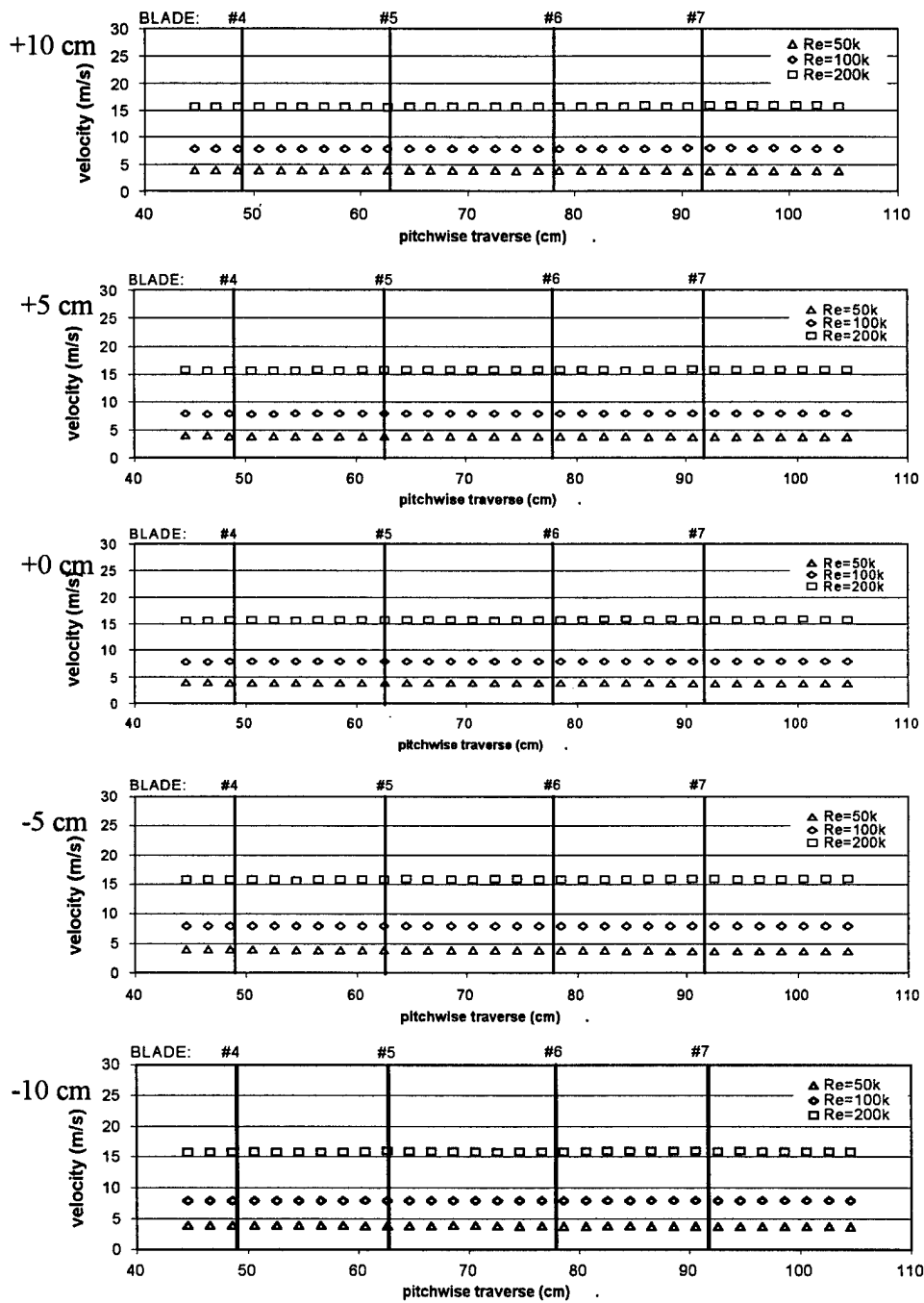


Figure 12. Inlet velocity traverse for slot #1 at +10 cm , +5 cm, 0 cm, -5 cm, -10 cm, and  $Tu = 1\%$ .

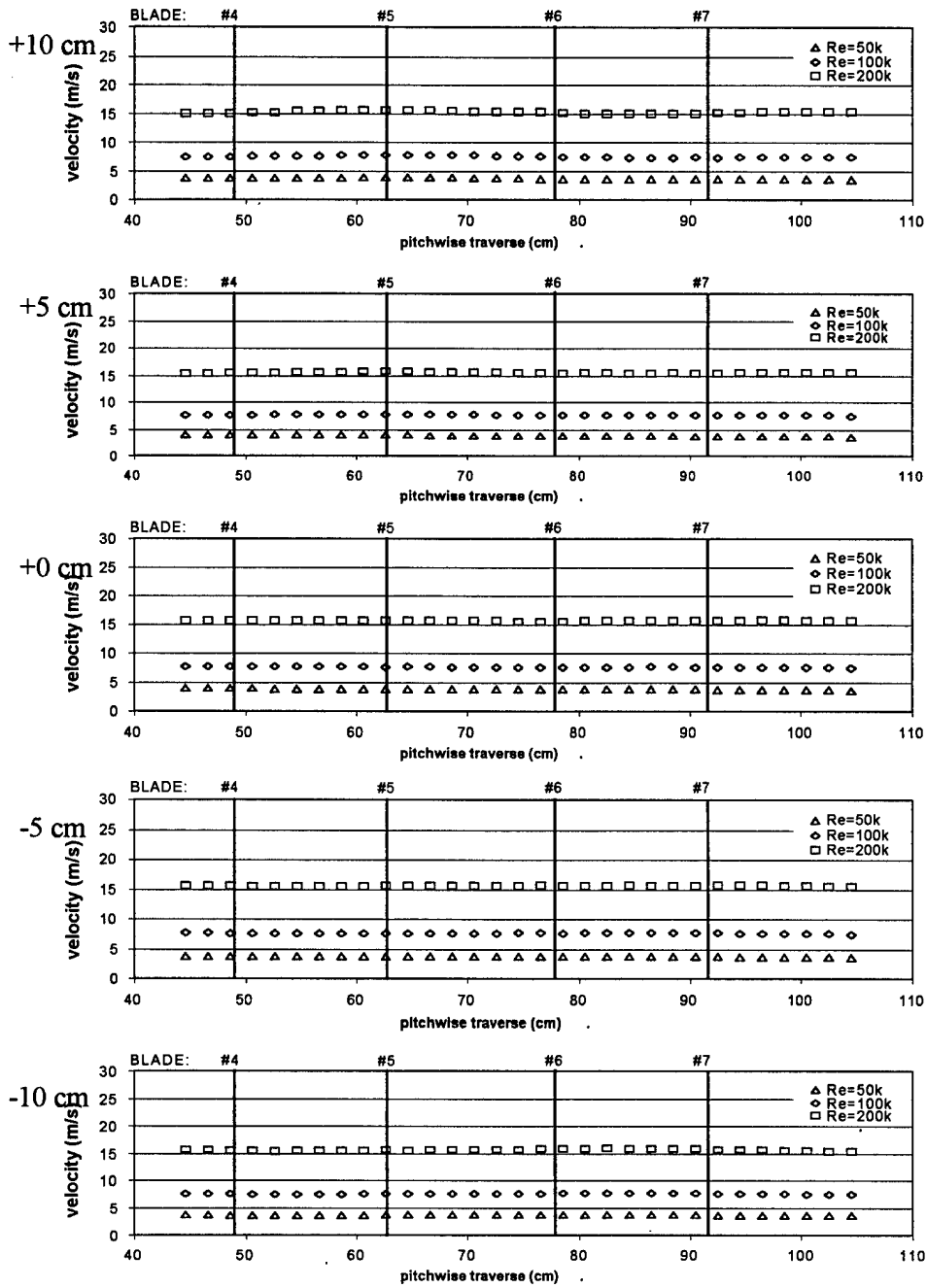


Figure 13. Inlet velocity traverse for slot #1 at +10 cm , + 5 cm, 0 cm, -5 cm, -10 cm, and  $Tu = 4\%$ .

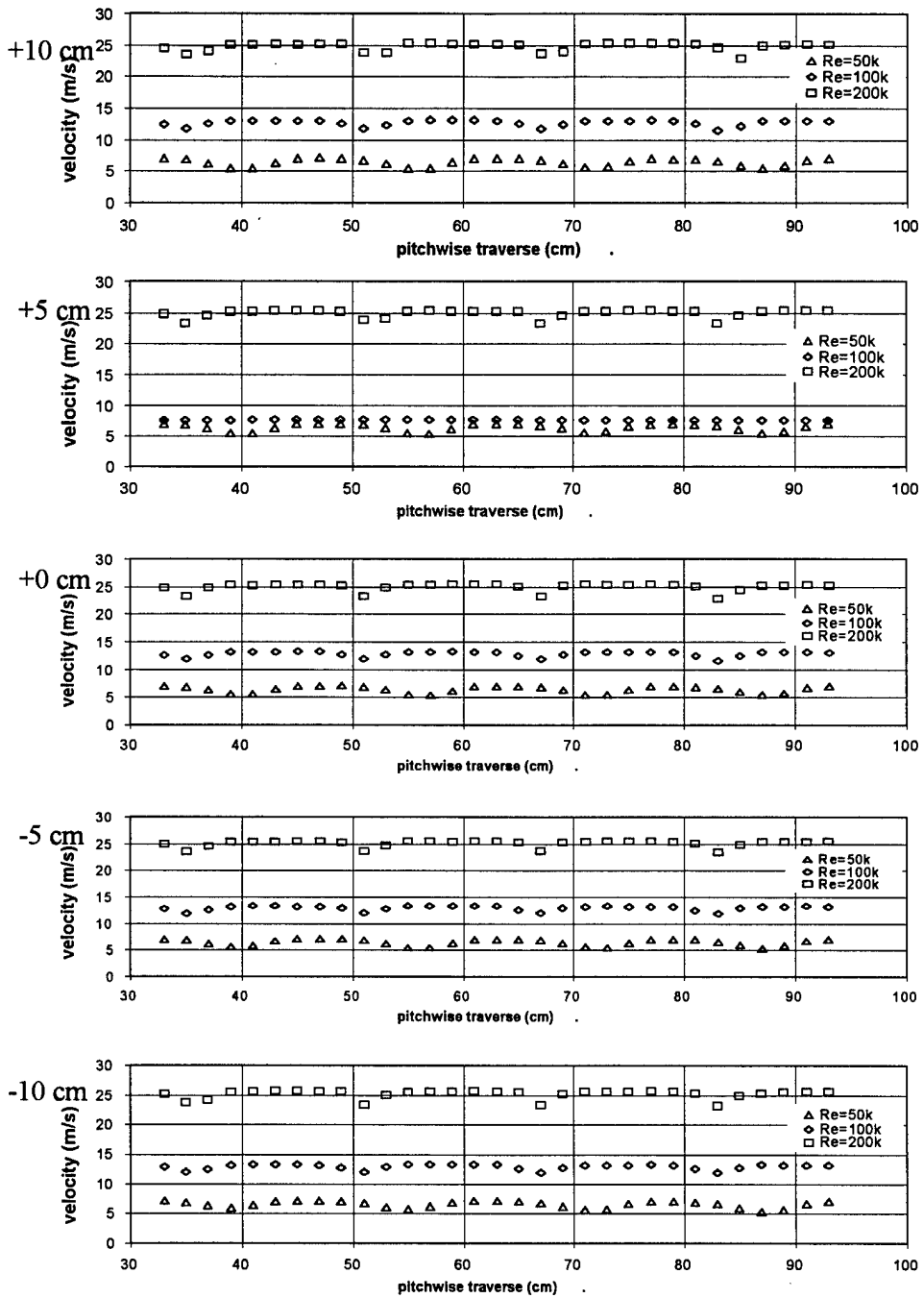


Figure 14. Exit velocity traverse for slot #3 at +10 cm , + 5 cm, 0 cm, -5 cm, -10 cm, and  $Tu = 1\%$ .

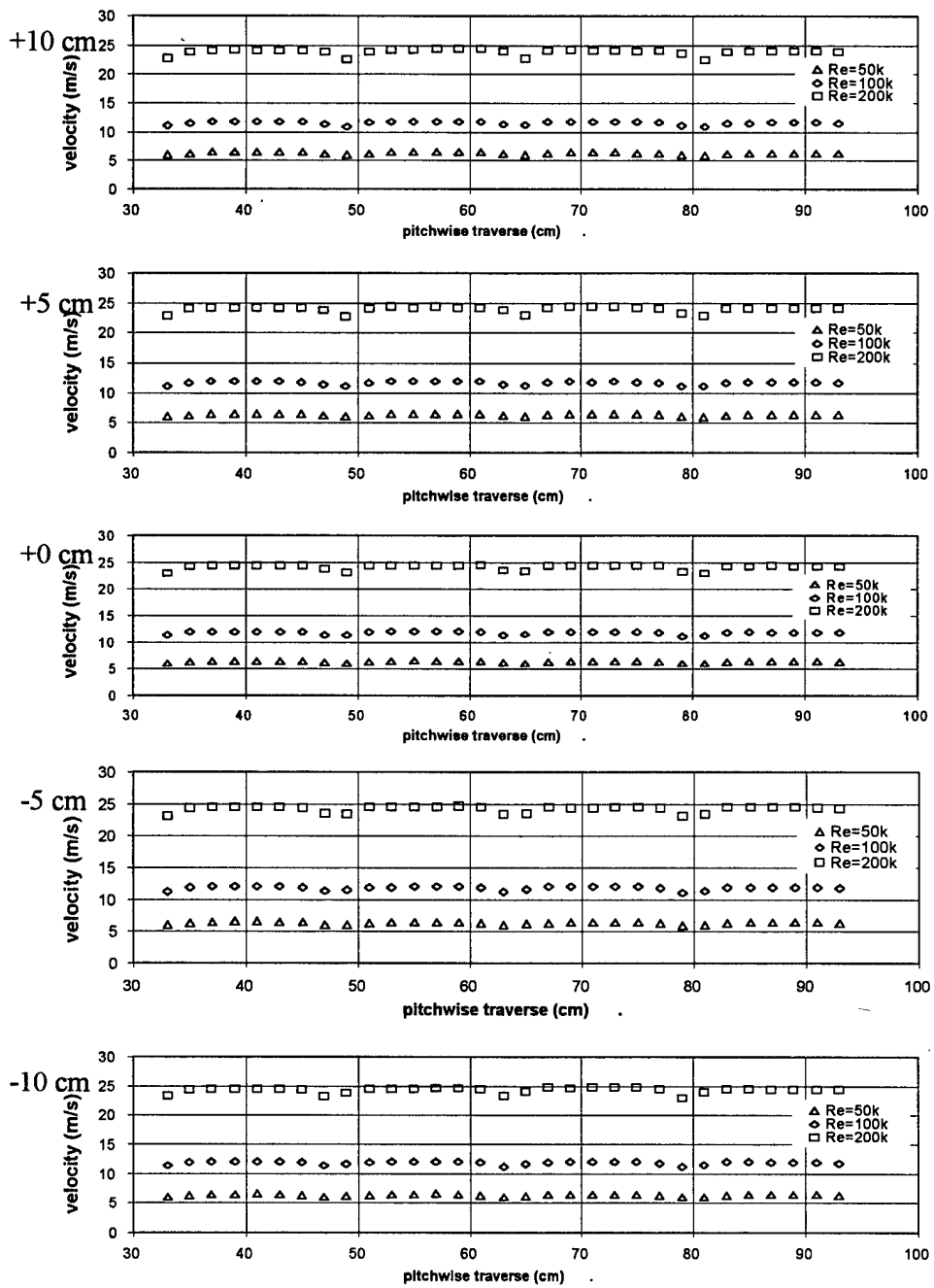


Figure 15. Exit velocity traverse for slot #3 at +10 cm , + 5 cm, 0 cm, -5 cm, -10 cm, and  $Tu = 4\%$ .

### 3.4 Test Section Inlet Turbulence Scale Measurements

To calculate the length scales of the turbulence within the tunnel test section, velocity data was collected with the Auto-Correlation VI (see Appendix D.9) software using the TSI 1210-T1.5 hot wire probe. The hot wire probe was inserted 19.69 cm (7.75 inches) upstream of the blade cassette. The software collected  $2^{16}$  velocity sample measurements at 20,000 Hz which resulted in a duration of 3.28 seconds. The high data collection frequency was chosen to capture all of the frequencies which exist in a low subsonic freestream. The power spectrum of the collections is shown in Figures 16 and 17 for Reynolds numbers of 50k, 100k, and 200k.

The y-axis of Figures 16 and 17 are the single-sided auto power spectrum of the rms velocity component squared ( $[u']^2$ ) divided by the period of the sampling signal (1/20,000 Hz). This division by the sampling period results in the y-axis having units of  $m^2/sec$ . When the curves present in Figure 17 were integrated, the resulting value was the square of the rms velocity ( $[u']^2$ ) for that Reynolds number and turbulence intensity. For example, the power spectrum for  $Re = 50k$  and  $Tu = 4\%$  when integrated (using the trapezoidal rule) resulted in a rms velocity value of 0.129 m/s compared to the direct measurement of 0.124 m/s. The length scales for an inlet freestream turbulence level of 4% were determined to be 2.87 cm (1.13 inches), 4.50 cm (1.77 inches), and 6.93 cm (2.73 inches) for Reynolds numbers of 50k, 100k, and 200k, respectively. The software used in the determination of the length scale is discussed in Appendix D.

The lower freestream turbulence curves of Figure 16 do not correlate as well to the direct measurements of rms velocity due to a low signal to noise ratio for the  $Tu = 1\%$  case. When integrated using the trapezoidal rule, the area under the curves of Figure 16 result in an inaccurate estimate of the square of the rms velocity. This was evident with the measurements for  $Re = 50k$  and  $Tu = 1\%$  where the power spectrum integrated to an estimated rms velocity of 0.044 m/s compared to the direct measurement of 0.020 m/s. With the limitations for the  $Tu = 1\%$  case, the length scales of the

turbulence for the inlet flowfield at Reynolds numbers of 50k, 100k, and 200k were determined to be 77.3 cm (30.43 inches), 1.231 m (48.46 inches), and 1.533 m (60.35 inches), respectively. The large length scales are indicative of the size of the test section. The equipment used for determination of the velocity is explained further in Chapter 4.

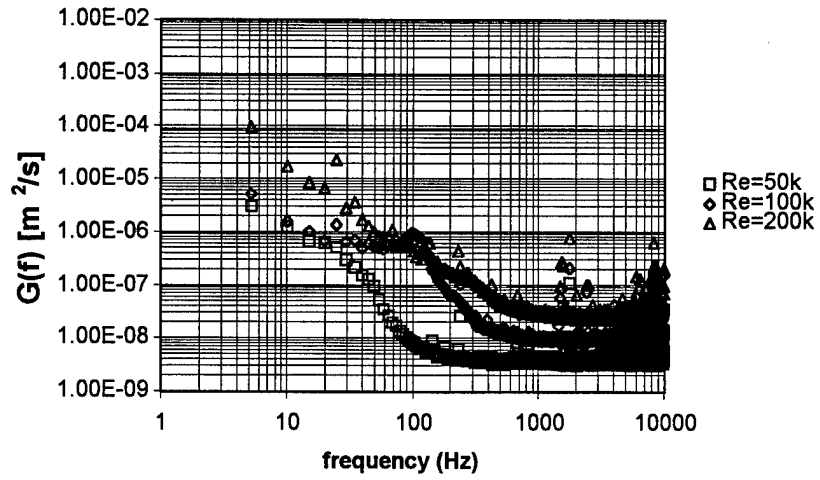


Figure 16. Power spectrum of inlet flowfield for  $Tu = 1\%$ .

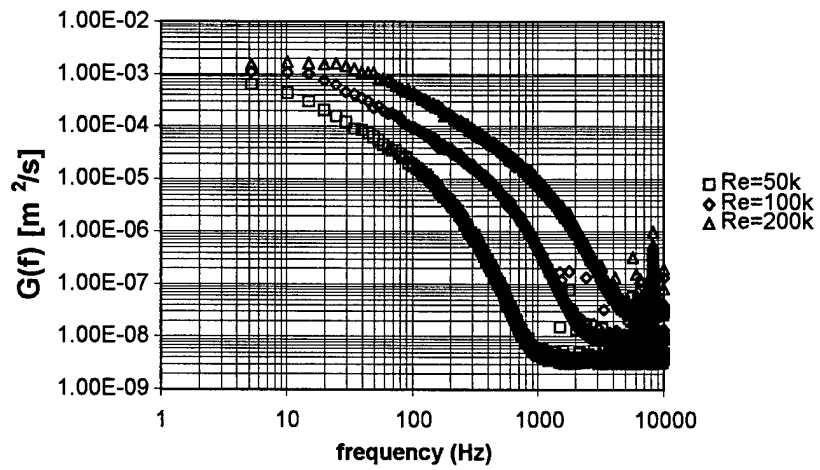


Figure 17. Power spectrum of inlet flowfield for  $Tu = 4\%$ .

## Chapter 4 - Data Collection Instruments

### 4.1 Velocity Measurements Using TSI 1210-T1.5 Hot Wire

A TSI model 1210-T1.5 single hot wire was used for making velocity magnitude measurements upstream and downstream of the test blades. Moving the hot wire pitchwise in the traverse slots allowed the uniformity and periodicity of the velocity into and exiting the blade cassette to be measured. Several pieces of equipment were used together to facilitate the hot wire data measurements.

The hot wire sensor was moved using a 3-axis Dantec model IMC-2 traverse. The traverse is capable of moving 60 cm (23.62 inches) in each axis which provides access to the flow properties  $\pm 30.0$  cm ( $\pm 11.81$  inches) to either side of blade #5. Y-axis (pitch direction) probe location was measured with a Sony SR50-075A linear scale and displayed using a Sony LY-51 digital display. This display provided traverse position information accurate to  $\pm 0.005$ cm ( $\pm 0.00197$  inches). Using the traverse to hold the probe, the hot wire was calibrated while in the tunnel.

The hot wire was calibrated using a pitot static air pressure probe co-located approximately 1 axial chord length upstream of blade #5 with approximately 10.16 cm (4 inches) of space between the probes. The pitot probe was connected to a 5.08 cm (2 inch) Dwyer Instruments inclined manometer. Software was used to match hot wire voltage output to tunnel pitot-static pressures using the equipment illustrated in Figure 18. The calibration was completed with a non-dimensional curve fit between Nusselt Number and Reynolds number of the form (Bruun [31]):

$$Nu = C_{int} + D_{slo} \cdot Re^{0.45} \quad (16)$$

where  $C_{int}$  and  $D_{slo}$  are the intercept and slope, respectively, of the calibration curve. The exponential value of 0.45 was chosen as it provided an acceptable curve fit for measuring low speed flow.

As shown in Figure 18, the hot wire(b) can move across the pitch axis of the blade row(a) through the traverse slot(c). The hot wire was powered by an IFA-100 Intelligent Flow Analyzer(d) which provided a milli-volt output to a National Instruments SCB-68 data collection card located within the wind tunnel control room pc. The total-static pressure probe(e) provided  $P_{total} - P_{static}$  for the air flow inside the tunnel test section. A 5.08 cm (2 inch) inclined manometer was used to read the pitot-static probe pressure differential. A transducer(f) could also have been used to read the total probe. The HP 3852A(g) collects the temperature readings and passes the data from the J-type thermocouple within the tunnel to the computer(h). The calibration software is discussed in further detail in Appendix D. The method for calibrating the TSI 1210-T1.5 hot wire probe was also used to calibrate the TSI 1276-10A subminiature hot film probe using the same pitot probe, inclined manometer and software.

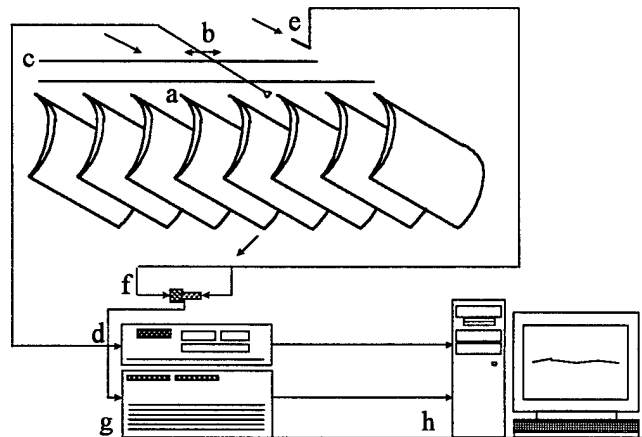


Figure 18. Hot wire data collection diagram.

## 4.2 Boundary Layer Velocity Measurements Using TSI 1279S-10A Miniature Hot Film Probe

The TSI 1279S-10A hot film probe is a modified version of the TSI 1276-10A subminiature probe. Unlike the straight TSI 1276-10A, the filament support prongs of the TSI 1279S-10A are

turned into the airflow 45° as shown in Figure 19. The hot film probe was mounted on a micro-traverse mechanism to provide accurate boundary layer measurements of the test blade. Five locations along the suction surface of the test blade were chosen for boundary layer measurements. To maintain structural stability for the small probe additional hardware was constructed.

The hot film probe was supported using a 3.175 mm (0.125 inches) diameter tube that was 10.16 cm (4 inches) long. This small probe holder extends the length of the short probe while minimizing aerodynamic interference within the blade passage. The hot film probe and the small probe holder were supported by a 9.53 mm (0.375 inches) diameter tube 43.18cm (17 inches) long. This larger tube provided the additional length necessary to reach from the traverse mechanism to the blade passage. The longer tube was connected to the micro traverse through a rectangular slot cut through the outer tail board. The micro traverse mechanism is in the non-moving air space between the outer tail board and outer test section wall.

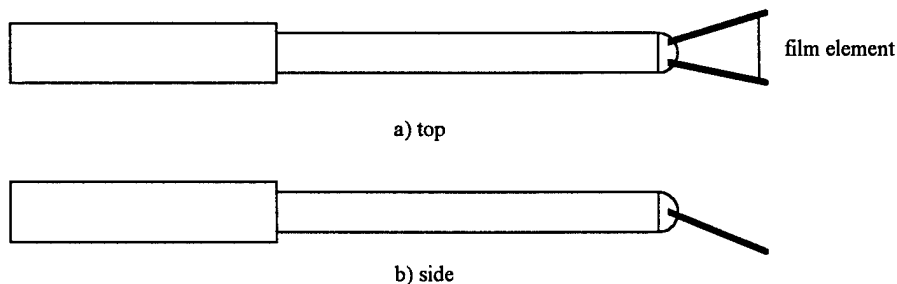


Figure 19. TSI 1279S-10A subminiature boundary layer probe (not to scale).

The National Aperture, Inc. motorized 5.08 cm (2 inch) MM-3M micro traverse has a movement resolution of 20157.4 revolutions per cm (51199.8 turns per inch). The traverse position encoder provides a linear spatial resolution of  $\pm 5.08 \times 10^{-5}$  cm ( $\pm 0.00001$  inches). The traverse position was controlled and powered by a National Aperture, Inc. MC-3SA servo amplifier system connected to a National Instruments PC-Servo-2A motion control board located within the wind

tunnel control room computer. The operating software is described in more detail in Appendix D. The software in combination with the high position accuracy allow very detailed measurements of the boundary layer.

The boundary layer probe was used to measure velocity and turbulence profiles over five different surface locations on the baseline smooth blade and the modified blades. As seen in Figure 20, the measurement locations span the region of separated flow over the suction surface from 67.2% axial chord to 89.8%. The dimple center and V-groove start locations were upstream of the points where the boundary layer was measured.

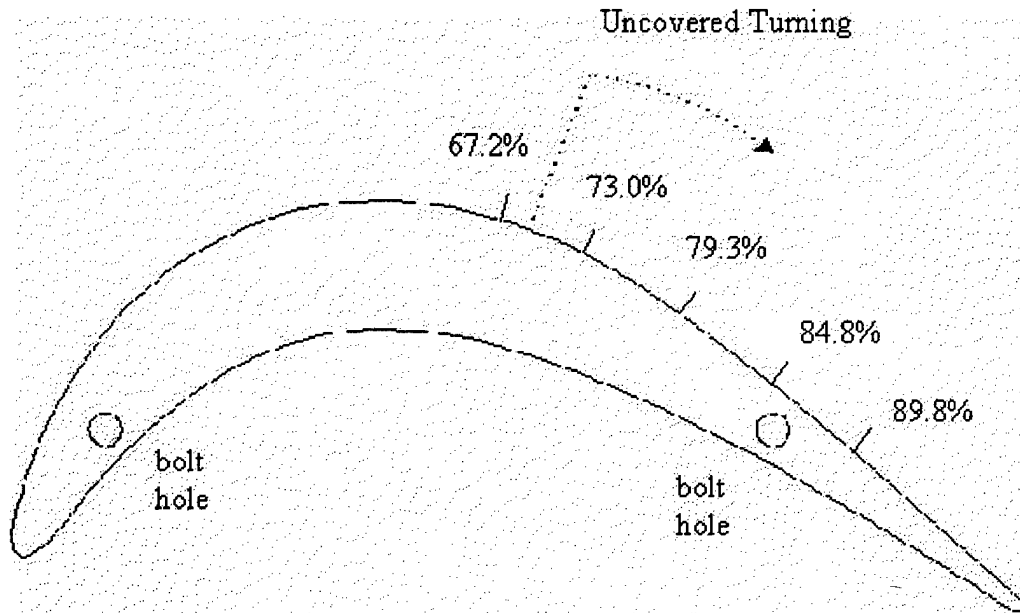


Figure 20. Locations of boundary layer measurements over the suction surface.

### 4.3 Temperature Measurements Using J-Type Thermocouples

Temperature measurements within the tunnel were made using four J-type thermocouples. The first thermocouple was placed at the bell mouth inlet with the second thermocouple located 1.45 m (57 inches) upstream of blade #1. The third thermocouple was placed 25.4 cm (10 inches) down

from the top of blade #1 at the 40% axial chord point. The final thermocouple was located 76.2 cm (30 inches) downstream of blade #1. A Kaye Instruments Ice Point Thermocouple Reference provided a 0°C (32°F) reference and a Hewlett Packard 3852A Data Acquisition/Control Unit using an HP 44708F (20 channel solid-state multiplexer: thermocouple compensation) card was used to capture the voltages. The voltages were then measured by an HP 44701A (5½ digit voltmeter) card within the HP 3852A Data Acquisition/Control Unit. The voltages were then relayed to the wind tunnel data collection computer via GP-IB data connection. The thermocouples are accurate to within ±0.11 °K (± 0.2 ° F). Air density was calculated using the measured temperature along with the atmospheric pressure of the wind tunnel laboratory.

#### **4.4 Pressure Measurements**

Different instruments were used to measure the various pressure readings necessary for the collection of data. Room atmospheric pressure was read from a Wallace and Tiernan FA-129 pressure gauge which is accurate to ± 3.5 kg/m<sup>2</sup> (± 0.005 psi). Pitot pressure readings used in hot wire calibration were taken using a 5.08 cm (2 inch) Dwyer Instruments, Inc. inclined manometer. Exit total pressure and surface static pressure readings in the tunnel were measured using Druck Incorporated 351.6 kg/m<sup>2</sup> (0.5 psi) differential pressure transducers.

Calibration of the transducers was completed by using a Druck Incorporated DPI 600 Digital Pressure Indicator and pressure source along with calibration software described in Appendix D. After calibration the transducers have an accuracy of ± 1.25 kg/ms<sup>2</sup> (± 0.005 in-H<sub>2</sub>O). The accuracy of the calibration degrades with changes in transducer temperature. Temperature changes shift the zero setting in the transducer calibration. To prevent zero shift in transducer calibration, the transducers were placed inside an insulated box. Temperature changes within the transducer box were controlled by an Omega Engineering, Inc. model 6102 Temperature Controller which operated

an Omegalux silicone rubber fiberglass insulated flexible heater placed within the insulated transducer box. The controller maintained the temperatures at a desired temperature setting to within  $\pm 0.56^{\circ}\text{C}$  ( $1.0^{\circ}\text{F}$ ).

#### 4.4.1 Blade Surface Static Pressure Measurements

Blade surface pressure profile measurements were made using 0.76 mm (0.03 inch) diameter surface pressure taps leading to tubes within the blades. The pressure tubes within the blade were cast in during the molding process using templates. The templates were cut from a sample blade into 0.794 cm (0.3125 inch) wide segments. Holes were then drilled into the templates to support the pressure tap tubes. Three templates were used in each pressure tap blade to provide adequate support of the tubes over the span of the blade until the tubes exit the blade on one end. Blade #4 has 37 working taps, while blade #6 has 40 usable taps. Problems with manufacturing clogged taps #0, #17, and #21 on blade #4. The pressure tap hole pattern is spread across the center 22.86 cm (9 inches) span of the surface of the blade. The hole locations were staggered at an angle of  $30^{\circ}$  to prevent the previous hole from interfering with it. The experimental data was collected from these pressure taps using several different pieces of equipment and a computer.

The pressure tap locations are shown in Figure 21. The taps begin with #0 near the trailing edge and proceed up to #12 near the leading edge for a total of 12 taps on the pressure side. The thirteenth tap was located near the leading edge stagnation point, while taps #14 through #39 were on the suction surface. The pressure tap layout provided detailed measurement of the region of separation in the aft 50% of the suction surface.

Figure 22 illustrates the surface pressure tap data collection process. The pressure tubes from the surface ports on the blade(a) are connected to a Scanivalve Corporation 48-channel 48J9-1 multiplexer(b). The current tap read by the transducer is indicated on a Px Scanner Position Display(c).

The multiplexer power is supplied by a CTRL 10P/S2-S6 Solenoid Controller(d) and remotely operated using an HP 44728A (8 channel relay actuator) card within the HP 3852A Data Acquisition/Control Unit(g). Each blade with pressure taps is connected to its own scanivalve, the output of each is connected to a Druck Incorporated 351.6 kg/m<sup>2</sup> (0.5 psi) pressure transducer(f). The transducers used in taking data from the surface pressure taps are differential transducers, allowing the total port of the inlet pitot probe(e) to provide the high side pressure while the pressure tap supplies the low side. After the pressure tap data is acquired, a reading of zero pressure differential is read on the transducers to ensure minimal thermal shift in the results with any result taken out from the acquired data set. The voltage output of the transducers is read by the HP 3852A Data Acquisition/Control Unit(g) using an HP 44711A (24 channel high speed FET multiplexer) card with the output relayed to the data collection pc(h).

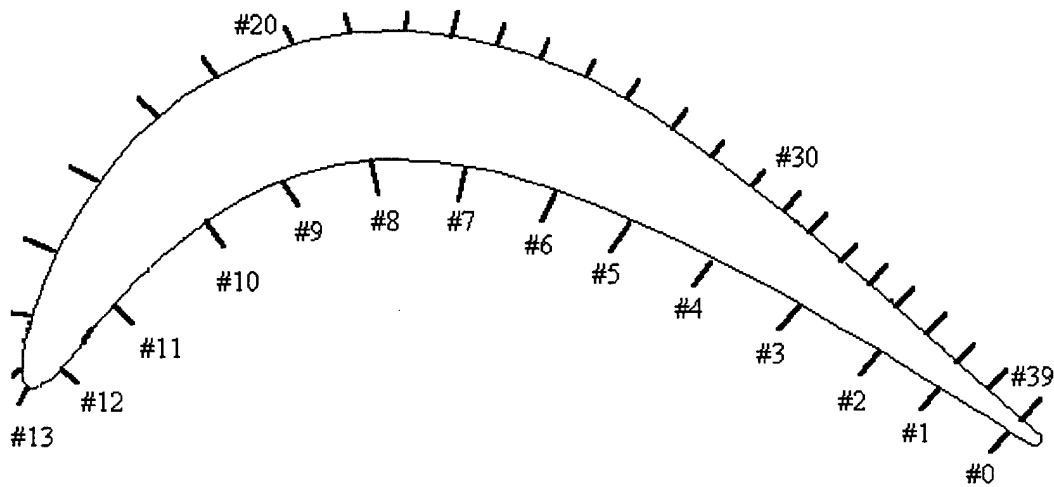


Figure 21. Surface static pressure port locations molded within blades #4 and #6.

#### 4.4.2 Exit Total Pressure Measurements

A pitot probe was used to record the total pressure in the downstream wake of the test blades. The downstream pitot probe was connected to one side of a Druck Incorporated 351.6 kg/m<sup>2</sup> (0.5

psi) differential transducer while the upstream pitot probe was connected to the other. The usage of two pitot probes allowed direct measurement of  $P_{0,inlet} - P_{0,exit}$  which was necessary for the determination of the loss coefficient. The hot wire was also placed downstream of the blades to record the exit velocity. Together the differential pressure measurement and the exit velocity measurement allowed easy determination of the loss coefficient. The baseline Pak-B loss coefficient is documented in the next chapter while the software used in collection of this data is described further in Appendix D.

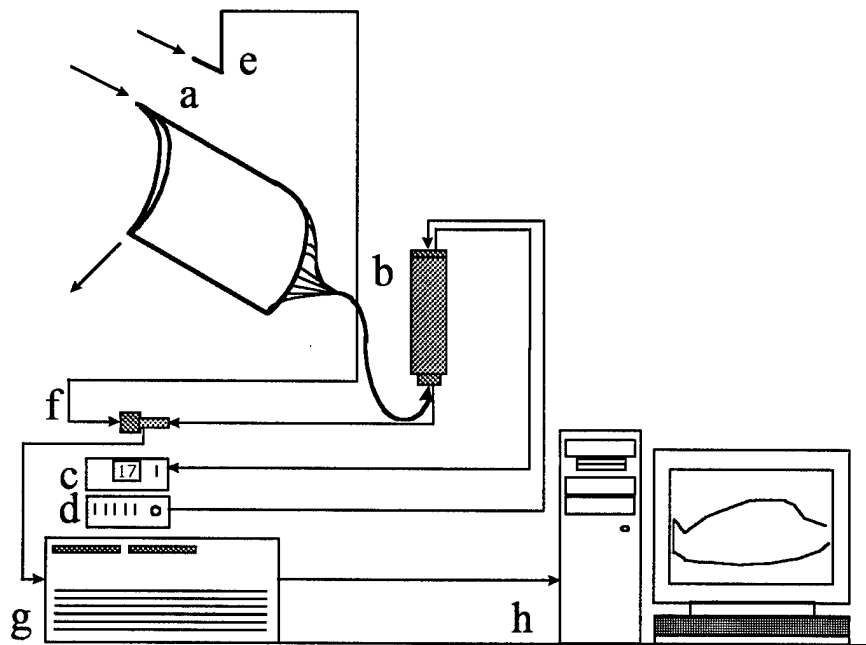


Figure 22. Blade surface pressure data collection diagram.

## Chapter 5 - Numerical Simulation of Turbine Cascade

### 5.1 Overview of Allison Software code

The Vane-Blade Interaction (VBI) code developed by Allison Gas Turbines simulates flow passages in a turbine engine. Developed in 1992 for 2-D flow; the code can model a cascade of turbine blades using a combination of airfoil wrapping O-grids and passage filling H-grids. While the O-grids provided a high grid density near the surface, the 2-D grid generation program was unable to model the three dimensional discontinuous surfaces tested in the tunnel for reduction in separation losses. The baseline Pak-B shape was simulated to provide an initial estimation of the surface pressure coefficient for the blade.

### 5.2 Grid Generation Around Pak-B Airfoil

The grid generation developed by Rao et al. [32] is a combination of airfoil conforming O-grids embedded within an H-grid that conforms to the passage shape. These two different grids overlap at their boundaries to exchange information. Airfoil boundary layer information from the O-grid is transferred through this chimera overlap region to the H-grid. An example of the Pak-B blade placed within this O-H grid is presented in Figure 23.

### 5.3 VBI Computational Method

The VBI software used an explicit 5-stage Runge-Kutta ordinary differential equation (ODE) solution scheme for the Navier-Stokes equations. Rao et al., [32] used a combination of second and fourth order artificial dissipation terms with this 2-D version. A more detailed description of the software inputs and the calculation of turbulent viscosity  $\mu_t$  is provided in Appendix E.

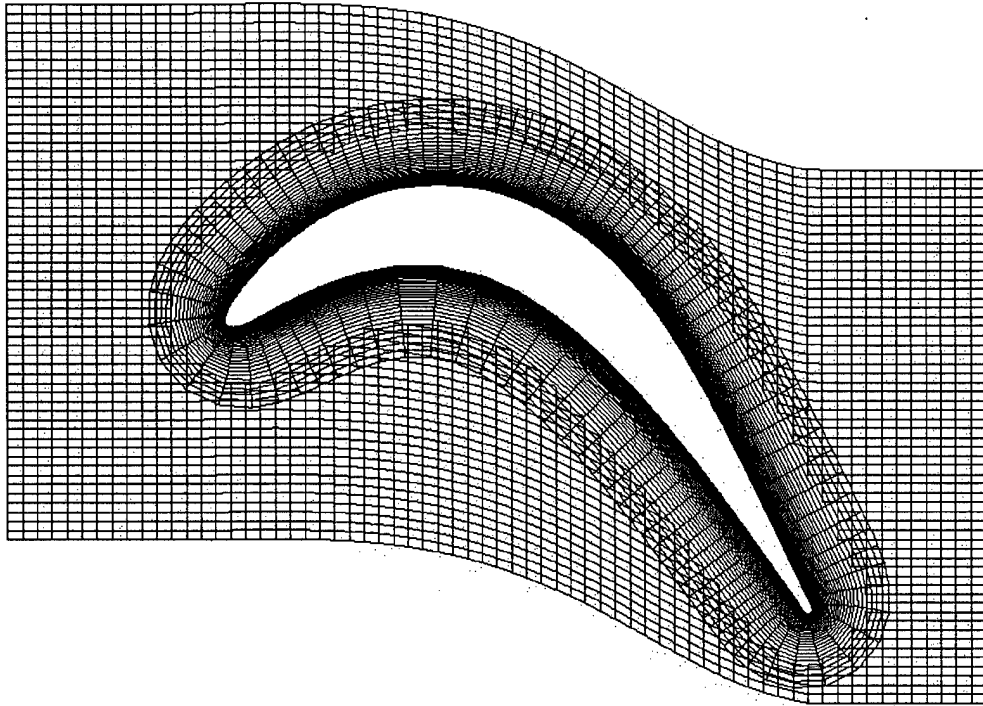


Figure 23. O-H grid surrounding Pak-B airfoil

#### 5.4 Two-Dimensional Software Results

VBI results include surface pressure contours and boundary layer velocity profiles calculated over the blade surface. The surface pressure distribution diagrams are steady-state solutions. The boundary layer velocity plots are presented for the same axial chord locations as the experimental data presented in Chapters 6 through 9.

A pressure distribution diagram can reveal areas of likely separation over the surface of the blade. A region of separated flow will appear as a horizontal line with little or no change in  $C_p$ . Figure 24 shows the pressure distributions obtained using the VBI code for the Pak-B blade shape. As can be seen in Figure 24, the code was unable to simulate the large regions of separation found on the actual blade at  $Re = 50,000$ , described in more detail in Chapter 6.

The VBI-2D pressure coefficient results agree with the experimental data very well along the pressure surface, and the first 40% of the suction surface. Figure 24 shows the ideal design pressure curve over the aft 60% of the suction surface. The code did predict a small separation as Reynolds number was decreased to 50k. This separation is also observable from the boundary layer velocity plots presented in Figure 25.

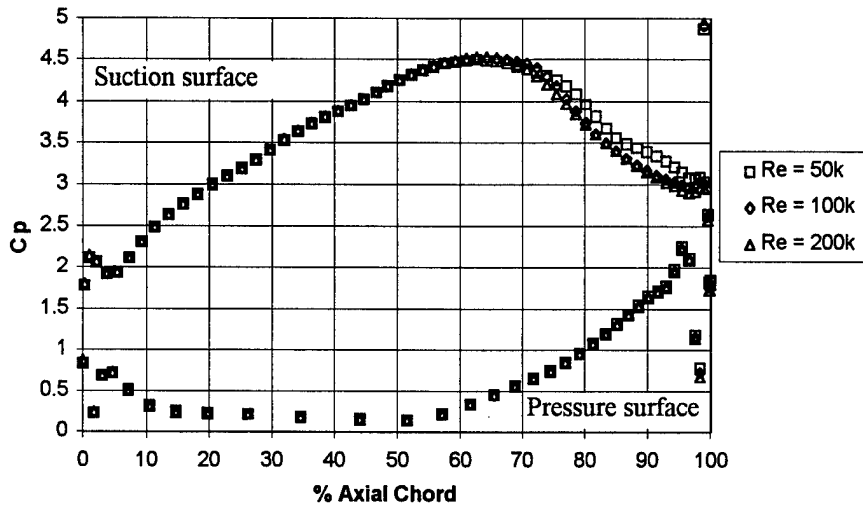


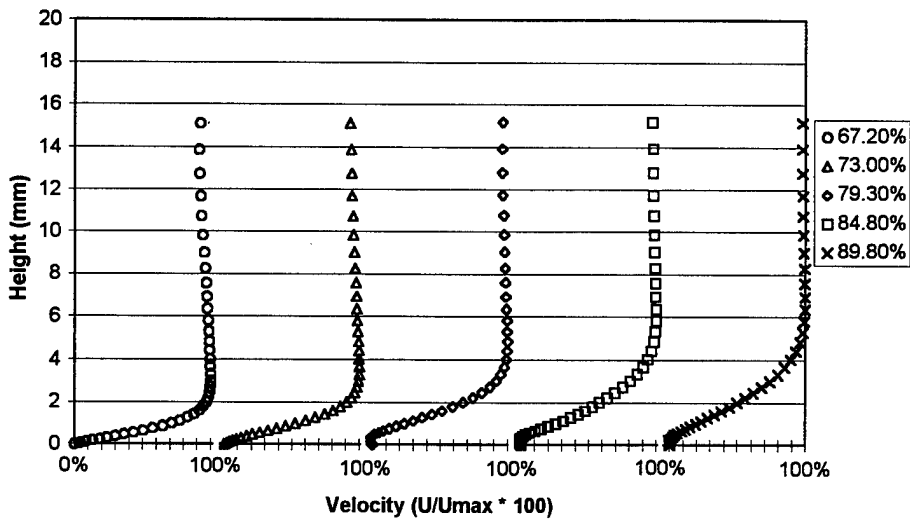
Figure 24. Two dimensional VBI code surface pressure coefficient results.

#### 5.4.1 VBI 2-D Code Results For Reynolds Number = 50k

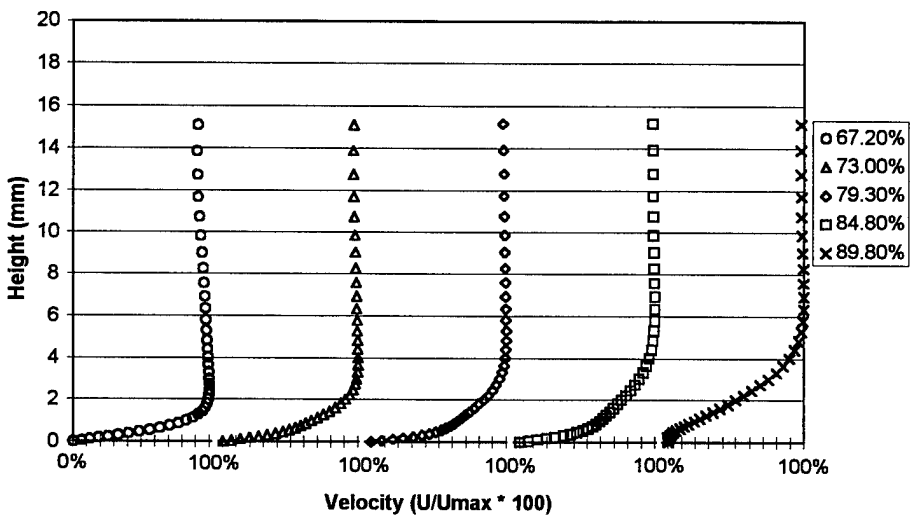
Figure 25a illustrates the boundary layer velocity profiles for the simulated case of Reynolds number equal to 50,000 based upon inlet velocity and axial chord. The size of the separation zone shown in Figure 25a is unusually thin due to the lack of proper transitional modeling with the software code. The simulated flow transitions at a single point, unlike the actual blade which undergoes transition over an extended period after flow separation. The turbulence model used was unable to simulate freestream turbulence conditions which are a significant factor in determining the separation size and location.

#### **5.4.2 VBI 2-D Code Results For Reynolds Number = 100k**

The VBI 2-D boundary layer velocity profile results for the 100k Reynolds number case are presented in Figure 25b. As seen in Figure 25b, there was no separation bubble present on the suction surface of the blade. Experimentally collected boundary layer measurements shown in Chapter 6 show separation bubbles for freestream turbulence levels of both 1% and 4%. The code was unable to model the separated transition and re-attachment that occurs on the suction surface at  $Re = 50k$  and  $Re = 100k$  at a freestream turbulence level of 1%.



a) simulated boundary layer at  $Re = 50k$  and  $Tu = 1\%$



b) simulated boundary layer at  $Re = 100k$  and  $Tu = 1\%$

Figure 25. 2-D VBI code simulations of boundary layer velocity.

## Chapter 6 - Baseline LPT Blade Performance

### 6.1 Baseline Pak-B Overview

The Pratt and Whitney Pak-B LPT blade shape was chosen for this study for two reasons. The first reason was that it was designed for use at low Reynolds numbers typical of UAV flight conditions. The second reason the Pak-B blade shape was selected was because the airfoil suffers from losses due to flow separation at low Reynolds numbers despite being designed to operate under this condition as a highly aft loaded airfoil. To illustrate these losses a linear cascade tunnel was used to collect several types of experimental data for the Pak-B blade. Surface static pressure measurements, boundary layer velocities and turbulence profiles and loss coefficients were obtained. The results from this investigation are presented in this chapter.

### 6.2 Experimental and Simulated Surface Static Pressures

To ensure proper simulation of the approximately 2-D flowfield around the mid-span surface of the blade, surface static pressure measurements from blade #4 and #6 were compared to each other and the VBI 2-D code results. Similar results from blade #4 and #6 indicated a good uniformity in flowfield characteristics for the blade cassette. The pressure coefficient curves shown in Figures 26 through 31 were made using the following definition:

$$C_p = \frac{P_{0,inlet} - P_{s,x}}{\frac{1}{2}\rho\bar{U}_{inlet}^2} \quad (17)$$

where  $P_{0,inlet}$  and  $\bar{U}_{inlet}$  were the total pressure and mean velocity, respectively, measured upstream of the blade cassette. The inlet pressure and velocity were measured 1 axial chord length upstream of the test blades. The surface static pressure measurement for each tap is denoted  $P_{s,x}$  while  $\rho$  was the density based upon room pressure and tunnel temperature. No compressibility corrections to the

density were made due to the low Mach numbers of the flow. Pressure curve data was obtained for the baseline Pak-B blade at  $Re = 50k, 100k, 200k$  at freestream turbulence levels of 1% and 4%.

As seen in Figure 26, the definition given in equation 17 defines the pressure coefficient values as positive, with the pressure surface values on the lower curve and the suction surface values on the upper curve. The data for each Reynolds number and turbulence intensity was collected three times and the average values are shown in Figures 26 through 31. The solid line present in Figures 26 through 31 are the result from the VBI-2D code. The VBI code was explained in Chapter 5.

### **6.2.1 Cp Curves for $Re = 50k$**

The pressure tap blades have  $C_p$  distributions that agree with the predicted VBI-2D code results for regions of attached flow on the pressure surface and the initial 40% of the suction surface. For the aft 60% of the suction surface the code fails to capture the strong effect separation has on the surface pressure. As seen in Figure 26, the separation zone extends from the 62% axial chord line back to the trailing edge of the blade. The experimental data and separation region agree with that obtained previously by Murawski et al. [4].

For the increased freestream turbulence level of 4%, the large separation bubble present in the laminar flow case of  $Tu = 1\%$  shrinks to a region extending from the 75 to 87% axial chord line on the suction surface. The VBI-2D code is incapable of modeling the increased freestream turbulence of 4%, but the previously shown VBI results are included with the higher turbulence graphs for easier comparison.

### **6.2.2 Cp Curves for $Re = 100k$**

The higher Reynolds number case of 100k shows a reduction of the size of the separation bubble that was present in the  $Re = 50k$  and  $Tu = 1\%$  case. The size and location of the separation bubble for this higher Reynolds number case were similar to those measured with a higher turbulence

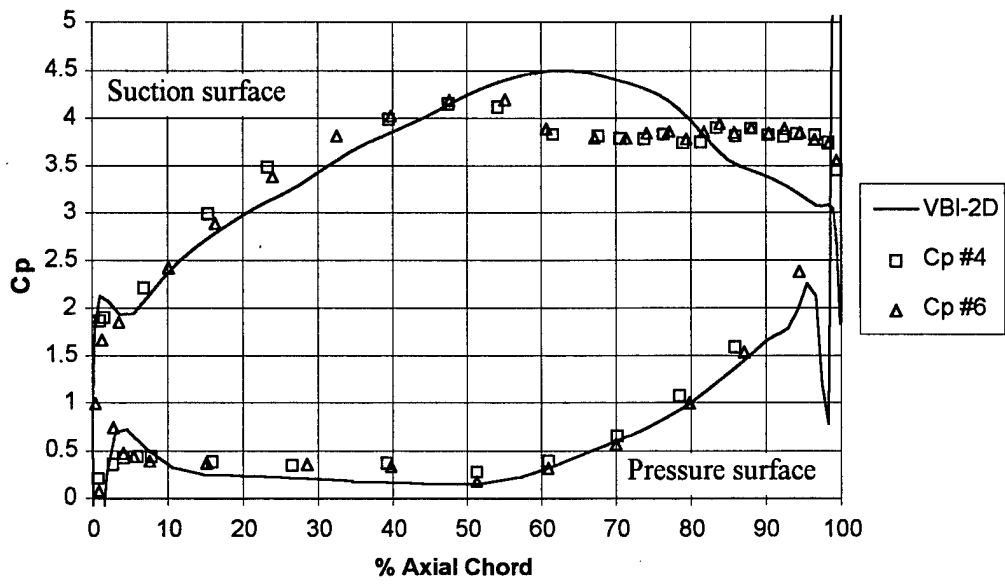


Figure 26. Experimental and simulated  $C_p$  curves for  $Re = 50k$  and  $Tu = 1\%$ .

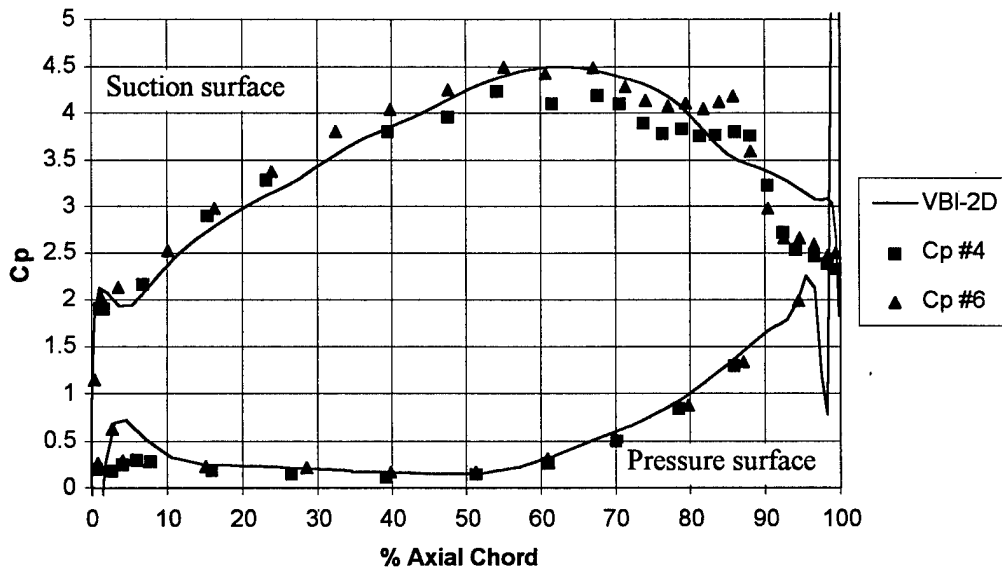


Figure 27. Experimental and simulated  $C_p$  curves for  $Re = 50k$  and  $Tu = 4\%$ .

level of 4% for the  $Re = 50k$  case. With the increased energy in the flow, the separation bubble was reduced to a location starting at 74% and reaching to 87% axial chord.

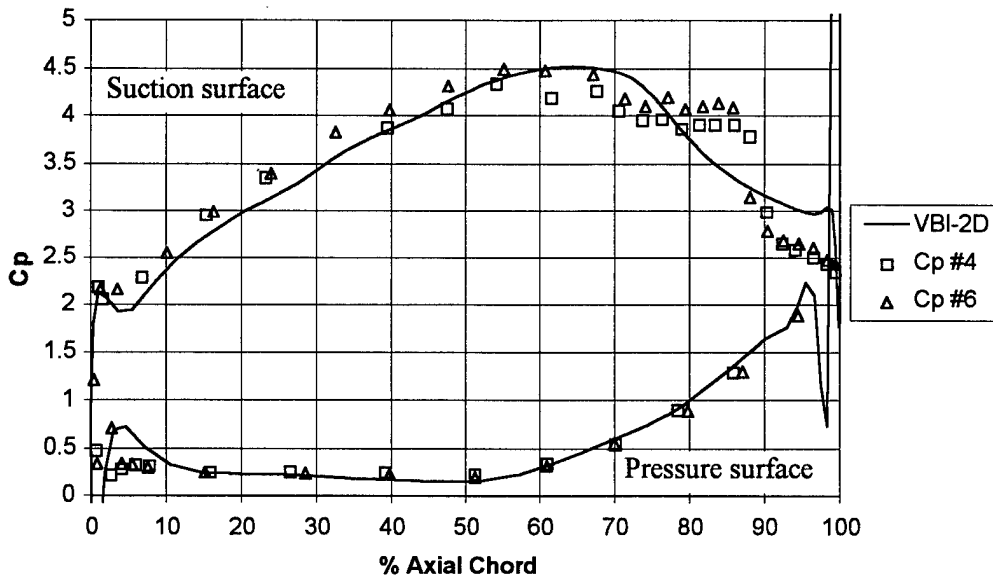


Figure 28. Experimental and simulated Cp curves for  $Re = 100k$  and  $Tu = 1\%$ .

The effect of increasing the turbulence level for the 100k case is clearly evident when comparing Figure 29 to Figure 28. The separation bubble was further reduced to a smaller range of 80 to 86% axial chord. The trend in decreasing separation bubble size with increasing Reynolds number or turbulence continues with the experimental results of  $Re = 200k$ .

### 6.2.3 Cp Curves for $Re = 200k$

Figure 30 illustrates the effect that higher flow velocities have over the low pressure turbine blade. The separation bubble is reduced to a region of 75% to 83% axial chord. The size of the measured separation bubble was again dependent upon freestream turbulence level as in the previously discussed cases.

The flow condition that most closely approaches ideal fully attached flow over the surface of the blade is the high Reynolds number, high freestream turbulence level case. The combined effect

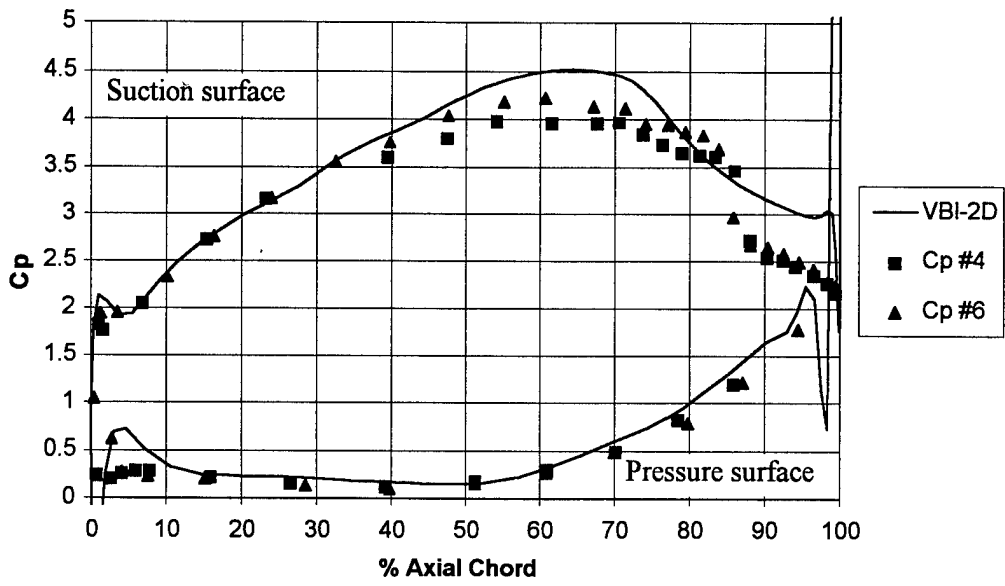


Figure 29. Experimental and simulated Cp curves for  $Re = 100k$  and  $Tu = 4\%$ .

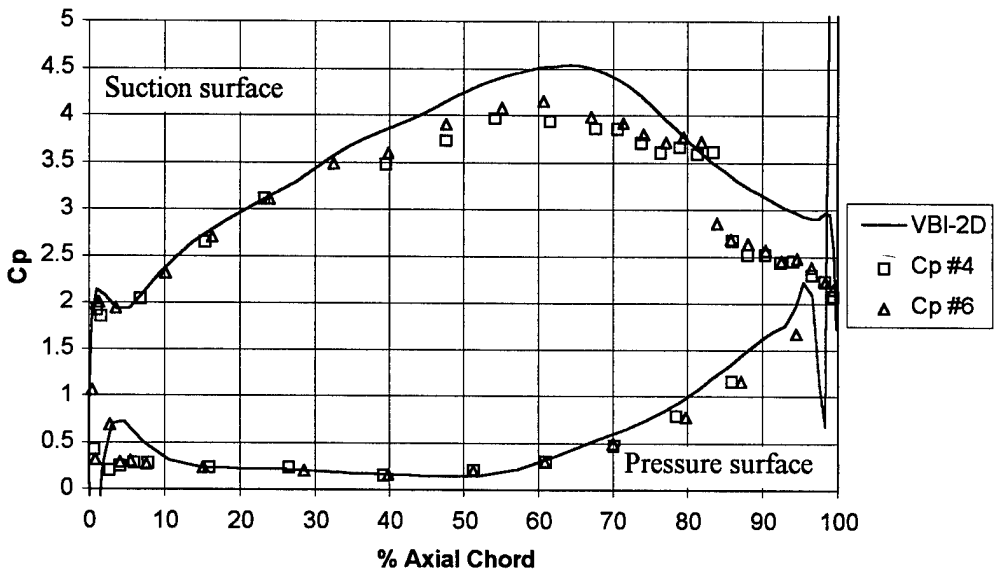


Figure 30. Experimental and simulated VBI-2D Cp curves for  $Re = 200k$ .

of both freestream turbulence and high flow energy help maintain attached flow for a longer distance than in the lower Reynolds number and turbulence level cases. The effect the increase in flowfield energy is evident in Figure 31 where the separation bubble has shrunk to a region extending from 78% to 82% axial chord. The presence of a separation bubble under these high energy conditions indicates there is room for reduction in the loss coefficient for high Reynolds numbers and turbulence intensities in addition to the large improvements possible at lower Reynolds numbers.

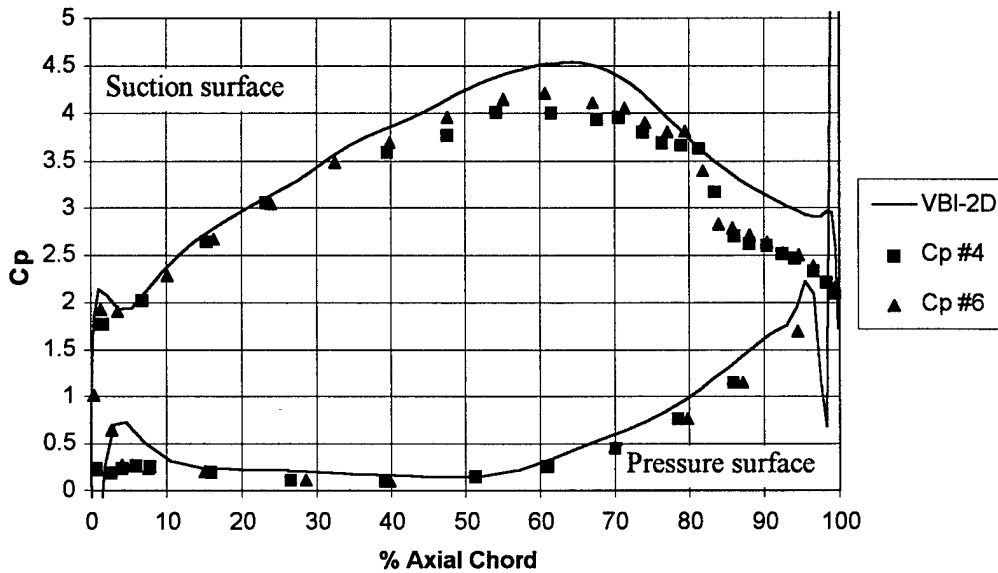


Figure 31. Experimental and simulated Cp curves for  $Re = 200k$  and  $Tu = 4\%$ .

The axial chord location of the start of separation on the suction surface was plotted in Figure 32. Figure 32 illustrates the effect both increased Reynolds number and turbulence intensity have on delaying separation. To determine a cause of the separation locations seen in Figures 26 through 31, surface curvature was examined. However, limitations in the original coordinate data and differencing scheme prevented any useful insights into a cause of separation (see Appendix G). The Cp measurements used to make Figure 32 were taken with differential pressure transducers. A description of the measurement uncertainty estimation follows.

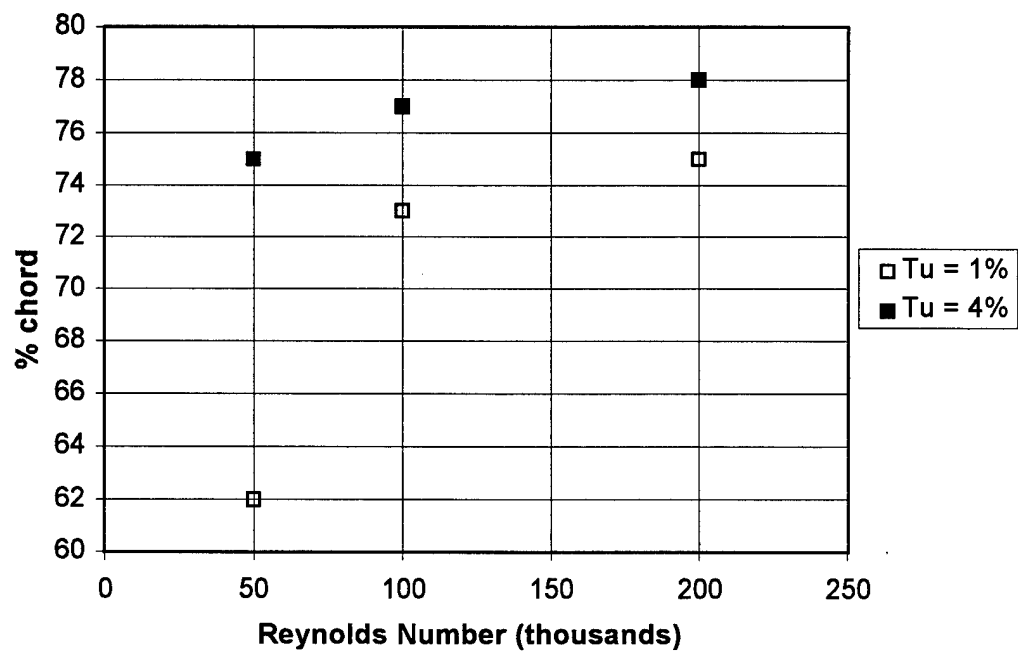


Figure 32. Variation of separation start with Reynolds number and turbulence intensity.

## 6.2.4 Uncertainty in $C_p$ Measurements

The uncertainty in the  $C_p$  measurements was calculated using the method described by Kline and McClintok [33]. Using this method the  $C_p$  uncertainties are  $\pm 0.59$ ,  $\pm 0.18$ , and  $\pm 0.04$  for Reynolds numbers of 50k, 100k, and 200k, respectively. The errors decrease with increasing Reynolds number because the measured pressures increase with increasing speed. The increased pressure provides a larger range for the pressure transducers to read, thus decreasing the effect of calibrator limitations. The error calculations for the  $C_p$  curves are presented in Appendix I. The velocity of the boundary layer downstream of separation was measured directly using a small hot film probe.

## 6.3 Boundary Layer Velocity and Turbulence Profiles

The boundary layer velocity and turbulence measurements were made over the aft portion of the suction surface at 67.2%, 73.0%, 79.3%, 84.8%, and 89.8% axial chord. These five locations span the region most effected by the separation bubble. Measurements were made at  $Re = 50k$  and 100k for turbulence levels of 1% and 4%. The boundary layer measurements of velocity and turbulence were made with a TSI 1279S-10A hot film probe. This probe was moved by a National Aperture, Inc. MM-3M 5.08 cm (2 inch) micro traverse controlled by a National Aperture, Inc. MC-3SA servo amplifier system. The software for this system is explained in more detail in Appendix D.

### 6.3.1 Boundary Layer Measurements at $Re = 50k$

Figure 33 illustrates the magnitude of the suction surface separation problem typical of high altitude, low speed flight. Defining the boundary layer thickness to be the height at which the velocity is 99% of the freestream value, the separation bubble has a maximum thickness of 31.0 mm (1.22 inches) at the 89.8% axial chord location. The x-axis of Figure 33 is the non-dimensional velocity for each of the axial chord locations where the boundary layer measurements were taken.

Each velocity reading is nondimensionalized by dividing by the freestream velocity at that chordwise location and multiplied by 100. The height of the boundary layer is determined from the y-axis which is in millimeters.

The growth of the suction surface boundary layer shown in Figure 33a appears to be nonlinear with the suction surface. The nonlinear shape was due to the convex geometry of the surface of the blade, coupled with the convex shape of the separation bubble itself. The combination of the two convex conditions give the nonlinear appearance seen in Figure 33a when the measured velocities are plotted on an orthogonal graph. The same physical conditions which influence the velocity graphs also affect the turbulence graphs.

In Figures 33b through 36b the turbulence intensity shown was calculated using:

$$Tu\% = \left( \frac{\sigma}{\bar{U}_y} \right) \cdot 100 \quad (18)$$

where  $\sigma$  is the rms of the mean velocity  $\bar{U}$  recorded at height  $y$  above the blade surface thus defining the local turbulence intensity. The definition provided in equation 18 was used to provide direct comparison with the previously published results of Murawski et al. [4]. While the turbulence intensity within the boundary layer does match the levels previously documented by Murawski et al. [4], the high turbulence levels seen in the figures are much smaller when calculated using the freestream velocity above the boundary layer instead of the local velocity used in equation 18. For example, a turbulence intensity of 50% within the boundary layer is only 10.3% when calculated with the freestream velocity. The turbulence intensity shown in Figure 33b illustrates an initially laminar boundary layer quickly separating with the associated increase in turbulence intensity to a maximum of 77.26% at the 73% axial chord position. Downstream of 73% axial chord the recirculation within the separation bubble is significant enough to cause an almost steady turbulence level

of 35-45%. These high turbulence levels are consistent with the previously published Pak-B data (Murawski et al. [4]).

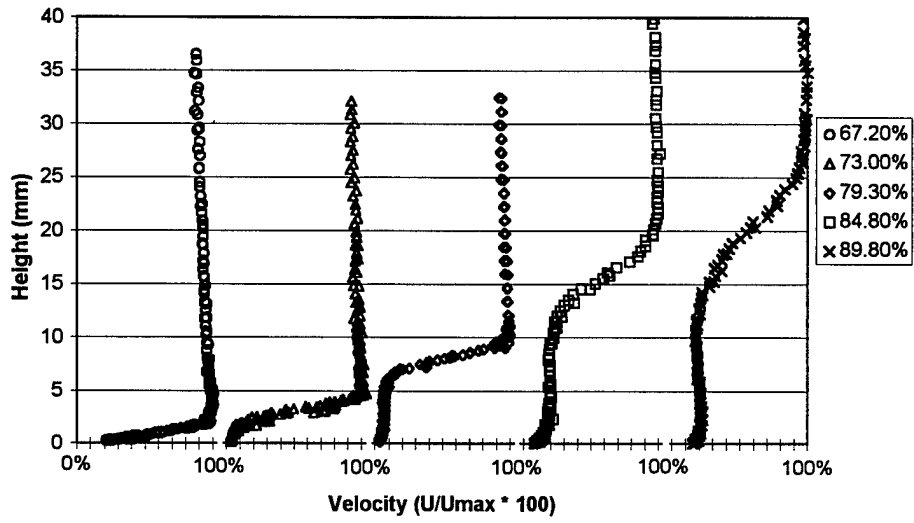
The effect of increased freestream turbulence is clear when Figure 34 is compared to Figure 33. The separation which continued to grow to the trailing edge in the laminar flow case was reduced to a thin bubble with a maximum thickness of only 6.38 mm (0.252 inches) at the 89.8% axial chord line. The recirculation region of the separation bubble was delayed from the 73% chord to the 79.3% axial chord line.

Increasing the freestream turbulence level to 4% shows a delay in the tripping of the boundary layer from the 73% chord position to 84.8% axial chord line. The peak turbulence at 84.8% chord is 61.3% at a height of 1.059 mm (0.042 inches). The maximum turbulence at the 89.8% chord line was only 45.3% as compared to 52.2% for the laminar flow case at the same location.

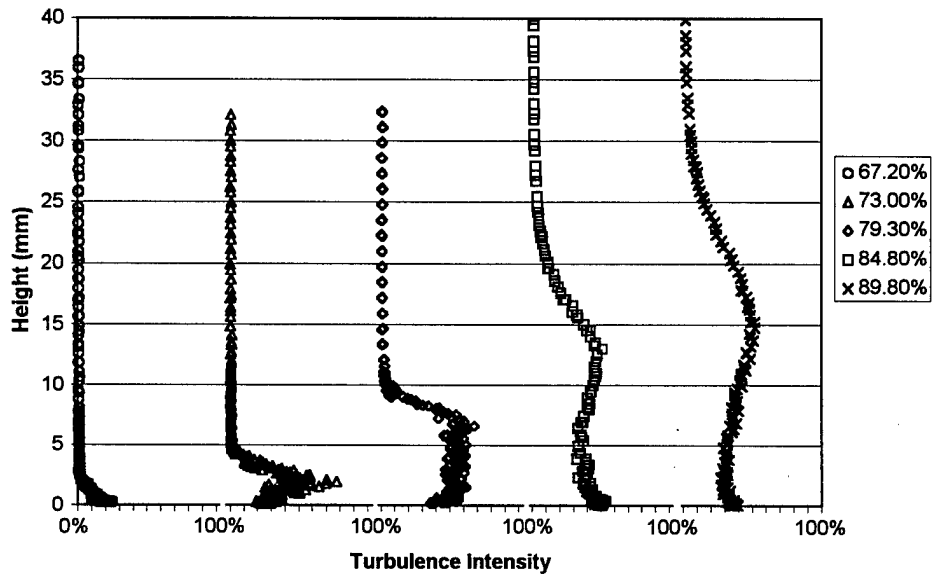
### **6.3.2 Boundary Layer Measurements at $Re = 100k$**

The higher energy in the flow for the  $Re = 100k$  case reduces the separation present over the suction surface significantly while a recirculation region still exists at the 84.8% chord line. Comparing the velocity and turbulence curves in Figure 35a and b, respectively, it can be seen that the laminar flow separates upstream of the 79.3% axial chord line. Downstream of the 84.8% chord line, the flow undergoes transition to turbulent flow and reattaches upstream of the 89.8% chord line.

The combined effects of increased Reynolds number and freestream turbulence greatly reduce the separation over the suction surface of the unmodified Pak-B blade. The completely separated flow seen in Figure 33 has been reduced to a small separation bubble near the 85% axial chord line. The uncertainty in the velocity measurements for Figures 33 through 36 follows.

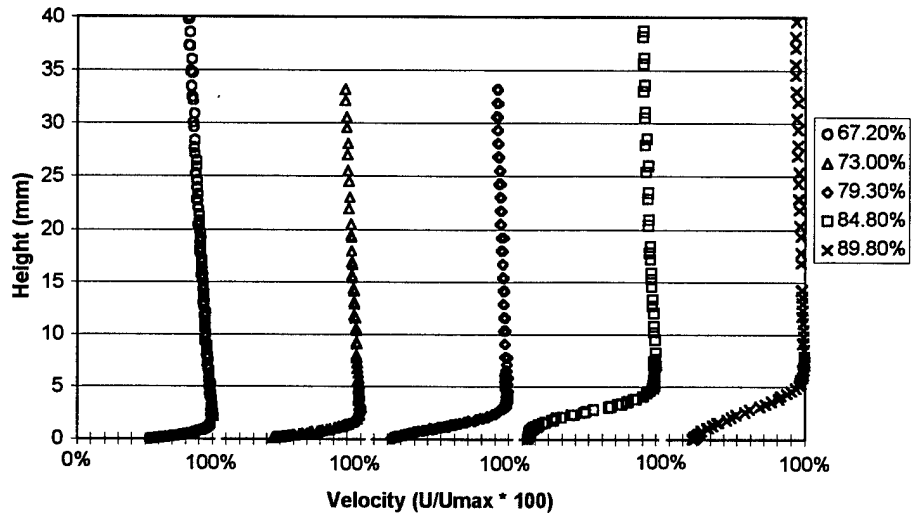


a) boundary layer at  $Re = 50k$  and  $Tu = 1\%$

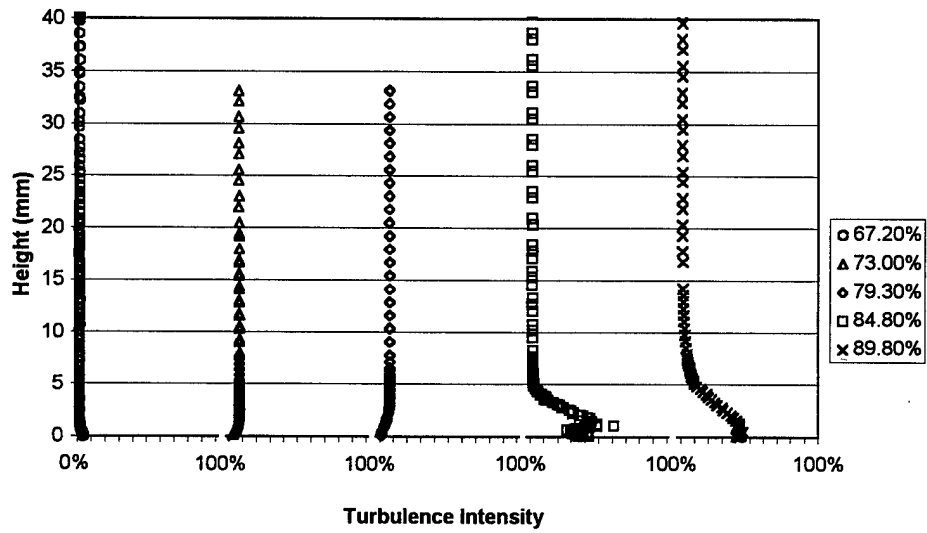


b) boundary layer at  $Re = 50k$  and  $Tu = 1\%$

Figure 33. Baseline velocity and turbulence profiles over the suction surface.

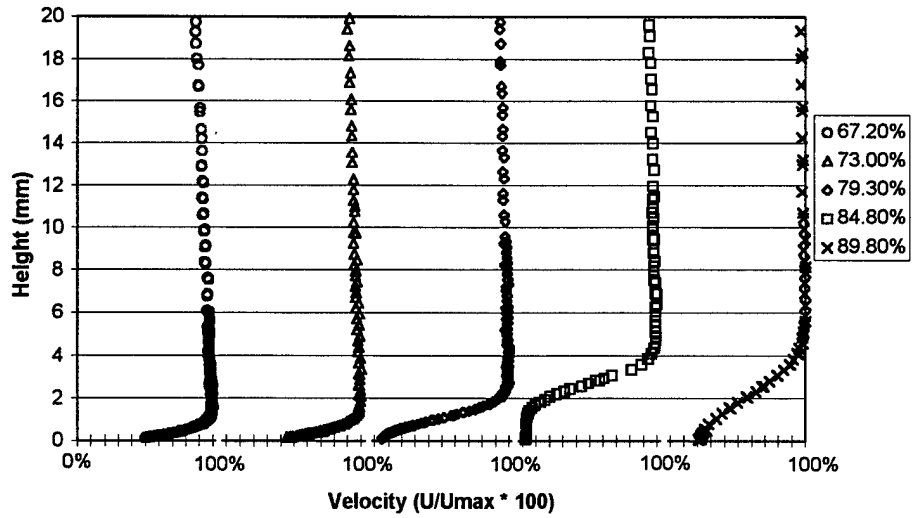


a) boundary layer at  $Re = 50k$  and  $Tu = 4\%$

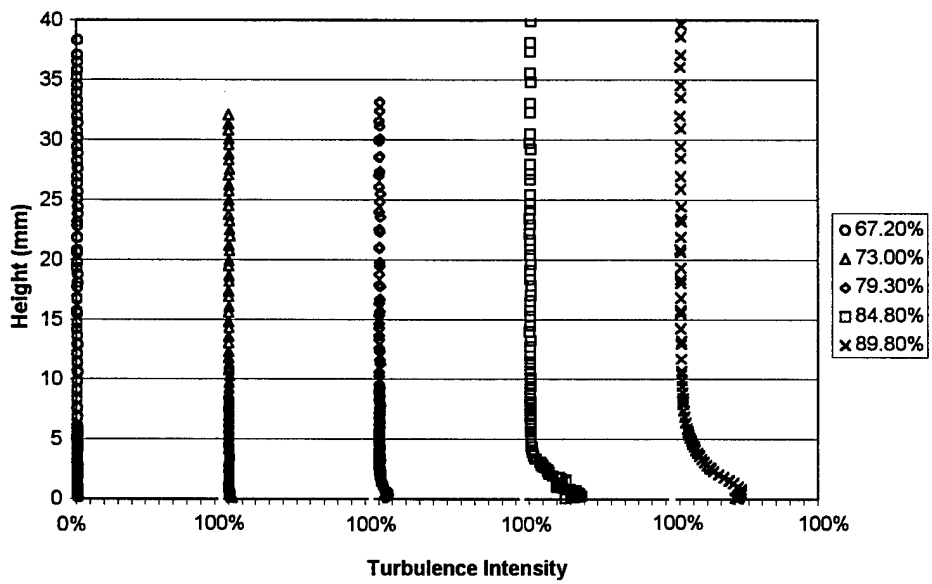


b) boundary layer at  $Re = 50$  and  $Tu = 4\%$

Figure 34. Baseline velocity and turbulence profiles with increased freestream turbulence.



a) boundary layer at  $Re = 100k$  and  $Tu = 1\%$



b) boundary layer at  $Re = 100k$  and  $Tu = 1\%$

Figure 35. Baseline velocity and turbulence profiles for  $Re = 100k$ .

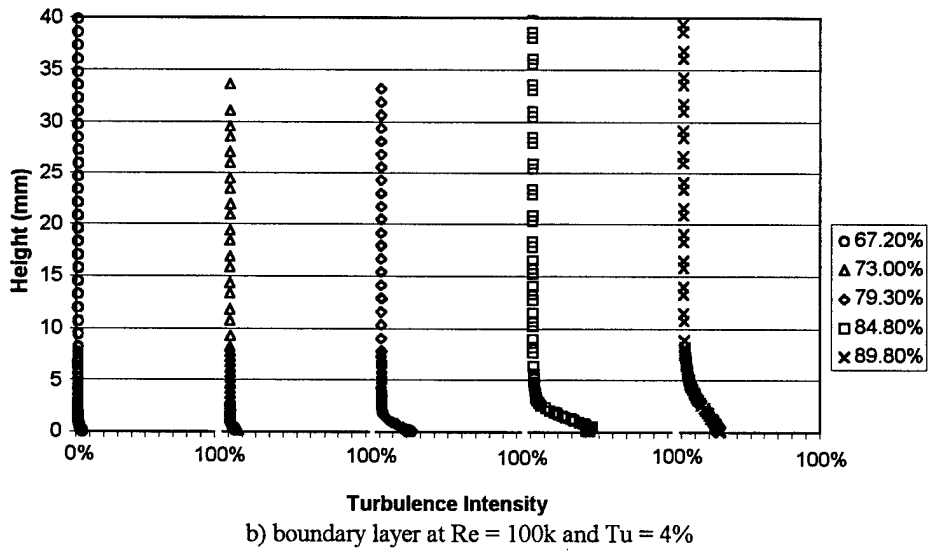
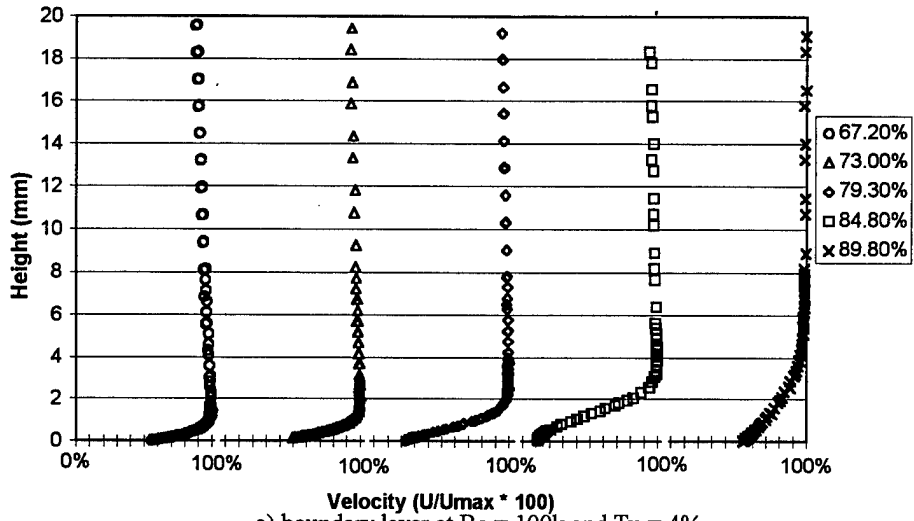


Figure 36. Baseline velocity and turbulence profiles with moderate freestream turbulence.

### 6.3.3 Uncertainty in Boundary Layer Measurements

The method used for calculating the uncertainty in the boundary layer hot film velocity measurements was described by Kline and McClintok [33]. Using this method the velocity uncertainties are  $\pm 0.24$  m/s and  $\pm 0.15$  m/s for Reynolds numbers of 50k and 100k, respectively. The errors decrease with increasing Reynolds number since the measured pressures used in calibration of the hot film increase with increasing speed thus reducing the effect of calibrator limitations. The boundary layer error calculations are presented in Appendix I along with the error analysis for the hot wire measurements for the exit wake profiles.

## 6.4 Exit Velocity Wake Profiles

The exit velocity profile for the Pak-B blade was measured  $\frac{1}{2}$  axial chord lengths downstream of blade #5. The velocity was measured using a TSI 1210-T1.5 single hot wire probe mounted on the 3-axis Dantec traverse. The velocity measurements were taken every 0.5 cm across the 15.75 cm (6.2 inches) wake. The velocity data was then used to calculate the momentum wake deficit for the smooth blade.

### 6.4.1 Exit Velocity Wake Data

The measured exit velocity profiles are displayed in Figures 37 and 38 where the pressure side of blade #5 is the left portion of the wake from 60 cm to 66 cm. The suction side of the wake extends from 66 cm to the right. Figure 37 contains the velocity wake data for Reynolds numbers of 50k, 100k, and 200k for an inlet freestream turbulence of 1%. The x-axis of Figure 37 displays the probe location within the tunnel where the hot wire was positioned when the data point was collected. The trailing edge of blade #5 is approximately at 66 cm on Figure 37. The y-axis of Figures 37 and 38 are the measured velocities. The bottom curve of Figure 37 was for an inlet Reynolds number of

50k. The middle and upper curves of Figures 37 and 38 were for inlet Reynolds numbers of 100k and 200k respectively.

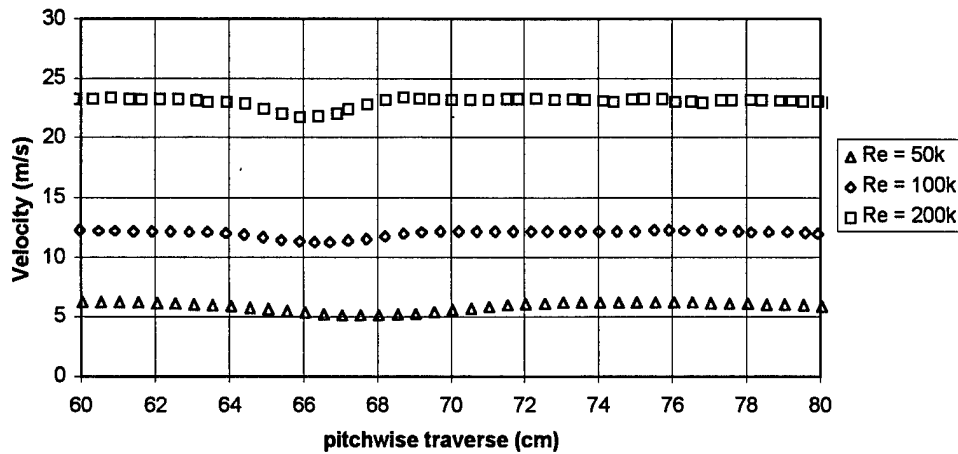


Figure 37. Baseline Pak-B exit velocity profiles for  $Tu = 1\%$ .

Noticeable in Figure 37 is how the center of the wake shifts to the left with increasing Reynolds number. The shift in wake location was due to the decreasing size of the boundary layer with increased speed. As seen in Figures 33 through 36 as the Reynolds number increases, the thickness of the boundary layer decreases. The decrease in boundary layer thickness leads to a smaller wake closer to the suction surface.

Figure 38 contains exit wake velocity data for an increased freestream turbulence of 4%. At the higher turbulence level the boundary layer has more energy and therefore less separation. The decrease in boundary layer thickness reduces the amount of wake shift compared to the laminar case of Figure 37. All the velocity wake curves in Figure 38 have less of a velocity deficit than their counterparts for the laminar freestream case of Figure 37. The velocity wake data was used to calculate a momentum deficit value for each flow condition tested.

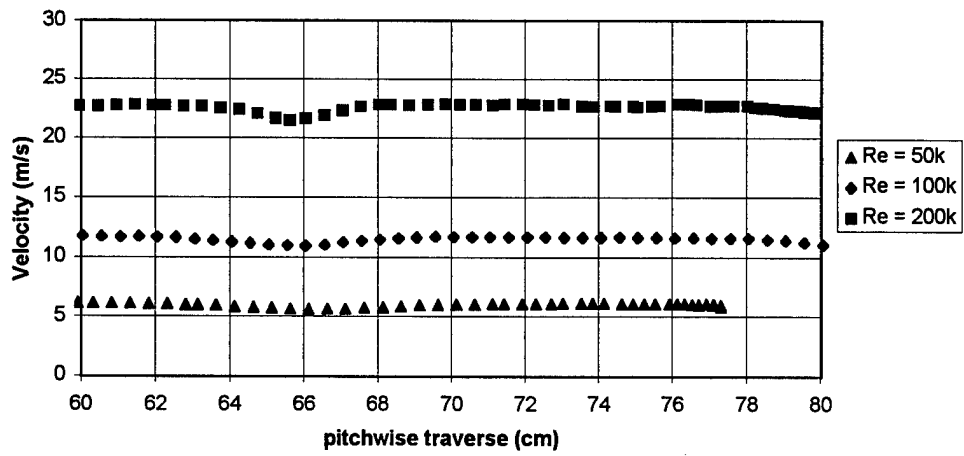


Figure 38. Baseline Pak-B exit velocity profiles at  $Tu = 4\%$ .

### 6.4.2 Exit Momentum Deficit Calculations

Using the velocity information in Figures 37 and 38 the wake momentum deficits were calculated. The momentum wake deficit was calculated using:

$$\Theta = \sum \left( \frac{U_w}{U_\infty} \right) \left( 1 - \frac{U_w}{U_\infty} \right) dy \quad (19)$$

where  $U_w$  was the wake velocity measured at pitchwise position  $y$  within the 15.75 cm wake. The freestream (maximum) velocity between blades in the downstream wake is denoted as  $U_\infty$ . Figure 39 illustrates the drop in loss coefficient with increasing Reynolds number and turbulence level. The difference between the two turbulence cases for a Reynolds number of 50k seen in Figure 39 is due to the strong effect fully separated flow has upon blade losses. The problem of maintaining attached flow over the blade at low Reynolds numbers is the key goal to this research.

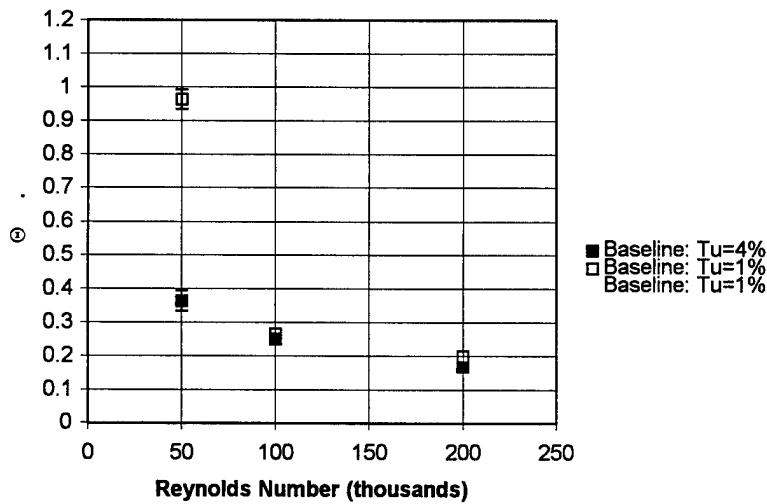


Figure 39. Baseline Pak-B blade momentum deficit measurements.

### 6.4.3 Uncertainty in Wake Momentum Deficit Measurements

The uncertainty in the exit wake momentum deficit measurements were calculated using the method described by Taylor [34]. Using this method the wake momentum uncertainties were cal-

culated to be  $\pm 0.030$  m,  $\pm 0.009$  m, and  $\pm 0.003$  m for Reynolds numbers of 50k, 100k and 200k, respectively. The uncertainties decrease with increasing Reynolds number since the measured pressures used in calibration of the hot wire increase with increasing speed, thus reducing the effect of scale limitations from the manometer. Even with the uncertainty of the experimental data, the trend of decreasing losses with increasing Reynolds number is clearly evident from Figure 39. This trend can also be observed from total pressure coefficient loss measurements.

## 6.5 2-D Profile Loss Coefficient Measurements

The performance of the baseline LPT Pak-B blades were also characterized by the total pressure loss coefficient. The loss coefficient was measured using a total pressure probe located approximately  $\frac{1}{2}$  axial chord lengths downstream of the blade cassette. The loss coefficient definition is restated here:

$$\gamma = \frac{P_{0,inlet} - \overline{P_{0,exit}}}{\frac{1}{2}\rho\overline{U}_{exit}^2} \quad (20)$$

where  $P_{0,exit}$  and  $U_{exit}$  were averaged over the exit plane of blade #5 by dividing the sum by the number of samples. The inlet total pressure  $P_{0,inlet}$  was measured approximately one axial chord length upstream of blade #5. The exit velocity for the experiments was small compared with the speed of sound so no density correction for compressibility effects was used. The measurements were made in 0.5 cm (0.197 inches) increments across the blade wake in the center span of the 87.63 cm (34.5 inches) high blade. Taking loss coefficient measurements in the center span provides the 2-D loss coefficient which does not account for tip losses, corner vortices, or 3-D effects.

### 6.5.1 Exit Pressure Data

Each exit pressure data point was measured independently three different times and then ensemble averaged. The ensemble averaged  $P_{0,inlet} - P_{0,y}$  values for  $Re = 50k, 100k, 200k$ , and for a

freestream turbulence level of 1% are in Figure 40. The x-axis of Figure 40 is the traverse location of the probe as described previously for Figures 37 and 38. The y-axis of Figure 40 is the difference in total pressure between  $P_{0,inlet}$  and  $P_{0,exit}$  measured in units of  $kg/m.s^2$ .

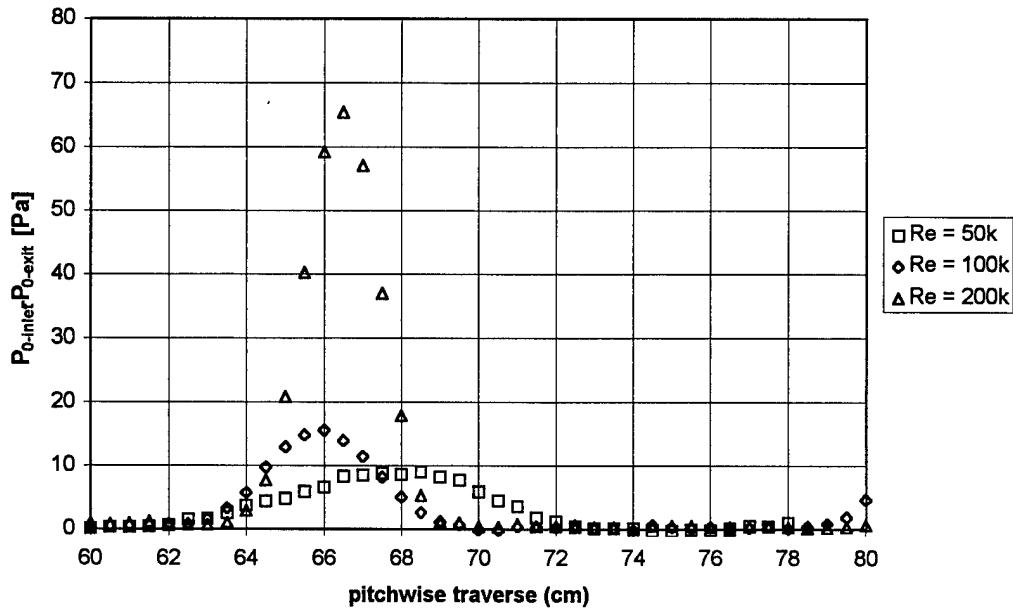


Figure 40. Baseline Pak-B exit stagnation pressure loss at  $Tu = 1\%$ .

### 6.5.2 Baseline Performance Loss Coefficients

Using the pressure curves in Figures 40 and 41 the loss coefficients were calculated. The resulting values for freestream turbulence levels of 1% and 4% are both in Figure 42. For the 1% turbulence case the loss coefficient drops quickly with increasing Reynolds number from 0.155 at 50k down to only 0.032 at 200k. For the increased turbulence of 4%, the loss coefficient also decreases with increasing Reynolds number, although not as dramatically as for the case of  $Tu = 1\%$ . For increased freestream turbulence, the loss coefficient is 0.058 at  $Re = 50k$ , and drops to only 0.037 at  $Re = 200k$ . The measured values of loss coefficient agree with estimations and curve fits using previously recorded data from other turbine blades. The early experiments by Ainley [35] and

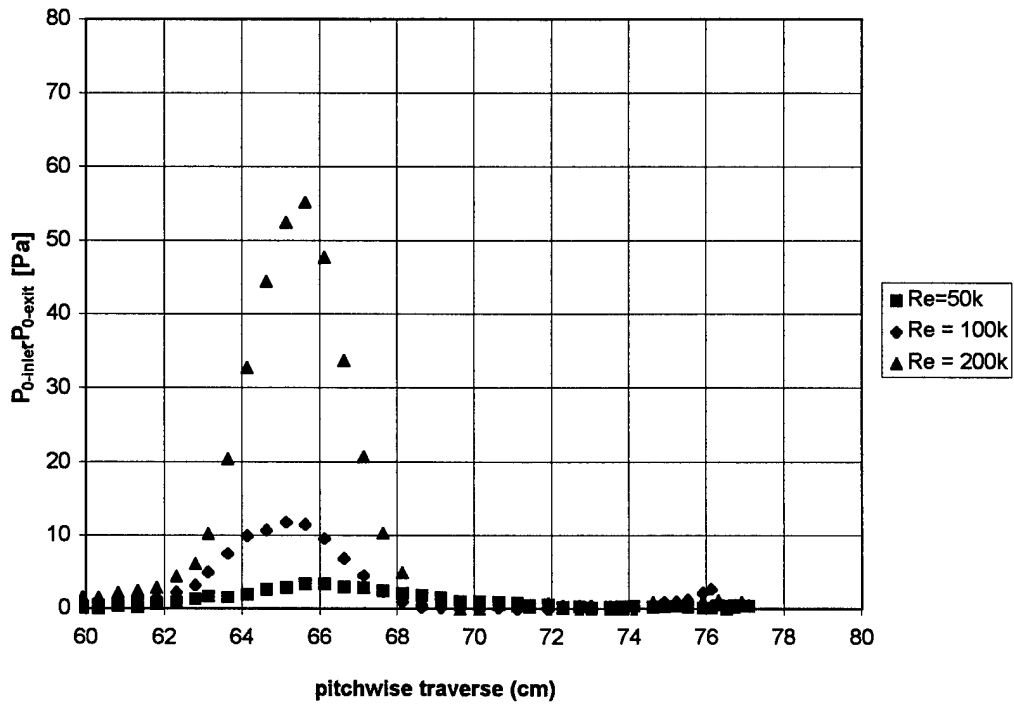


Figure 41. Baseline Pak-B exit stagnation pressure loss at  $Tu = 4\%$ .

Ainley and Mathieson [36] with the T.6 blade shape provide comparable results to the experimental data of the Pak-B blade. The curve fits calculated from Horlock [37–39] are slightly above the measured loss coefficient for  $Tu = 4\%$  due to the differences in thickness-to-chord ( $\frac{t}{c}$ ) ratio which the curve fits can not account for. The relations of Craig and Cox [40] go further to include the effect of blade solidity ( $\frac{c}{s}$ ) and trailing edge thickness. The Craig and Cox [40] curve fits provide the most accurate estimation of the loss coefficient when the flow is attached to the blade at the trailing edge. More information on the estimation of loss coefficient is in Appendix F.

### 6.5.3 Uncertainty in Loss Coefficient Measurements

The experimental values represented in equation 20 were taken using the same instruments as in equation 17. Because of the similarity between equations 17 and 20, the uncertainty analysis for each was very similar. Using the method described in Appendix I for the surface pressure coefficients, the uncertainty for the loss coefficients are  $\pm 0.014$ ,  $\pm 0.003$ , and  $\pm 0.0006$  for  $Re = 50k$ ,  $100k$ , and  $200k$  respectively.

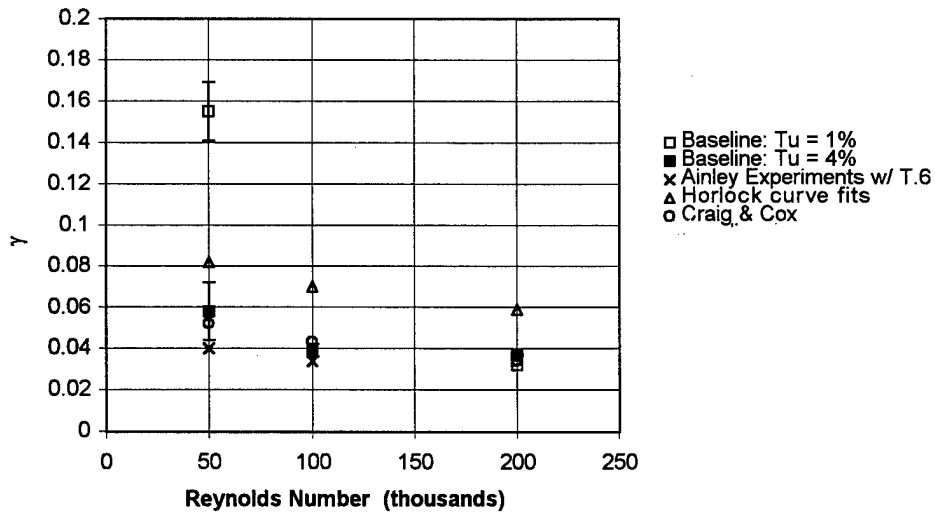


Figure 42. Baseline Pak-B exit loss coefficients.

## Chapter 7 - Performance of Pak-B blade With Boundary Layer

### Trip at 35% Chord

#### 7.1 Trip Configurations Tested

The losses associated with separated flow from the Pak-B blade can also be controlled with a simple boundary layer trip. To ensure a fully turbulent boundary layer over the suction surface of the blade, four different methods were examined and compared. Each method was tested to determine if it could produce an initially attached turbulent boundary layer for the region near the 67% axial chord line where separation began on the baseline blade. The methods tested include surface roughness (sandpaper) applied to the leading edge of the blade, roughness extending from the leading edge to the 50% axial chord line, a small trip wire, and a large trip wire. Only the large trip wire produced a turbulent boundary layer over the aft portion of the Pak-B blade.

The height ( $k_{crit}$ ) of the sandpaper roughness necessary to trip the boundary layer was determined using (Schlichting [41]):

$$\frac{u_k^* k_{crit}}{v} = 15 \quad (21)$$

where  $u_k^*$  was defined as (Schlichting [41]):

$$u_k^* = \sqrt{\frac{\tau_0}{\rho}} \quad (22)$$

and  $\tau_0$  was the shearing stress at the blade surface. The value of  $k_{crit}$  determined from equations 21 and 22 for an inlet Reynolds number of 50k was 0.87 mm (0.0341 inches). Sandpaper with this thickness was first applied to the leading edge of the Pak-B blade, extending to the 15% chord line. With the leading edge sandpaper in place, a boundary layer velocity profile was acquired with the hot film probe located at 67% axial chord. As can be seen in Figure 43, the resulting velocity profile

was still laminar. In addition to taking experimental data, typical relations for laminar and turbulent flow were also graphed on Figure 43. The laminar relation used was (White [42]):

$$u_y = U_\infty \left[ \frac{2y}{\delta} - \frac{y^2}{\delta^2} \right] \quad (23)$$

where  $U_\infty$  was the freestream velocity and  $\delta$  was the boundary layer thickness. The turbulent boundary layer estimation used was (White [42]):

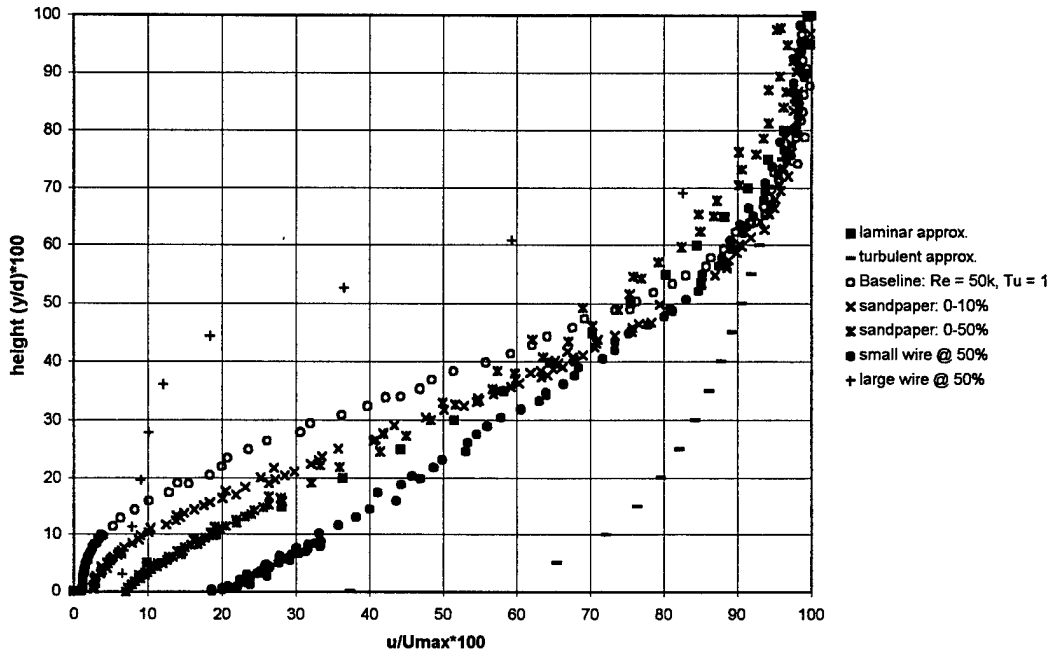
$$u_y = U_\infty \left[ \frac{y}{\delta} \right]^{1/7}. \quad (24)$$

The sandpaper was extended to the 50% axial chord location; however, this attempt was also insufficient in producing a turbulent boundary layer at the 67% chord line at a Reynolds number of 50k. Further attempts were made to produce a turbulent boundary layer.

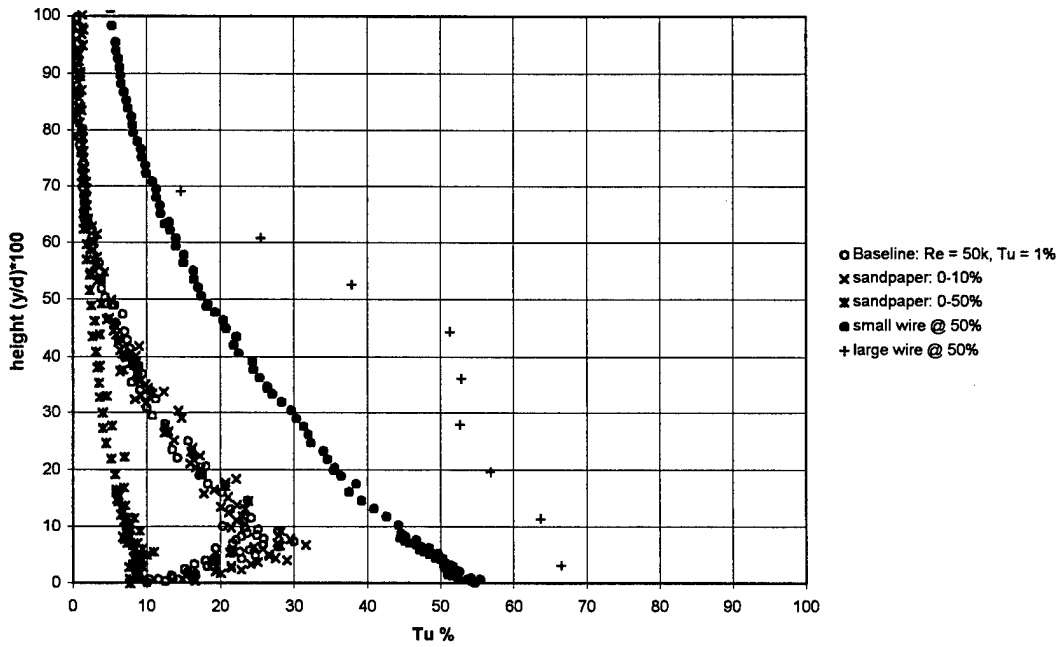
A small trip wire was attached to the suction surface of the Pak-B blade. The small wire diameter was determined using (Schlichting [41]):

$$\frac{uk_{crit}}{\nu} \geq 900. \quad (25)$$

Use of equation 25 estimated the minimum wire diameter to trip the boundary layer to be 1.83 mm (0.072 inches). A wire of this minimum diameter failed to trip the boundary layer into a turbulent state when placed at the 50% axial chord line. A larger wire with a diameter of 2.77 mm (0.109 inches) was then used at the 10%, 20%, 35%, and 50% axial chord locations to find the optimum location. With the large wire at the 10% chord line, the flow was tripped to a turbulent state, but had partially re-laminarized by the 67% chord position (see Figures 44 and 45). The same decay in the turbulence was also measured with the trip wire at the 20% chord line (see Figures 46 and 47). With the large wire at the 35% chord line, the boundary layer was determined to be fully turbulent at the 67% chord line. However, the large wire created a region of separated flow when placed further

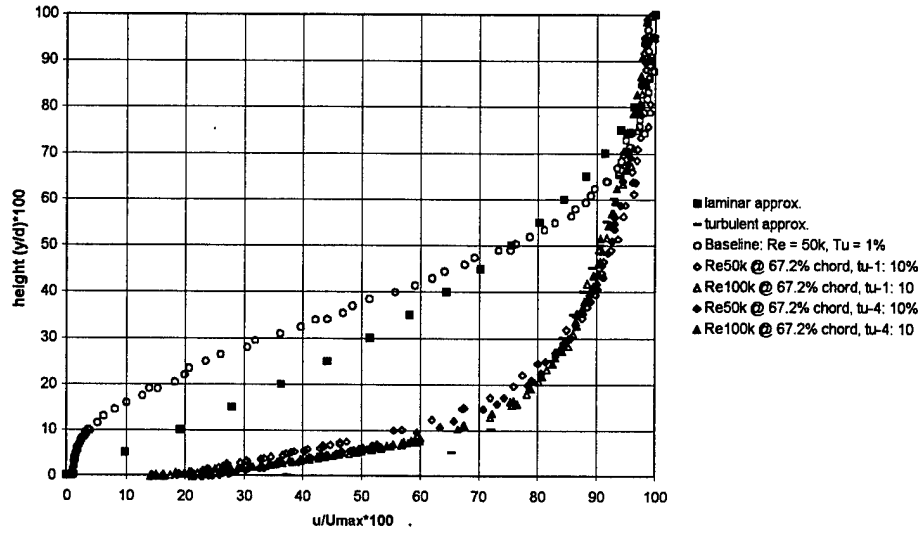


a) velocity profile at freestream turbulence of 1%

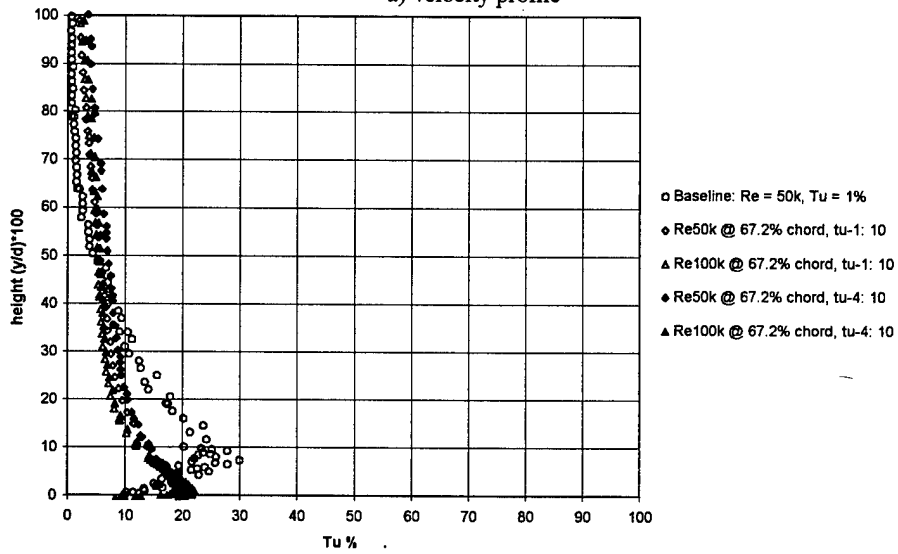


b) local turbulence profile at freestream turbulence of 1%

Figure 43. Boundary layer trip attempts measured at 67.2% axial chord for Re = 50k.

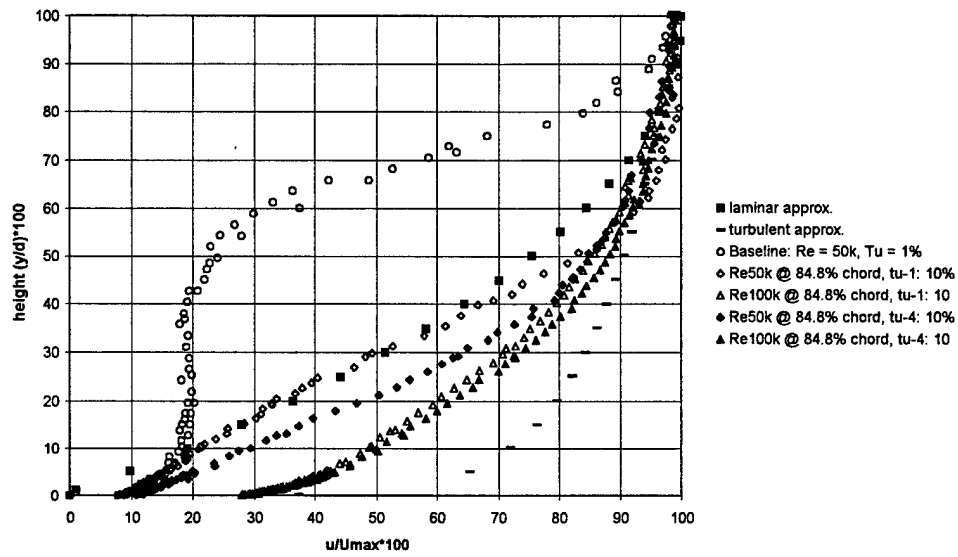


a) velocity profile

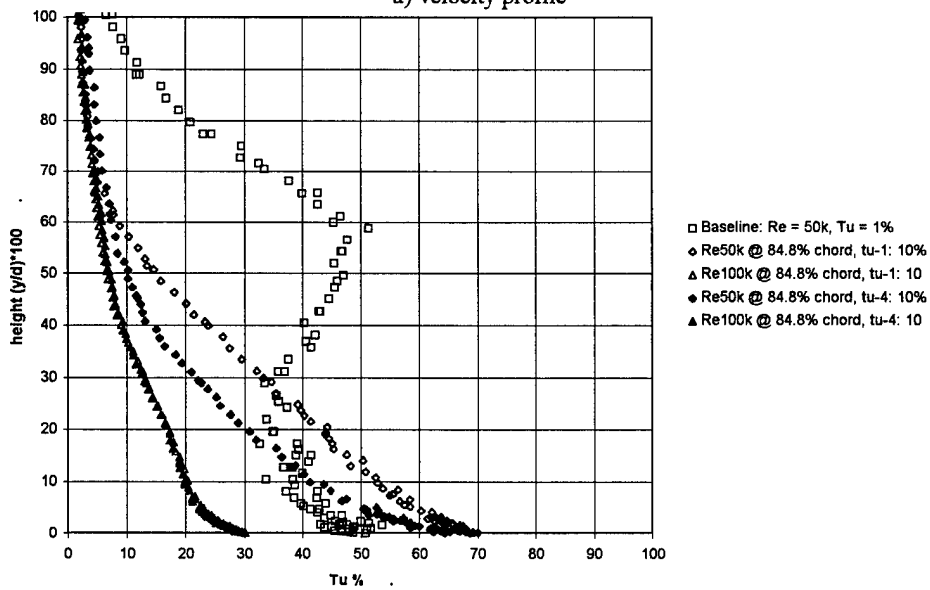


b) local turbulence profile

Figure 44. Boundary layer profiles measured at 67% chord with trip wire at 10% axial chord.

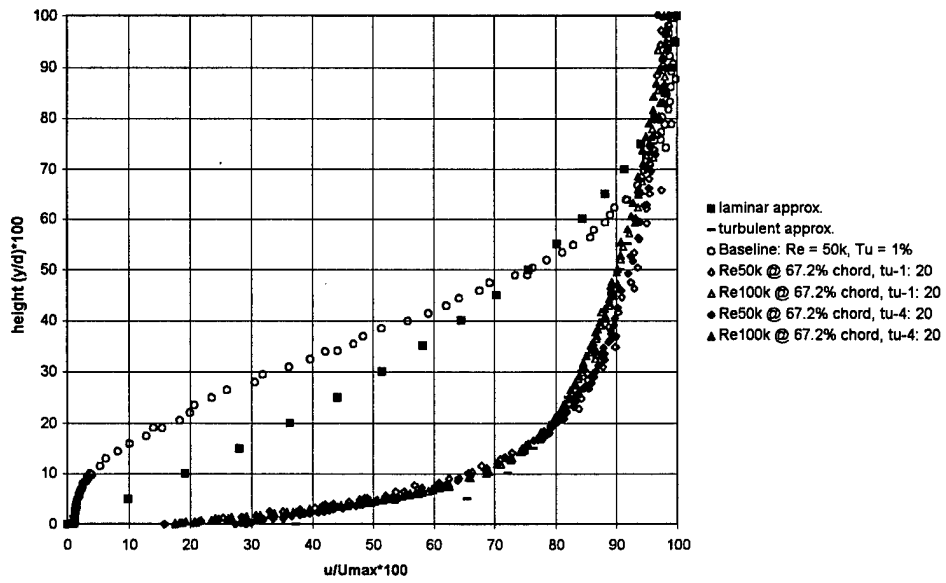


a) velocity profile

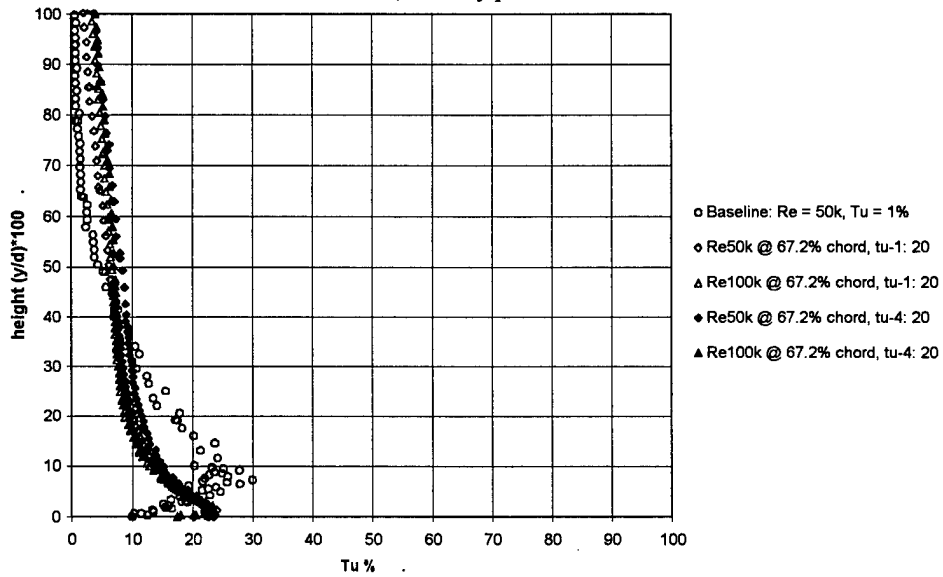


b) local turbulence profile

Figure 45. Boundary layer profiles measured at 84.8% chord with trip wire at 10% axial chord.

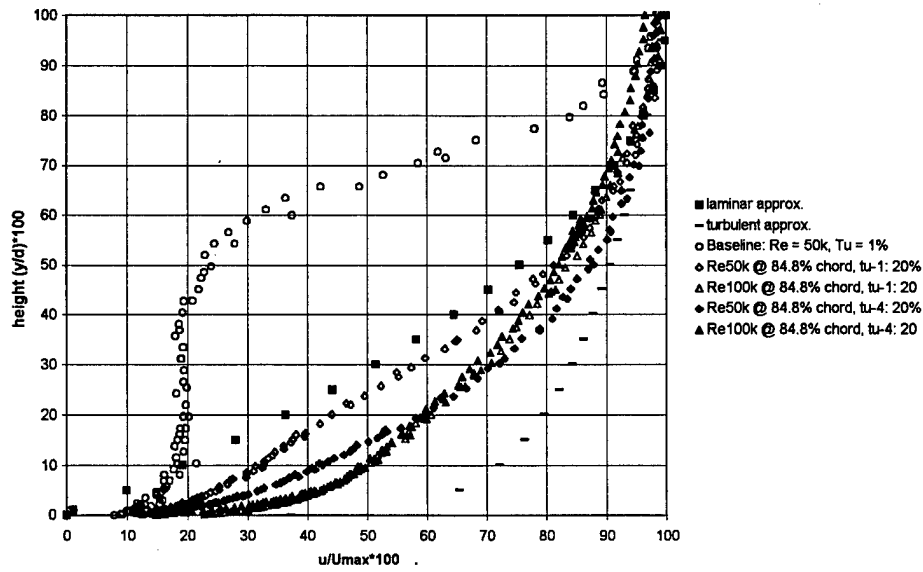


a) velocity profile

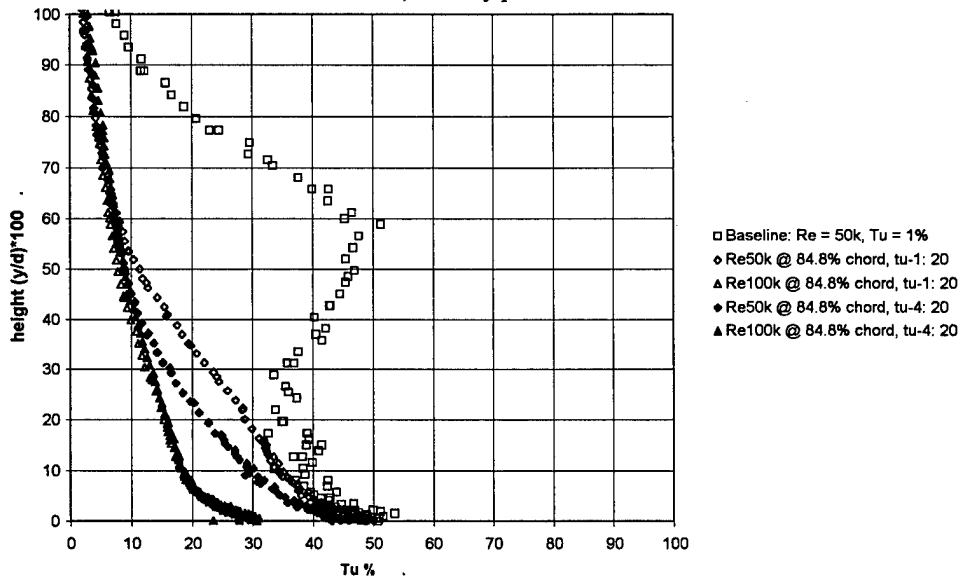


b) local turbulence profile

Figure 46. Boundary layer profiles measured at 67% chord with trip wire at 20% axial chord.



a) velocity profile



b) local turbulence profile

Figure 47. Boundary layer profiles measured at 84.8% chord with trip wire at 20% axial chord.

aft at the 50% axial chord line (see Figure 43). It was determined that when the flow was tripped to an initially attached and turbulent state, the boundary layer remained attached to the suction surface for all Reynolds numbers and freestream turbulence intensities tested.

## **7.2 Boundary Layer Profiles Using Large Trip Wire**

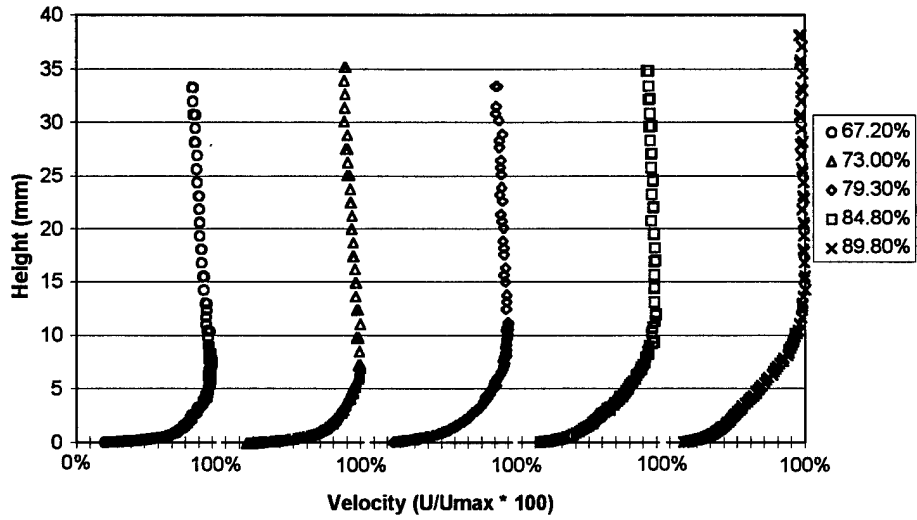
Figures 48 through 51 show the boundary layer profiles over the aft portion of the suction surface when a 2.77 mm (0.109 inches) diameter trip wire was placed at the 35% axial chord location. The flow remains attached over the entire suction surface even for a low Reynolds number of 50k. Noteworthy in Figures 48 through 51 was the gradual re-laminarization of the boundary layer. This was evident from the initially turbulent velocity profile at 67.2% chord line to the transitional velocity profile at 89.8% chord. The transitional, attached boundary layer at the exit from the blade resulted in a smaller velocity wake profile downstream for a Reynolds number of 50k.

## **7.3 Exit Velocity Wake Measurements Using Large Trip Wire**

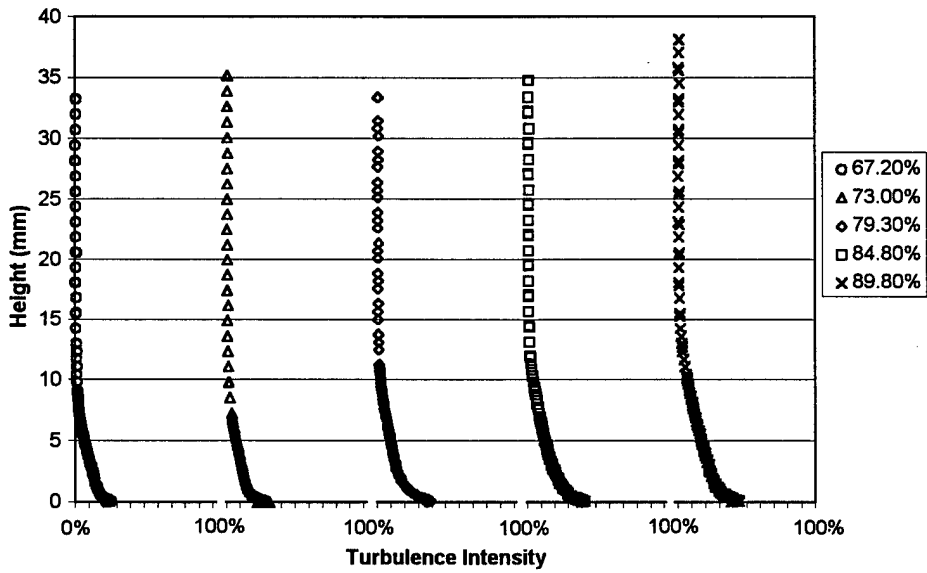
The exit velocity profile was measured using the TSI 1210-T1.5 hot wire approximately  $\frac{1}{2}$  axial chord lengths downstream from the blade with the wire trip. As seen in Figure 52, the tripped velocity profile was smaller than the baseline blade for a Reynolds number of 50k and a freestream turbulence level of 1%. At all other Reynolds numbers and turbulence intensities the velocity wakes were larger for the tripped blade than the baseline blade. This was due to the fact that the unmodified boundary layer did not have large regions of flow separation at higher Reynolds numbers and turbulence intensities. The trip wire created a turbulent and transitional boundary layer which increased the losses when the flow would otherwise be attached and laminar.

## **7.4 Loss Coefficient Measurements Using Large Trip Wire**

The trend in increased losses for Reynolds numbers of 100k and 200k was also evident with the exit pressure data (see Figure 53). The exit total pressure wakes were measured at the same down-

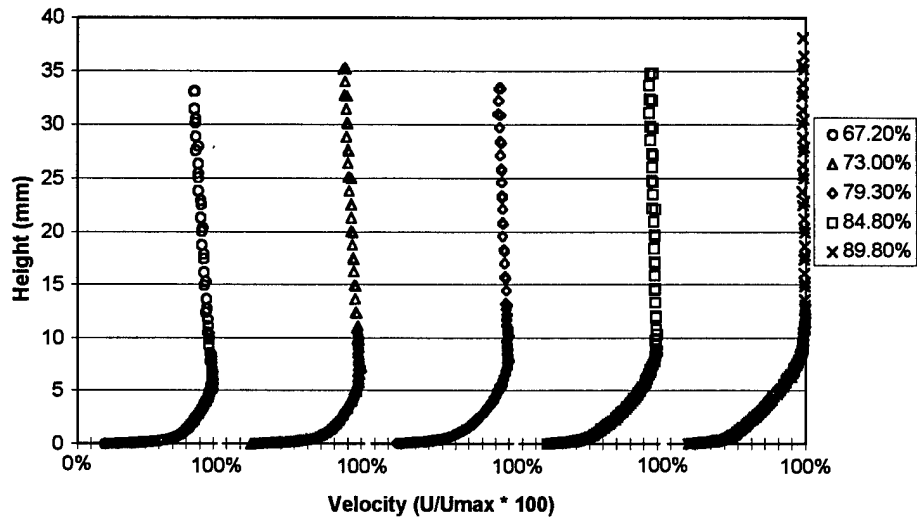


a) boundary layer velocity measurements at  $Re = 50k$  and  $Tu = 1\%$

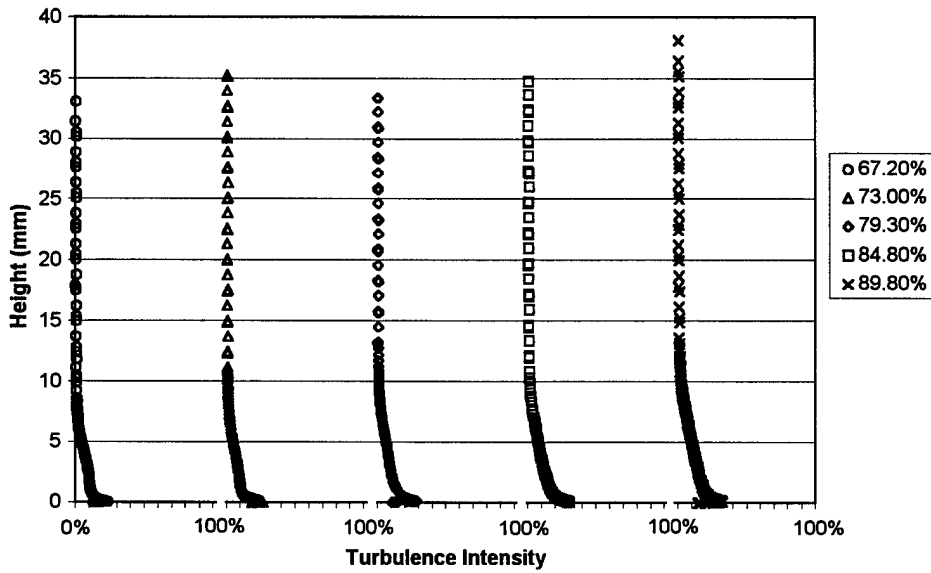


b) boundary layer turbulence measurements at  $Re = 50k$  and  $Tu = 1\%$

Figure 48. Measured velocity and turbulence profiles for baseline blade with trip at 35%.

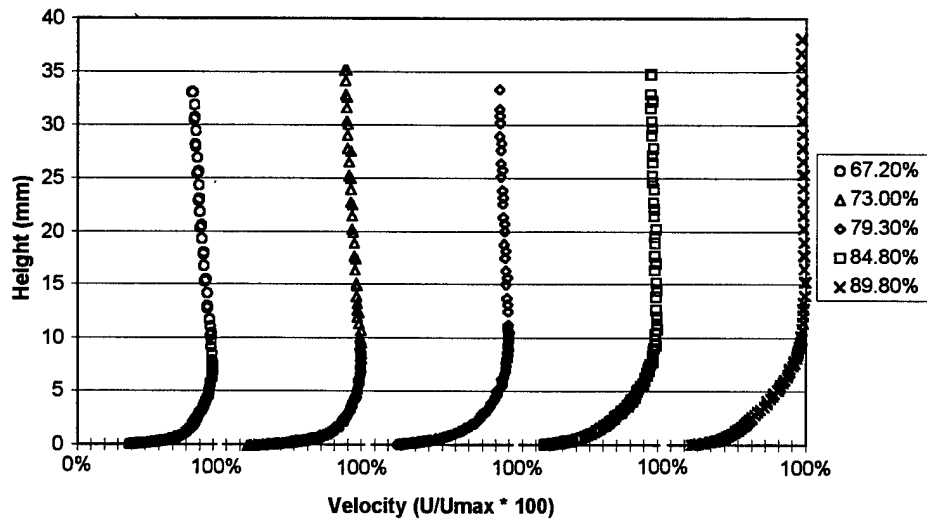


a) boundary layer velocity measurements at  $Re = 100k$  and  $Tu = 1\%$

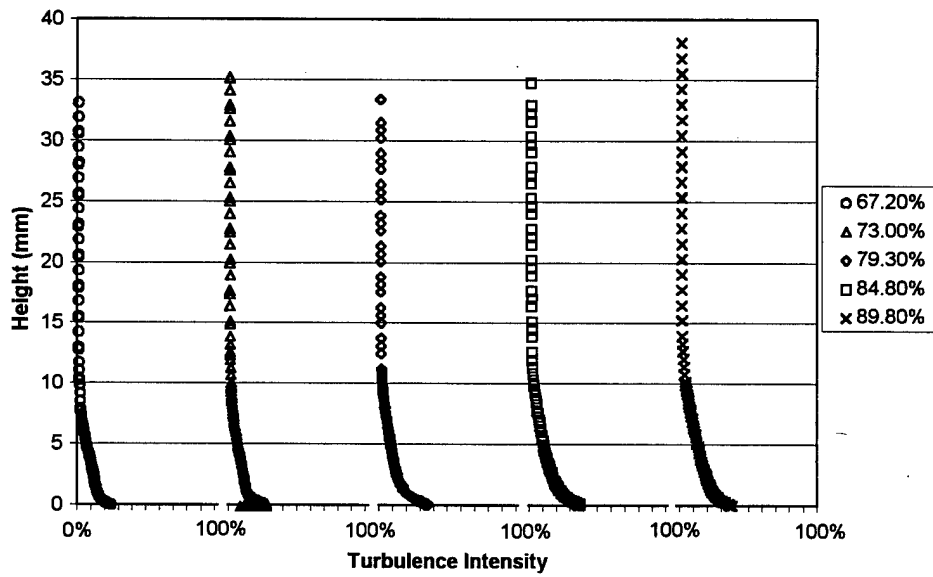


b) boundary layer turbulence measurements at  $Re = 100k$  and  $Tu = 1\%$

Figure 49. Measured velocity and turbulence profiles for baseline blade with trip at 35%.

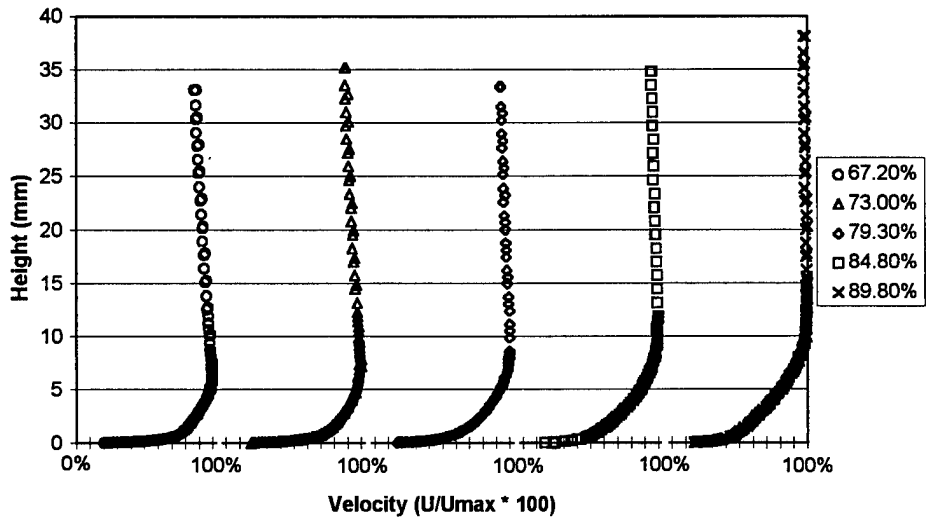


a) boundary layer velocity measurements at  $Re = 50k$  and  $Tu = 4\%$

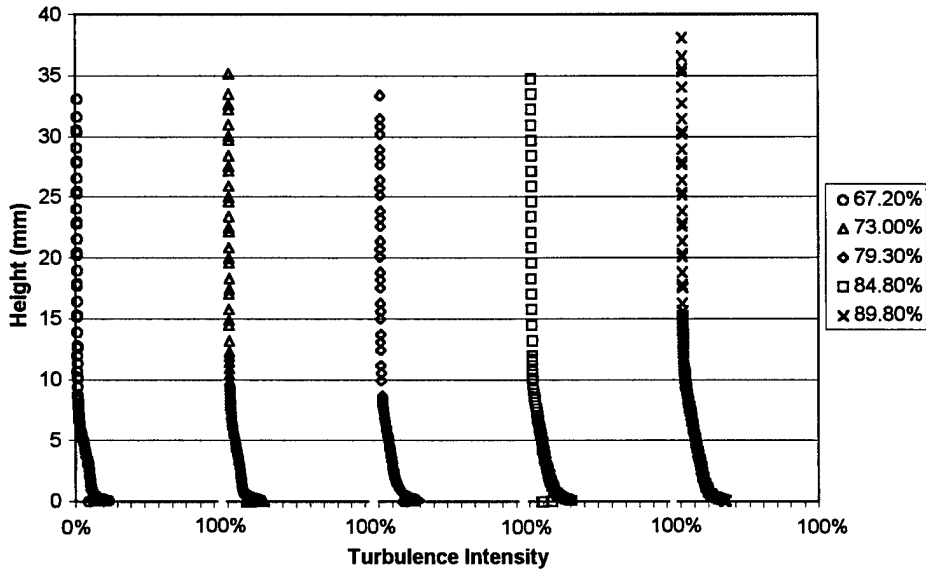


b) boundary layer turbulence measurements at  $Re = 50k$  and  $Tu = 4\%$

Figure 50. Measured velocity and turbulence profiles for baseline blade with trip at 35% with  $Tu = 4\%$ .

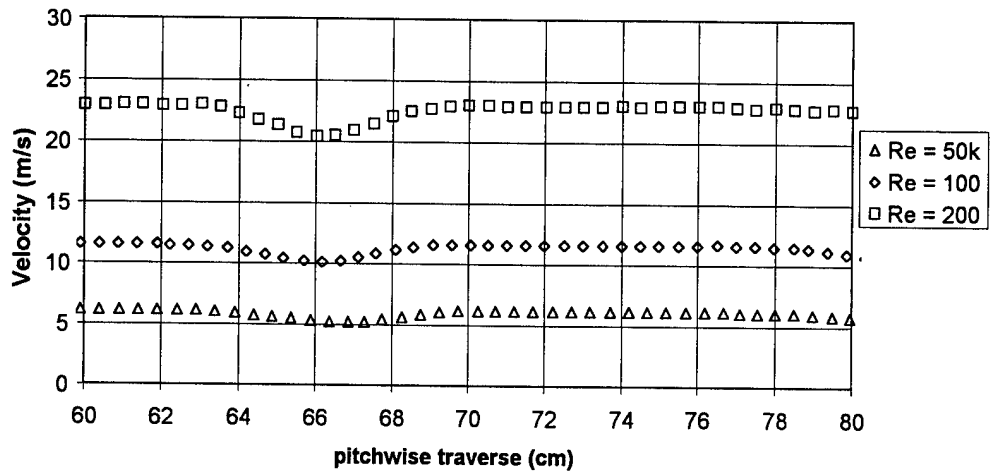


a) boundary layer velocity measurements at  $Re = 100k$  and  $Tu = 4\%$

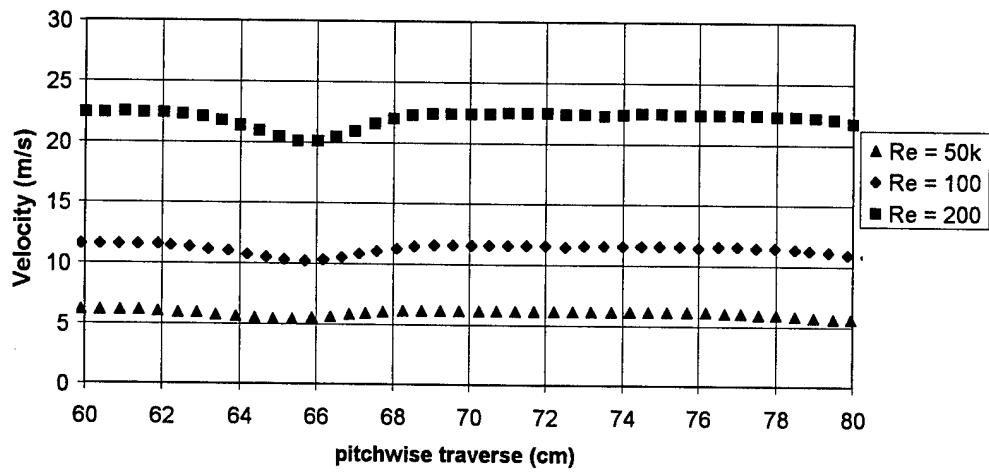


b) boundary layer turbulence measurements at  $Re = 100k$  and  $Tu = 4\%$

Figure 51. Measured velocity and turbulence profiles for baseline blade with trip at 35% with  $Tu = 4\%$ .



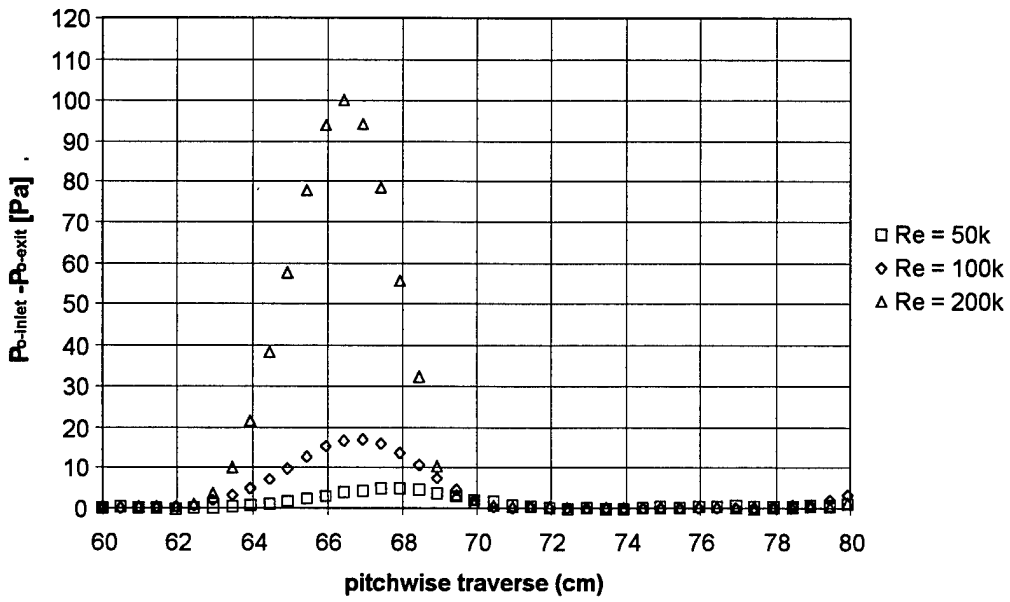
a) Exit velocity profiles for Tu = 1%



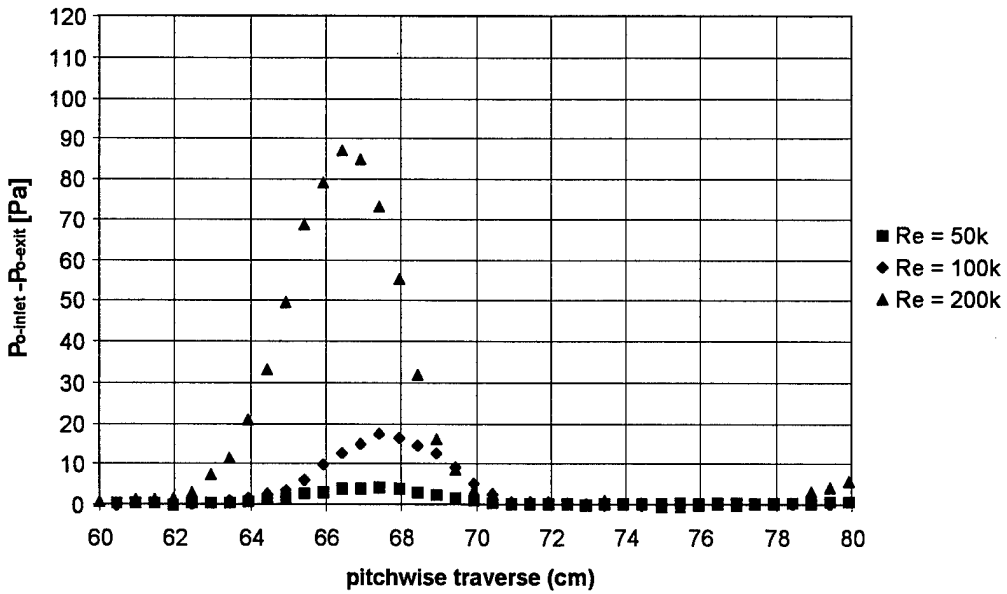
b) Exit velocity profiles for Tu = 4%

Figure 52. Exit velocities for baseline blade with trip at 35%.

stream locations as the exit velocities. Only the case of a Reynolds number of 50k and freestream turbulence level of 1% showed a reduction in the losses through its prevention of the large separation bubble that occurs for the baseline blade. Figure 54 illustrates the increase in losses generated using the trip wire at higher Reynolds numbers and turbulence intensities.

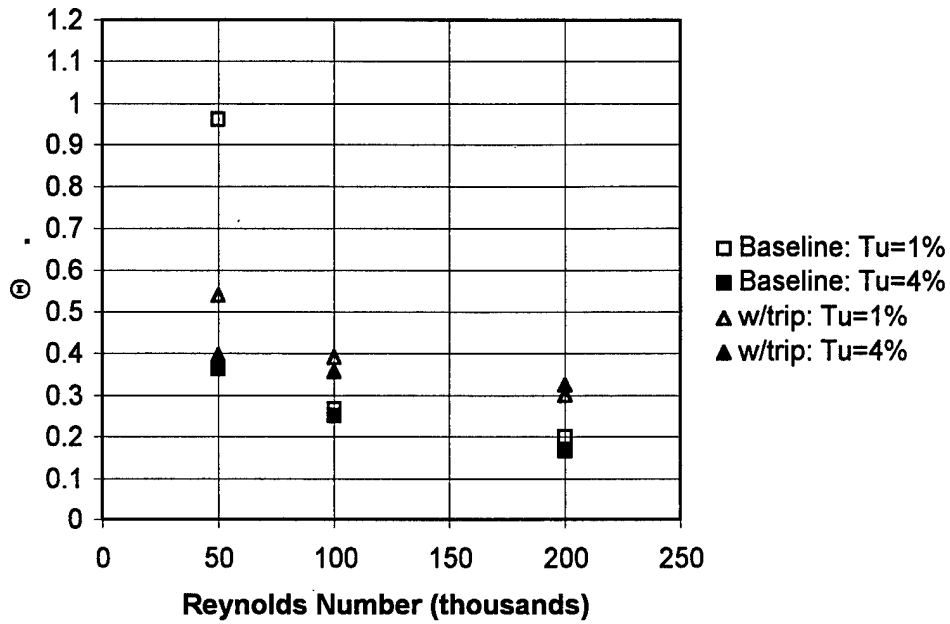


a) Exit pressure data for baseline blade with trip wire and  $Tu = 1\%$

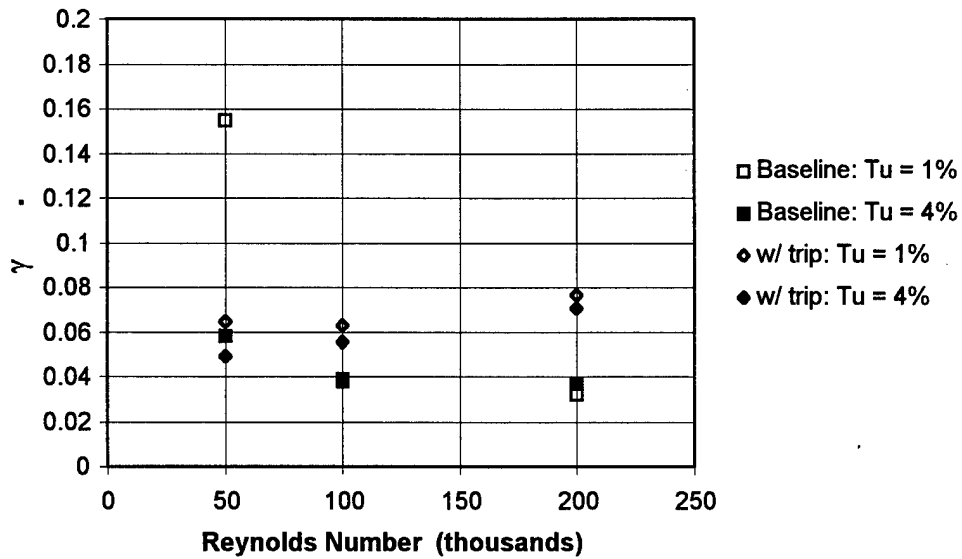


b) Exit pressure data for baseline blade with trip wire and  $Tu = 4\%$

Figure 53. Stagnation pressure loss for baseline blade with trip wire at 35% axial chord.



a) Wake momentum values for baseline blade and with trip wire



b) Loss coefficient for baseline blade and with trip wire

Figure 54. Wake velocity and total pressure loss coefficients for baseline blade with trip wire at 35%.

## Chapter 8 - Loss Reduction Using Dimples

### 8.1 Background and Separation Control Methodology

The existing separation problem on the low pressure turbine blades could have been solved in a variety of ways. As seen in Figure 55 two basic possibilities exist. One possibility was to redesign the blades which allowed the engineer to retain nothing of the original shape if that was found to be desirable. The other solution was to modify the existing blades in some way that simply corrects the separation problem while leaving the other aerodynamic characteristics unchanged. Modifying the existing blades was the quickest and most cost effective solution, and was examined in this research.

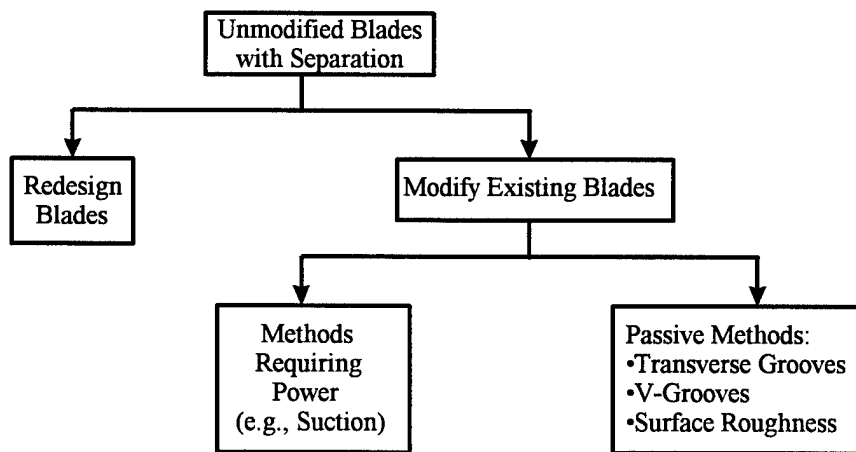


Figure 55. Diagram of considered separation control methods.

The modifications can be further categorized into two major divisions, those requiring auxiliary power and those that do not (Chang [43]). Johnston and Nishi [44] have described methods requiring auxiliary power such as blowing jets, boundary layer suction, and actuated vortex generators. These methods were not considered for this project due to their increased complexity, and the additional engine modifications that would be necessary to implement them.

Considering these possibilities, only passive surface modifications were examined for the reduction of separation losses. The simple implementation of passive techniques provided the goal of maximum efficiency and lowest implementation cost and time required for installation. This research provided a simple and economical solution to the problem of airflow separation on low-pressure turbine blades that can be easily adapted to a variety of engines and conditions, while not impeding performance that was otherwise nominal.

An extensively tested economical means for reducing separation is the use of vortex generators. Many vortex generators are typically small winglets attached to the problem surface (flat plate, diffuser, wing, etc.). The winglet devices energize the slower fluid within the boundary layer by moving higher speed fluid from the upper boundary layer or freestream down into the slower boundary layer (Taylor [45]). This mixing is aided by the creation of trailing vortices which extend downstream into the boundary layer. The efficiency and effect of this vortex is dependent on the flow conditions, vortex generator design, and most importantly the height of the vortex generator. Lin et al. [18] have shown that submerged vortex generators with overall height less than the boundary layer thickness have less drag than those which extend fully into the freestream, but accordingly have a shorter distance of effectiveness downstream. Halstead and Solomon [24] expressed concerns that the increased height of vortex generators which extend into the freestream can make these devices difficult to manufacture and clean once in use. Rejected passive methods initially considered such as riblets, ramps, and vanes are discussed in Appendix J. These difficulties have indicated that the best options for modifying the Pak-B blades were submerged design concepts that use vortex generation such as engraved dimples.

## 8.2 Previous Studies Using Recessed Dimples

The vortex generating dimple surface treatments used in this research were based upon the golf-ball dimple structure previously tested by Bearman and Harvey [16, 17] and Kimura and Tsutahara [46]. Bearman and Harvey [16] first tested the recessed dimple structures on a sphere to simulate the effects on a golf ball. Comparison between a smooth sphere and the dimpled sphere showed a sustained drag reduction for  $6 \times 10^5 < Re_D < 3 \times 10^6$  where  $Re_D$  is the Reynolds number based upon sphere diameter. Bearman and Harvey [16, 17] cut the dimples to a specific depth using a non-dimensional roughness ratio of  $\frac{k}{D} = 9 \times 10^{-3}$  where  $k$  is the maximum depth of the impression and  $D$  is the sphere diameter. Additional tests by Bearman and Harvey [16, 17] using hexagonal dimples instead of circular ones showed an increase in  $C_L$  by 20% and a reduction in  $C_D$  by 8%. The hexagonal dimples have six sharp edges with which to generate downstream vortices which aid in the reduction of separation more efficiently than standard circular dimples. Dimple results were later observed and confirmed to reduce the size of the separation zone by Nakayama et al. [47] using a test sphere.

Bearman and Harvey [17] also tested the dimples on a cylinder to reduce drag at low Reynolds numbers. The dimples were cut completely around the cylinder, each row proceeding spanwise along its length with subsequent rows staggered to provide a honeycomb appearance. Each dimple on the cylinder was cut using  $\frac{k}{D} = 9 \times 10^{-3}$  as in the previous spherical experiments. Results from the dimpled cylinder showed a significant drag reduction, however, no attempts were made to optimize the dimple size, location, or pattern.

## 8.3 Dimple Variations Previously Tested

Kimura and Tsutahara [46] tested the effects of cutting a channel along the span of a cylinder to simulate a 2-D golf ball dimple. Three cylinders were tested using three different channels. The

channels were cut to different depths using three different  $\frac{k}{D}$  values,  $1.2 \times 10^{-2}$ ,  $1.7 \times 10^{-2}$ , and  $7 \times 10^{-3}$ . The tests were performed at  $Re_D = 2200$  and a freestream turbulence of 2%. Each cylinder was rotated to study the effects of placing the single channel at different downstream locations from the initial stagnation point. Results indicated that separation was reduced over the surface of the cylinder when the groove was placed at  $83^\circ$  from the stagnation line. Separation occurred at  $92^\circ$  for the smooth cylinder, and was delayed only to  $94.5^\circ$  for the best groove tests. The spanwise grooves were found to be most effective when recirculation regions formed within the channel. The 2-D nature of the surface modification minimized the creation of downstream vortices, making the 2-D channel technique less effective in separation control than the 3-D dimples chosen for this experiment.

#### 8.4 Experiment Test Article

Using a scale based upon boundary layer thickness, the dimple structures from the previous experiments of Bearman and Harvey [16, 17] were cut into the suction surface of the test blade. Each dimple was cut to a depth of 1.588 mm (1/16th of an inch) using a 5.08 cm (2 inch) diameter ball end mill. Since the surface of the blade is curved, the resulting impressions are elliptical with a streamwise length of 15.13 mm (0.60 inches) and a spanwise length of 17.53 mm (0.69 inches). The dimples are 2.22 cm (0.875 inches) apart center-to-center. The resulting blade is in Figure 56. The axial chord length of the blade used in the tests is seven times engine scale, so the resulting impressions on a operational engine blade would be only 2.16 mm (0.086 inches)  $\times$  2.50 mm (0.099 inches) which could be easily molded into the surface of the blade during initial manufacturing.

As seen in Figure 56, there are three sets of dimples engraved into the blade at the 65%, 55%, and 50% axial chord lines. The combination of three locations on a single blade allowed for multiple data collections to be performed with a single test article. The benefits of having dimples at different

upstream locations from the separation bubble was measured using a single test blade. Each set of dimples were cut to the same size and depth. The standardization of dimple size allowed for easier comparison of boundary layer measurements between the different sets of dimples.

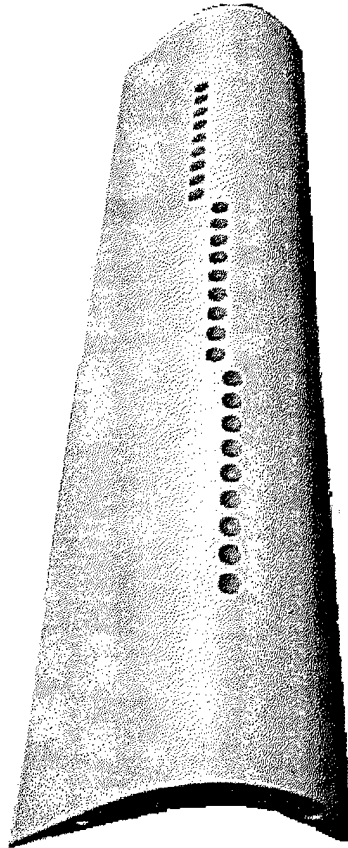


Figure 56. Dimples milled into the suction surface of the blade at three different locations.

### **8.5 Boundary Layer Velocity and Turbulence Measurements Downstream of Dimples**

Boundary layer measurements of velocity and turbulence were made with the same TSI 1279S-10A hot film probe used previously with the baseline blade described in Section 6.3. Using the hot film probe, velocity and turbulence measurements were made over the aft portion of the modified suction surface at five different axial chord locations at two different spanwise locations. Measure-

ments were made both directly downstream of a dimple and between adjacent dimples (see Figure 57). These ten locations span the region most effected by the dimples cut into the surface. The software for this system is explained in more detail in Appendix D.

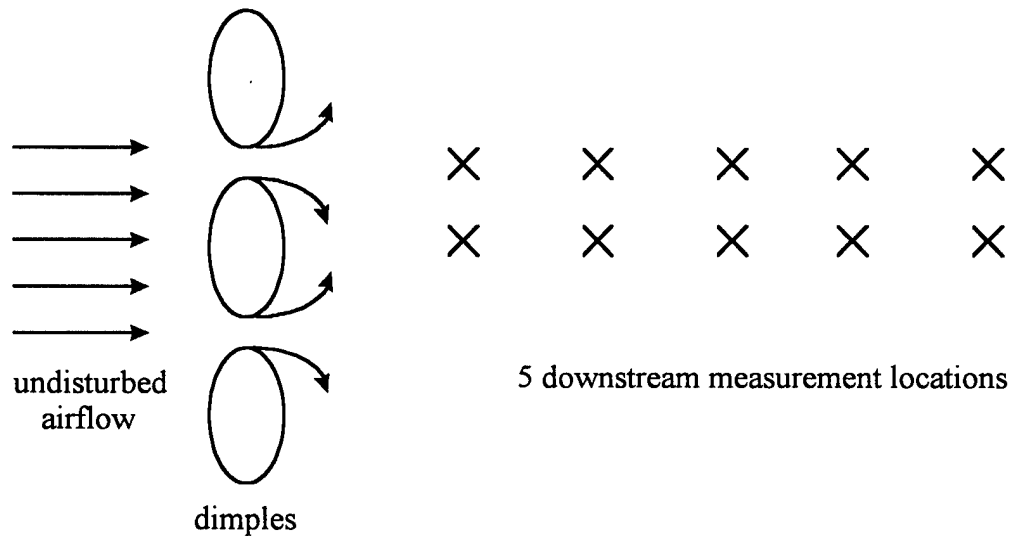
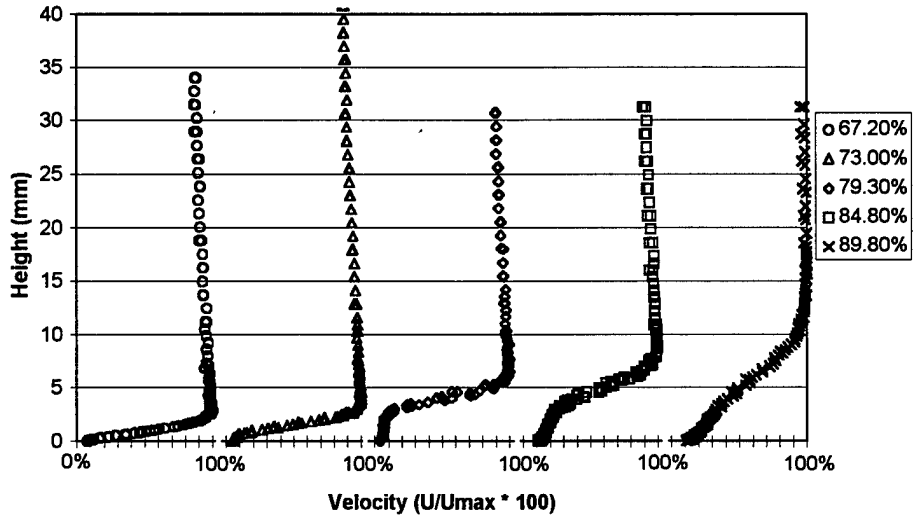


Figure 57. Detail of ten downstream measurement locations for dimples (not to scale).

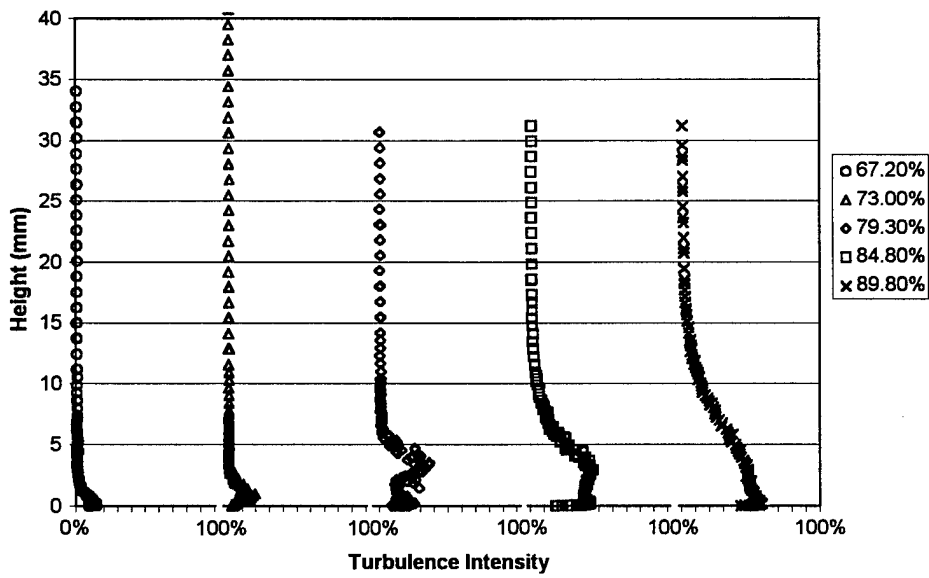
### 8.5.1 Boundary Layer Measurements at $Re = 50k$ for Dimples at 50%, 55% and 65% axial chord

The data illustrated in Figures 58 and 60 present the dramatic difference in boundary layer thickness reduction for the dimple surface modifications. The boundary layer now remains attached with only a small separation zone starting at 73.0% and extending to the 79.3% chord line. Downstream of the 79.3% chord line the flow re-attaches. Additional figures are presented in Appendix A which show very little difference in the velocity profiles behind a dimple and between dimples. The turbulence levels downstream of the dimples shows the progression and dissipation of the turbulence near the surface. The effect of increased freestream turbulence can be seen in Appendix A (Figures 102 and 103) where a further reduction in boundary layer size was evident. The difference

between the baseline and dimpled blade velocity and turbulence profiles were also reduced with the greater freestream turbulence.



a) boundary layer velocity measurements at  $Re = 50k$  and  $Tu = 1\%$



b) boundary layer turbulence measurements at  $Re = 50k$  and  $Tu = 1\%$

Figure 58. Measured velocity and turbulence profiles behind a dimple at 50%.

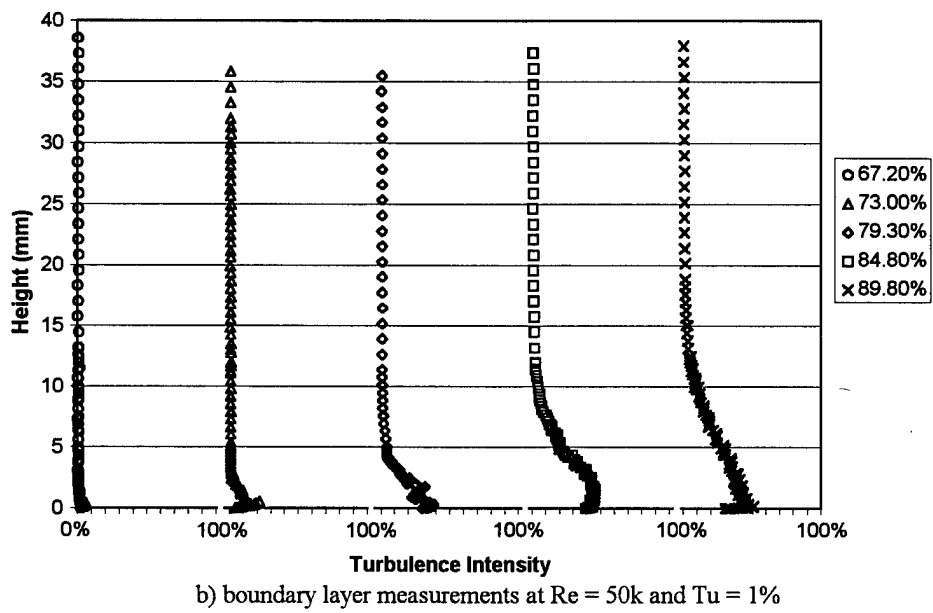
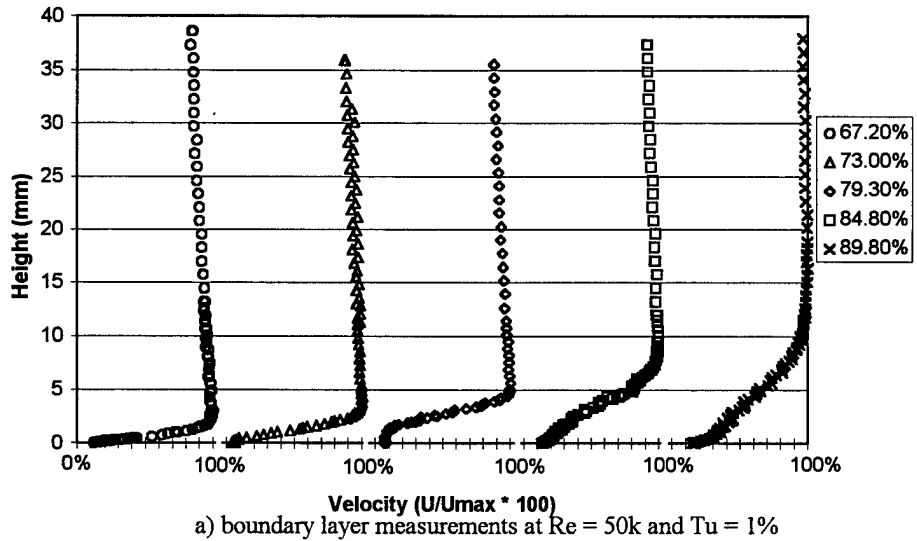
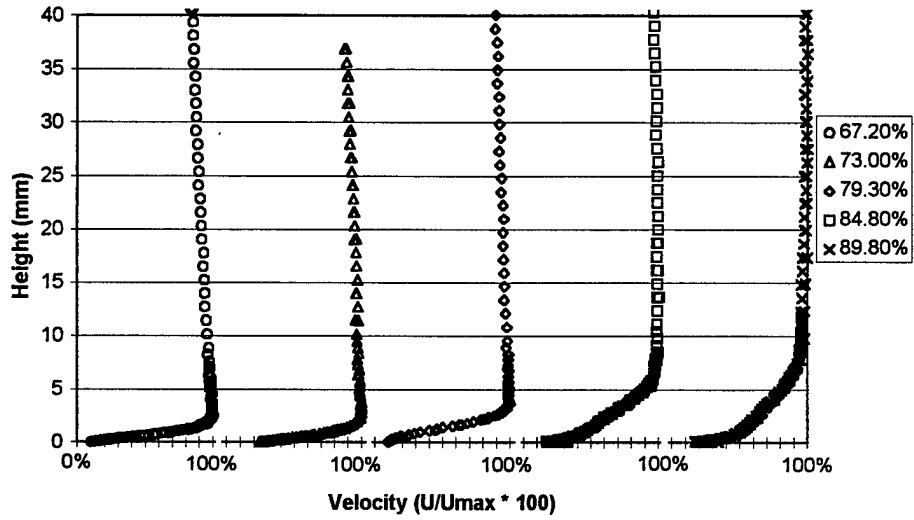
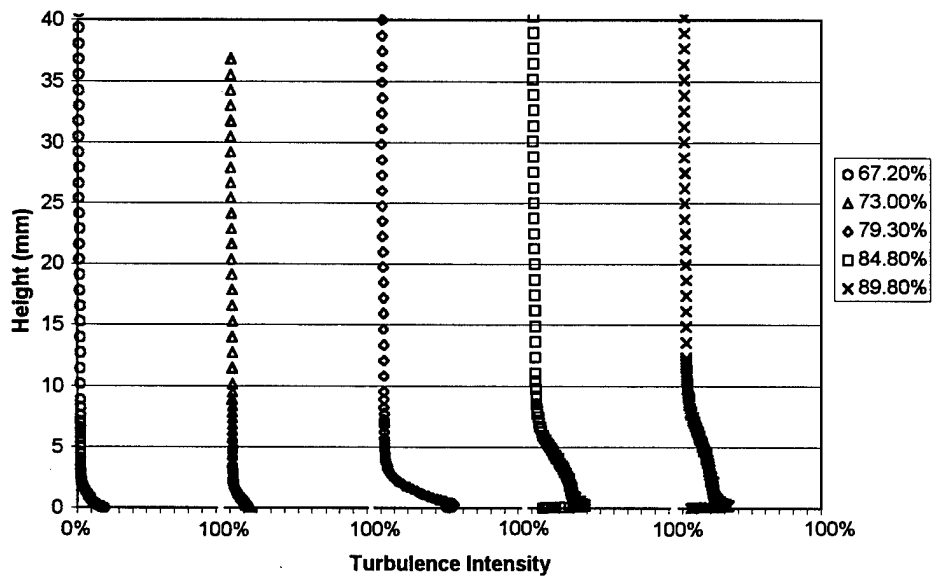


Figure 59. Measured velocity and turbulence profiles behind a dimple at 55%.



a) boundary layer velocity measurements at  $Re = 50k$  and  $Tu = 1\%$

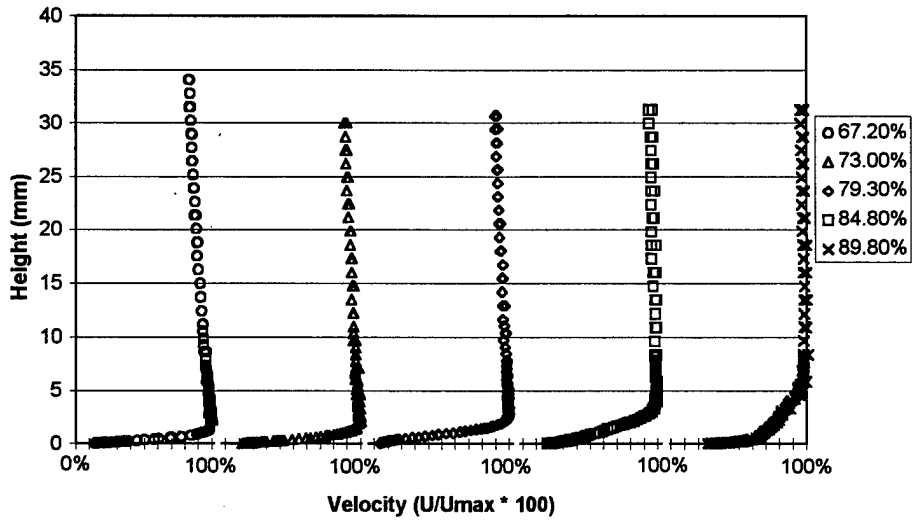


b) boundary layer turbulence measurements at  $Re = 50k$  and  $Tu = 1\%$

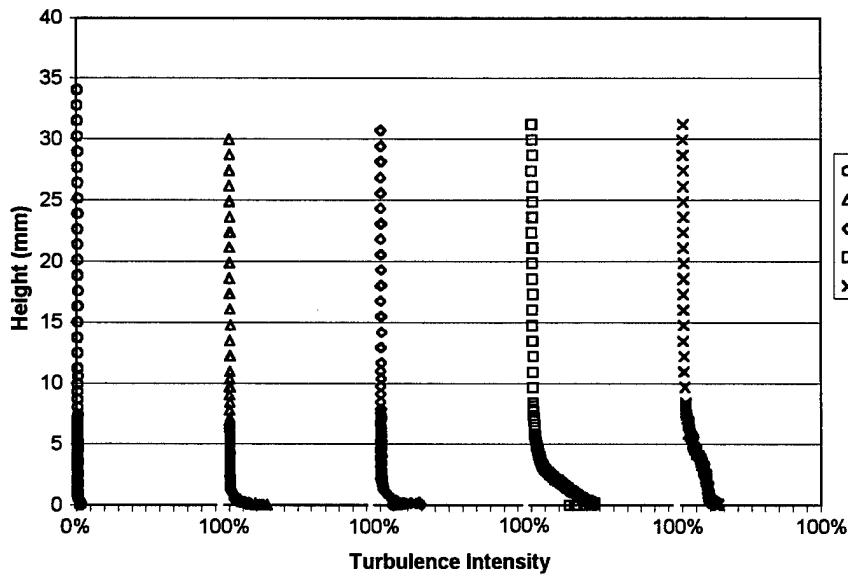
Figure 60. Measured velocity and turbulence profiles behind a dimple at 65%.

### **8.5.2 Boundary Layer Measurements at $Re = 100k$ for Dimples at 50%, 55% and 65% axial chord**

The data in Figures 61 through 63 illustrates the diminishing effect dimples have at higher Reynolds numbers and increased freestream turbulence. The profiles still show an improvement over the baseline blade performance; however, the effect was not as strong as at the lower Reynolds numbers and freestream turbulence. While the turbulence profiles were nearly identical between dimples and downstream of a dimple, the velocity profile at 79.3% chord still shows a small separation zone between the dimples (see Figure 110 in Appendix A). The effect of the dimples at all three locations was fully mixed downstream of the 84.8% chord line, which allowed measurement of the exit velocity wake at a single spanwise location.

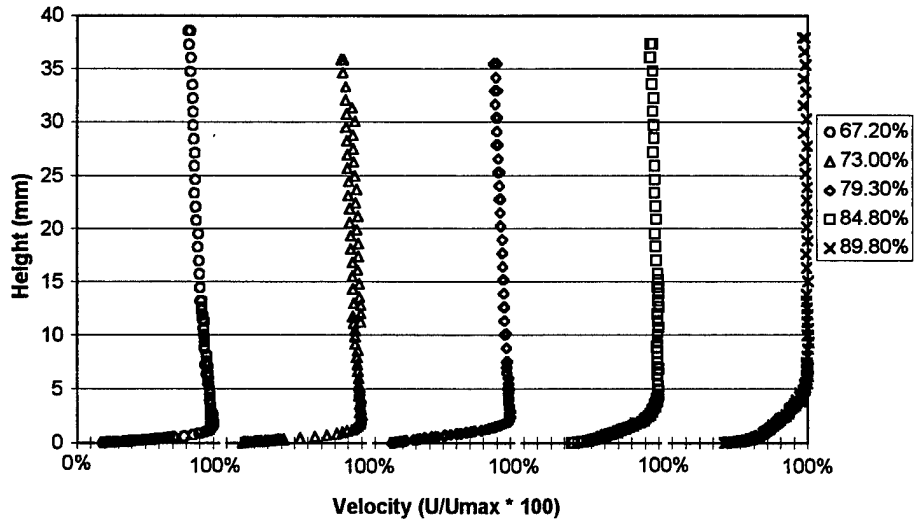


a) boundary layer velocity measurements at  $Re = 100k$  and  $Tu = 1\%$

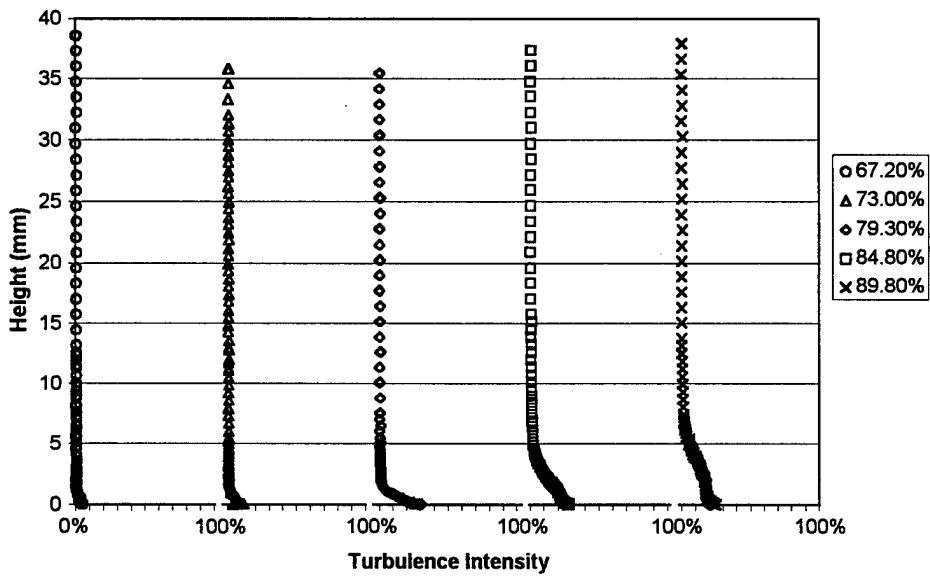


b) boundary layer turbulence measurements at  $Re = 100k$  and  $Tu = 1\%$

Figure 61. Measured velocity and turbulence profiles behind a dimple at 50%.

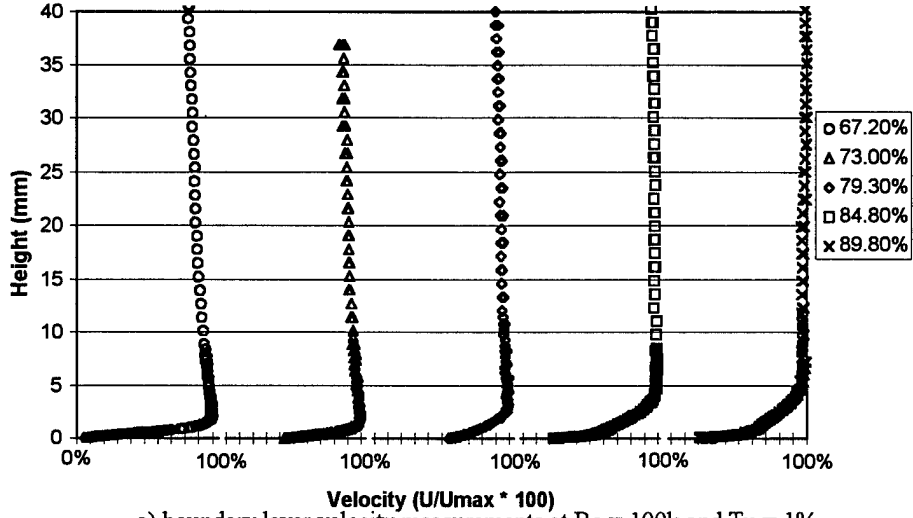


a) boundary layer at  $Re = 100k$  and  $Tu = 1\%$

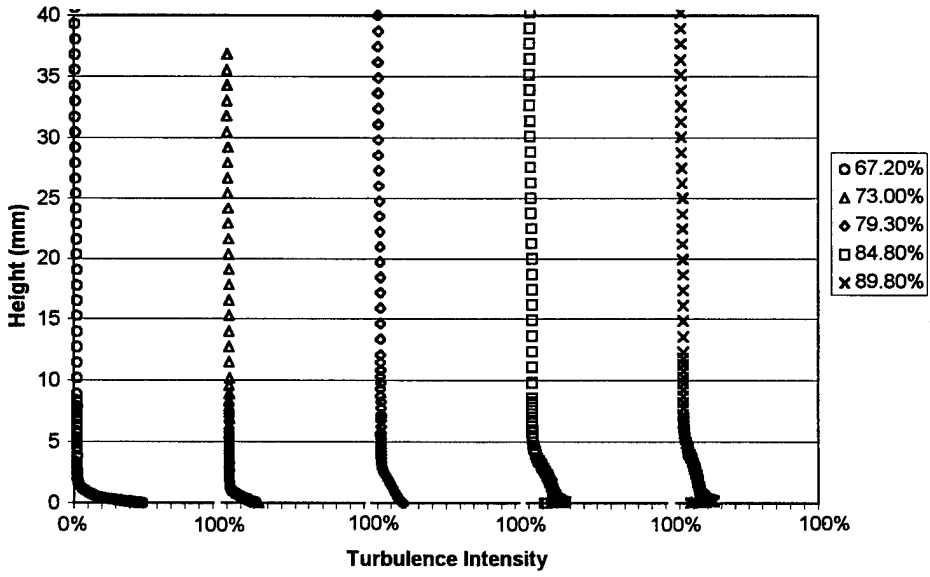


b) boundary layer at  $Re = 100k$  and  $Tu = 1\%$

Figure 62. Measured velocity and turbulence profiles behind a dimple at 55%.



a) boundary layer velocity measurements at  $Re = 100k$  and  $Tu = 1\%$



b) boundary layer turbulence measurements at  $Re = 100k$  and  $Tu = 1\%$

Figure 63. Measured velocity and turbulence profiles behind a dimple at 65%.

## 8.6 Exit Velocity Wake Profiles For Dimpled Blade

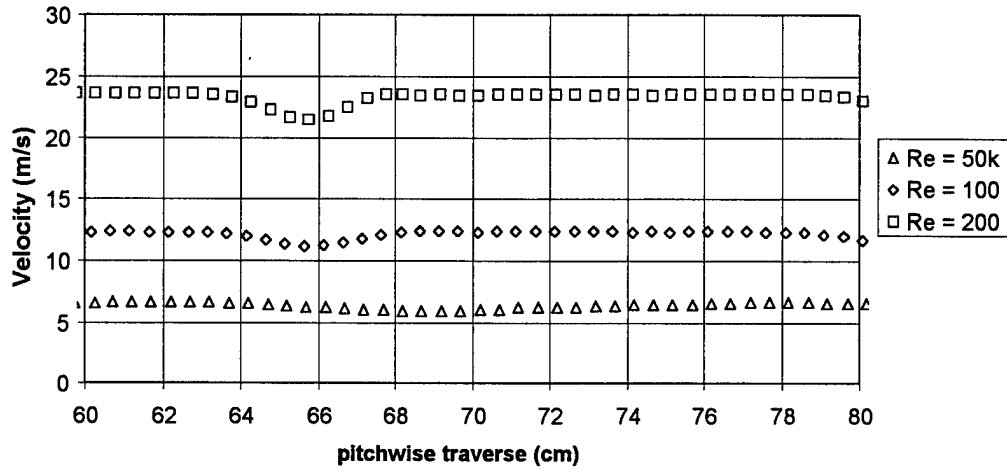
The exit velocity wake data was collected using the same instruments as described in Section 6.4. The Dantec traverse moved the hot wire probe across the wake of the dimpled blade at a location  $\frac{1}{2}$  chord length downstream. The velocity information collected every 0.5 cm (0.197 inches) was then used to calculate the wake momentum deficit.

Figures 64 through 66 show the exit velocity wakes for the dimples located at 50%, 55%, and 65% axial chord and for freestream turbulence levels of 1% and 4%. The inlet Reynolds numbers of 50k, 100k, and 200k are presented as three horizontal bands at approximately 6 m/s, 13 m/s and 25 m/s, respectively. The difference between the graphs for  $Tu = 1\%$  and  $Tu = 4\%$  illustrate the effect increased turbulence has on the size of the blade wake. The increased turbulence energizes the flow at low Reynolds numbers which reduces the separation considerably.

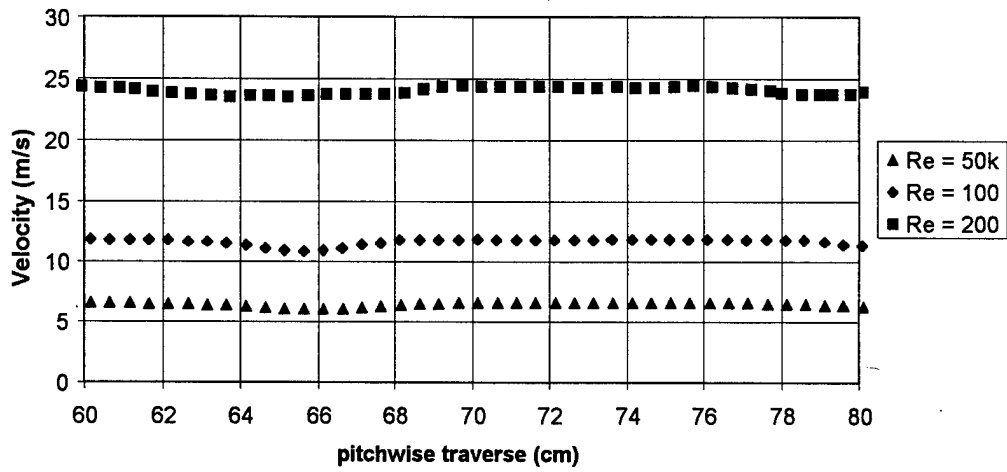
As with the baseline blade, as Reynolds number and turbulence level increases, the size of the separation zone on the suction side of the blade decreases. As the separation zone decreases in size, the wake diminishes. The suction side of the blade affected the flow from 66cm to the right side of Figure 64a and b. This shrinking of the boundary layer thickness with increased Reynolds number explains why the velocity wake shifts to the left with increased velocity.

### 8.6.1 Exit Momentum Deficit Calculations

The calculated momentum deficits for the blade modified with dimples are shown in Figure 67. The greatest impact the dimples had was at  $Re = 50k$ , where even at higher turbulence levels of 4%, the wake was significantly reduced over the baseline blade. At higher Reynolds numbers the beneficial influence of the dimples decreases. The trend of decreasing benefit with increasing Reynolds number and freestream turbulence was also evident with the measured loss coefficients.

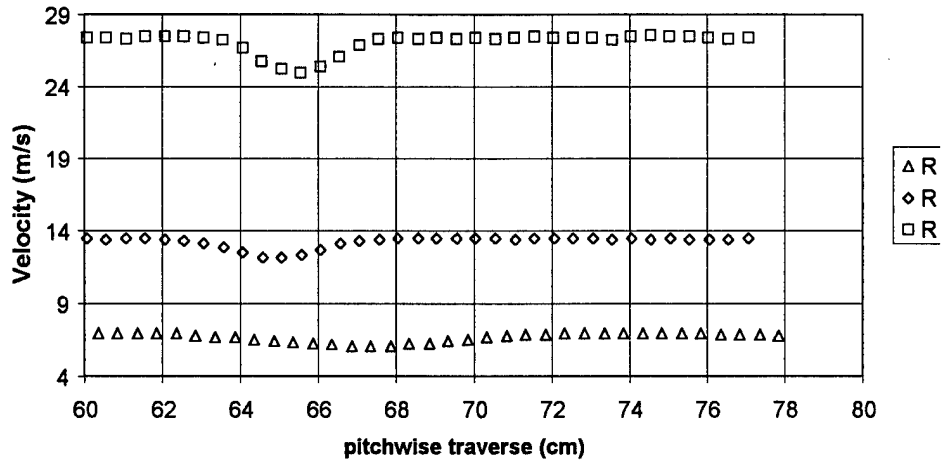


a) Exit velocity profiles for  $Tu = 1\%$

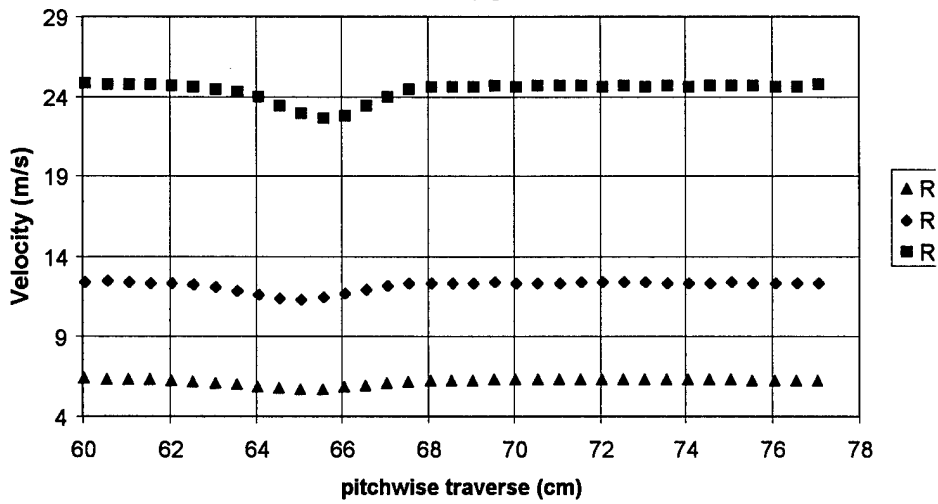


b) Exit velocity profiles for  $Tu = 4\%$

Figure 64. Exit velocity profiles for Dimples at 50% chord.

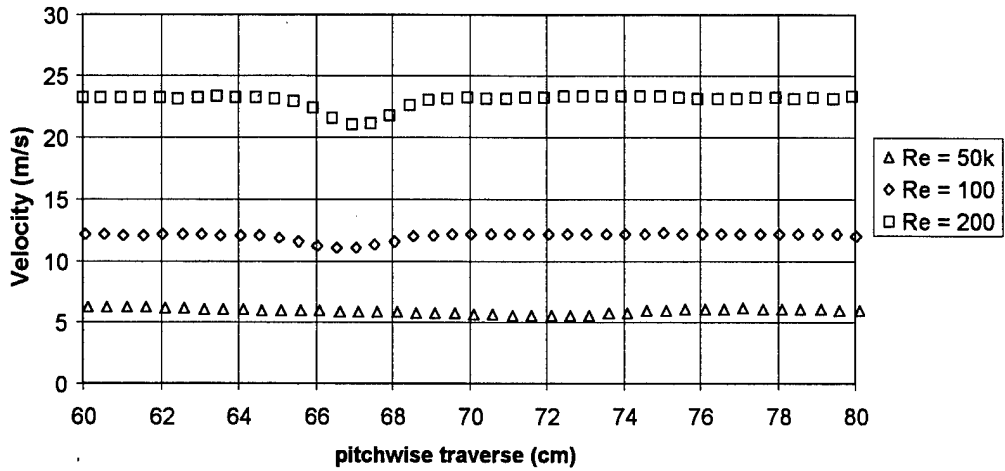


a) Exit velocity profiles for  $Tu = 1\%$

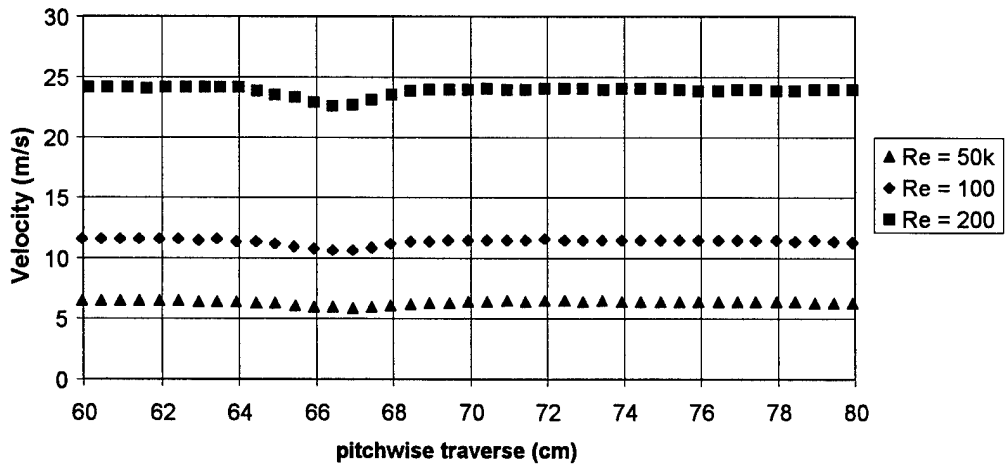


b) Exit velocity profiles for  $Tu = 4\%$

Figure 65. Exit velocity profiles for Dimples at 55% chord.

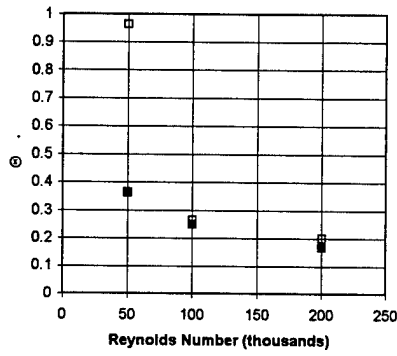


a) Exit velocity profiles for  $Tu = 1\%$

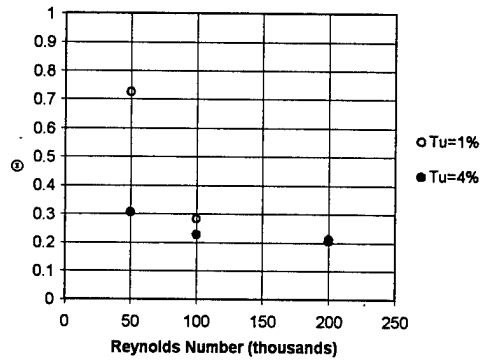


b) Exit velocity profiles for  $Tu = 4\%$

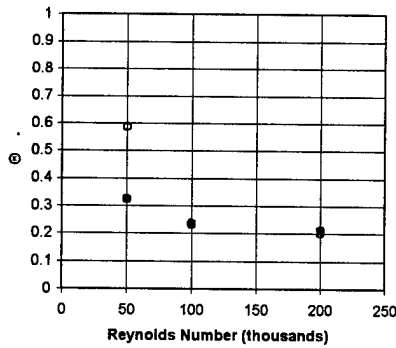
Figure 66. Exit velocity profiles for Dimples at 65% chord.



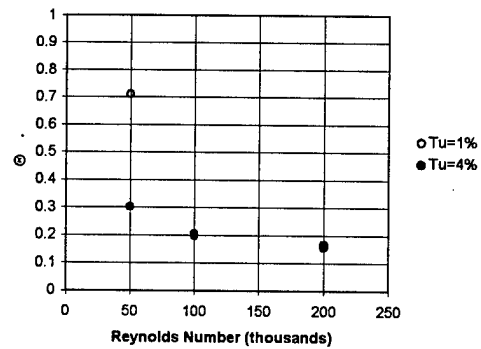
a) Baseline Pak-B blade



b) Dimples at 50% chord



c) Dimples at 55% chord



d) Dimples at 65% chord

Figure 67. Wake momentum values for baseline blade, and dimples at 50%, 55%, and 65% chord.

## 8.7 Loss Coefficient Reduction Using Dimples

The loss coefficient pressure data was collected using the same total pressure probe as described in Section 6.5. The total pressure wake data was collected  $\frac{1}{2}$  axial chord lengths downstream of the dimpled blade. The probe was moved across the wake of the blade in 0.5 cm (0.197 inches) increments using the Dantec 3-axis traverse and the Pitot Traverse Data Acquisition VI. The software is explained in more detail in Appendix D. The software saved to a file the exit total pressures, velocity, turbulence intensity and location of the wake measurements.

### 8.7.1 Exit Pressure Data For $Tu = 1\%$

The exit pressures are similar in form and magnitude to the baseline blades, but with reductions in width and depth. These reductions give the modified blade improved efficiency. As with the exit velocity profiles as the Reynolds number increases the width of the blade wake decreases, and so the wakes appear to shift to the left. Since the separation bubble is much smaller on the dimpled blade surface, the wake shift effect for the dimpled blade was less than the smooth blade tested under the same circumstances. This shifting was also reduced with increased freestream turbulence.

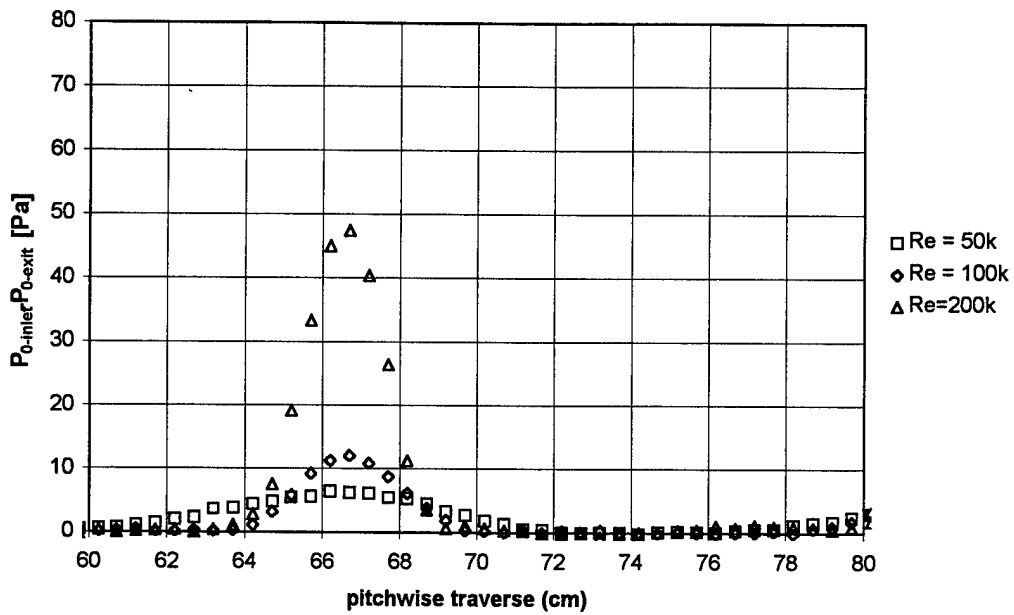


Figure 68. Exit stagnation pressure loss for dimples at 50%.

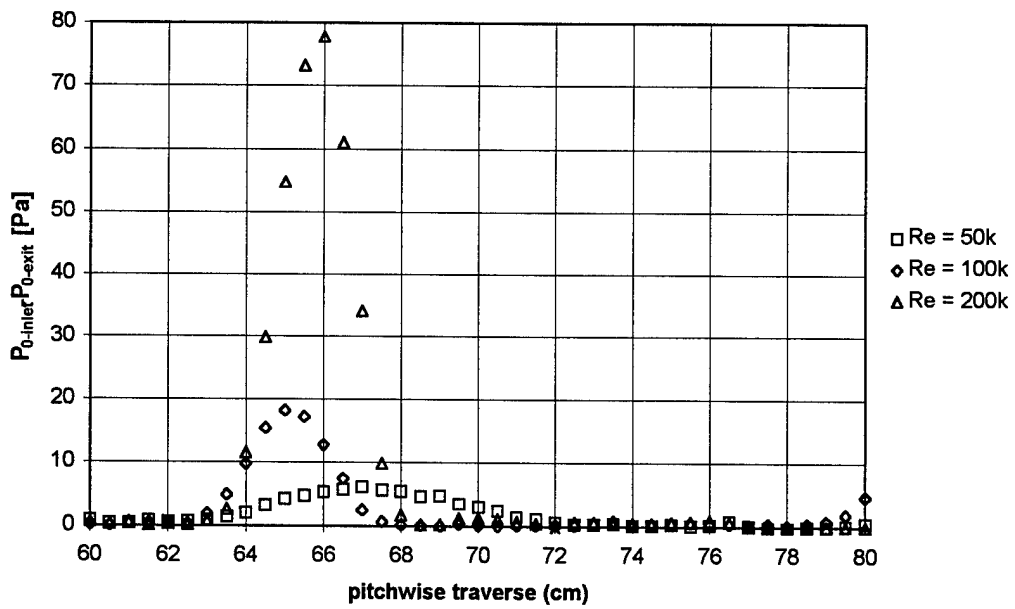


Figure 69. Exit stagnation pressure loss for dimples at 55%.

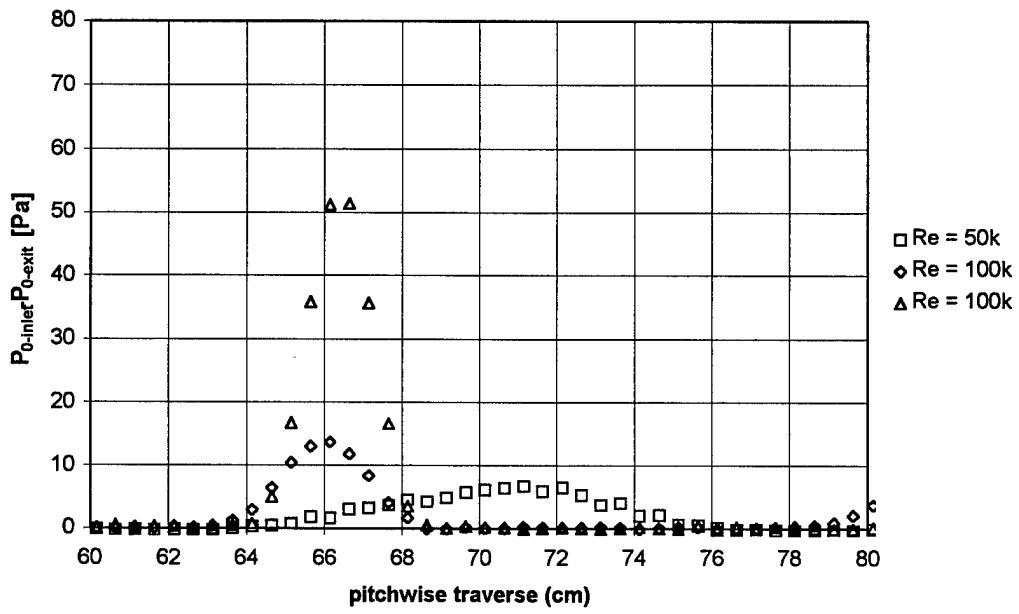


Figure 70. Exit stagnation pressure loss for dimples at 65%.

### 8.7.2 Exit Pressure Data for $Tu = 4\%$

The increased freestream turbulence energized the boundary layer sufficiently to prevent large separation bubbles forming on the suction surface. The lack of separation at all Reynolds numbers indicates there should not be significant variation in the centerline of the downstream wake of the blade. The expected alignment of the blade wakes is shown in Figures 71 through 73. The exit pressures were also used to determine the loss coefficients for the different dimple studies.

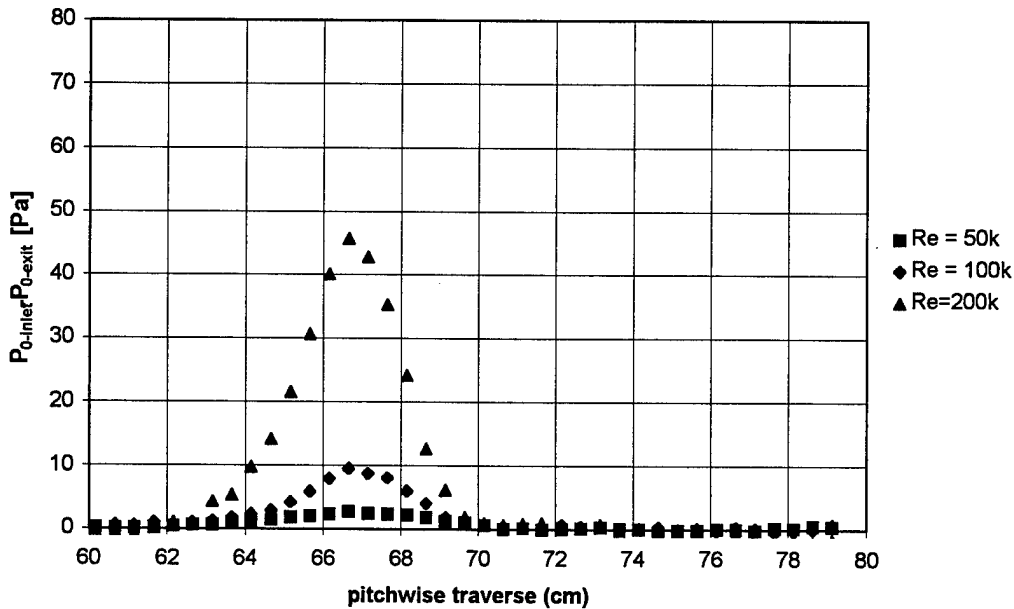


Figure 71. Exit stagnation pressure loss for dimples at 50% with  $Tu = 4\%$ .

### 8.7.3 Loss Coefficient for Dimpled Blade

The loss coefficients for the dimpled blade are illustrated in Figure 74. Comparing Figure 74 to the baseline blade loss coefficients in Section 6.5 shows how much the dimples help. The loss coefficient at  $Re = 50k$  and  $Tu = 1\%$  was reduced by 19% to 42% with the dimples. The coefficient was also reduced at  $Re = 100k$  and  $Re = 200k$ . At  $Re = 200k$ , the loss coefficients for the baseline

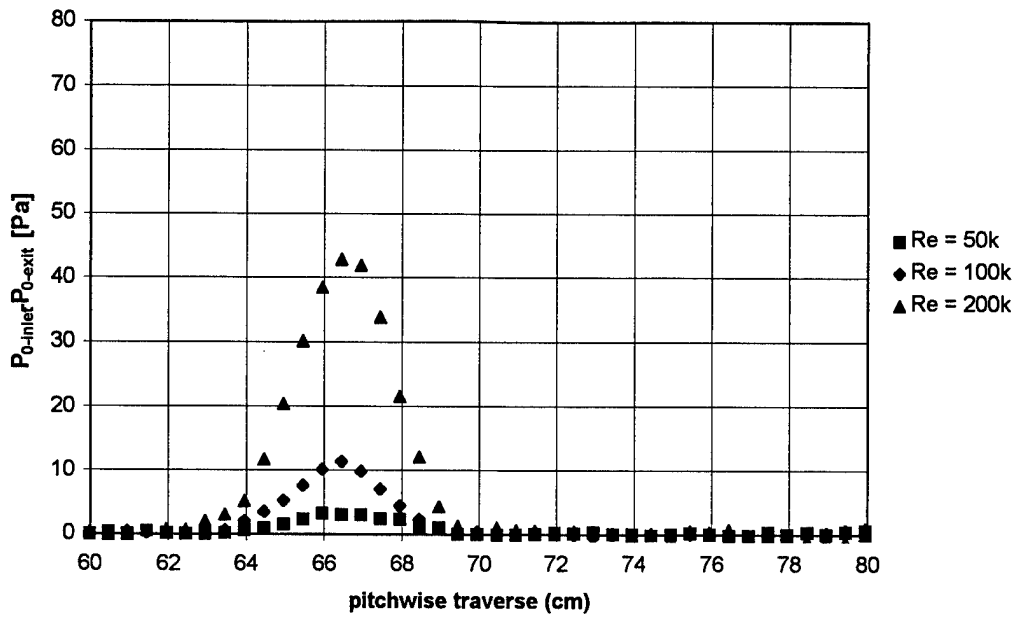


Figure 72. Exit stagnation pressure loss for dimples at 55% with  $Tu = 4\%$ .

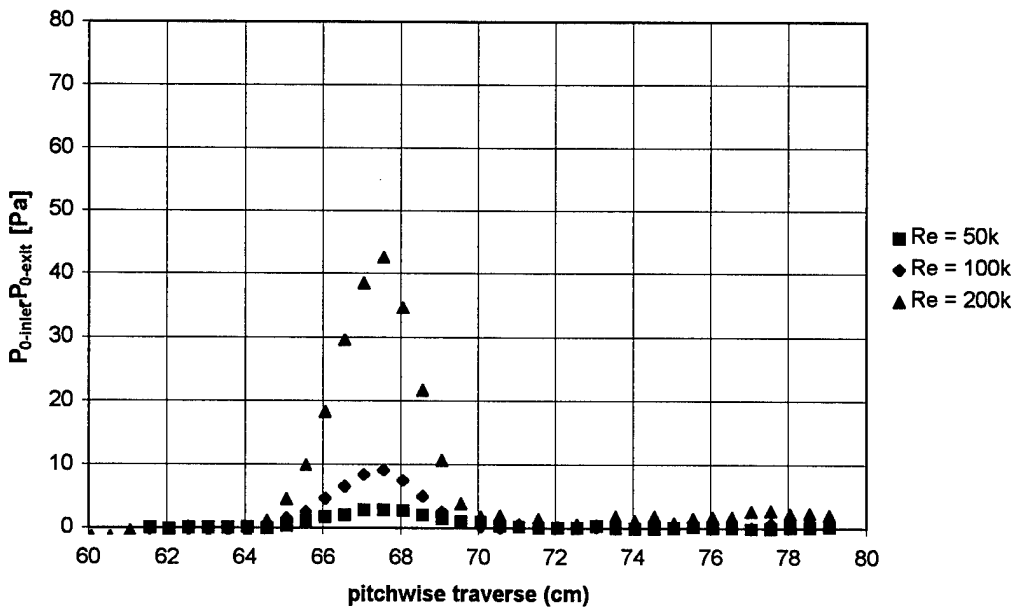


Figure 73. Exit stagnation pressure loss for dimples at 65% with  $Tu = 4\%$ .

blade were slightly more than the dimpled blade, illustrating the non-damaging nature of the dimples at higher Reynolds numbers.

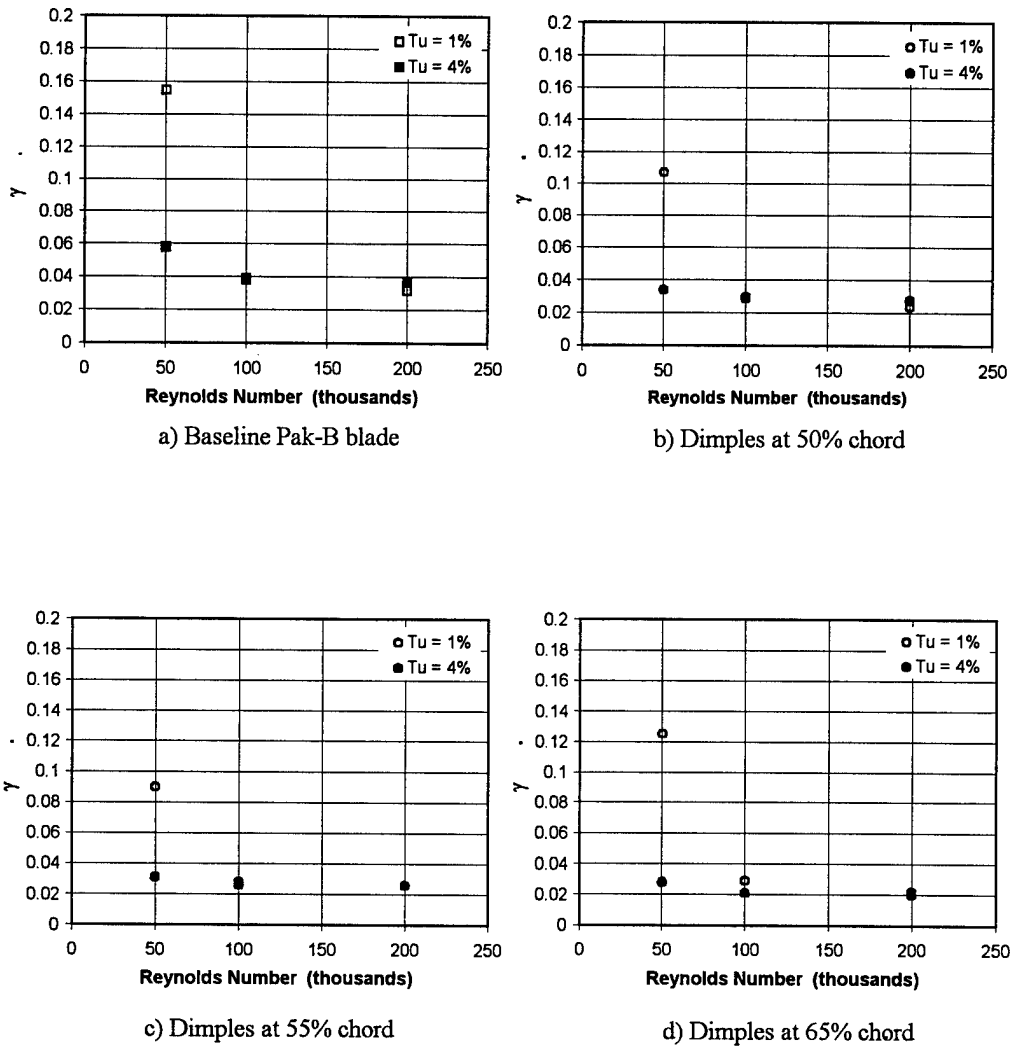


Figure 74. Loss coefficient for baseline blade and dimples located at 50%, 55%, and 65% axial chord.

## Chapter 9 - Loss Reduction Using V-Grooves

### 9.1 Background and Previous Studies

The V-groove concept is very similar to riblets. However, the V-grooves are much larger in size than the riblet concept and were engraved into the surface with regions of unmodified surface separating each groove (see Figure 75). The V-grooves tested were machined to a depth of  $h = 0.769\delta_0$ , a width of  $w = 1.538\delta_0$ , and a spacing of  $s = 3.077\delta_0$  where  $\delta_0$  is the original unmodified thickness of the boundary layer. Tested by Lin et al. [18] these V-grooves delayed the onset of separation by 1.27 cm (0.5 inches) and reduced the overall reattachment distance by up to 66% using a convex curved ramp with no pressure gradient and a tripped boundary layer. Recommended placement of the grooves was from just upstream of the baseline separation point to the trailing edge of the surface when there exists a turbulent boundary layer that is separated.

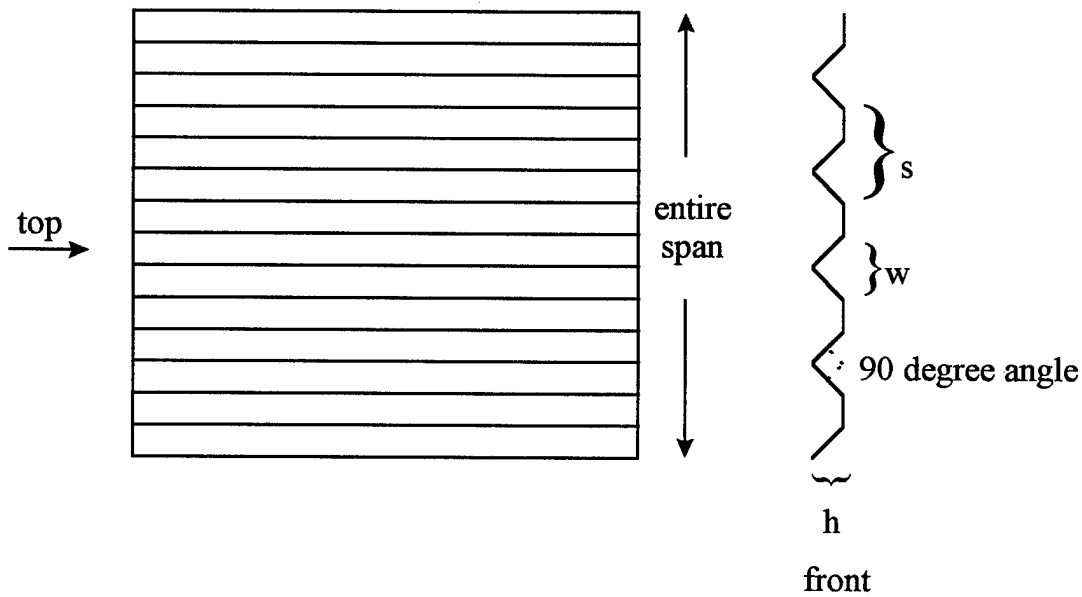


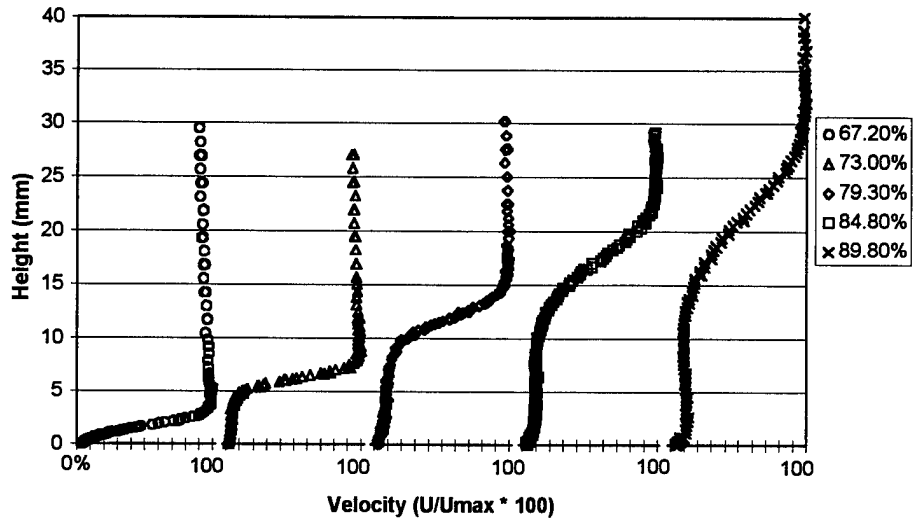
Figure 75. Large scale V-groove separation control design.

## 9.2 V-Groove Experiment Test Article

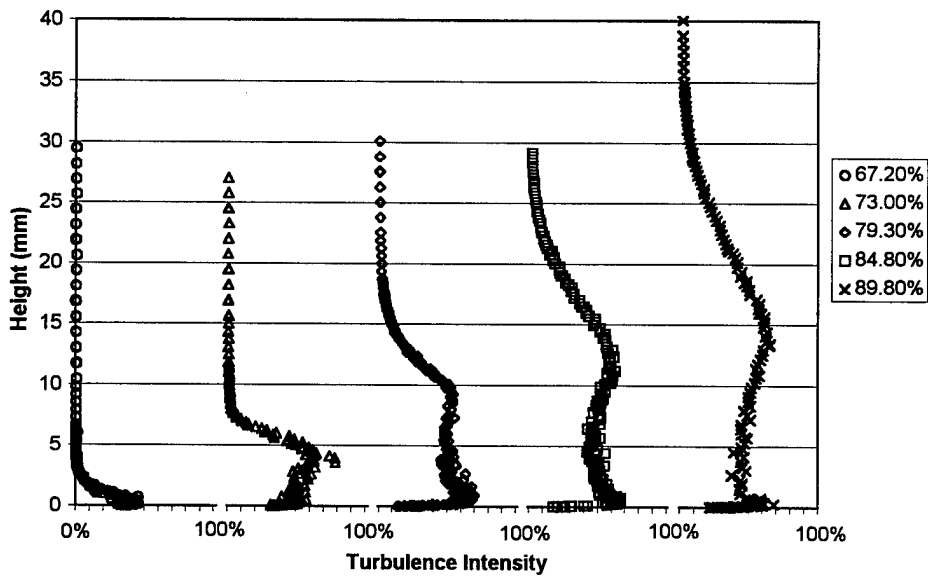
A smooth Pak-B blade was modified to include engraved V-grooves over the aft portion of the suction surface. Two variants of the V-grooves were tested. The first set of V-grooves started at the 55% axial chord location and extended back to the 95% chord. The second V-groove application used the grooves starting at the 60% chord location. Testing two different sets of V-grooves allowed the determination start location had upon separation loss reduction. The size of the V-grooves was determined from using the boundary layer thickness of the previous experiment of Lin et al. [18] and scaling this to the Pak-B. Each engraved groove was cut using a 6.35 mm (0.25 inch) diameter V-shaped router bit. The resulting grooves were 2.51 mm (0.099 inches) deep, 5.03 mm (0.198 inches) wide and spaced 10.0 mm (0.395 inches) apart. Each set of V-grooves spanned 19.05 cm (7.5 inches) of the test blade z-axis. Measurements of the exit total pressure, exit velocity and boundary layer were completed as in the previous case of the dimpled blade.

## 9.3 Boundary Layer Velocity and Turbulence Measurements with V-Grooves at 55% and 60% Chord for $Re = 50k$

Figures 76 and 77 show the velocity and turbulence profiles for the blade with V-grooves engraved in the suction surface at an inlet Reynolds number of 50k. Boundary layer velocity and local turbulence intensity measurements were taken at two different spanwise locations for each of the five axial chord positions. One set of boundary layer profiles were taken down to the surface separating the V-grooves. The second set of data was collected over a V-groove with the probe extending 0.9 mm (0.035 inches) into the V-groove itself (see Appendix B). As can be seen by comparing the boundary layer in Figure 76 and 116 (Appendix B), the V-groove has minimal effect on the velocity and turbulence levels above the surface of the blade. Boundary layer measurements were also taken at a Reynolds number of 100k.

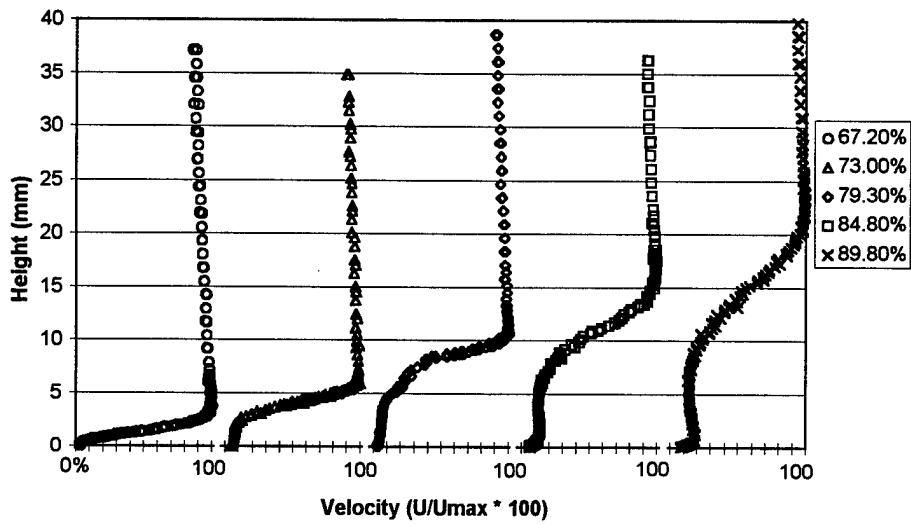


a) boundary layer velocity measurements at  $Re = 50k$  and  $Tu = 1\%$

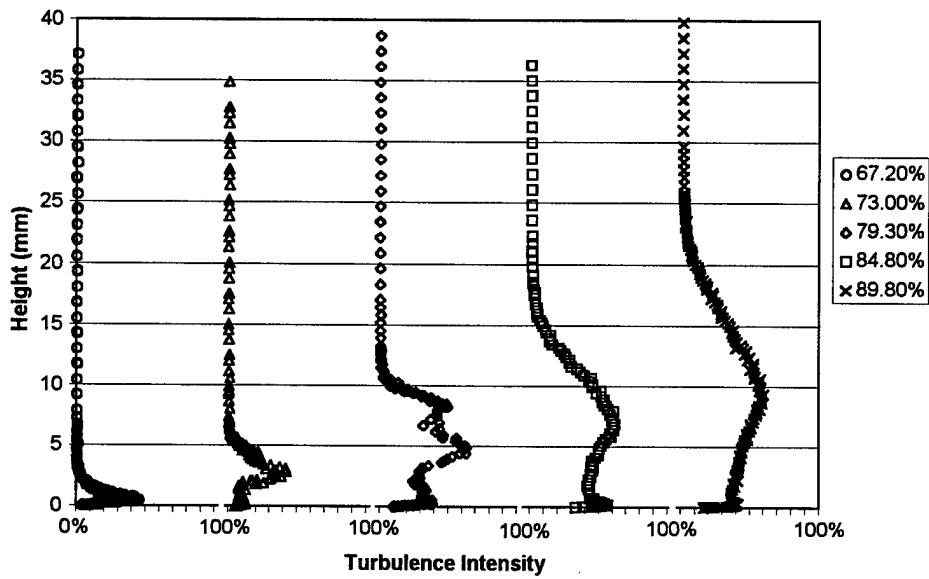


b) boundary layer turbulence measurements at  $Re = 50k$  and  $Tu = 1\%$

Figure 76. Measured velocity and turbulence profiles between V-grooves starting at 55%.



a) boundary layer velocity measurements at  $Re = 50k$  and  $Tu = 1\%$



b) boundary layer turbulence measurements at  $Re = 50k$  and  $Tu = 1\%$

Figure 77. Measured velocity and turbulence profiles between V-grooves starting at 60%.

#### **9.4 Boundary Layer Velocity and Turbulence Measurements with V-Grooves at 55% and 60% Chord for $Re = 100k$**

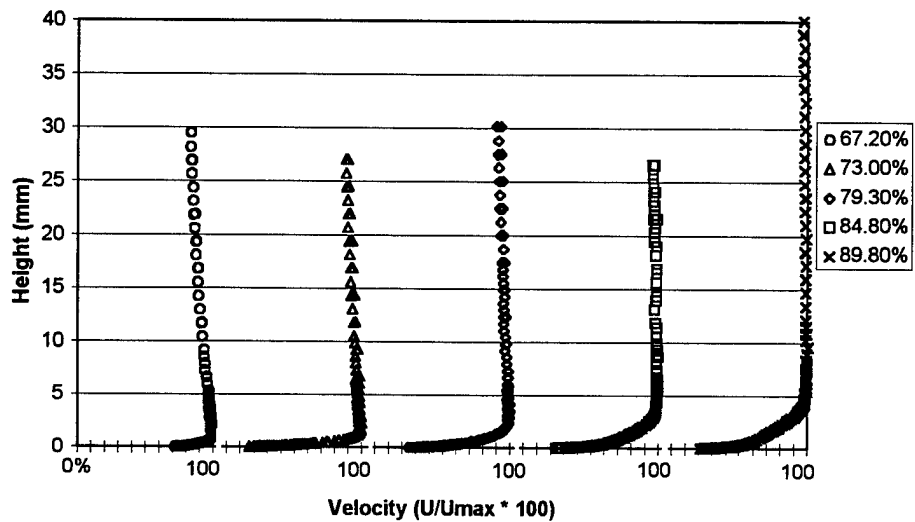
The boundary layer velocity profiles in Figures 78 and 79 illustrate attached boundary layer present using the V-grooves with an initially laminar boundary layer. The attached flow measured at  $Re = 100k$  was very different from the separated boundary layer measured at  $Re = 50k$  for the V-groove and baseline blades. Figures 78 and 79 also highlight how effective the V-grooves were at eliminating boundary layer separation at a Reynolds number of 100k compared to the baseline blade. The baseline and V-groove blades were also tested with a boundary layer trip to better emulate the turbulent boundary layer conditions of the previous experiment by Lin et al. [18].

#### **9.5 Turbulent Boundary Layer Measurements with V-Grooves at 55% and 60% Chord**

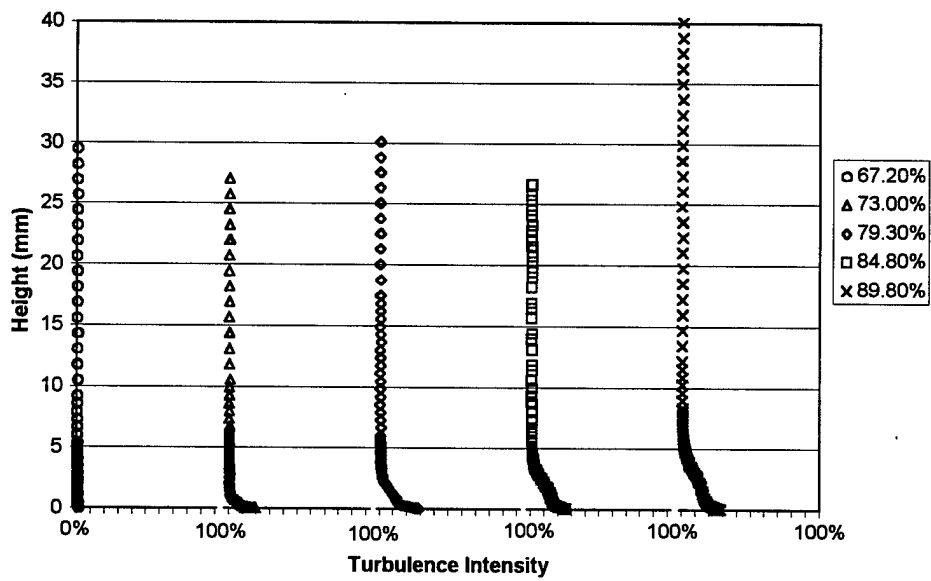
A trip wire was placed upstream of the V-grooves at the 35% axial chord line to create a turbulent boundary layer. The wire was 2.77 mm (0.109 inches) in diameter and spanned across the V-groove region of the blade. To illustrate the turbulent boundary layer created over the V-grooves, approximations for a laminar and turbulent boundary layer(White [42]) are included in Figures 80 through 83.

#### **9.6 Exit Velocity Wake Profiles for V-Grooves**

The exit velocity wake data was collected for the V-grooves using the same technique described in Section 6.4. The hot wire probe was inserted through traverse slot #3 into the wake of the V-groove blade approximately  $\frac{1}{2}$  axial chord lengths downstream. Figures 84 and 85 show the wake velocity for the V-groove blade with turbulence levels of 1% and 4%. In addition to the initially laminar boundary layer results shown in Figures 84 and 85, experimental data was also collected for the V-groove blade with a boundary layer trip wire.

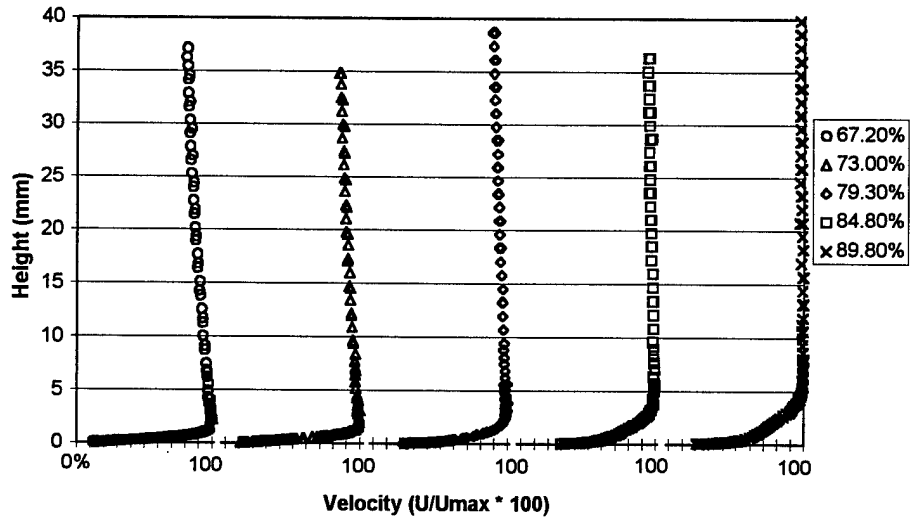


a) boundary layer velocity measurements at  $Re = 100k$  and  $Tu = 1\%$

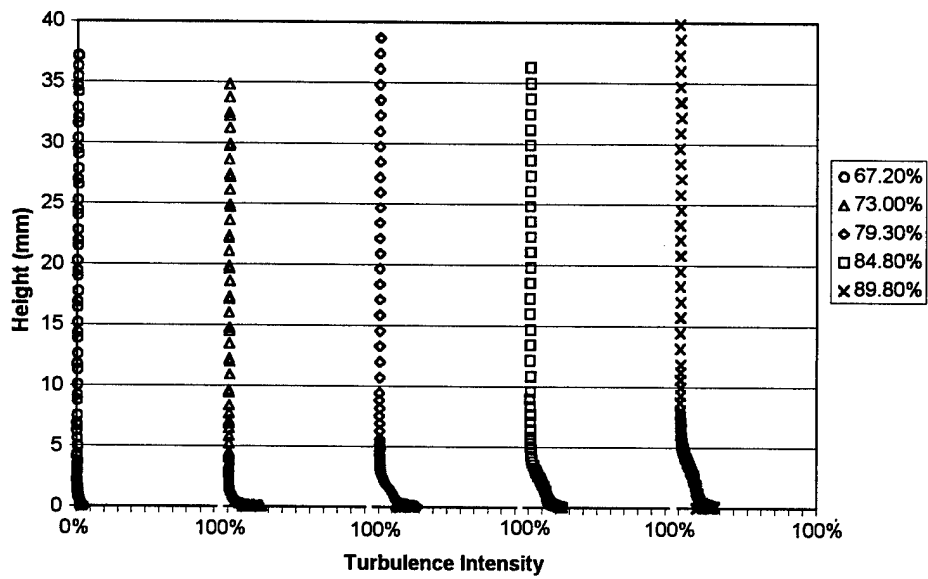


b) boundary layer turbulence measurements at  $Re = 100k$  and  $Tu = 1\%$

Figure 78. Measured velocity and turbulence profiles between V-grooves starting at 55%.



a) boundary layer velocity measurements at  $Re = 100k$  and  $Tu = 1\%$



b) boundary layer turbulence measurements at  $Re = 100k$  and  $Tu = 1\%$

Figure 79. Measured velocity and turbulence profiles between V-grooves starting at 60%.

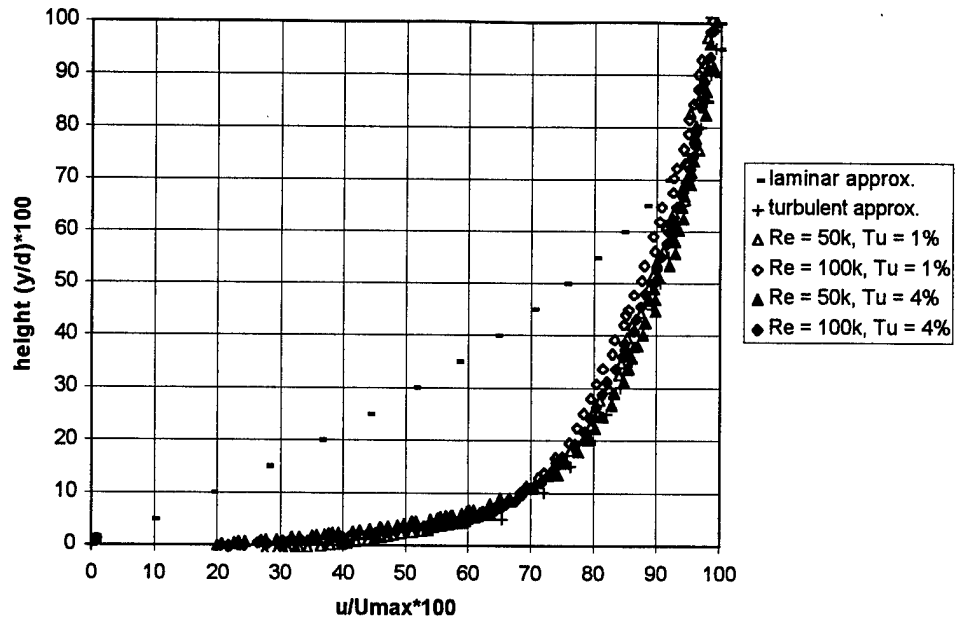


Figure 80. Tripped boundary layer profiles at 67% chord for V-grooves starting at 55%.

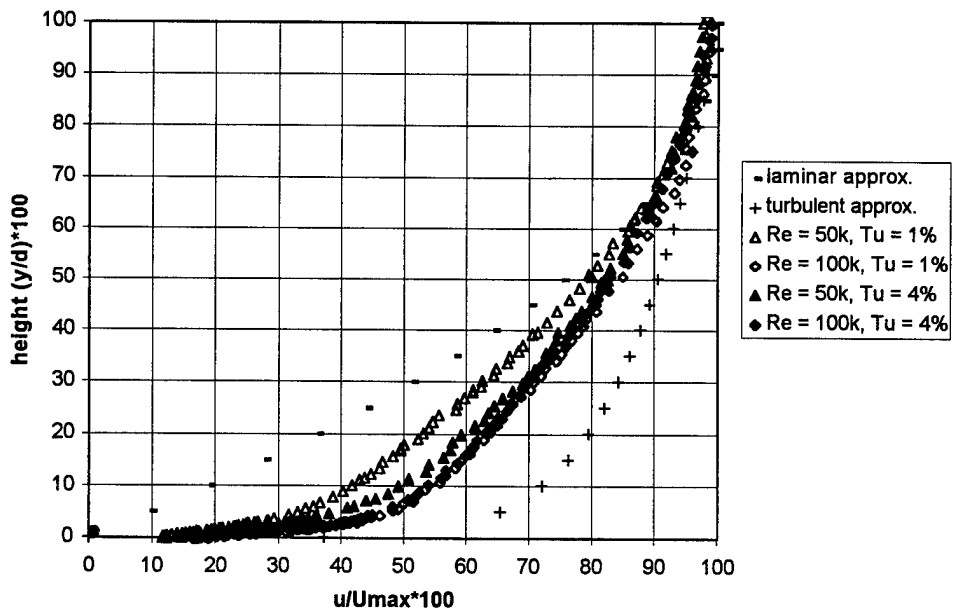


Figure 81. Tripped boundary layer profiles at 84.8% chord for V-grooves starting at 55%.

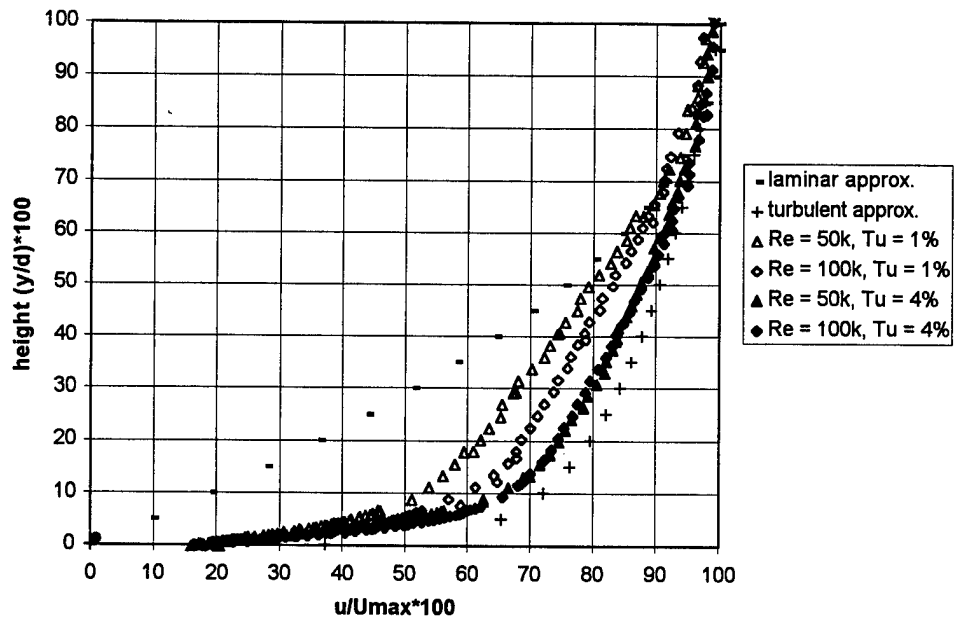


Figure 82. Tripped boundary layer profiles at 67% chord for V-grooves starting at 60%.

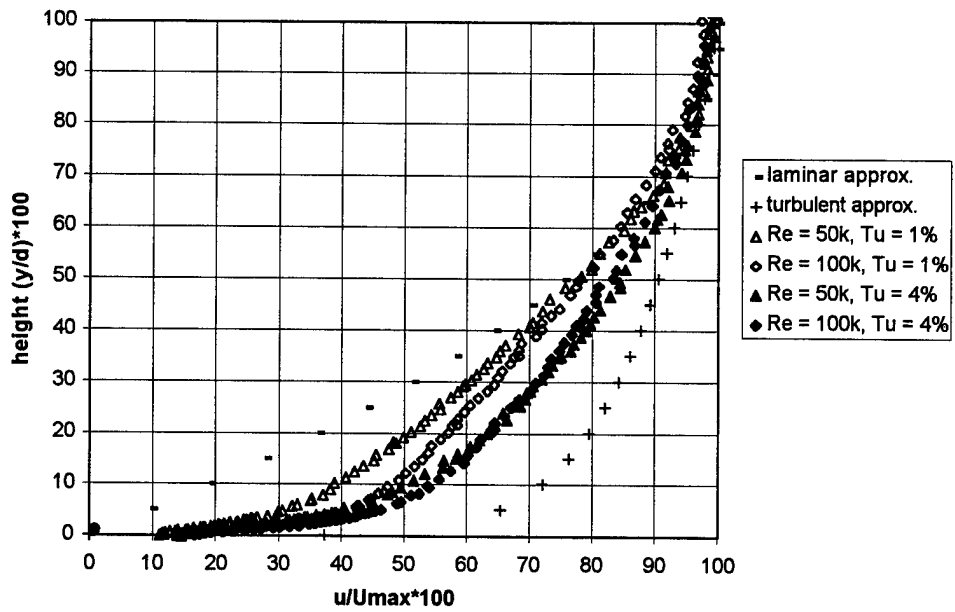


Figure 83. Tripped boundary layer profiles at 84.8% chord for V-grooves starting at 60%.

The 2.77 mm (0.109 inches) diameter trip wire was placed at the 35% chord line upstream of the V-grooves which provided a turbulent boundary layer. While the trip wire did provide a turbulent boundary layer, the boundary layer did not separate from the baseline smooth blade as the turbulent boundary layer did in the experiments performed by Lin et al. [18]. The lack of separation over the blade with a turbulent boundary layer prevented reductions in the blade wake when V-grooves were used compared to a smooth blade with a boundary layer trip (see Figures 86 and 87).

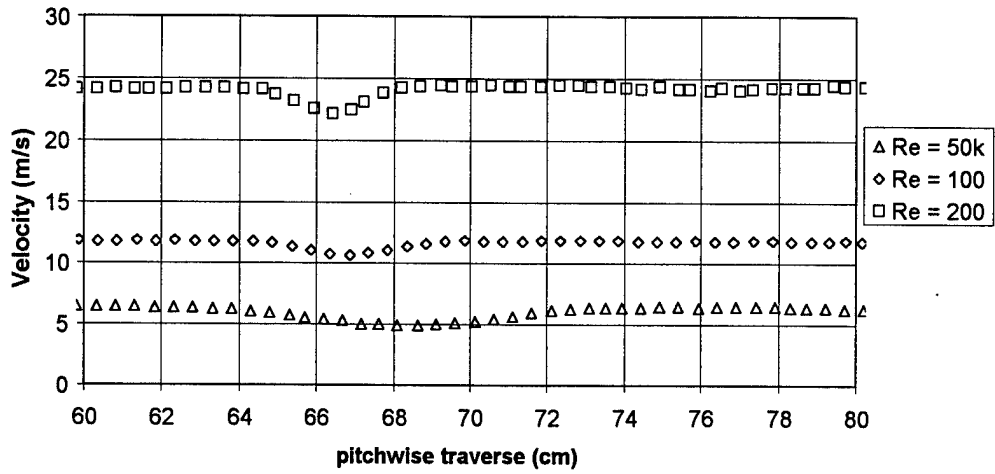
### **9.7 Exit Momentum Deficit Calculations for V-Grooves**

Given the exit velocity profiles in Figures 84 through 87, the wake momentum deficit ( $\Theta$ ) for the V-grooves was calculated. Figure 88 illustrates wake momentum deficits for the V-groove blade with a baseline blade comparison provided. For the case of no boundary layer trip, both V-groove configurations provided improvements ranging from 3% to 25.5% in the wake momentum deficit at Reynolds numbers of 100k and 200k with a freestream turbulence level of 1%. For a Reynolds number of 50k, only the V-grooves starting at 60% chord provided a reduction in  $\Theta$  by 30.2% and 10.7%, for freestream turbulence levels of 1% and 4%, respectively.

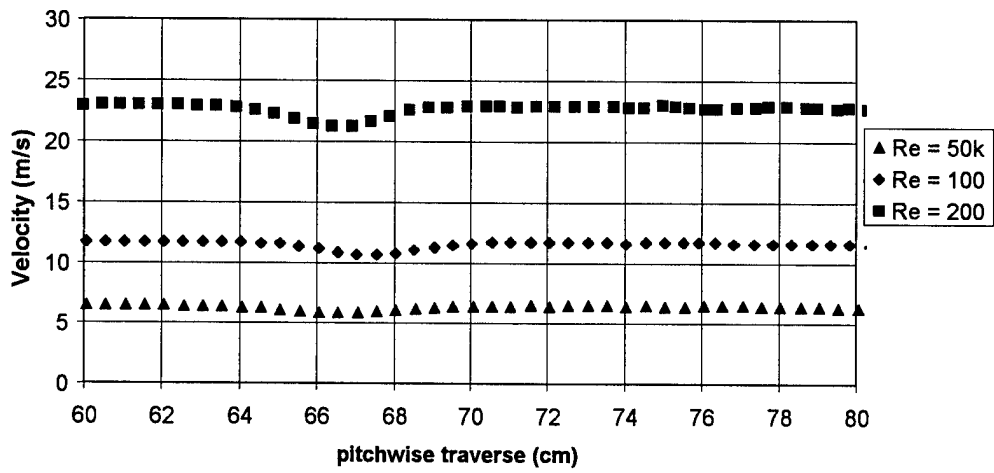
Figure 88 also contains  $\Theta$  values for the V-grooves tested with a boundary layer trip at 35% axial chord. The wake momentum deficit values for the V-grooves were higher than the baseline tripped blade for Reynolds numbers of 100k and 200k. At a Reynolds number of 50k, both the V-grooves starting at 55% and 60% axial chord provided a small reduction in  $\Theta$  by 11.1% and 5.2%, respectively, for a freestream turbulence level of 1%. At the higher freestream turbulence level of 4%, no reduction in wake momentum deficit was measured for the V-grooves.

### **9.8 Loss Coefficient Measurement for V-Grooves**

The loss coefficient was calculated using the previously described exit velocity profiles along with the measured total pressure in the wake of the V-groove blade. The total pressure probe was

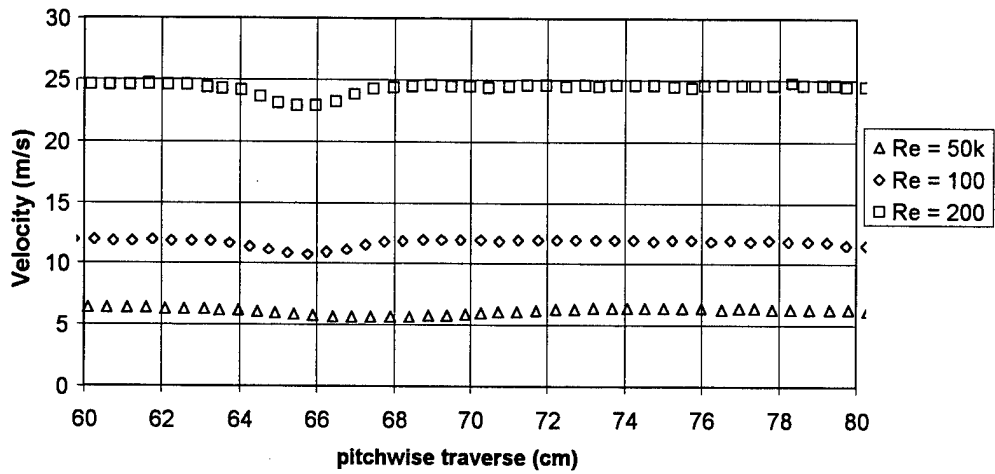


a) Exit velocities for  $Tu = 1\%$

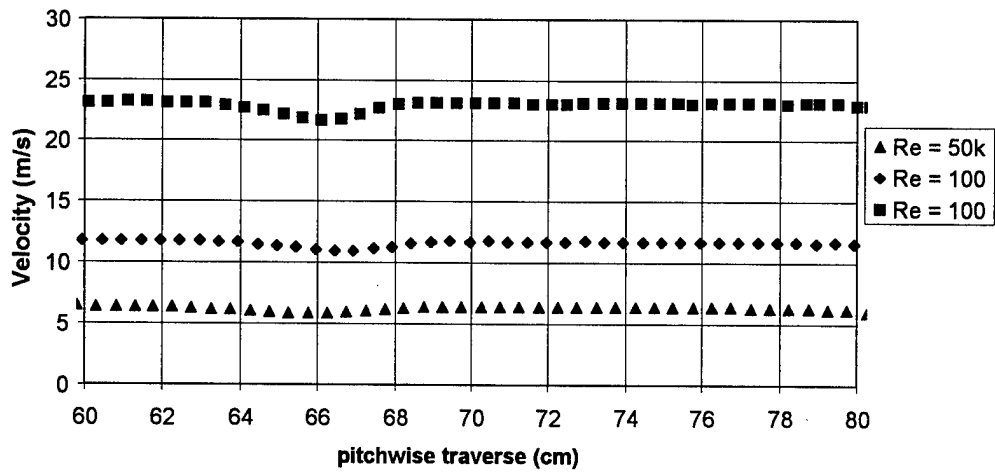


b) Exit velocities for  $Tu = 4\%$

Figure 84. Exit velocity profiles for V-grooves starting at 55% chord.

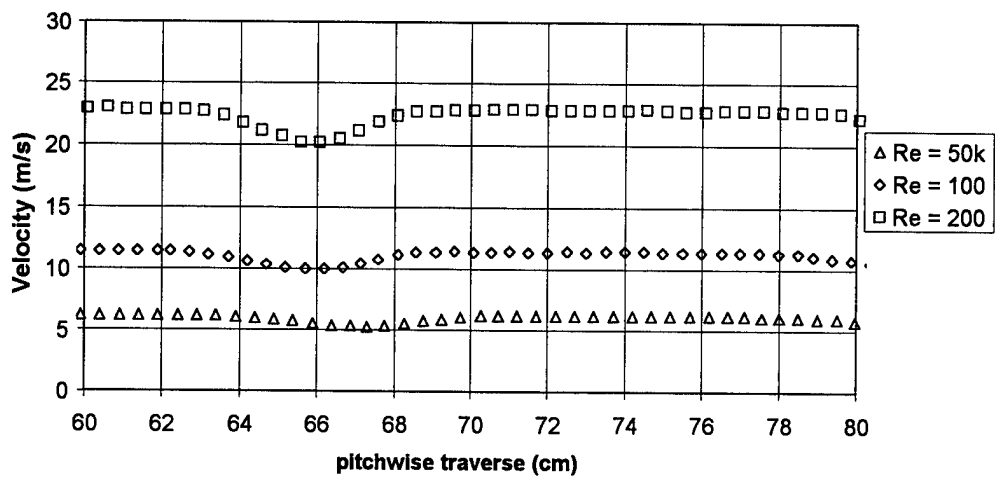


a) Exit velocities for Tu = 1%

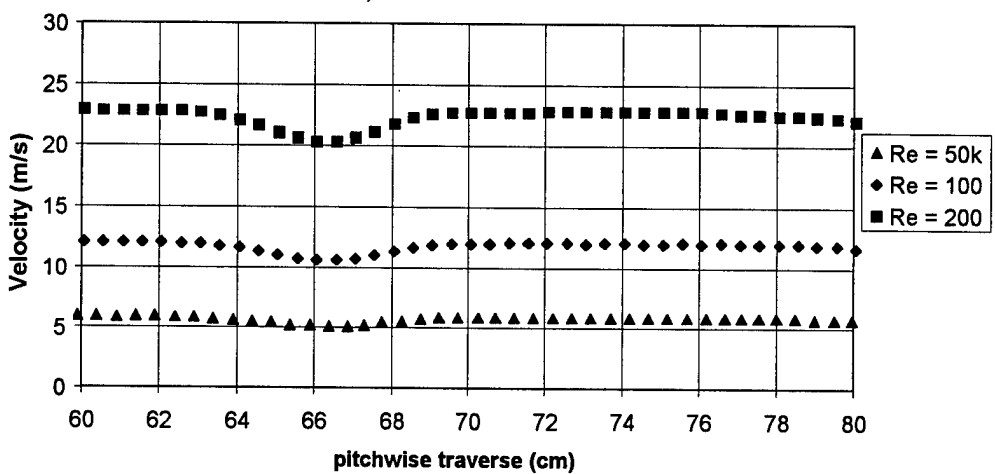


b) Exit velocities for Tu = 4%

Figure 85. Exit velocity profiles for V-grooves starting at 60% chord.

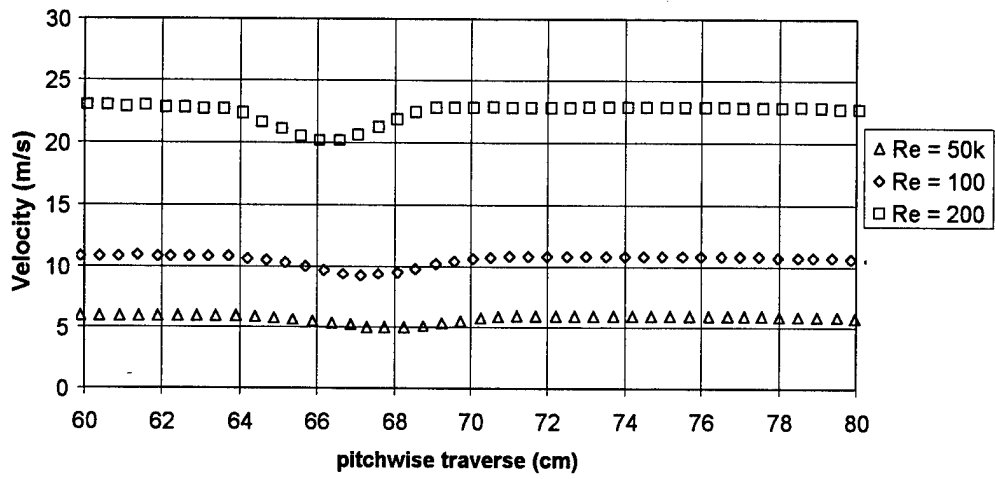


a) Exit velocities for Tu = 1%

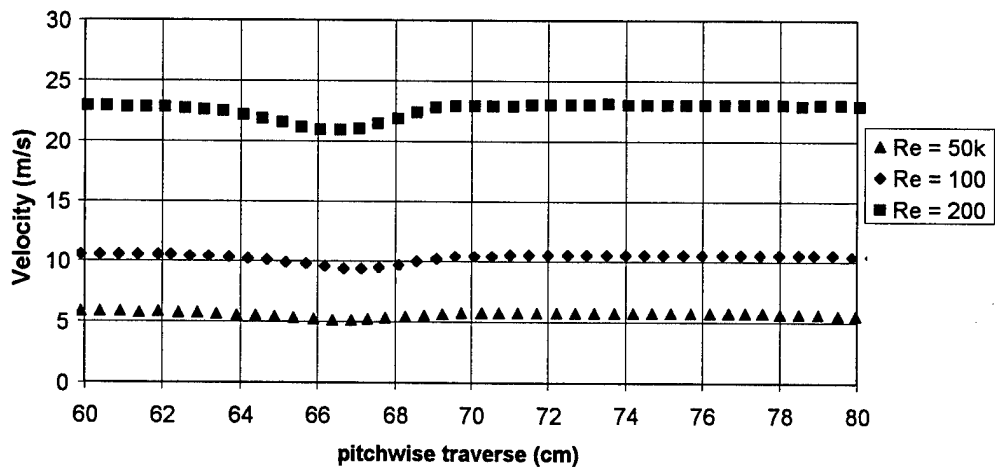


b) Exit velocities for Tu = 4%

Figure 86. Exit velocity profiles for V-grooves starting at 55% chord with boundary layer trip.

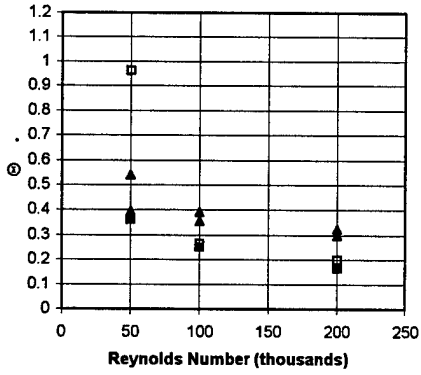


a) Exit velocities for Tu = 1%

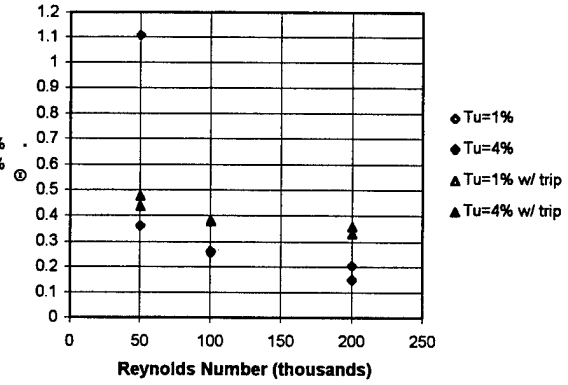


b) Exit velocities for Tu = 4%

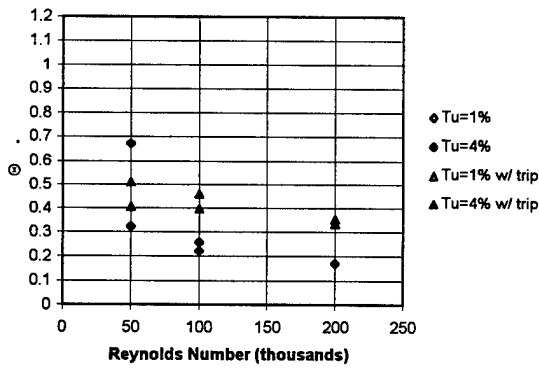
Figure 87. Exit velocity profiles for V-grooves starting at 60% chord with boundary layer trip.



a) Baseline Pak-B blade



b) V-grooves at 55% chord



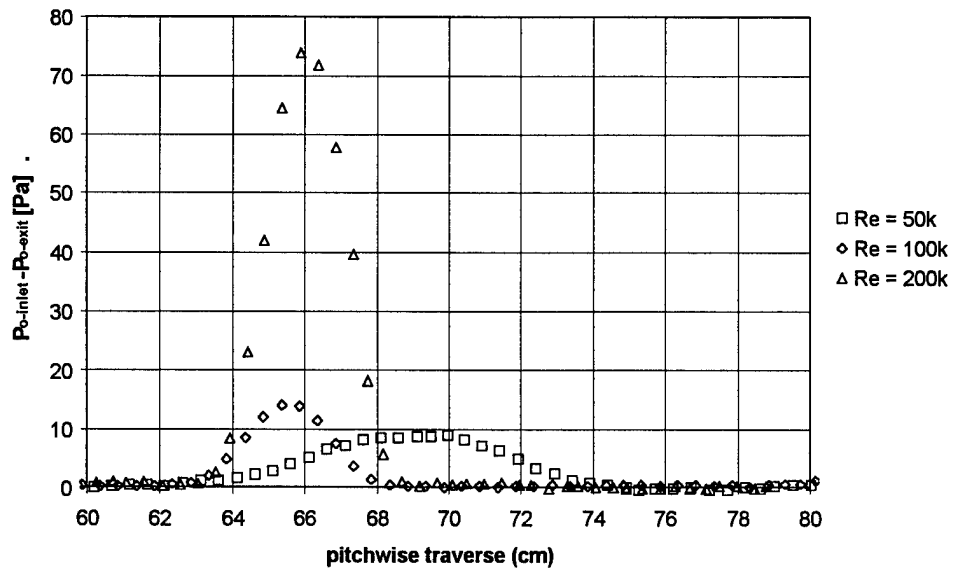
c) V-grooves at 60% chord

Figure 88. Wake momentum values for baseline blade, and V-grooves starting at 55% and 60% chord.

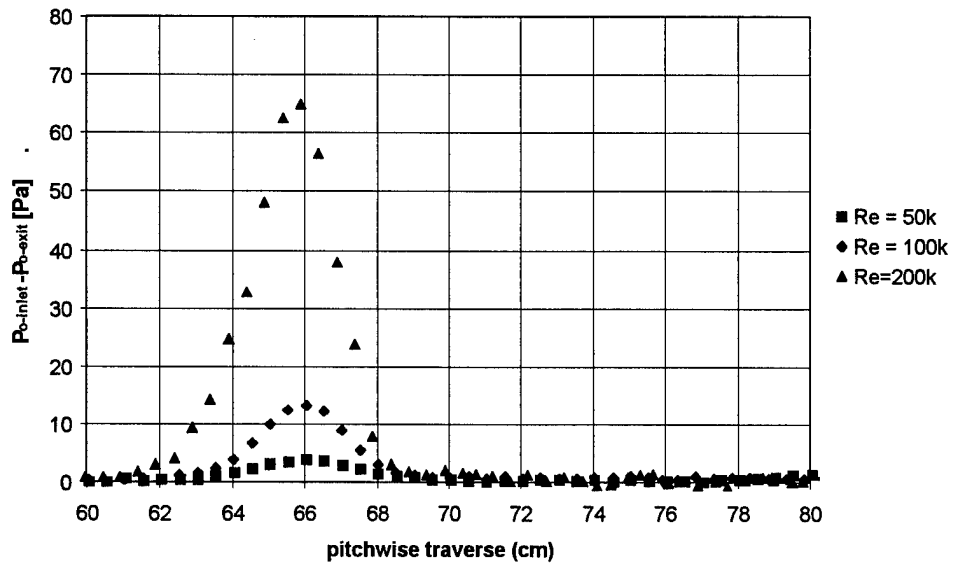
moved across the V-groove blade wake approximately  $\frac{1}{2}$  axial chord lengths downstream. Figures 89 and 90 show the exit total pressure measured for the V-grooves with an initially laminar boundary layer. The size of the wakes were reduced by a small amount compared to the baseline smooth blade. For the case of a tripped boundary layer the total pressure wake of the V-grooves was greater than the smooth blade with a trip (see Figures 91 and 92).

Using the exit velocity and total pressure measurements from Figures 84 through 92, the loss coefficient was calculated for the V-grooves. Figures 93 and 94 illustrate the two very different results V-grooves provide depending upon the initial state of the boundary layer. As seen in Figure 93, the V-grooves starting at 60% axial chord provided a beneficial reduction in the 2-D profile loss coefficient for Reynolds numbers of 50k and 100k. The maximum reduction in loss coefficient for the V-grooves starting at 60% occurred at a Reynolds number of 50k and freestream turbulence level where the loss was reduced by 36.8%. The V-grooves starting at 55%, however, only provided a reduction in the loss coefficient by 5.1% to 13.2% for a Reynolds number of 100k (for freestream turbulence levels of 1% and 4%), and a reduction in loss coefficient of 22.4% at a Reynolds number of 50k when the inlet freestream turbulence level was 4%. Both V-groove modifications provided essentially the same loss coefficient as the baseline blade at a Reynolds number of 200k for the initially laminar boundary layer.

For the tripped boundary layer, the V-grooves increased the 2-D loss coefficient slightly compared to the baseline smooth blade with a boundary layer trip. As seen in Figure 94, the loss coefficient increases with Reynolds number for the baseline blade and the V-grooves when the boundary is tripped with a wire.

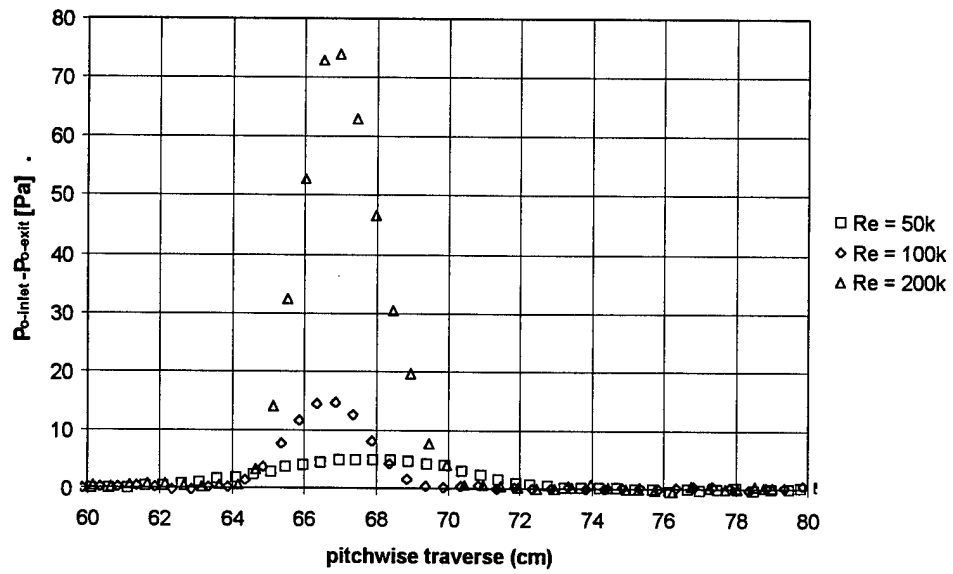


a) Exit pressure profiles for  $Tu = 1\%$

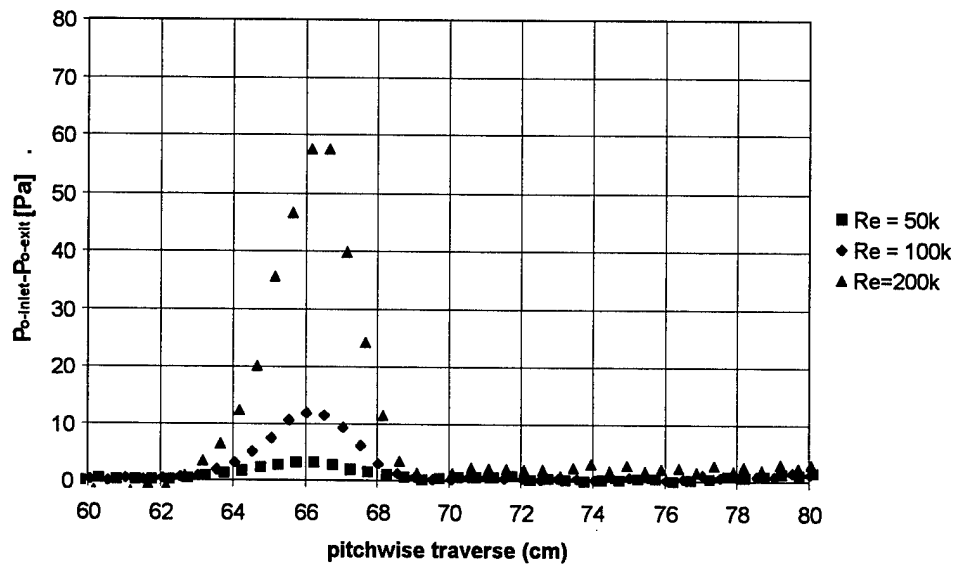


b) Exit pressure profiles for  $Tu = 4\%$

Figure 89. Exit stagnation pressure loss for V-grooves starting at 55% chord.

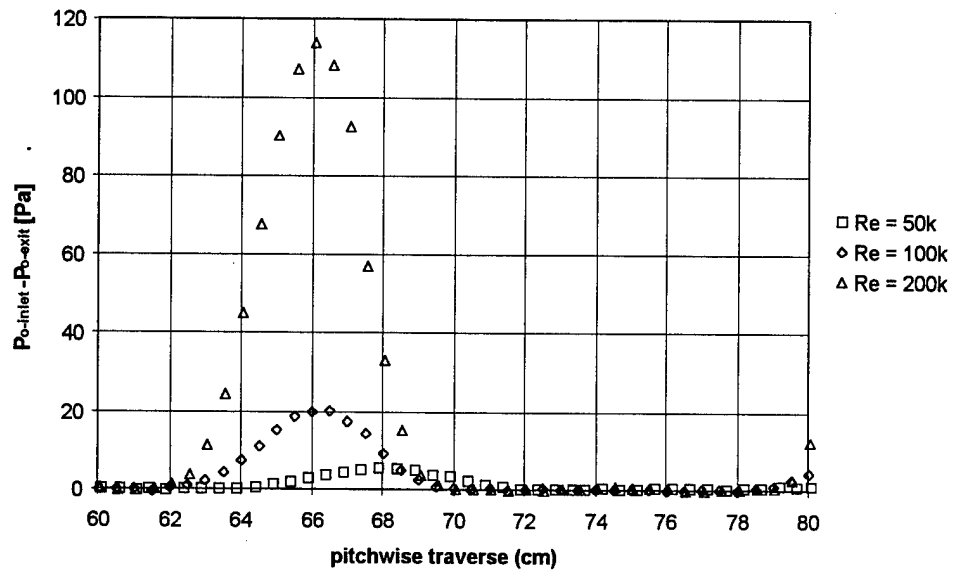


a) Exit pressure profiles for  $Tu = 1\%$

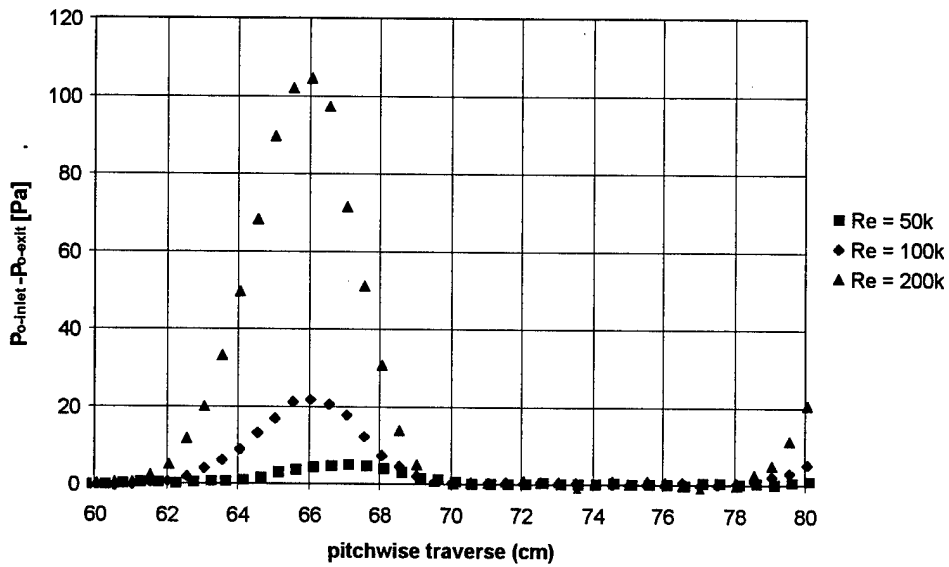


b) Exit pressure profiles for  $Tu = 4\%$

Figure 90. Exit stagnation pressure loss for V-grooves starting at 60% chord.

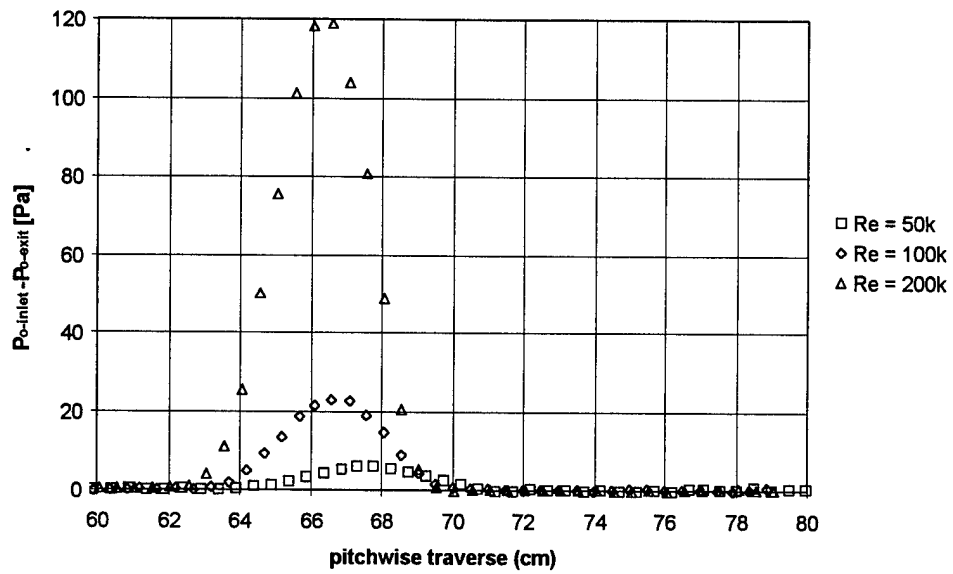


a) Exit pressure profiles for Tu = 1%

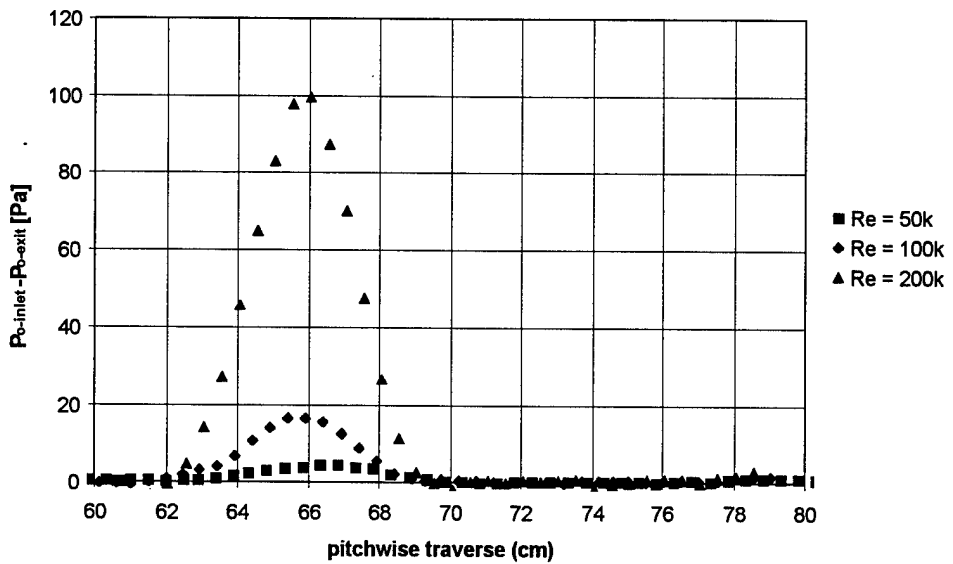


b) Exit pressure profiles for Tu = 4%

Figure 91. Exit stagnation pressure loss for V-grooves starting at 55% chord with boundary layer trip.

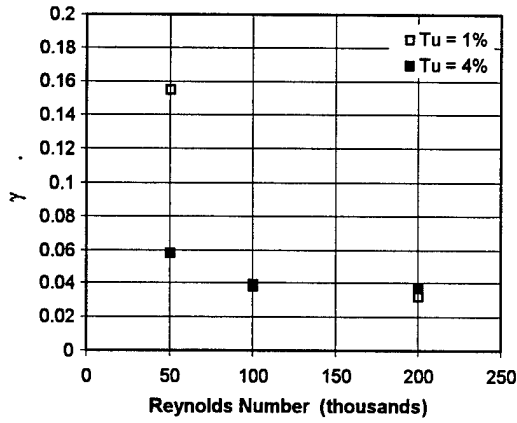


a) Exit pressure profiles for  $Tu = 1\%$

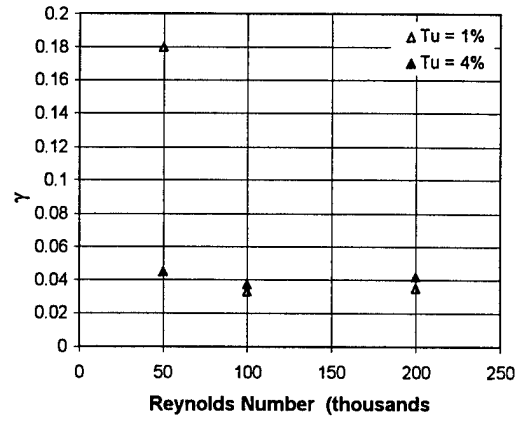


b) Exit pressure profiles for  $Tu = 4\%$

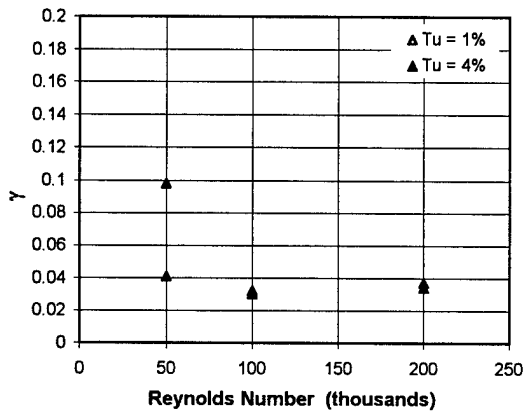
Figure 92. Exit stagnation pressure loss for V-grooves starting at 60% chord with boundary layer trip.



a) Baseline Pak-B blade

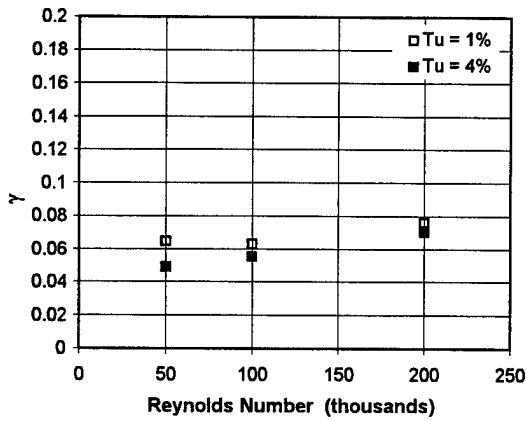


b) V-grooves starting at 55%

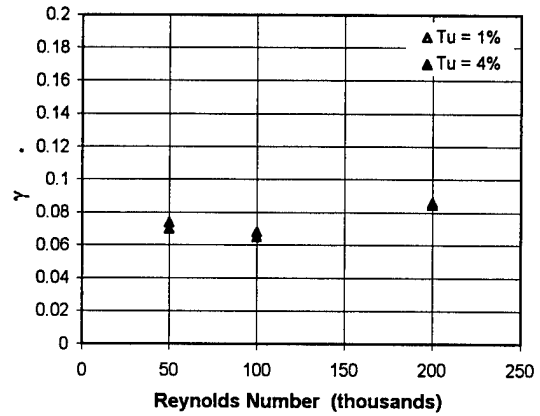


c) V-grooves starting at 60%

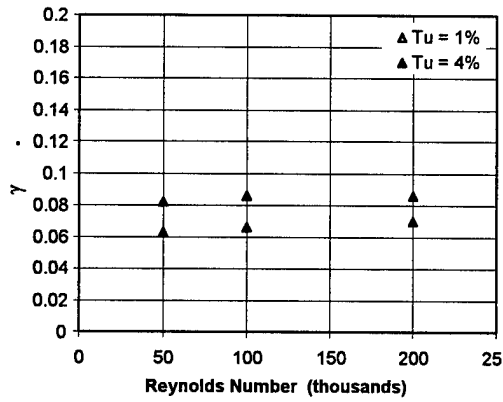
Figure 93. Loss coefficient for baseline blade and V-grooves starting at 55% and 60% chord.



a) Baseline Pak-B blade w/ trip



b) V-grooves starting at 55% w/ trip



c) V-grooves starting at 60% w/ trip

Figure 94. Loss coefficient for baseline blade and V-grooves starting at 55% and 60% chord with boundary layer trip.

## Chapter 10 - Summary and Conclusions

Unmanned aerial vehicles operating at high altitudes and low cruise velocities experience low Reynolds number flow over the aircraft and within the engine. The low pressure turbine (LPT) blades within the engine may suffer lower efficiencies than predicted while the aircraft is performing its mission phase at low Reynolds numbers. The lower engine efficiencies are due to flow separating from the surface of the LPT blades. The laminar separation problem was verified to exist with the Pratt and Whitney Pak-B blade.

A new linear cascade tunnel was used to simulate the low pressure turbine environment. The test section consisted of eight Pak-B blades and nine passages. The blades were tested for inlet Reynolds numbers of 50k, 100k and 200k and for freestream turbulence levels of 1% and 4%. These conditions cover the range under which the laminar separation problem is most prevalent within the jet engine. The efficiency of the Pak-B blades was measured in terms of the 2-D profile loss coefficient. The higher the profile loss coefficient, the lower the engine operating efficiency. For low Reynolds numbers and turbulence level ( $Re = 50k$  and  $Tu = 1\%$ ) the loss coefficient is largest due to the flow separating without reattachment to the blade.

Previous attempts to correct for the decrease in efficiency have been extensions of known active control methods, such as vortex generator jets. Passive techniques, however, have the advantage of not requiring additional power or controls. Installation into a pre-existing engine would mean replacement of the LPT blade spool with a set of modified blades. No additional controls or power would be required for installation. No information has been previously published on the successful implementation of a passive separation control technique for a jet engine blade until this document.

Of the twenty-one different passive separation control techniques initially considered, three were chosen for further examination. The first passive technique was the attachment of a wire to

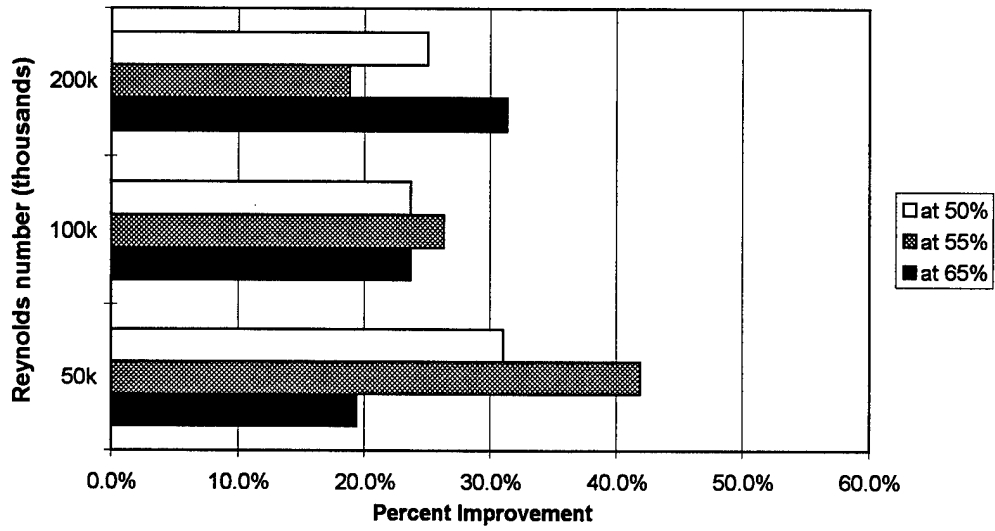
the suction surface of the blade at the 35% axial chord line. The initially laminar flow was tripped to a turbulent state. The turbulent flow remained attached over the surface of the blade downstream of the wire for all conditions tested. While the trip wire reduced the loss at a Reynolds number of 50k and freestream turbulence level of 1%, at all other conditions the trip wire increased the losses for the blade.

The second passive technique consisted of dimples machined into the suction surface of the airfoil. The dimples were successful in reducing the loss coefficient at low Reynolds numbers, while not degrading performance at the highest Reynolds number tested (see Figure 95). Three variations of dimples were tested, the chordwise location of the dimples in each test being changed to determine the effect of dimple location on loss reduction. The baseline separation location moves downstream with increasing Reynolds number and turbulence (62% to 78% axial chord). The most effective dimples are those upstream of separations located near separation. Dimples provided improved losses at all locations, including the location slightly downstream of separation, the low Reynolds number, low turbulence case (50k, 1%). The improved loss for the dimples downstream of the separation point was due to the thin separation (less than  $0.1\delta$ ) at that location, which allowed for partial effectiveness of the dimples.

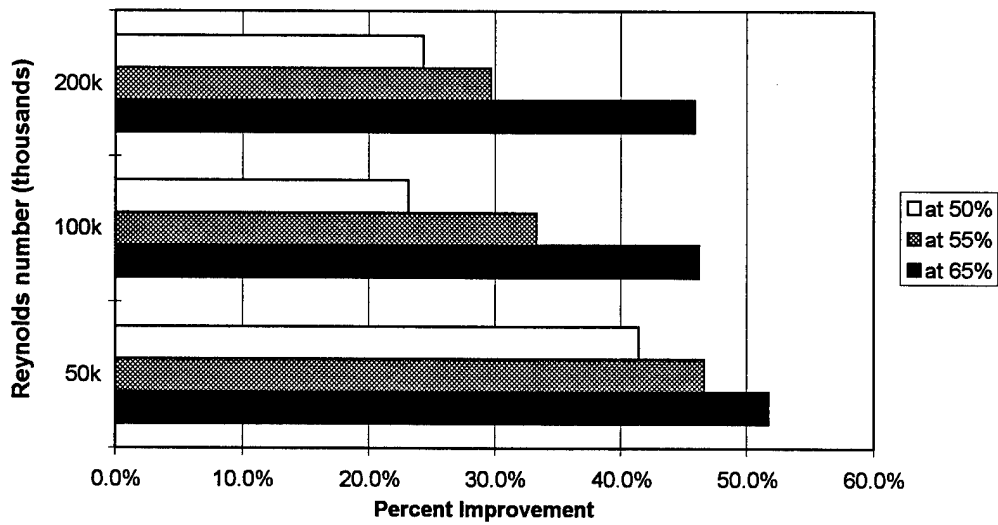
To take advantage of this new knowledge, guidance must be given for proper placement of the dimples on the suction surface. The loss coefficient was plotted for variation in axial chord distance between baseline separation locations and dimples in Figure 96. Figures 96a, b and c also show the baseline blade loss coefficients. As seen in Figure 96, a benefit was attained with the dimples at all three chord locations. Furthermore, for higher Reynolds numbers (comparing Figures 96a, b and c) the dimples reduce the loss coefficient to approximately the same value regardless of their location. This suggests that with a reduction in separation, losses are similar and due mainly to viscous effects which decrease slightly with Reynolds number. For turbulent reattachment, the skin

friction coefficient is proportional to  $1/Re^{1/7}$ , for which the values of loss coefficient scale as seen in Figure 96 (except for the low Reynolds number case for which the flow a separation zone remains).

The improvements in loss coefficient can be related to improvements in engine stage efficiency. For the reductions in loss coefficient (18.8% to 51.7%) made possible through the use of dimples, equation 10 of Chapter 1 indicates a typical increase of turbine stage efficiency of 1.1% to 2.9%. This improved efficiency of 2.9% can be expected to improve the specific thrust and specific fuel consumption (SFC) on a turbojet engine at Mach 2, 36,000 ft. (Mattingly [20]) by 0.54% and 0.54%, respectively. A decrease of 0.54% in SFC would increase range by about 1.41% and a reduction in fuel consumption by 0.59%.

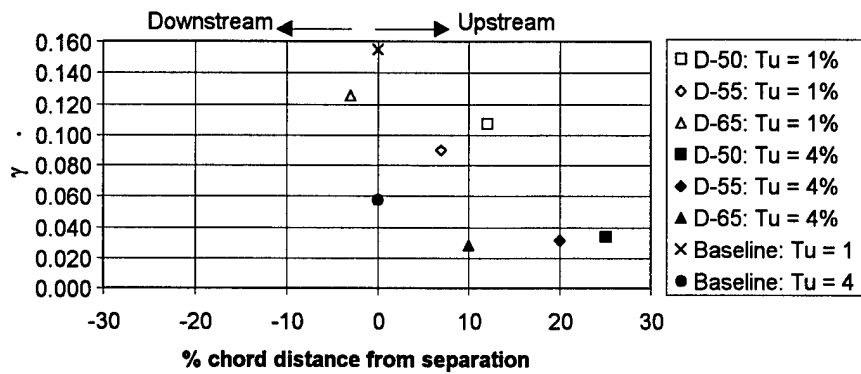


a)  $Tu = 1\%$

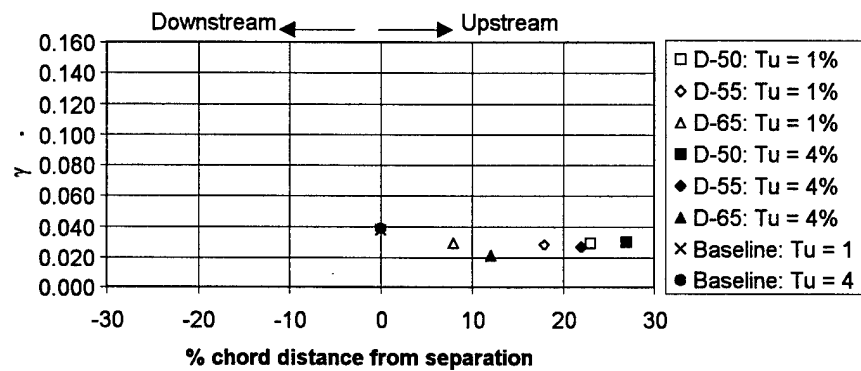


b)  $Tu = 4\%$

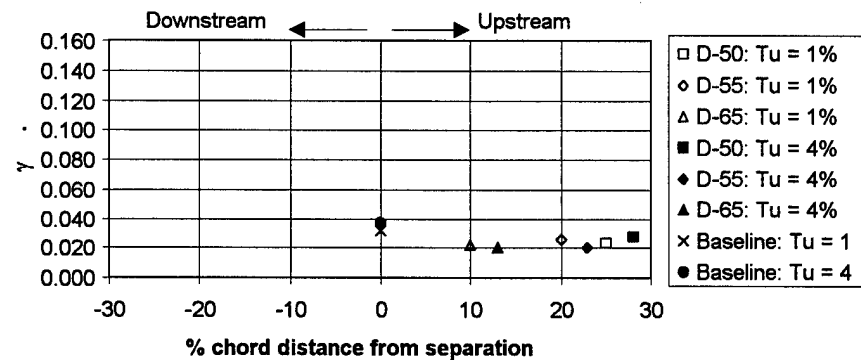
Figure 95. Improvement in loss coefficient using dimples at 50%, 55%, and 65% axial chord.



a)  $Re = 50k$



b)  $Re = 100k$



c)  $Re = 200k$

Figure 96. Effect of dimple distance from baseline separation on loss coefficient.

Streamwise V-grooves were tested in two different configurations. The axial chord starting location of the V-grooves was varied to determine the effect on loss reduction. For an initially laminar boundary layer, the V-grooves starting at 55% chord reduced the loss coefficient for a moderate Reynolds number and low turbulence intensity and low and moderate Reynolds numbers (50k and 100k) with high turbulence intensity. The V-grooves starting at 60% chord reduced the loss coefficient for low and moderate Reynolds numbers (see Figure 97) at low turbulence, and for all Reynolds numbers at high turbulence. Therefore the V-grooves are more beneficial when placed closer to the baseline separation point.

The two sets of V-grooves were also tested with a boundary layer trip located at the 35% axial chord line. A comparison of the results with those of the baseline blade with a boundary layer trip showed no net reduction in losses with a freestream turbulence level of 1%. At the higher turbulence level of 4%, the V-grooves provided a 0.8% reduction in loss coefficient at the highest Reynolds number (200k). In summary, the trip wire and V-groove experiments showed a decrease in loss coefficient for certain limited cases of Reynolds number and freestream turbulence level. Any passive technique for separation control must provide a reduction in the loss coefficient at low Reynolds numbers while not significantly increasing the losses at higher Reynolds numbers typical of take-off operations. Considering the performance of the V-grooves, only the V-grooves starting at 60% meet this criteria while the trip wire with V-groove combination should not be used in a jet engine.

In conclusion, the dimples consistently showed improved performance over the baseline blade and were the best passive technique examined for application to low pressure turbine blades. The dimples improved the low Reynolds number performance by energizing the flow sufficiently to prevent separation. At higher Reynolds numbers the submerged dimples did not increase the boundary layer thickness as the trip wire did. As with the baseline blade, the loss coefficient for the dimples

also decreased with increasing Reynolds number and turbulence intensity. The combination of separation prevention at low Reynolds numbers and efficient flow at high Reynolds numbers through a passive technique requiring no additional power or controls makes the dimple a significant new tool for the engine designer.

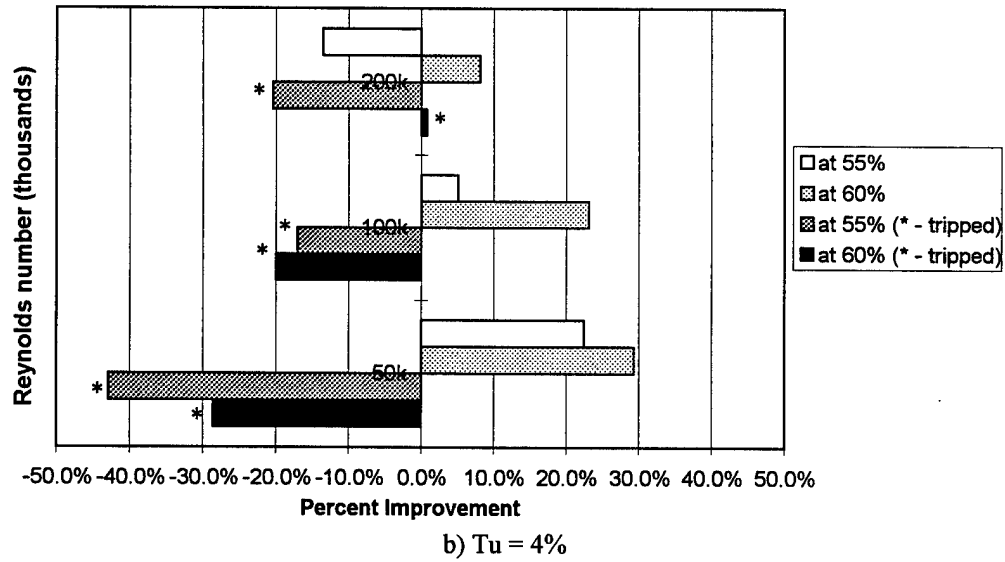
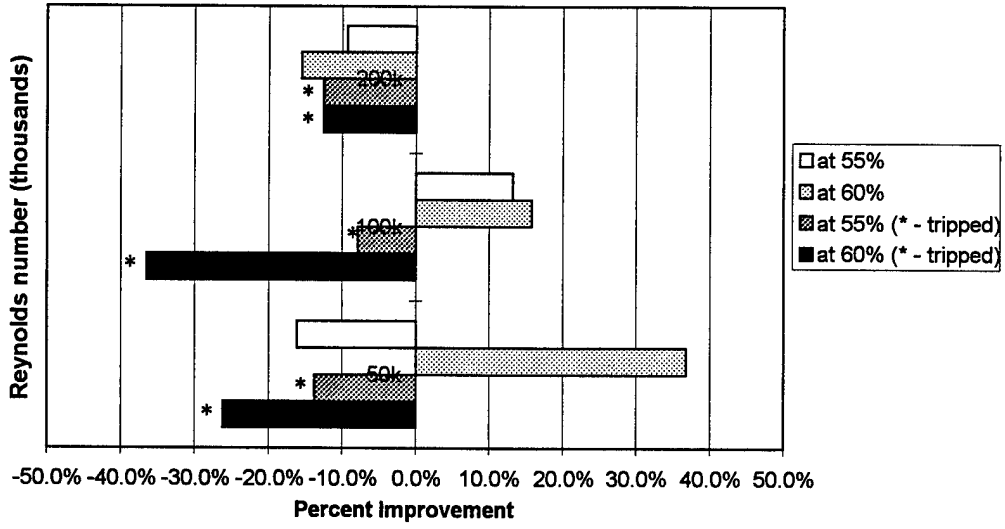


Figure 97. Change in loss coefficient using V-grooves with and without a trip wire.

## References

- [1] MacArthur, C. "Personal Communication with D. Helton." 1997.
- [2] Halstead, D.E., D.C. Wisler, T.H. Okiishi, G.J. Walker, H.P. Hodson and H.W. Shin. "Boundary Layer Development in Axial Compressors and Turbines Part 1 of 4: Composite Picture." International Gas Turbine and Aeroengine Congress and Exposition, Houston, TX, June 1995. ASME Paper No. 95-GT-461.
- [3] Halstead, D.E., D.C. Wisler, T.H. Okiishi, G.J. Walker, H.P. Hodson and H.W. Shin. "Boundary Layer Development in Axial Compressors and Turbines Part 3 of 4: LP Turbines." International Gas Turbine and Aeroengine Congress and Exposition, Houston, TX, June 1995. ASME Paper No. 95-GT-463.
- [4] Murawski, C.G., T.W. Simon, R.J. Volino and K. Vafai. "Experimental Study of the Unsteady Aerodynamics in a Linear Cascade with Low Reynolds Number Low Pressure Turbine Blades." International Gas Turbine and Aeroengine Congress and Exhibition, Orlando, FL, June 1997. ASME Paper No. 97-GT-95.
- [5] LaGraff, J.E. and D.E. Ashpis, editors. *An Experimental Investigation of Transition as Applied to Low Pressure Turbine Suction Surface Flows*, Lewis Research Center, September 1998. NASA, Minnowbrook II 1997 Workshop on Boundary Layer Transition in Turbomachines. NASA CP-1998-206958.
- [6] Simon, T.W. and R.J. Volino. "Separating and Separated Boundary Layers." Technical Report WL-TR-96-2092, Wright Laboratory, 1996.
- [7] Hourmouziadis, J. "Aerodynamic Design of Low Pressure Turbines," *AGARD*, pages 1-38 (1989). AGARD-LS-167.
- [8] Rivir, R.B. "Transition on Turbine Blades and Cascades at Low Reynolds Numbers." Technical Report WL-TR-96-2084, Wright Laboratory, 1996.
- [9] Qiu, S. and T.W. Simon. "An Experimental Investigation of Transition as Applied to Low Pressure Turbine Suction Surface Flows." International Gas Turbine and Aeroengine Congress and Exhibition, Orlando, FL, June 1997.
- [10] Baughn, J.W., R.J. Butler, A.R. Byerley and R.B. Rivir. "An Experimental Investigation of Heat Transfer, Transition and Separation on Turbine Blades at Low Reynolds Number and High Turbulence Intensity." Technical Report WL-TR-96-2093, Wright Laboratory, 1995.
- [11] Werle, M.J. "Compressor and Turbine Blade Boundary Layer Separation," *AGARD Conference Proceedings*, AGARD-CP-351 (1983).
- [12] Mayle, R.E. "The Role of Laminar-Turbulent Transition in Gas Turbine Engines," *Journal of Turbomachinery*, 113:509-537 (October 1991). ASME Paper No. 91-GT-282.
- [13] Halstead, D.E. "Boundary Layer Development in Multi-Stage Low Pressure Turbines." PhD dissertation, Iowa State University, 1996.
- [14] Chen, F., Y.P. Tang and M.Z. Chen. "An Experimental Investigation of Loss Reduction with Riblets on Cascade Blade Surfaces and Isolated Airfoils." Gas Turbine and Aeroengine Congress and Exposition, Brussels, Belgium, June 1990. ASME Paper No. 90-GT-207.
- [15] Occhipinti, A.C. "More Speed with Less Money," *Sport Aviation*, pages 77-79 (1998).

- [16] Bearman, P.W. and J.K. Harvey. "Golf Ball Aerodynamics," *The Aeronautical Quarterly*, 27(2):112-122 (May 1976).
- [17] Bearman, P.W. and J.K. Harvey. "Control of Circular Cylinder Flow by the Use of Dimples," *AIAA Journal*, 31(10):1753-1756 (October 1993).
- [18] Lin, J.C., F.G Howard and G.V Selby. "Turbulent Flow Separation Control Through Passive Techniques." AIAA 2nd Shear Flow Conference, Tempe, AZ, March 1989. AIAA Paper No. 89-0976.
- [19] Anderson, J.D. *Introduction To Flight* (Second Edition). McGraw-Hill, New York, (Second Edition), 1985.
- [20] Mattingly, J.D. *Elements of Gas Turbine Propulsion*. McGraw-Hill, Inc., New York, 1996.
- [21] Addison, J.S. and H.P. Hodson. "Modelling of Unsteady Transitional Boundary Layers." International Gas Turbine and Aeroengine Congress and Exposition, Orlando, FL, June 1991. ASME Paper No. 91-GT-282.
- [22] Dorney, Dan, "Personal Communication," January 1999.
- [23] Halstead, D.E., D.C. Wisler, T.H. Okiishi, G.J. Walker, H.P. Hodson and H.W. Shin. "Boundary Layer Development in Axial Compressors and Turbines Part 4 of 4: Computations and Analysis." International Gas Turbine and Aeroengine Congress and Exposition, Houston, TX, June 1995. ASME Paper No. 95-GT-464.
- [24] Halstead, D.E. and W.J. Solomon, "Personal Communication," November 1997.
- [25] Walker, G.J. "The Role of Laminar-Turbulent Transition in Gas Turbine Engines: A Discussion," *Journal of Turbomachinery*, 115:207-217 (April 1993).
- [26] Reed, H.L. and W.S. Saric. "Linear Stability Theory Applied to Boundary Layers," *Annual Review of Fluid Mechanics*, 28:389-428 (1996).
- [27] Sharma, O.P., R.A. Wells, R.H. Schlinker and D.A. Bailey. "Boundary Layer Development on Turbine Airfoil Suction Surfaces," *Journal of Engineering for Power*, 104:698-706 (July 1982).
- [28] Mueller, T.J., editor. *International Conference on the Aerodynamics at Low Reynolds Numbers Between 10,000 and 1,000,000*, London, 1987. U.S. Office of Naval Research.
- [29] Rivir, R.R., "Personal Communication," April 1999.
- [30] Yurchenko, N. "Development of Boundary Layer Control Techniques To Optimize Turbine Blade Performance." Institute of Hydromechanics, National Academy of Sciences, Kiev, 1997.
- [31] Bruun, H.H. *Hot-Wire Anemometry*. Oxford University Press, Oxford, 1995.
- [32] Rao, K.V., R.A. Delaney and M.G. Dunn. "Vane-Blade Interaction in a Transonic Turbine: Part 1 - Aerodynamics." AIAA/SAE/ASME/ASSEE 28th Joint Propulsion Conference and Exhibit, Nashville, TN, July 1992. AIAA Paper No. 92-3323.
- [33] Kline, S.J. and F.A. McClintok. "Describing Uncertainties in Single-Sample Experiments," *Mechanical Engineering*, 75(1):3-8 (January 1953).
- [34] Taylor, J.R. *An Introduction to Error Analysis*. University Science Books, Mill Valley, CA,

1982.

- [35] Ainley, D.G. "Performance of Axial-Flow Turbines," *Proceedings Institution of Mechanical Engineers*, 159(41):230-244 (November 1948).
- [36] Ainley, D.G. and G.C.R. Mathieson. "A Method of Performance Estimation for Axial-Flow Turbines," *British ARC, R and M*, 2974 (1951).
- [37] Horlock, J.H. "Review: Losses and Efficiencies in Axial-Flow Turbines," *International Journal of Mechanical Sciences*, 2:48-75 (1960).
- [38] Horlock, J.H. "Further Comments on Losses and Efficiencies in Axial-Flow Turbines," *International Journal of Mechanical Sciences*, 3:312-313 (1961).
- [39] Horlock, J.H. *Axial Flow Turbines*. Butterworth and Co. Ltd., London, 1966.
- [40] Craig, H.R.M. and H.J.A. Cox. "Performance Estimation of Axial Flow Turbines," *Proceedings of the Institution of Mechanical Engineers*, 185(32):407-424 (1971).
- [41] Schlichting, H. *Boundary-Layer Theory* (Seventh Edition). McGraw-Hill, Inc., New York, (Seventh Edition), 1987.
- [42] White, F.M. *Fluid Mechanics* (Third Edition). McGraw-Hill, Inc., New York, (Third Edition), 1994.
- [43] Chang, P.K. *Separation of Flow*. Pergamon Press, 1970.
- [44] Johnston, J. and M. Nishi. "Vortex Generator Jets - A Means for Passive and Active Control of Boundary Layer Separation." 27th Aerospace Sciences Meeting, Reno, NV, January 1989. AIAA Paper No. 89-0564.
- [45] Taylor, H.D. "Summary Report on Vortex Generators." Technical Report Report No. R-05280-9, United Aircraft Corporation Research Department, March 1950.
- [46] Kimura, T. and M. Tsutahara. "Fluid Dynamic Effects of Grooves on Circular Cylinder Surface," *AIAA Journal*, 29(12):2062-2068 (December 1991).
- [47] Y. Nakayama, K. Aoki, K. Wada M. Kato T. Okumoto. "Flow Visualization Around Golf Balls." In *Flow Visualization IV: Proceedings of the Fourth International Symposium on Flow Visualization*, pages 191-196, Ecole Nationale Supérieure de Techniques Avancées, August 1986.
- [48] Roach, P.E. "The Generation of Nearly Isotropic Turbulence by Means of Grids," *Heat and Fluid Flow*, 8(2):82-92 (June 1987).
- [49] Mayle, R.E., K. Dullenkopf and A. Schulz. "The Turbulence That Matters." IGTI Conference, Orlando, FL, 1997.
- [50] Gostelow, J.P. *Cascade Aerodynamics*. Pergamon Press Ltd., Oxford, 1984.
- [51] Giese, A., "Personal Communication," January 1998.
- [52] Hinze, J. O. *Turbulence*. McGraw-Hill Book Company, New York, 1959.
- [53] Bendat, J.S. and A.G. Piersol. *Random Data: Analysis and Measurement Procedures* (Second Edition). John Wiley and Sons, New York, (Second Edition), 1986.
- [54] Kececy, F.J. and R.A. Delaney. "Turbine Vane-Blade Interaction: Interim Research and

- Development Status Report for Contract F33615-90-C-2028." Technical Report, Allison Engine Co., 1995.
- [55] Mattingly, J.D., Heiser W.H. and D.H. Daley. *Aircraft Engine Design*. AIAA, Inc., Washington, DC, 1987.
- [56] Wilson, D.G. and T. Korakianitis. *The Design of High-Efficiency Turbomachinery and Gas Turbines* (Second Edition). Prentice Hall, Upper Saddle River, (Second Edition), 1998.
- [57] Reid, R.C., Prausnitz J.M. and B.E. Polling. *The Properties of Gases and Liquids* (fourth Edition). McGraw Hill, New York, (fourth Edition), 1987.
- [58] Austin, J.G. "Mach Number, Flow Angle, and Loss Measurements Downstream of a Transonic Fan-Blade Cascade." MS thesis, Naval Postgraduate School, March 1994.
- [59] Gamerding, P.M. and R.P. Shreeve. "The Effects of Low-Profile Vortex Generators on Flow in a Transonic Fan-Blade Cascade." 34th Aerospace Sciences Meeting and Exhibit, Reno, NV, January 1996. AIAA Paper No. 96-0250.
- [60] Rao, D.M. and T.T. Kariya. "Boundary-Layer Submerged Vortex Generators for Separation Control - An Exploratory Study." 1st National Fluid Dynamics Congress, 1988. AIAA Paper No. 88-3546-CP.
- [61] McCormick, D.C. "Shock-Boundary Layer Interaction Control with Low-Profile Vortex Generators and Passive Cavity." 30th Aerospace Sciences Meeting and Exhibit, January 1992. AIAA Paper No. 92-0064.
- [62] Wheeler, G.O., "Means for Maintaining Attached Flow of a Flowing Medium," June 1984. United States Patent No. 4,455,045.
- [63] Howard, F.G., B.F. Quass, L.M. Weinstein and D.M. Bushnell. "Longitudinal Afterbody Grooves and Shoulder Radiusing for Low-Speed Bluff Body Drag Reduction." The American Society of Mechanical Engineers Winter Annual Meeting, Washington, DC, November 1981.
- [64] Walsh, M.J. "Riblets as a Viscous Drag Reduction Technique," *AIAA Journal*, 21(4):485-486 (April 1983).
- [65] Walsh, M.J. "Turbulent Boundary Layer Drag Reduction Using Riblets." AIAA 20th Aerospace Sciences Meeting, Orlando, FL, January 1982. AIAA Paper No. 82-0169.
- [66] Walsh, M.J. *Viscous Flow Drag Reduction*, volume 72 of *Progress in Astronautics and Aeronautics*, chapter Drag Characteristics of V-Groove and Transverse Curvature Riblets, pages 168-184. AIAA, 1980.
- [67] Bacher, E.V. and C.R. Smith. "Turbulent Boundary-Layer Modification by Surface Riblets," *AIAA Journal*, 24(8):1382-1385 (August 1986).
- [68] Bacher, E.V. and C.R. Smith. "A Combined Visualization-Anemometry Study of the Turbulent Drag Reducing Mechanisms of Triangular Micro-Groove Surface Modifications." AIAA Shear Flow Control Conference, Boulder, CO, March 1985. AIAA Paper No. 85-0548.
- [69] Gallagher, J.A. and A.S.W. Thomas. "Turbulent Boundary Layer Characteristics Over Streamwise Grooves." AIAA 2nd Applied Aerodynamics Conference, Seattle, WA, August

1984. AIAA Paper No. 84-2185.
- [70] Choi, H., P. Moin and J. Kim. "On the Effect of Riblets in Fully Developed Laminar Channel Flows," *Physics of Fluids*, 3(8):1892-1896 (August 1991).
- [71] Wieck, T.D. "Effect of Riblets on Flow Separation From a Cylinder and an Airfoil." MS thesis, Air Force Institute of Technology, December 1989.
- [72] Reagan, M.K. "Effect of Riblets on Pressure Recovery in a Straight-Walled Diffuser." MS thesis, Air Force Institute of Technology, December 1990.
- [73] Rothenflue, J.A. "Experimental Investigation Into the Effects of Riblets on Compressor Cascade Performance." MS thesis, Air Force Institute of Technology, December 1991.
- [74] Rothenflue, J.A. "Riblet Effects on Gortler Vortex Development Over a Concave Surface." PhD dissertation, Air Force Institute of Technology, February 1996.
- [75] Rothenflue, J.A. and P.I. King. "Vortex Development over Flat Plate Riblets in a Transitioning Boundary Layer," *AIAA Journal*, 33(8):1525-1526 (1995).
- [76] Barber, T.J., J.S. Mounts and D.C. McCormick. "Boundary Layer Energization by Means of Optimized Vortex Generators." 31st Aerospace Sciences Meeting and Exhibit, Reno, NV, January 1993. AIAA Paper No. 93-0445.
- [77] Maciejewski, P.K. and R.B. Rivir. "Effects of Surface Riblets and Free-Stream Turbulence on Heat Transfer in a Linear Turbine Cascade." International Gas Turbine and Aeroengine Congress and Exposition, The Hague, Netherlands, June 1994. ASME Paper No. 94-GT-245.
- [78] Radeztsky, R.H., M.S. Reibert, W.S. Saric and S. Takagi. "Effect of Micron-Sized Roughness on Transition in Swept-Wing Flows." 31st Aerospace Sciences Meeting and Exhibit, Reno, NV, January 1993. AIAA Paper No. 93-0076.
- [79] Bloch, D.R. and T.J. Mueller. "Effects of Distributed Grit Roughness on Separation and Transition on an Airfoil at Low Reynolds Numbers," pages 152-161 (1986). AIAA Paper No. 86-1788.
- [80] Williams, L.D. "Effects of Surface Roughness on Pressure Distribution and Boundary Layer Over Compressor Blades at High Reynolds Number in a Two-Dimensional Cascade." MS thesis, Air Force Institute of Technology, December 1985.
- [81] Braslow, A.L., R.M. Hicks and R.V. Harris. "Use of Grit-Type Boundary-Layer-Transition Trips." Conference on Aircraft Aerodynamics, May 1966. NASA TN D-3579.
- [82] Bragg, M., M. Kerho and M. Cummings. "Airfoil Boundary Layer Due to Large Leading-Edge Roughness." 33rd Aerospace Sciences Meeting and Exhibit, Reno, NV, January 1995. AIAA Paper No. 95-0536.
- [83] Achenbach, E. "The Effects of Surface Roughness and Tunnel Blockage on the Flow Past Spheres," *Journal of Fluid Mechanics*, 65(part 1):113-125 (1974).
- [84] Crawford, M.E. and W.M. Kays. "STAN-5: A Program for Numerical Computation of Two-Dimensional Internal and External Boundary Layer Flows." Technical Report, 1976. NASA CR 2742.

# APPENDIX A - Boundary Layer Measurements for Blade with Dimples

## A.1 Velocity and Turbulence Measurements at $Re = 50k$ and $Re = 100k$

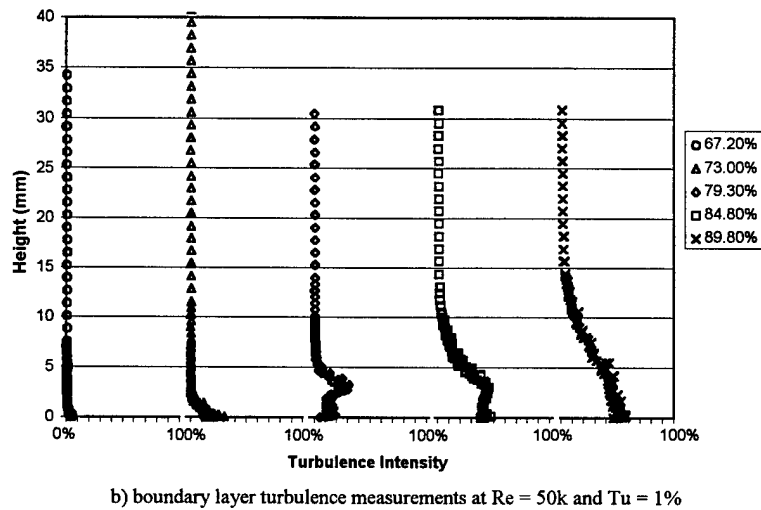
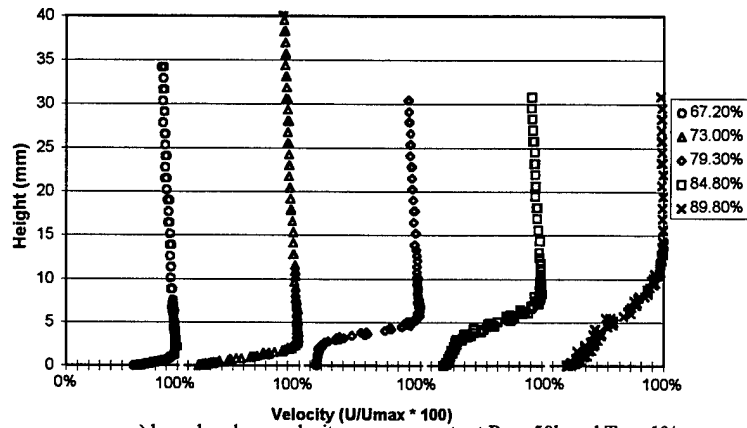


Figure 98. Measured velocity and turbulence profiles between dimples at 50%.

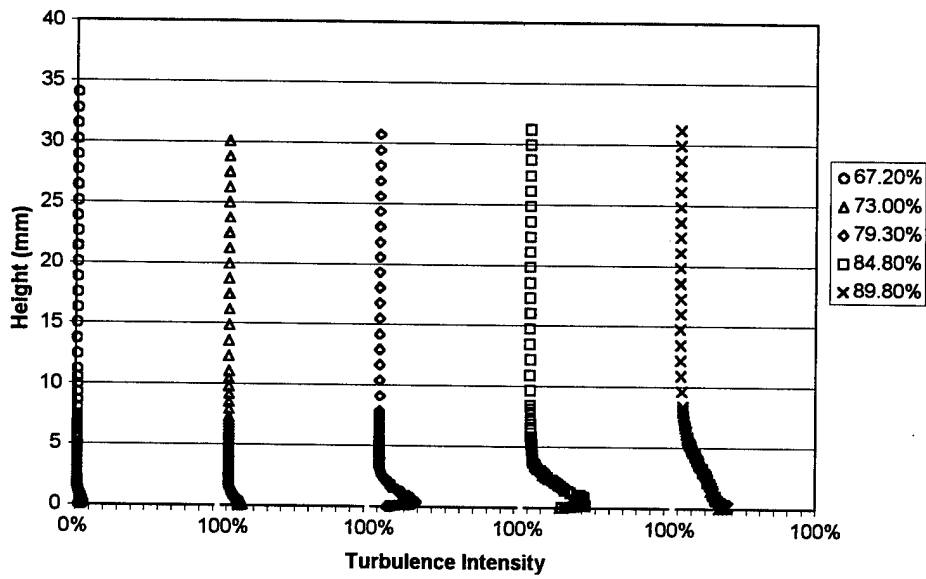
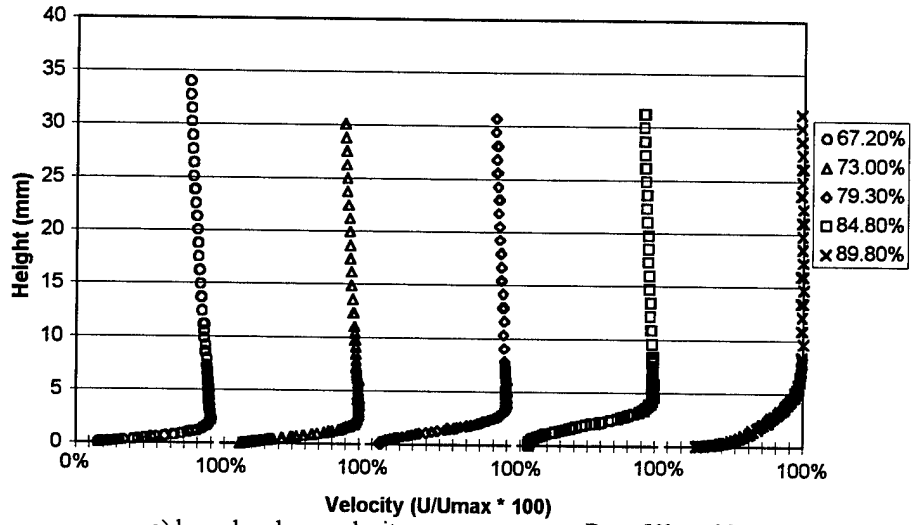
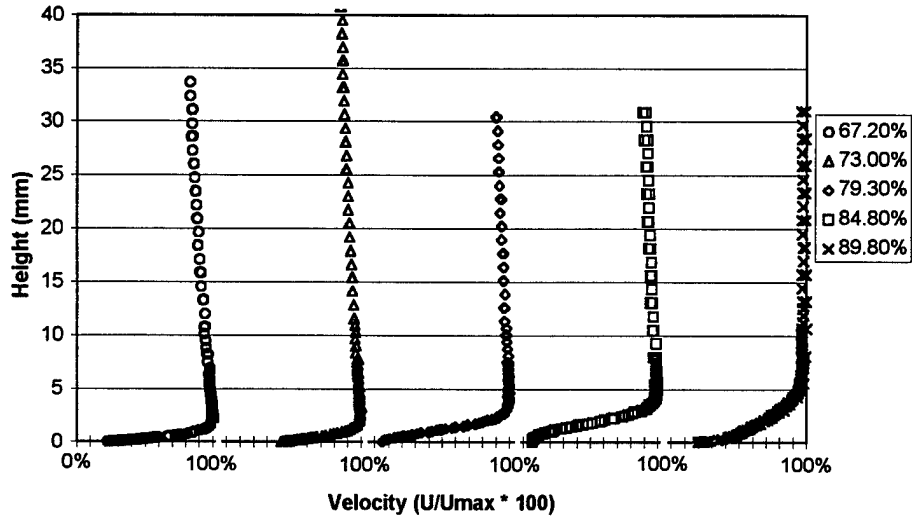
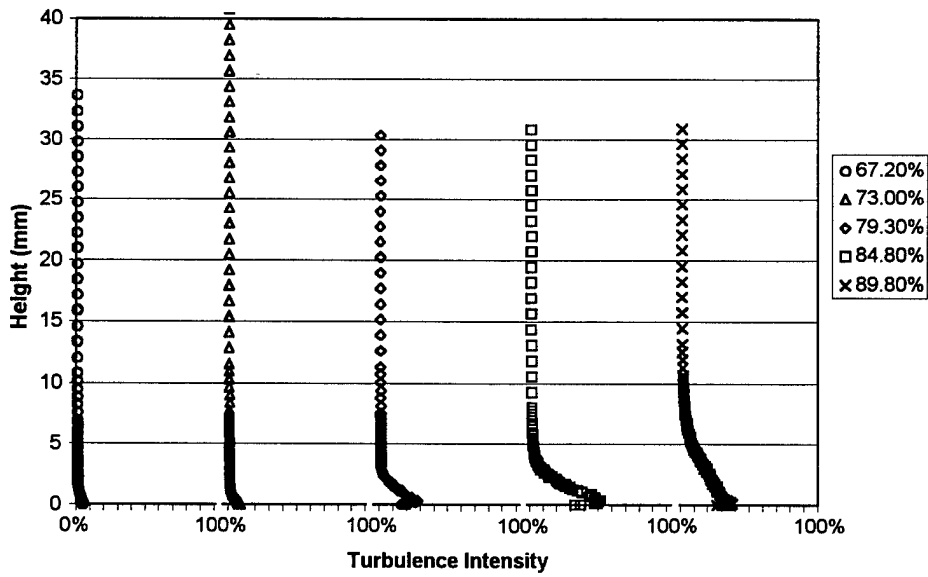


Figure 99. Measured velocity and turbulence profiles behind a dimple at 50% with  $Tu = 4\%$ .

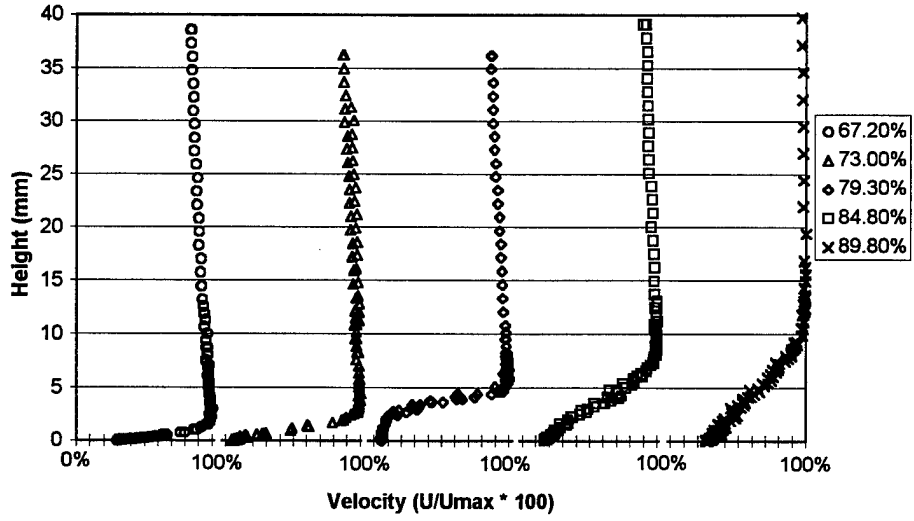


a) boundary layer velocity measurements at  $Re = 50k$  and  $Tu = 4\%$

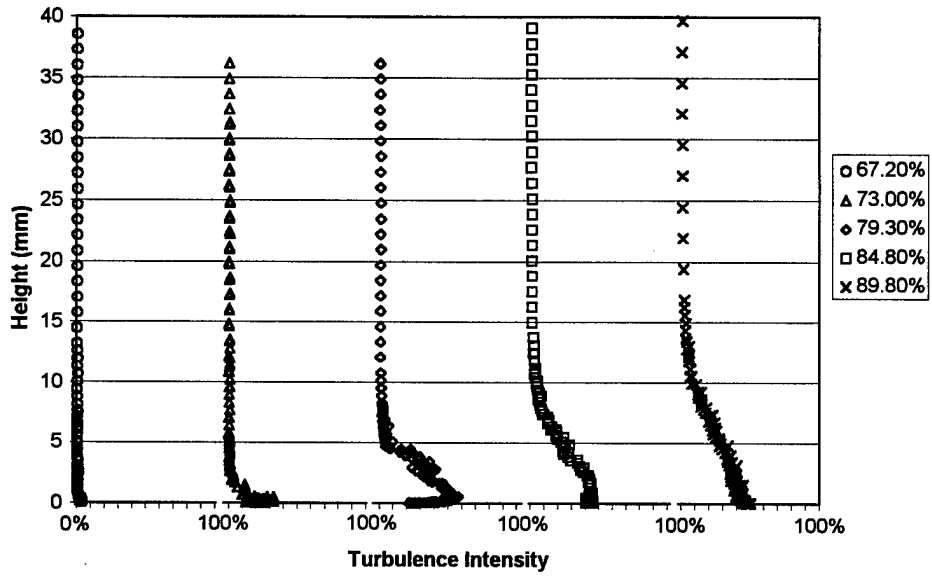


b) boundary layer turbulence measurements at  $Re = 50k$  and  $Tu = 4\%$

Figure 100. Measured velocity and turbulence profiles between dimples at 50% with  $Tu = 4\%$ .

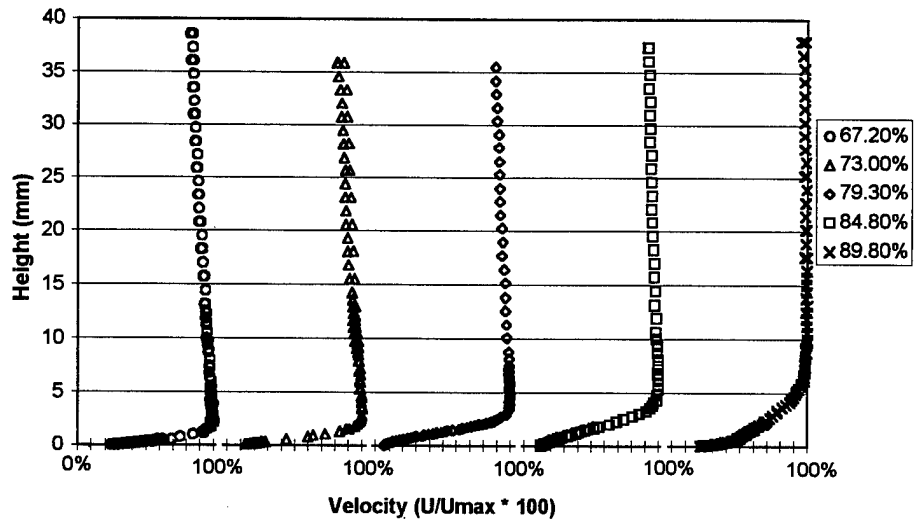


a) boundary layer measurements at  $Re = 50k$  and  $Tu = 1\%$

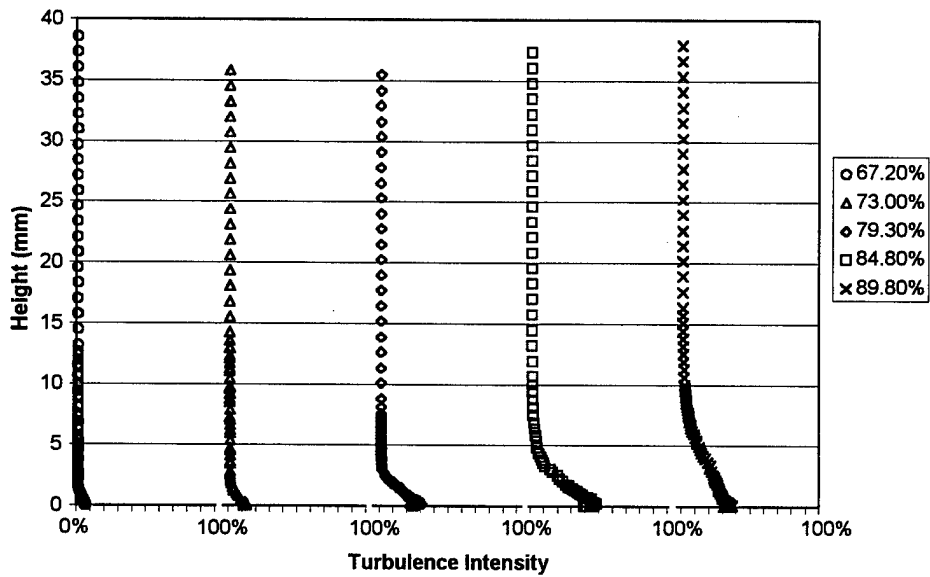


b) boundary layer measurements at  $Re = 50k$  and  $Tu = 1\%$

Figure 101. Measured velocity and turbulence profiles between dimples at 55%.

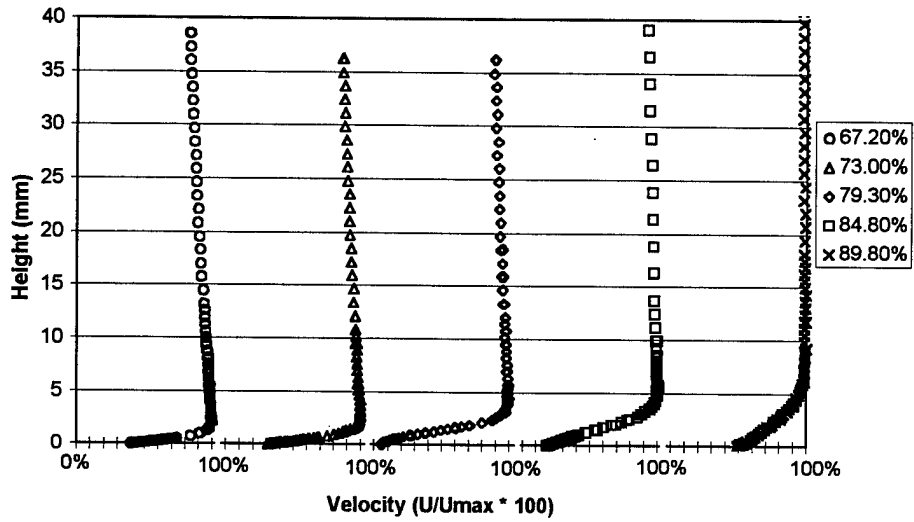


a) boundary layer measurements at  $Re = 50k$  and  $Tu = 4\%$

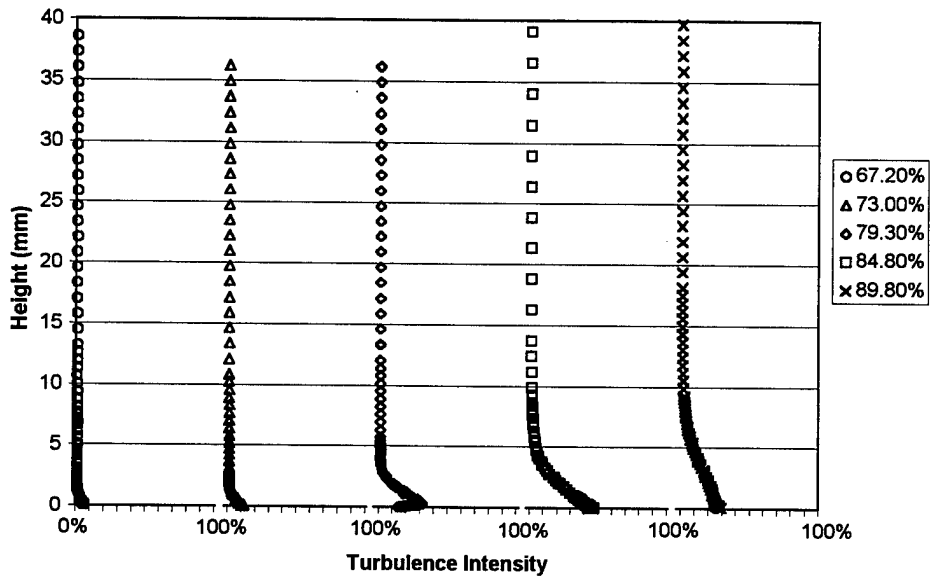


b) boundary layer measurements at  $Re = 50k$  and  $Tu = 4\%$

Figure 102. Measured velocity and turbulence profiles behind a dimple at 55% with  $Tu = 4\%$ .

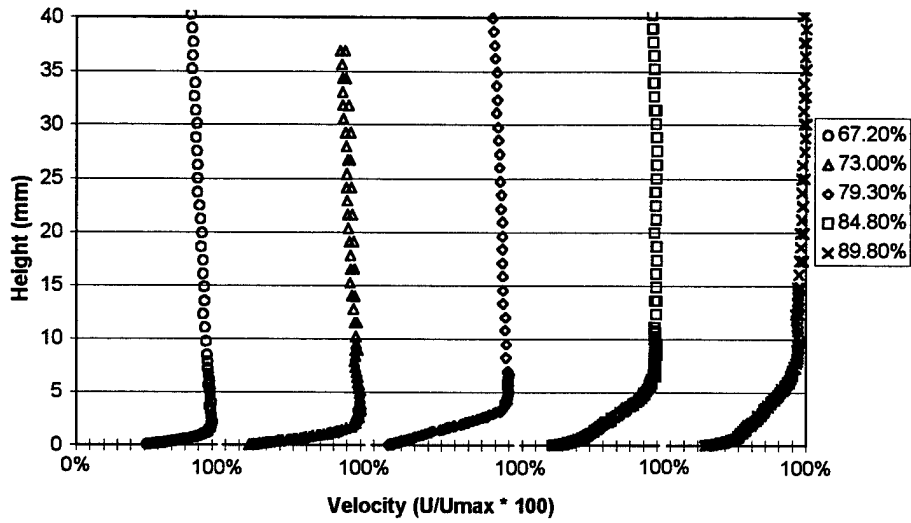


a) boundary layer measurements at  $Re = 50k$  and  $Tu = 4\%$

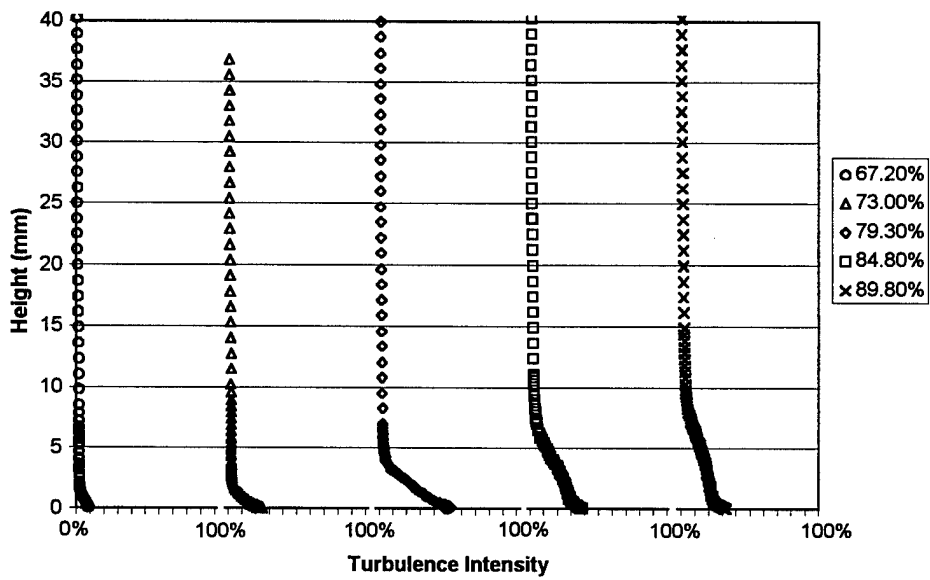


b) boundary layer measurements at  $Re = 50k$  and  $Tu = 4\%$

Figure 103. Measured velocity and turbulence profiles between dimples at 55% with  $Tu = 4\%$ .

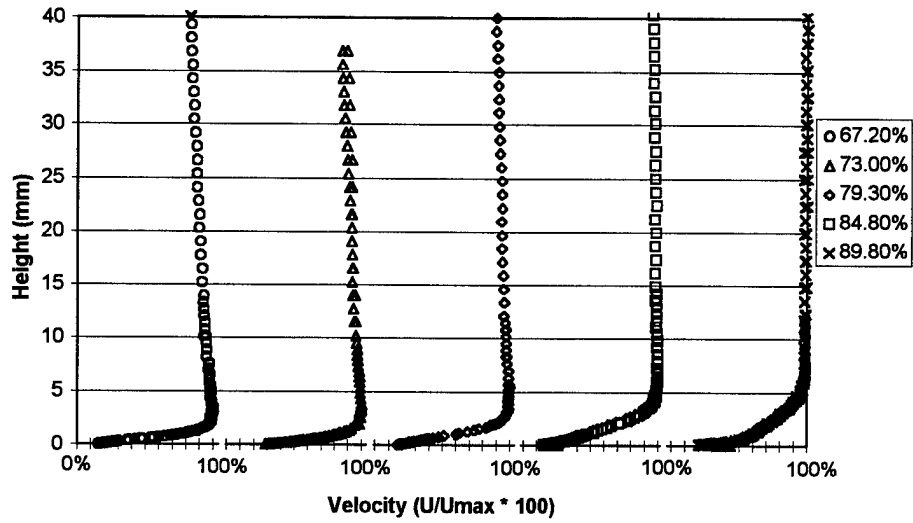


a) boundary layer velocity measurements at  $Re = 50k$  and  $Tu = 1\%$

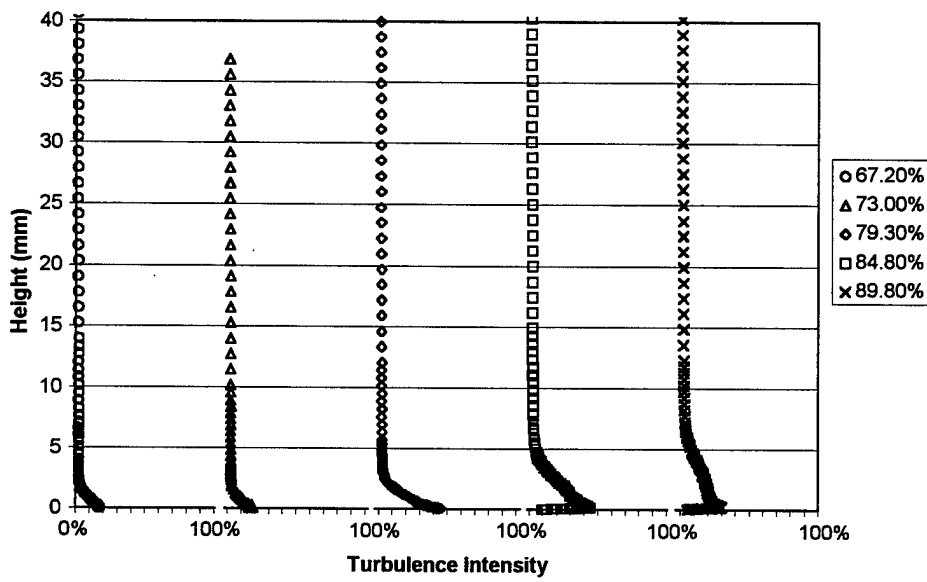


b) boundary layer turbulence measurements at  $Re = 50k$  and  $Tu = 1\%$

Figure 104. Measured velocity and turbulence profiles between dimples at 65%.

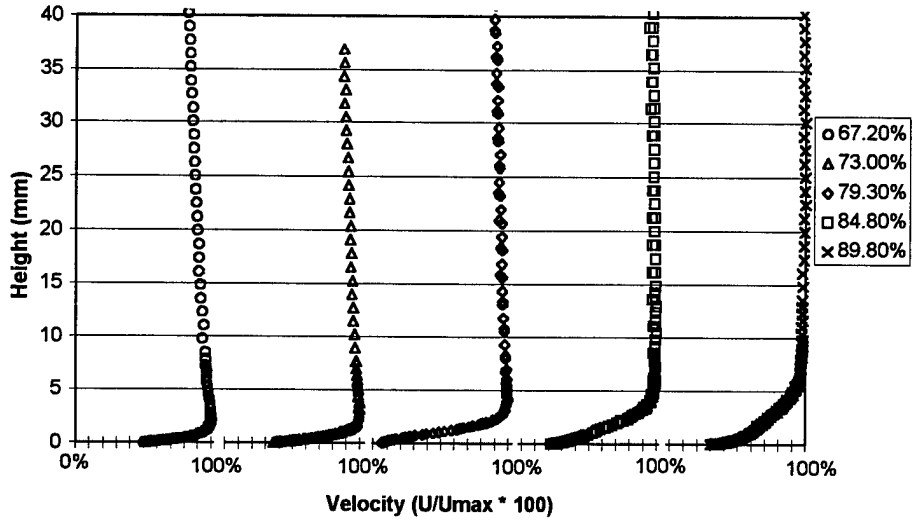


a) boundary layer velocity measurements at  $Re = 50k$  and  $Tu = 4\%$

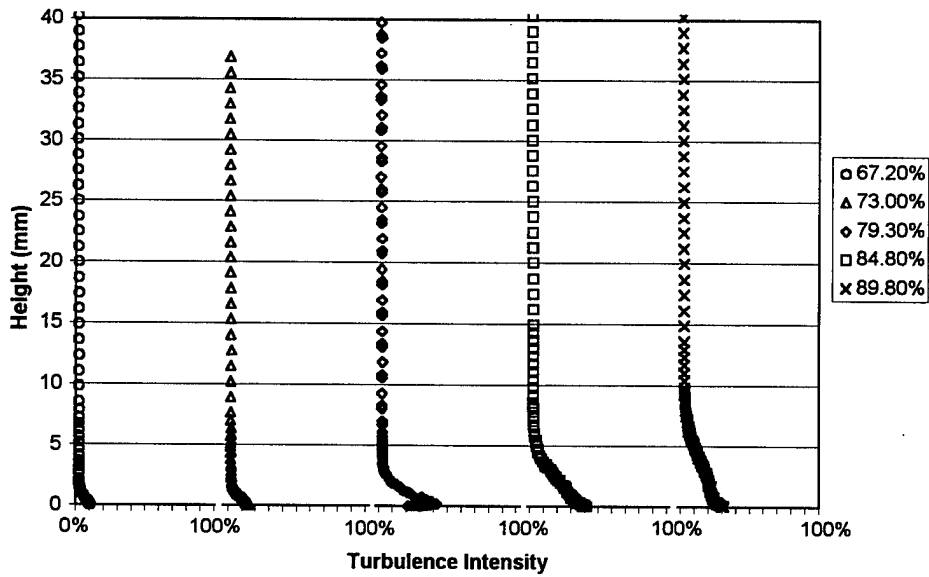


b) boundary layer turbulence measurements at  $Re = 50k$  and  $Tu = 4\%$

Figure 105. Measured velocity and turbulence profiles behind a dimple at 65% with  $Tu = 4\%$ .

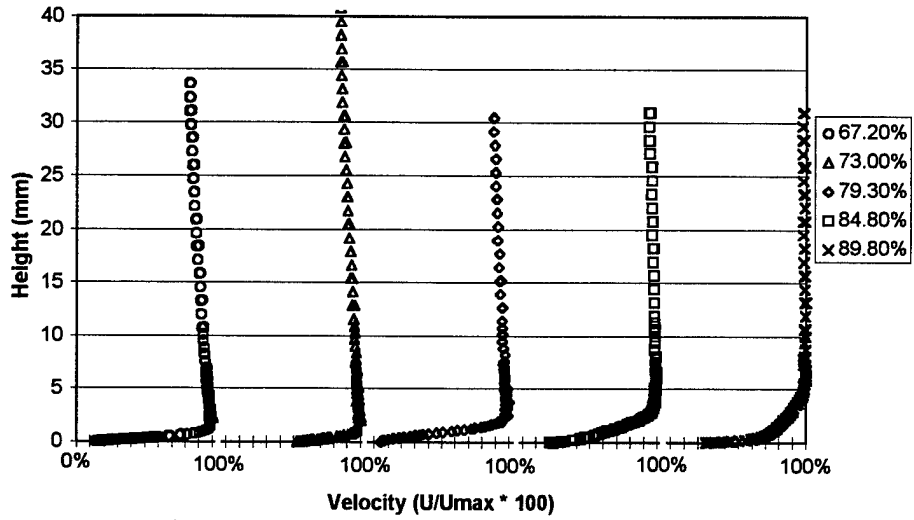


a) boundary layer velocity measurements at  $Re = 50k$  and  $Tu = 4\%$

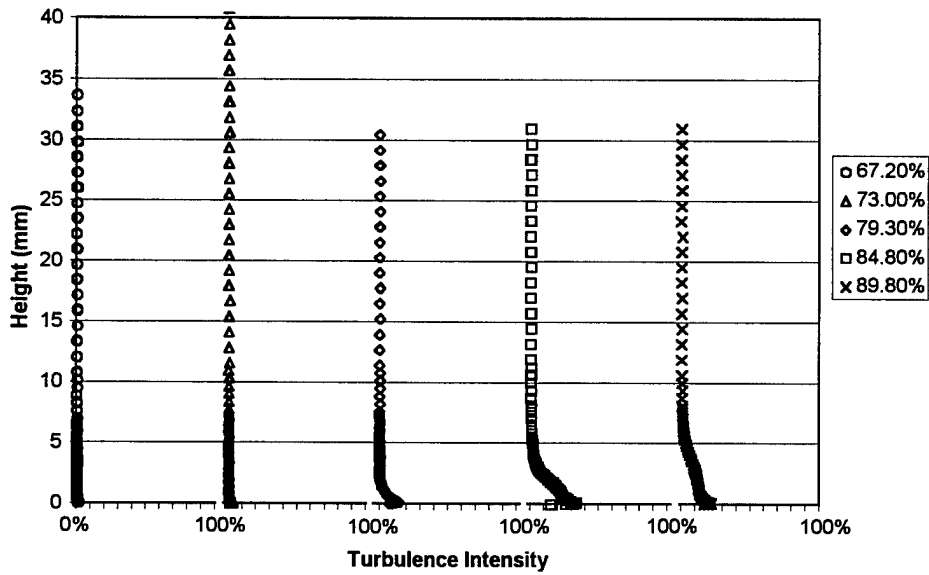


b) boundary layer turbulence measurements at  $Re = 50k$  and  $Tu = 4\%$

Figure 106. Measured velocity and turbulence profiles between dimples at 65% with  $Tu = 4\%$ .

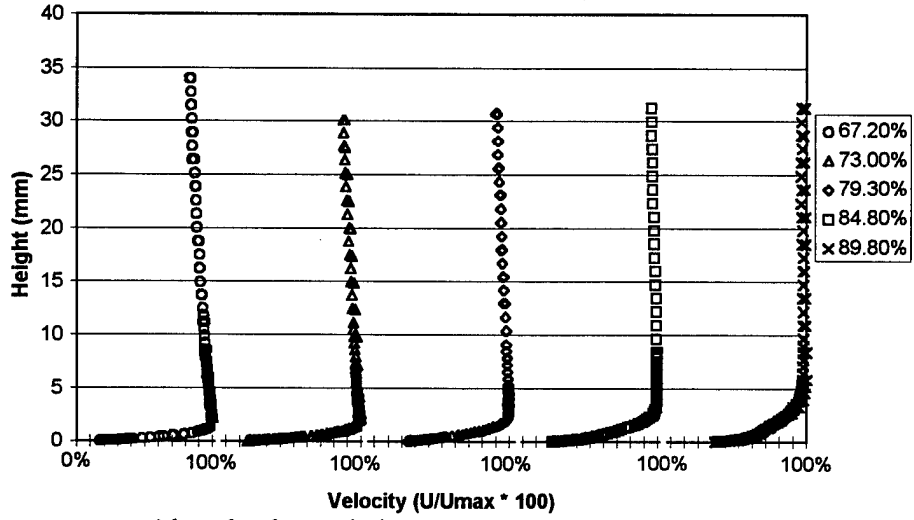


a) boundary layer velocity measurements at  $Re = 100k$  and  $Tu = 1\%$

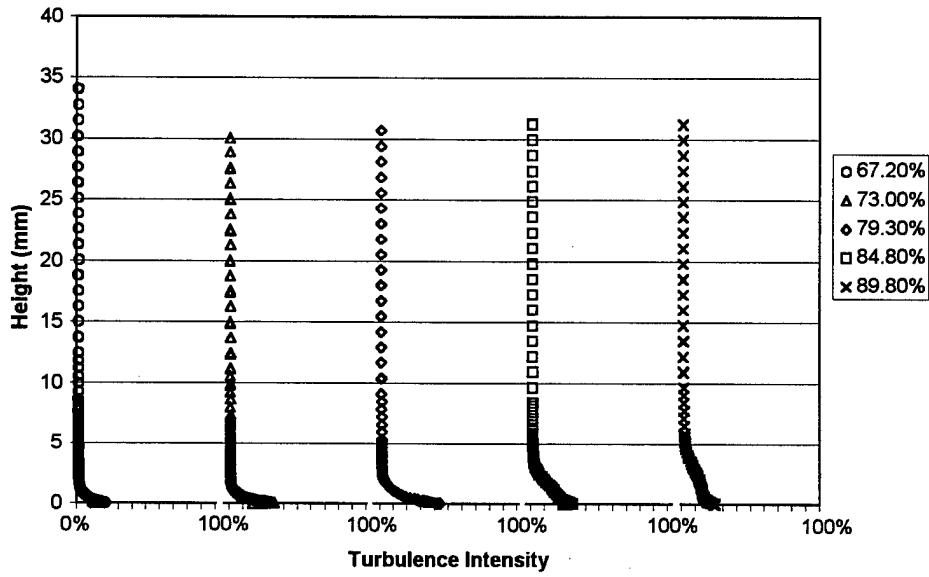


b) boundary layer turbulence measurements at  $Re = 100k$  and  $Tu = 1\%$

Figure 107. Measured velocity and turbulence profiles between dimples at 50%.

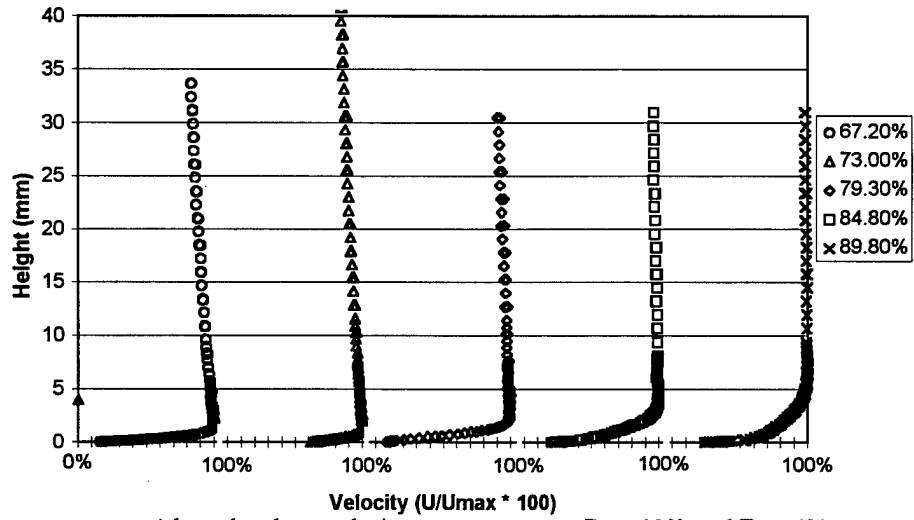


a) boundary layer velocity measurements at  $Re = 100k$  and  $Tu = 4\%$

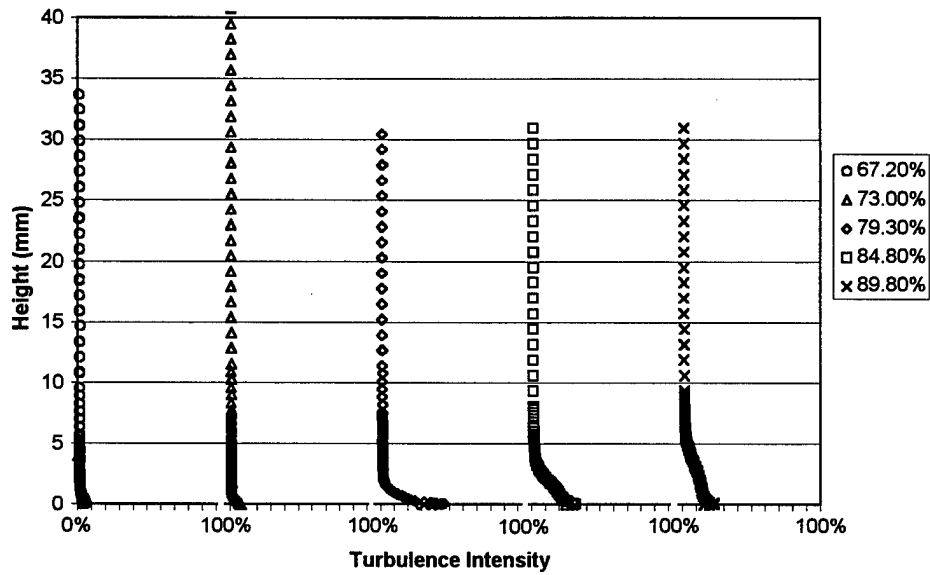


b) boundary layer turbulence measurements at  $Re = 100k$  and  $Tu = 4\%$

Figure 108. Measured velocity and turbulence profiles behind a dimple at 50% with  $Tu = 4\%$ .

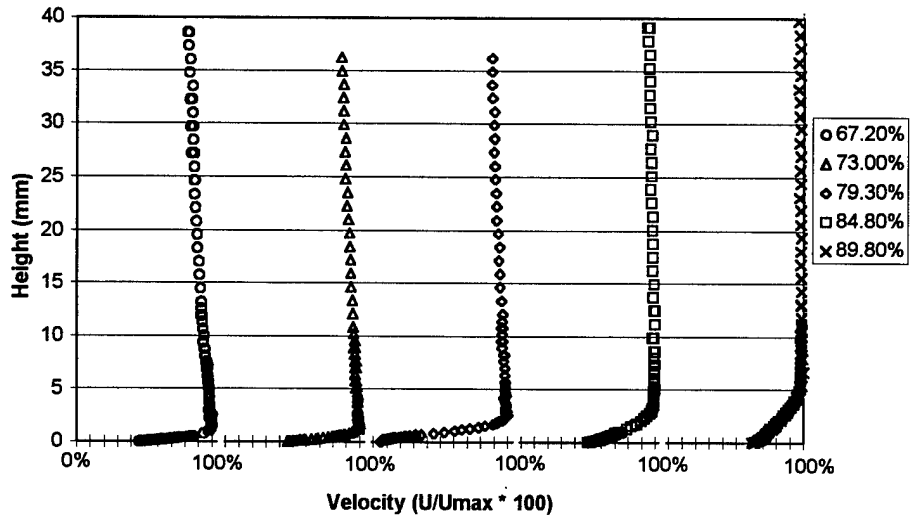


a) boundary layer velocity measurements at  $Re = 100k$  and  $Tu = 4\%$

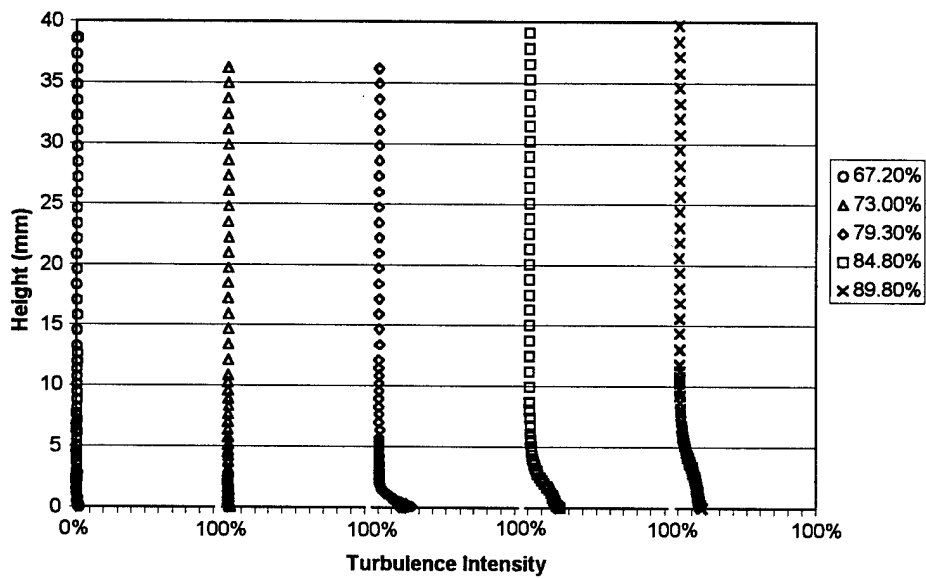


b) boundary layer turbulence measurements at  $Re = 100k$  and  $Tu = 4\%$

Figure 109. Measured velocity and turbulence profiles between dimples at 50% with  $Tu = 4\%$ .

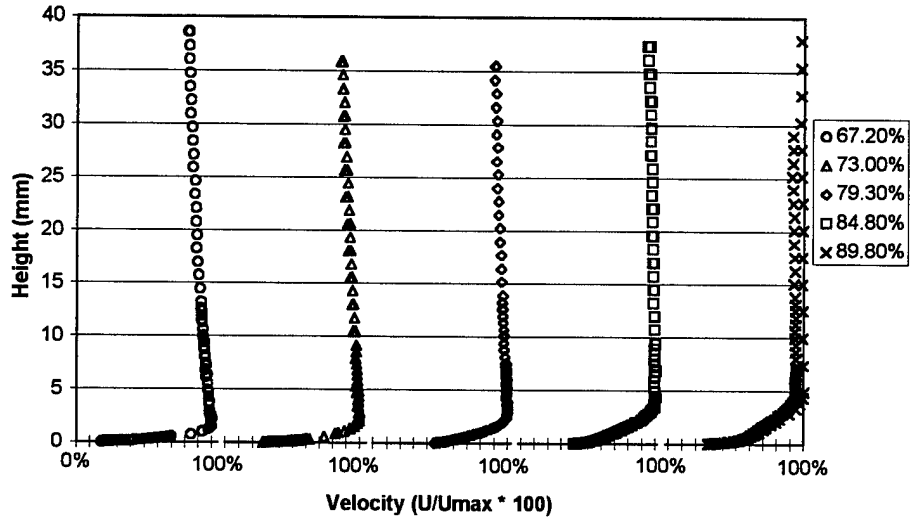


a) boundary layer at  $Re = 100k$  and  $Tu = 1\%$

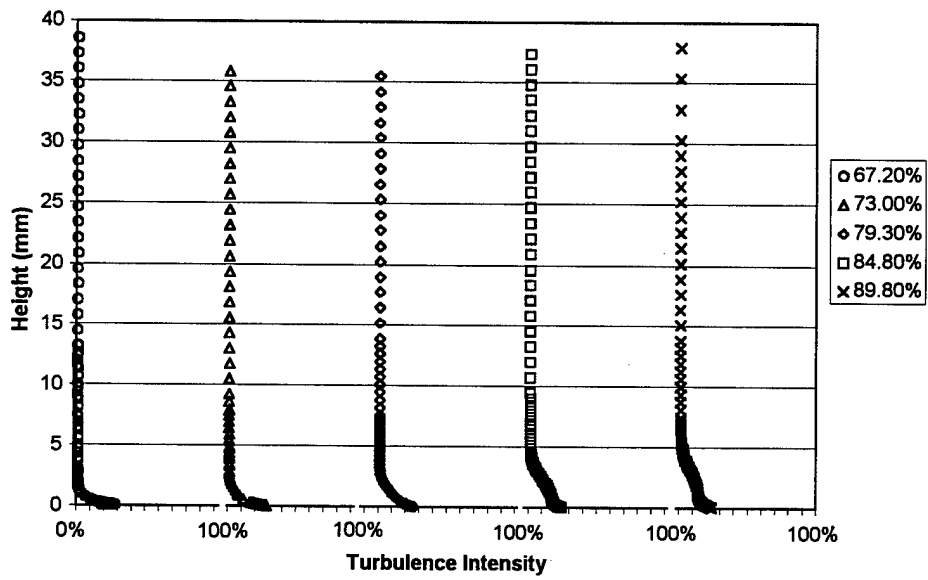


b) boundary layer at  $Re = 100k$  and  $Tu = 1\%$

Figure 110. Measured velocity and turbulence profiles between dimples at 55%.

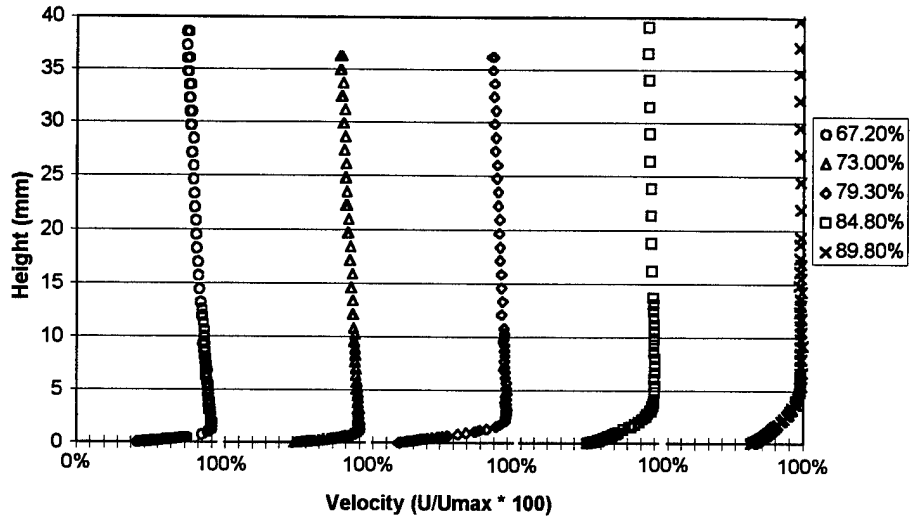


a) boundary layer at  $Re = 100k$  and  $Tu = 4\%$

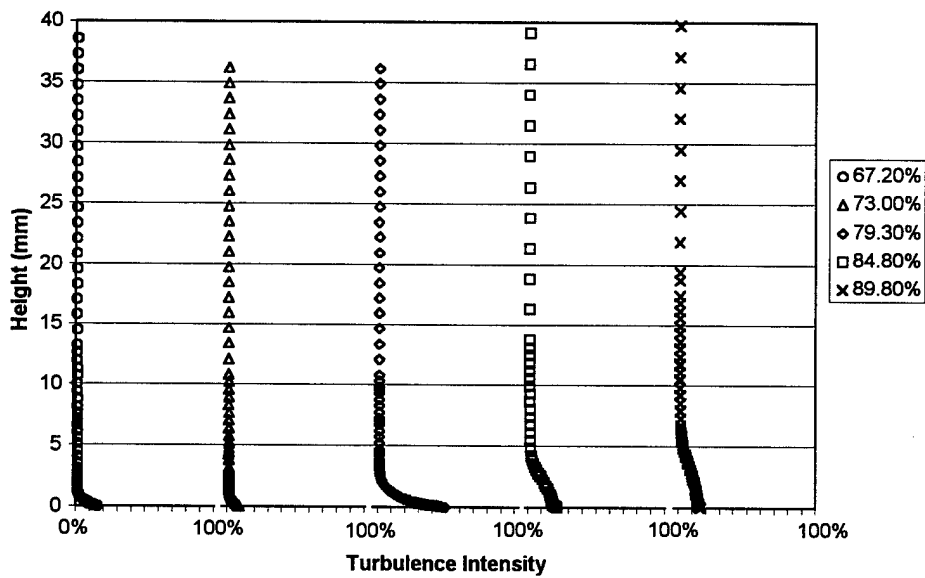


b) boundary layer at  $Re = 100k$  and  $Tu = 4\%$

Figure 111. Measured velocity and turbulence profiles behind a dimple at 55% with  $Tu = 4\%$ .

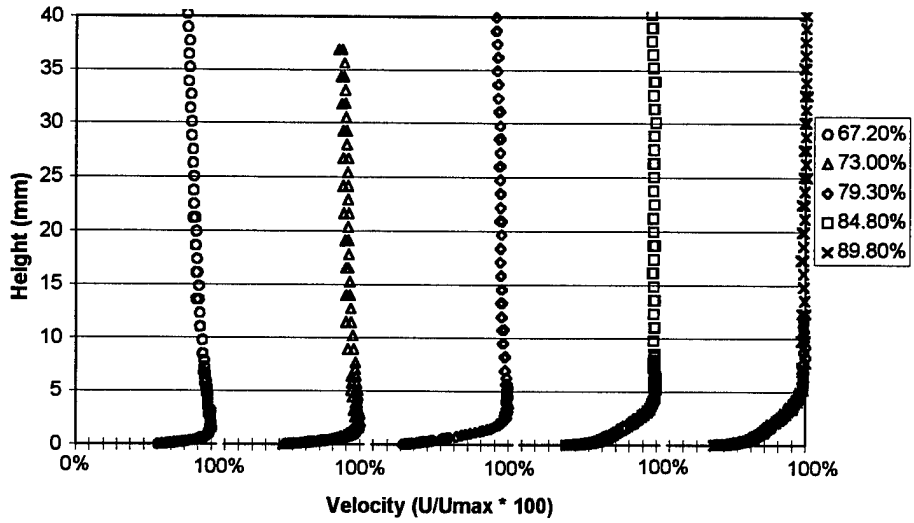


a) boundary layer at  $Re = 100k$  and  $Tu = 4\%$

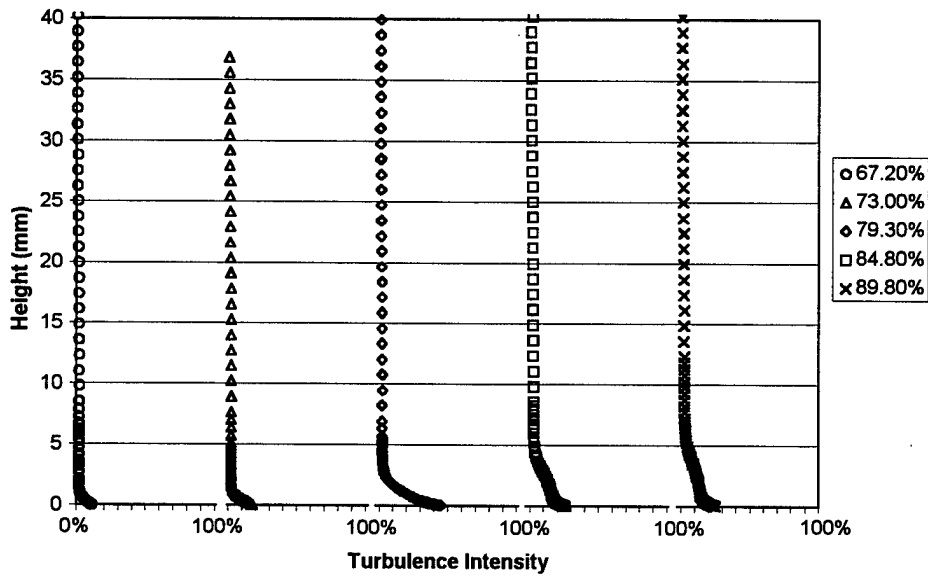


b) boundary layer at  $Re = 100k$  and  $Tu = 4\%$

Figure 112. Measured velocity and turbulence profiles between dimples at 55% with  $Tu = 4\%$ .

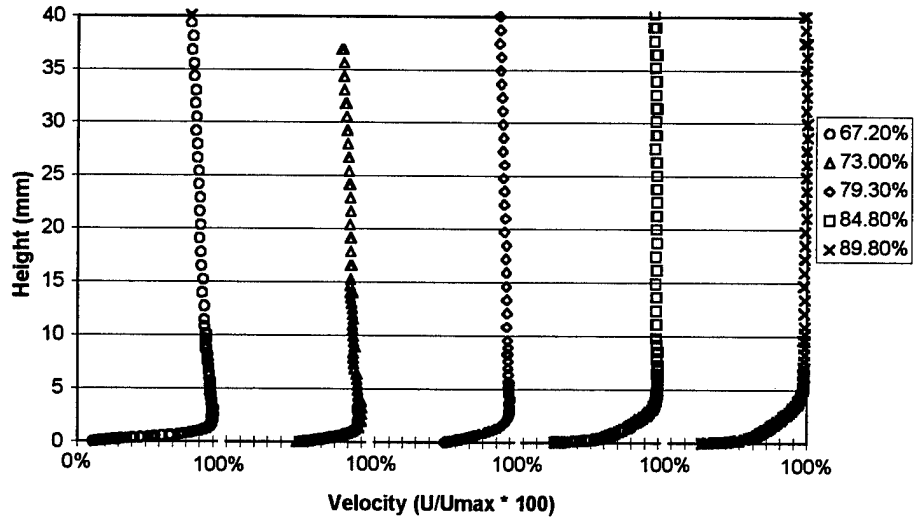


a) boundary layer velocity measurements at  $Re = 100k$  and  $Tu = 1\%$

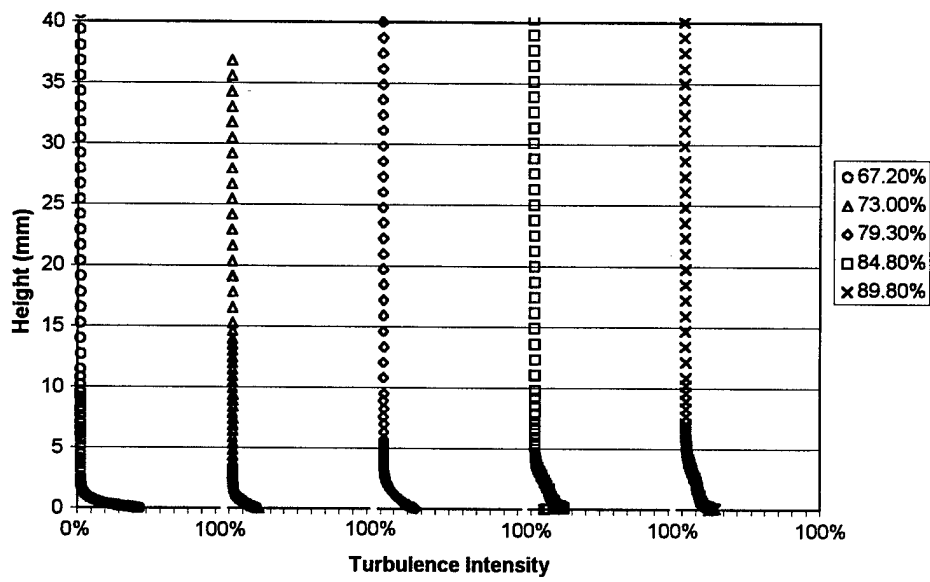


b) boundary layer velocity measurements at  $Re = 100k$  and  $Tu = 1\%$

Figure 113. Measured velocity and turbulence profiles between dimples at 65%.

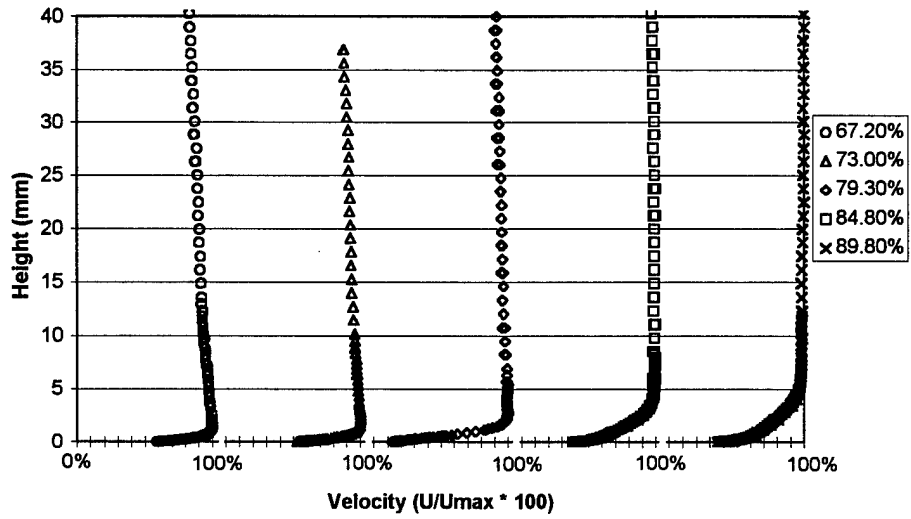


a) boundary layer velocity measurements at  $Re = 100k$  and  $Tu = 1\%$

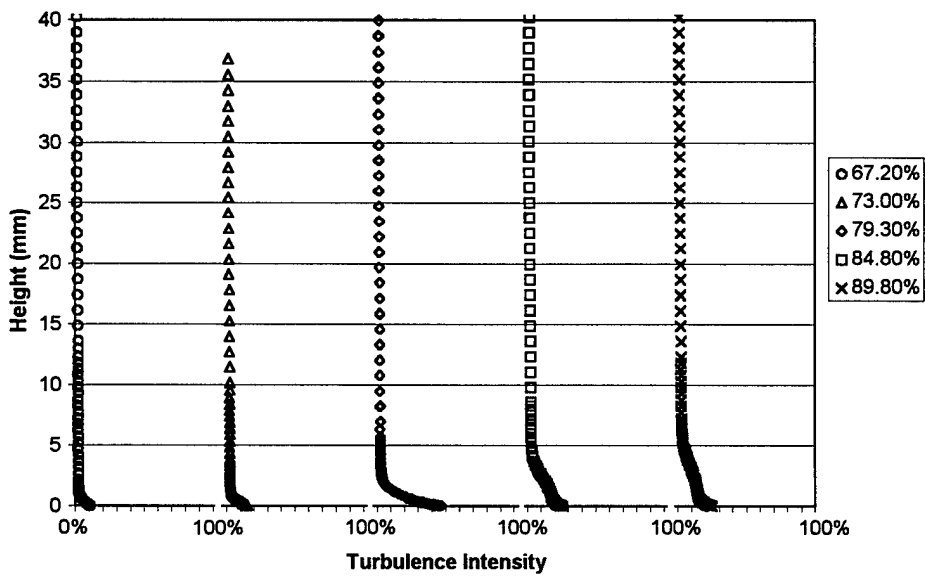


b) boundary layer velocity measurements at  $Re = 100k$  and  $Tu = 4\%$

Figure 114. Measured velocity and turbulence profiles behind a dimple at 65% with  $Tu = 4\%$ .



a) boundary layer velocity measurements at  $Re = 100k$  and  $Tu = 4\%$



b) boundary layer turbulence measurements at  $Re = 100k$  and  $Tu = 4\%$

Figure 115. Measured velocity and turbulence profiles between dimples at 65% with  $Tu = 4\%$ .

# APPENDIX B - Boundary Layer Measurements for Blade with V-Grooves

## B.1 Velocity and Turbulence Measurements at Re = 50k and Re = 100k

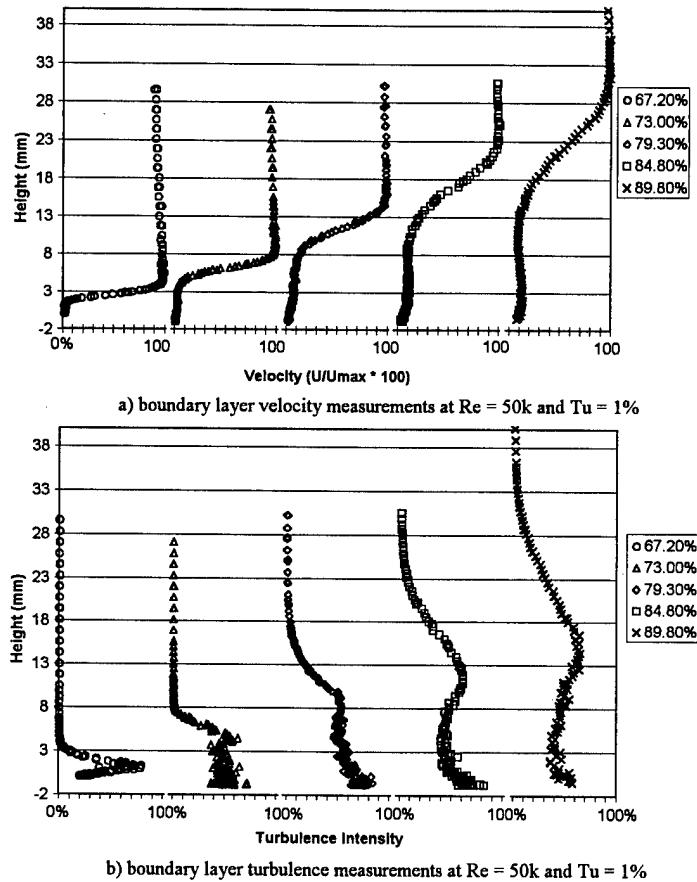
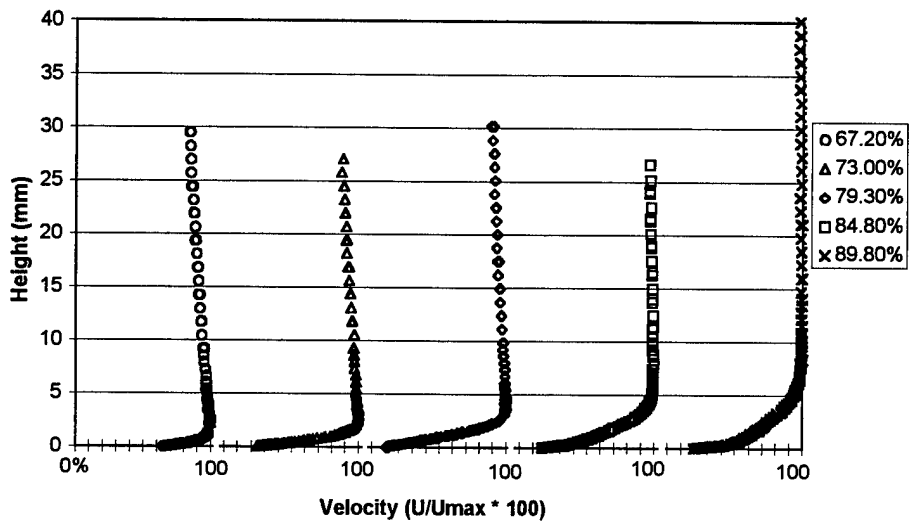
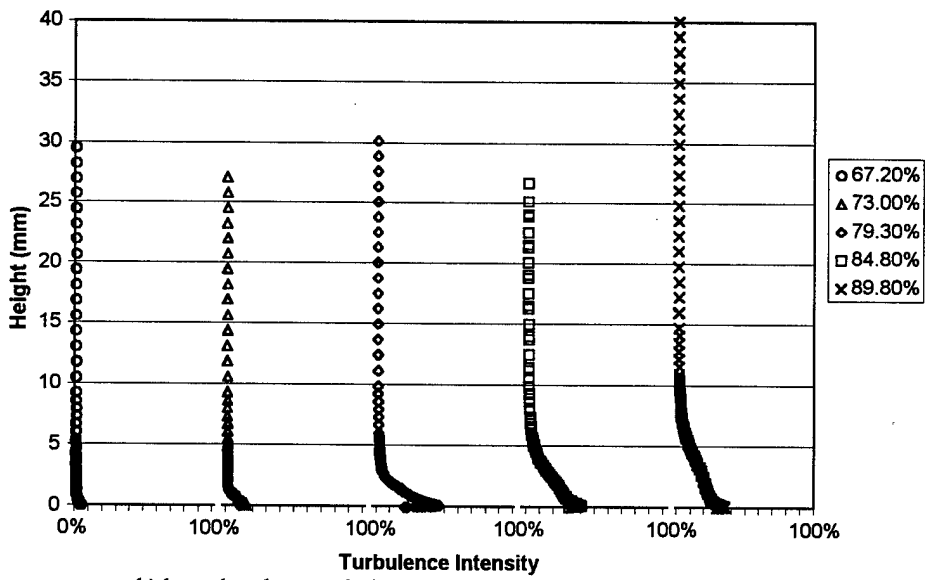


Figure 116. Measured velocity and turbulence profiles inside a V-groove starting at 55%.

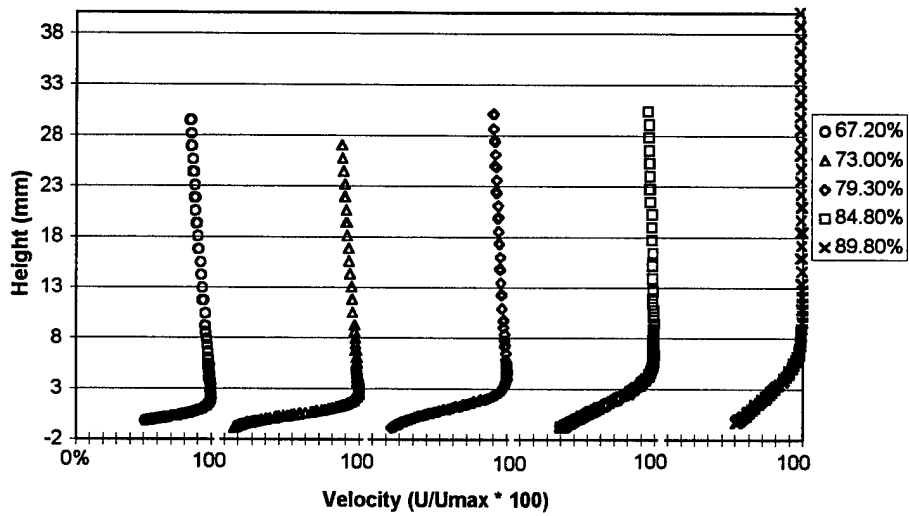


a) boundary layer velocity measurements at  $Re = 50k$  and  $Tu = 4\%$

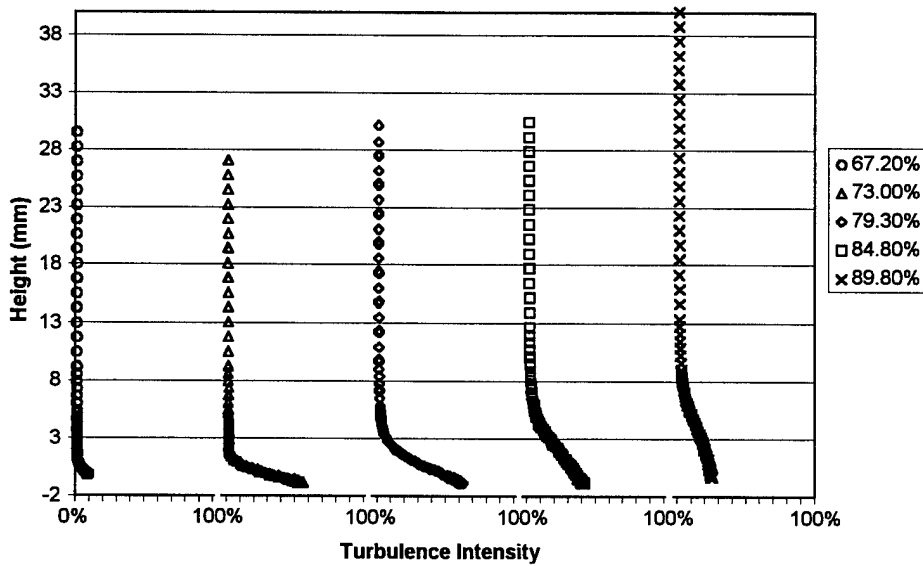


b) boundary layer turbulence measurements at  $Re = 50k$  and  $Tu = 4\%$

Figure 117. Measured velocity and turbulence profiles between V-grooves starting at 55% with  $Tu = 4\%$ .

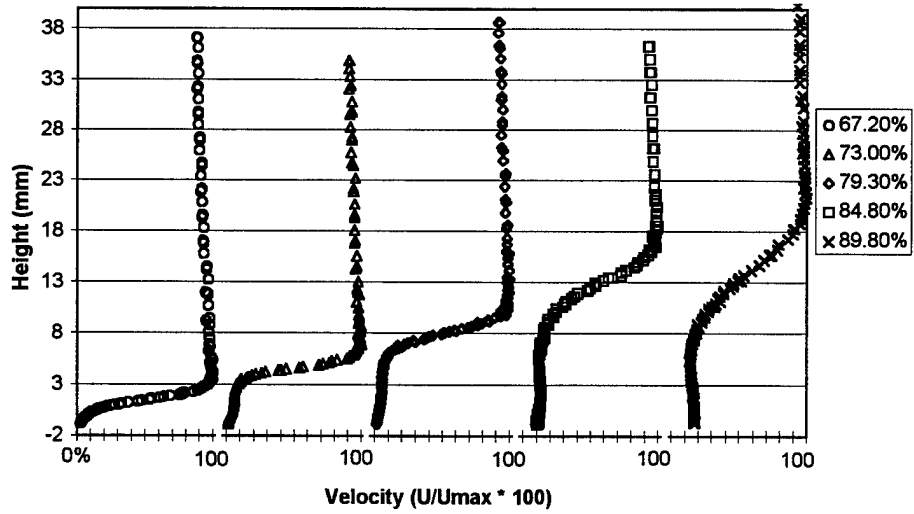


a) boundary layer velocity measurements at  $Re = 50k$  and  $Tu = 4\%$

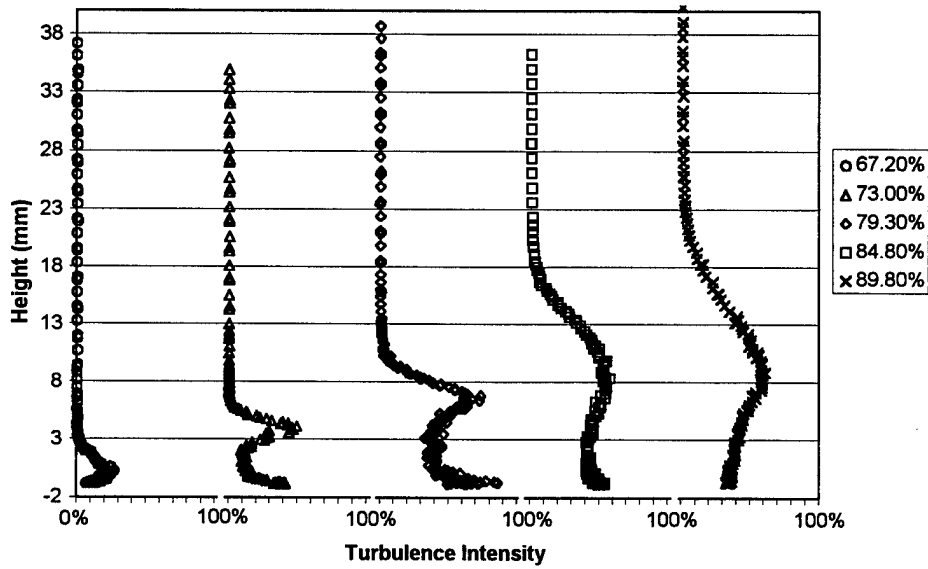


b) boundary layer turbulence measurements at  $Re = 50k$  and  $Tu = 4\%$

Figure 118. Measured velocity and turbulence profiles inside a V-groove starting at 55% with  $Tu = 4\%$ .

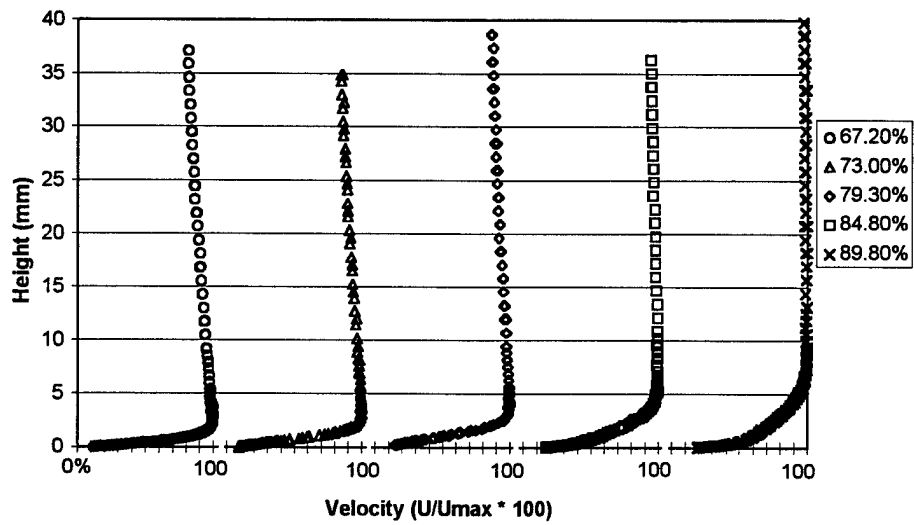


a) boundary layer velocity measurements at  $Re = 50k$  and  $Tu = 1\%$

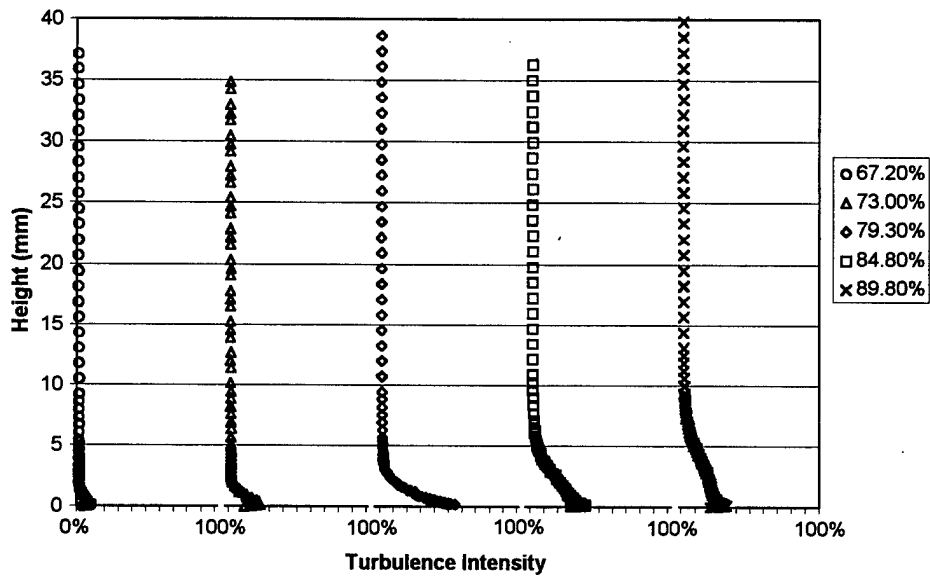


a) boundary layer velocity measurements at  $Re = 50k$  and  $Tu = 1\%$

Figure 119. Measured velocity and turbulence profiles inside a V-groove starting at 60%.

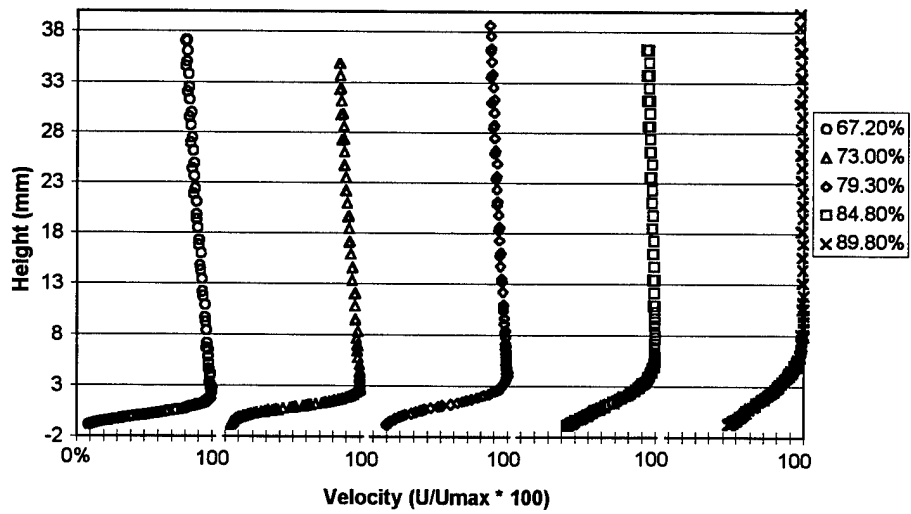


a) boundary layer velocity measurements at  $Re = 50k$  and  $Tu = 4\%$

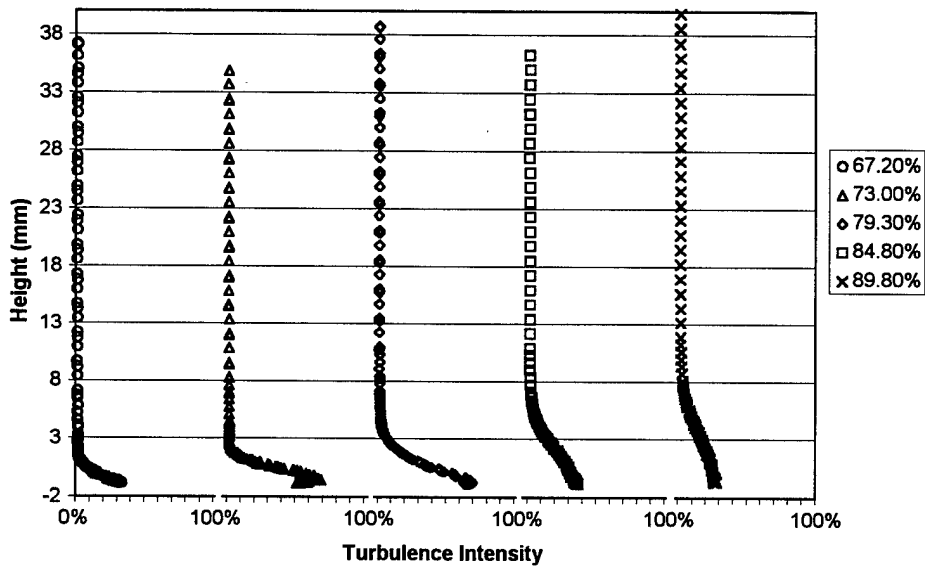


b) boundary layer turbulence measurements at  $Re = 50k$  and  $Tu = 4\%$

Figure 120. Measured velocity and turbulence profiles between V-grooves starting at 60% with  $Tu = 4\%$ .

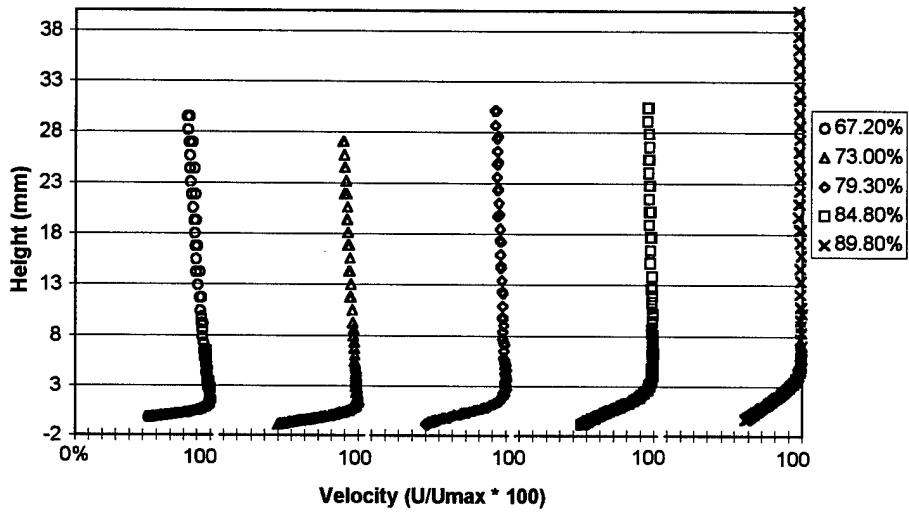


a) boundary layer velocity measurements at  $Re = 50k$  and  $Tu = 4\%$

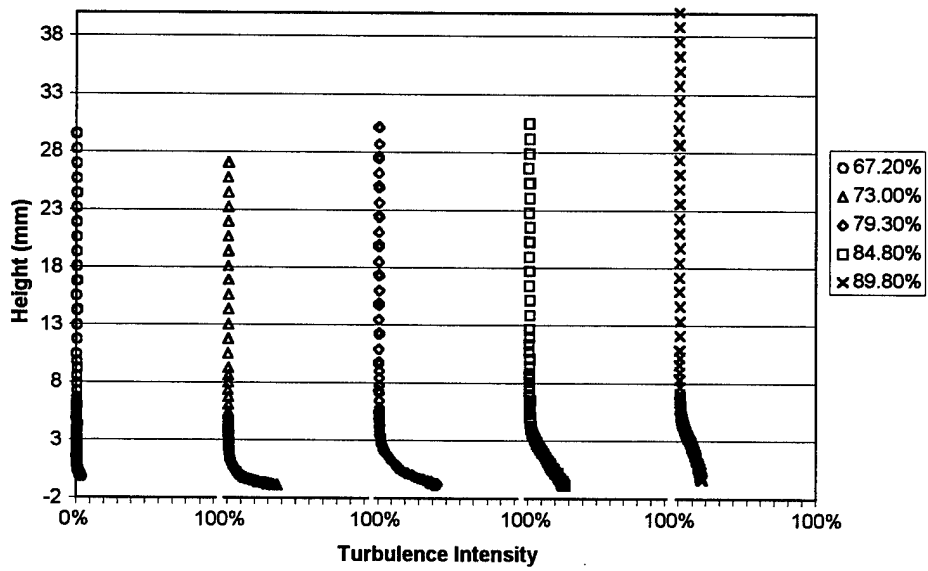


b) boundary layer turbulence measurements at  $Re = 50k$  and  $Tu = 4\%$

Figure 121. Measured velocity and turbulence profiles inside a V-groove starting at 60% with  $Tu = 4\%$ .

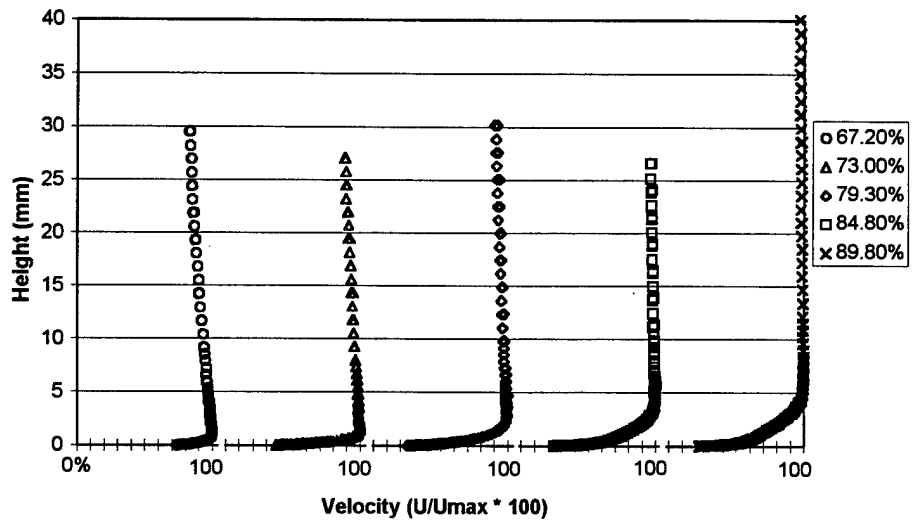


a) boundary layer velocity measurements at  $Re = 100k$  and  $Tu = 1\%$

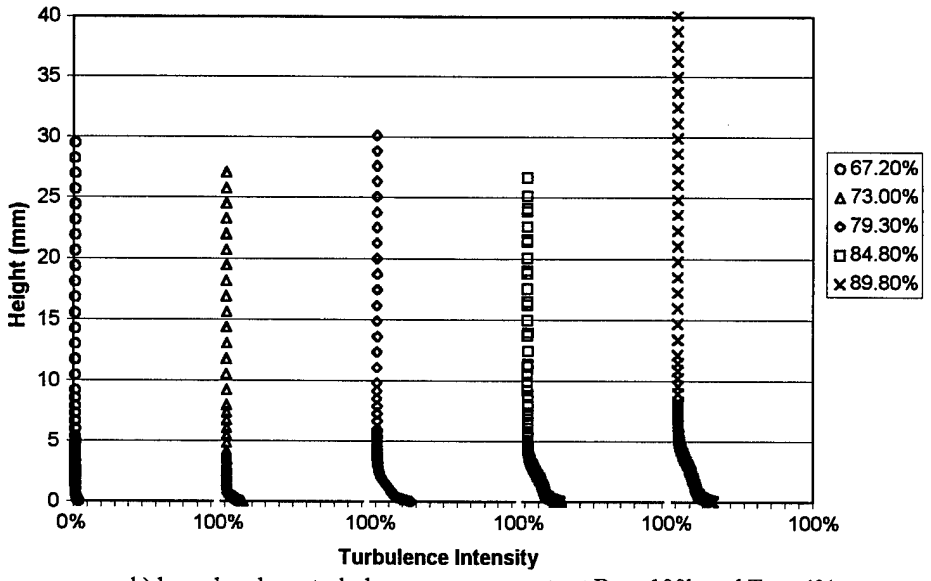


b) boundary layer turbulence measurements at  $Re = 100k$  and  $Tu = 1\%$

Figure 122. Measured velocity and turbulence profiles inside a V-groove starting at 55%.

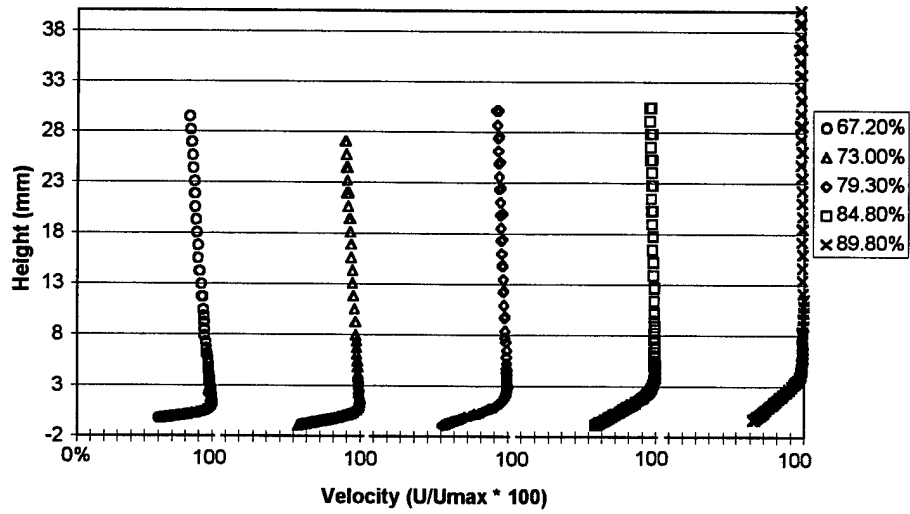


a) boundary layer velocity measurements at  $Re = 100k$  and  $Tu = 4\%$

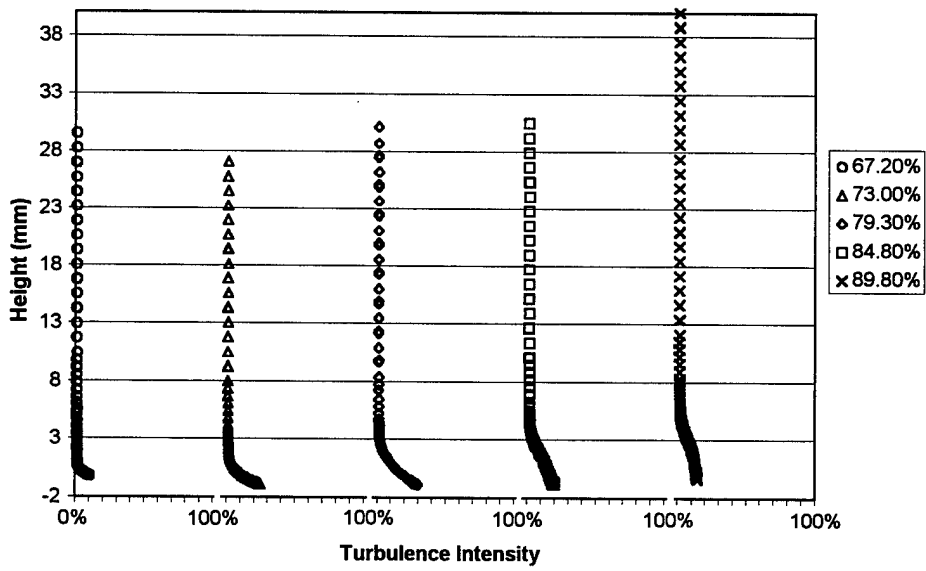


b) boundary layer turbulence measurements at  $Re = 100k$  and  $Tu = 4\%$

Figure 123. Measured velocity and turbulence profiles between V-grooves starting at 55% with  $Tu = 4\%$ .

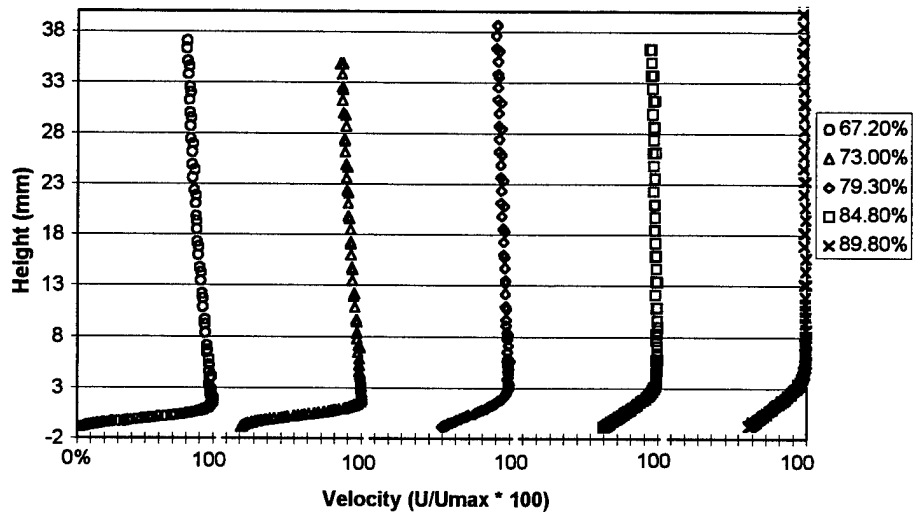


a) boundary layer velocity measurements at  $Re = 100k$  and  $Tu = 4\%$

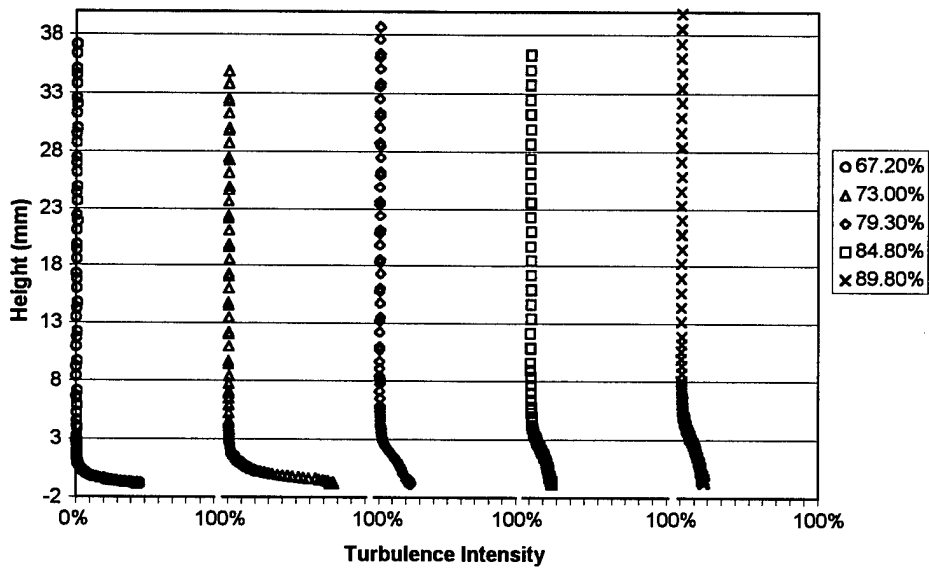


b) boundary layer turbulence measurements at  $Re = 100k$  and  $Tu = 4\%$

Figure 124. Measured velocity and turbulence profiles inside a V-groove starting at 55% with  $Tu = 4\%$ .

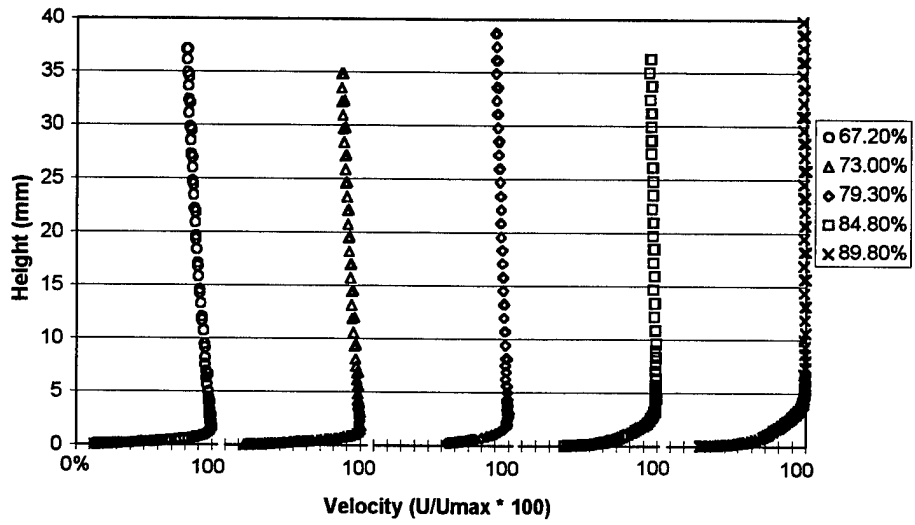


a) boundary layer velocity measurements at  $Re = 100k$  and  $Tu = 1\%$

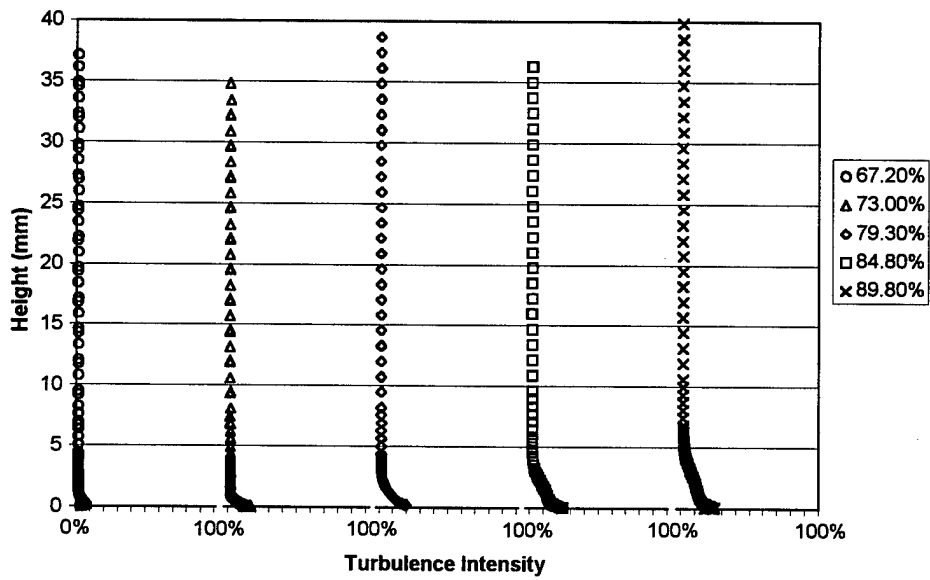


b) boundary layer turbulence measurements at  $Re = 100k$  and  $Tu = 1\%$

Figure 125. Measured velocity and turbulence profiles inside a V-groove starting at 60%.

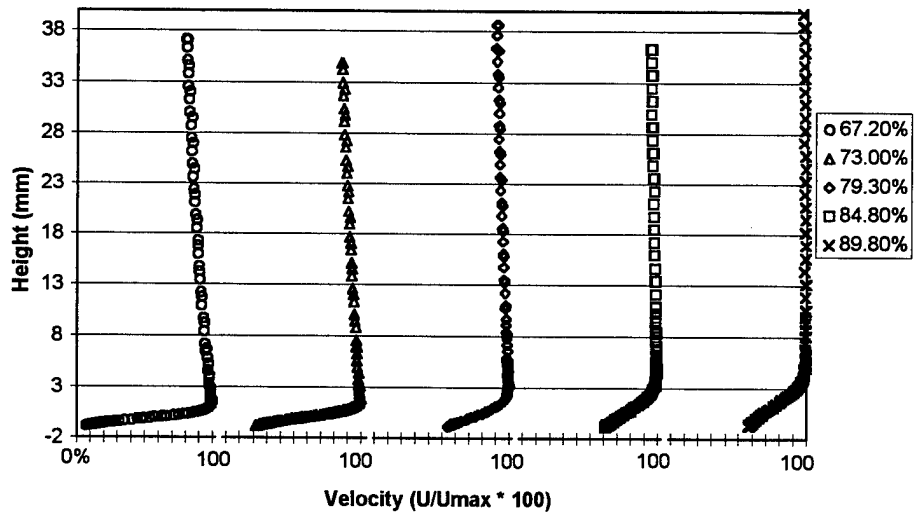


a) boundary layer velocity measurements at  $Re = 100k$  and  $Tu = 4\%$

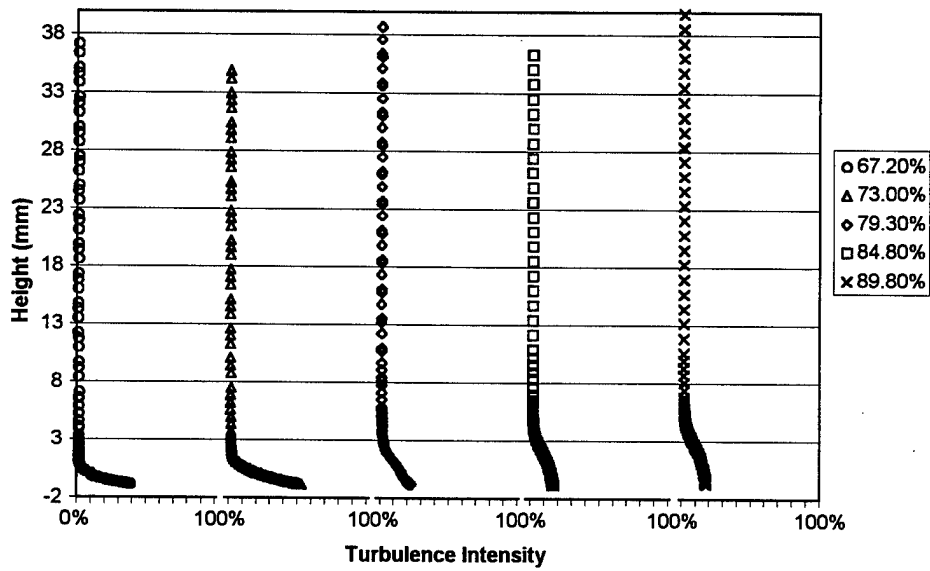


b) boundary layer turbulence measurements at  $Re = 100k$  and  $Tu = 4\%$

Figure 126. Measured velocity and turbulence profiles between V-grooves starting at 60% with  $Tu = 4\%$ .



a) boundary layer velocity measurements at  $Re = 100k$  and  $Tu = 4\%$



b) boundary layer turbulence measurements at  $Re = 100k$  and  $Tu = 4\%$

Figure 127. Measured velocity and turbulence profiles inside a V-groove starting at 60% with  $Tu = 4\%$ .

## APPENDIX C - Adjustable Linear Cascade Experimental Facility

### C.1 Baseline Wind Tunnel Design

The wind tunnel used in the experiment was a modified open loop Aerolab corporation draw-down tunnel using a test section with an interior area 121.9 cm (48 inches) wide by 85.1 cm (33.5 inches) high (see Figure 128). Air was pulled through the test section by means of a 93.2 kilowatt (125 HP) motor operating in the suction mode using a Joy Technologies Axivane axial flow fan with an outer radius of 114.3 cm (45 inches). The motor casing is 124.5 cm (49 inches) long, containing the electric motor, axial fan, exit vanes, and a wire mesh catcher system to minimize blade damage in the event of a test section structural failure. Air flow through the test section is controlled by a Harmon/Commonwealth Corporation variable frequency motor controller.

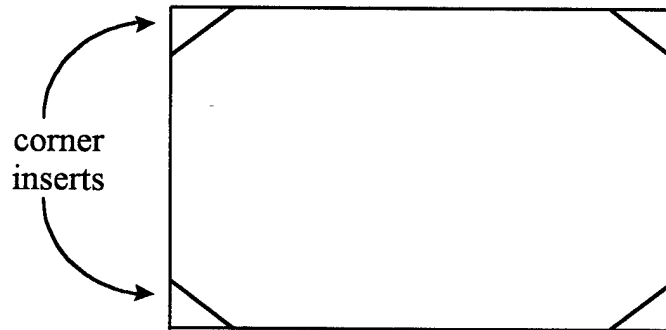


Figure 128. Cross-sectional area of wind tunnel.

The wind tunnel inlet bell-mouth has a 304.8 cm (120 inch) wide  $\times$  266.7 cm (105 inch) high rectangular inlet with a honeycomb flow straightener and a converging nozzle. The convergent portion of the inlet nozzle is 228.6 cm (90 inches) long and ends in a rectangular shape with the center outlet flow 121.9 cm (48 inches) wide by 85.1 cm (33.5 inches) high (see Figure 129).

Inserts serve to minimize corner vortices and extend into the test section 10.2 cm (4 inches) up and down from the top and bottom and 12.7 cm (5 inches) into it from the left and right. The

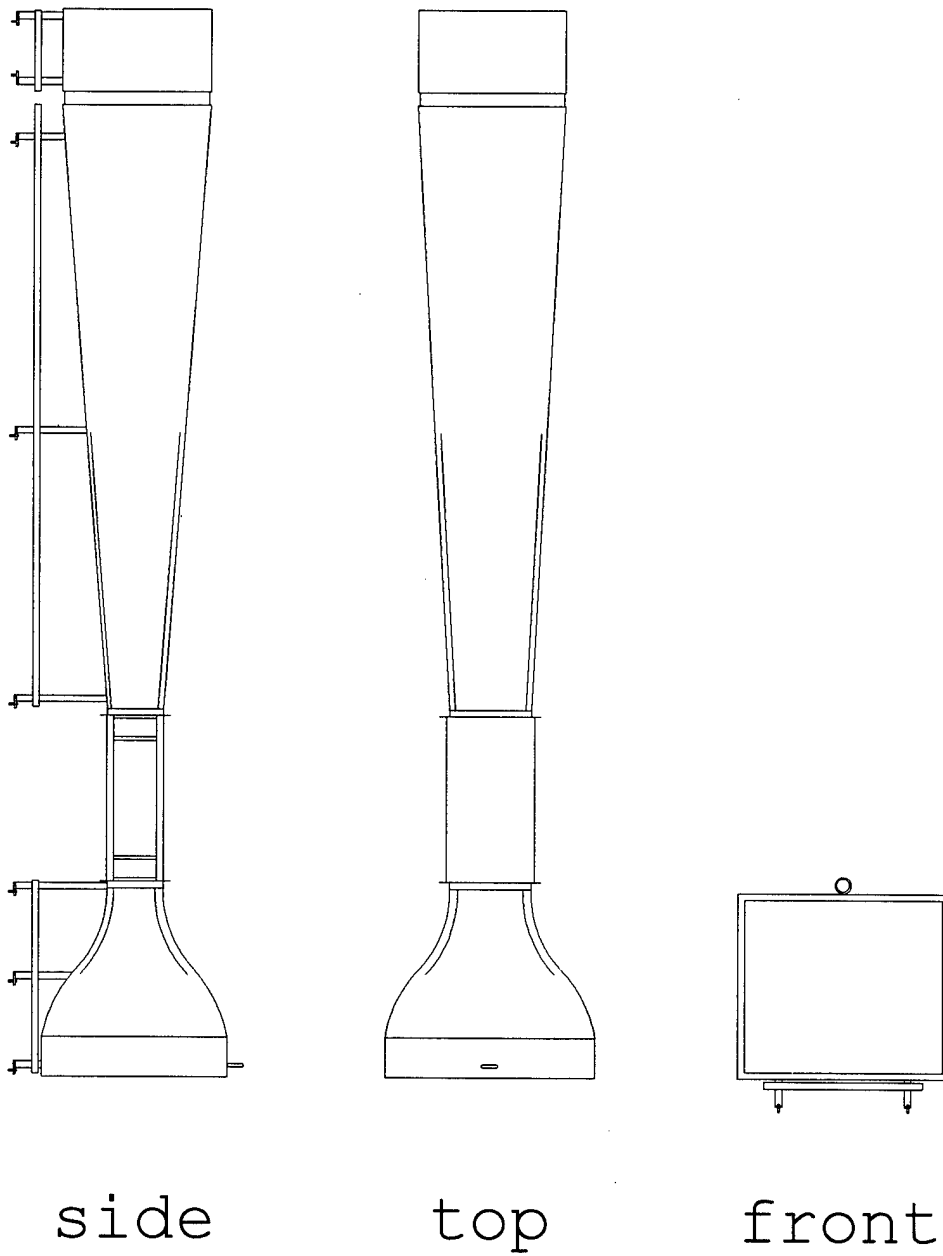


Figure 129. Unmodified Aerolab wind tunnel.

standard straight test section tapers these inserts down to 6.4 cm (2.5 inches) high in the vertical axis and 8.9 cm (3.5 inches) wide in the horizontal axis. With these inserts in place, the freestream turbulence level is less than 1.0%.

Modifications built by the AFIT shop for the wind tunnel did not include the corner inserts to minimize shop materials and construction time. To replicate their effectiveness, however, styrofoam inserts were cut and placed in the new tunnel sections to maintain the same corner vortex minimizing effect. With these inserts in place, the new test section has a freestream turbulence of approximately 1%.

## C.2 Active/Passive Turbulence Generator

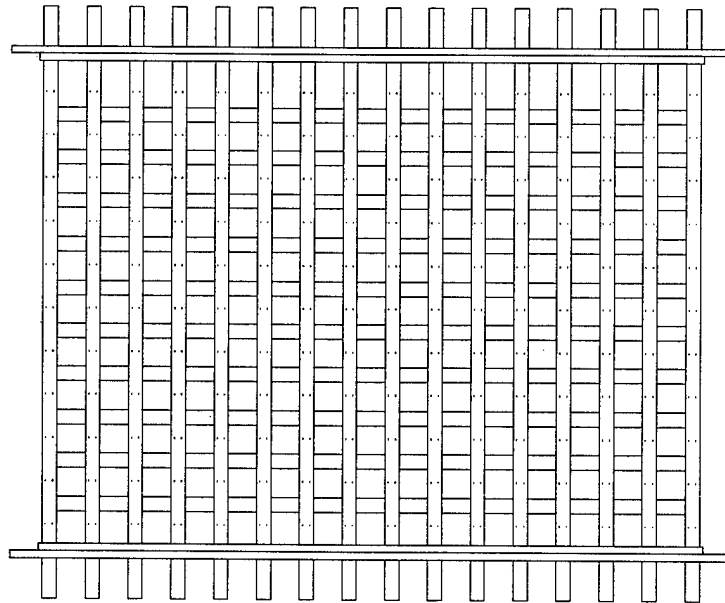


Figure 130. Turbulence grid capable of producing high turbulence levels with and without blowing air.

The turbulence generator housing consists of a straight channel 76.2 cm (30 inches) long in the flow direction and has the same cross-sectional area of the straight test section. The turbulator

grid itself (see Figure 130) is a removable square-mesh array of 2.54 cm (1 inch) diameter round stainless steel tubes that can provide both passive and active means of turbulence generation. The tubes are spaced 7.6 cm (3 inches) apart, center-to-center and were designed in accordance with Roach's [48] isotropic turbulence grid guidelines.

Operated passively, the turbulator disturbed the air to a freestream turbulence level of 3.5% to 4.5% (see Figure 131) at a distance of 127 to 254 cm (50 - 100 inches) downstream of the grid. The turbine blade cassette is located within this downstream distance of the new variable angle test section. Also included in Figure 131 are the decay correlations determined from experiments of Baughn et al. [10] and Roach [48].

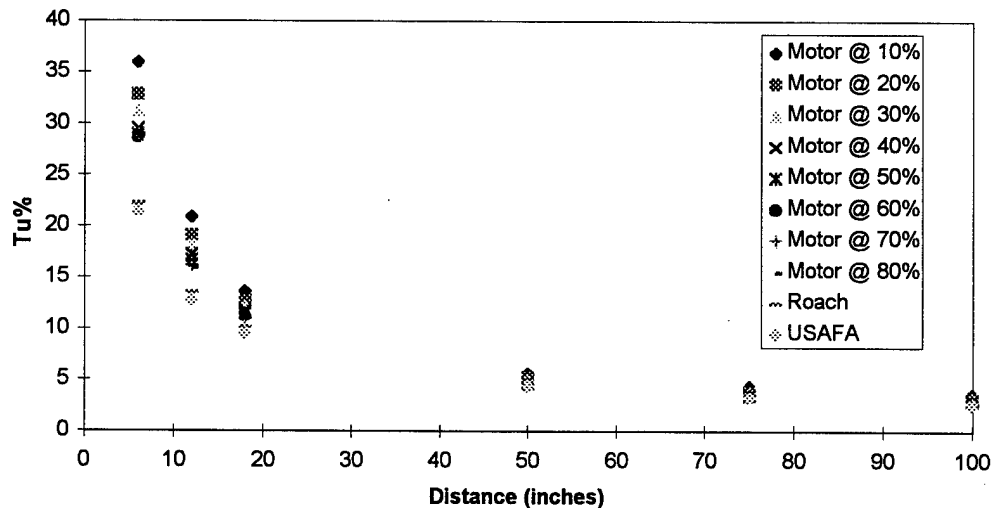


Figure 131. Decay of passive grid turbulence with downstream position.

Measurement of the generated turbulence decay and length scales were completed inside the new adjustable test section. The recorded turbulence data was then examined to ensure proper isotropy and length scales in accordance with Mayle et al. [49]. Length scales were determined by taking several repeated measurements and using Wright Laboratory provided software to integrate and average the data. The turbulence measurements were made using a single hot-wire probe im-

mersed in the air flow. The baseline straight test section with the turbulence generator in place is depicted in Figure 132.

### **C.2.1 Active Turbulence Generation**

To create higher turbulence levels across the blade cassette, air can be blown through the 0.8 mm (1/32 inch) diameter holes spaced evenly through the vertical bars. The freestream turbulence level can be increased to as high as 20% at a distance of 127 to 254 cm (50 - 100 inches) downstream of the grid. Control of the air through the vertical bars would be maintained through the stainless steel Octopus Air Control System seen in Figure 133. This system has four independent pressure chambers, each fitted with a pressure gauge and four air exhaust ports. Accurate control of the air through the exhaust ports is maintained through a gross adjustment 2.54 cm (1 inch) inner diameter valve and a 1.27 cm (0.5 inch) inner diameter fine control needle valve. Air is passed to the turbulence generating grid through 2.54 cm (1 inch) inside diameter high pressure hose fitted with quick disconnects at both ends. Using this system air can be delivered to any 4, 8, 12, or all 16 of the vertical tubes in any combination. Active turbulence generation using the blown grid requires a large compressor capable of producing 150+ psi continuously. A large compressor was not available for this research and the grid was only used passively for turbulence levels of 4% inside the new adjustable test section.

### **C.3 Adjustable Inlet and Exit Angle Cascade Test Section**

The test section contains a linear, 2-D airfoil cascade consisting of 8 low pressure turbine blades with 9 airflow passages in between the blades and walls. Blade #1 is located near the inside bend, with subsequent blades #2 through #8 following outward towards the outer corner. The blade row is 198 cm (78 inches) downstream of the turbulence generator at its nearest point and 300 cm (118 inches) downstream at its farthest. The Pak-B blades were designed by Pratt and Whitney and

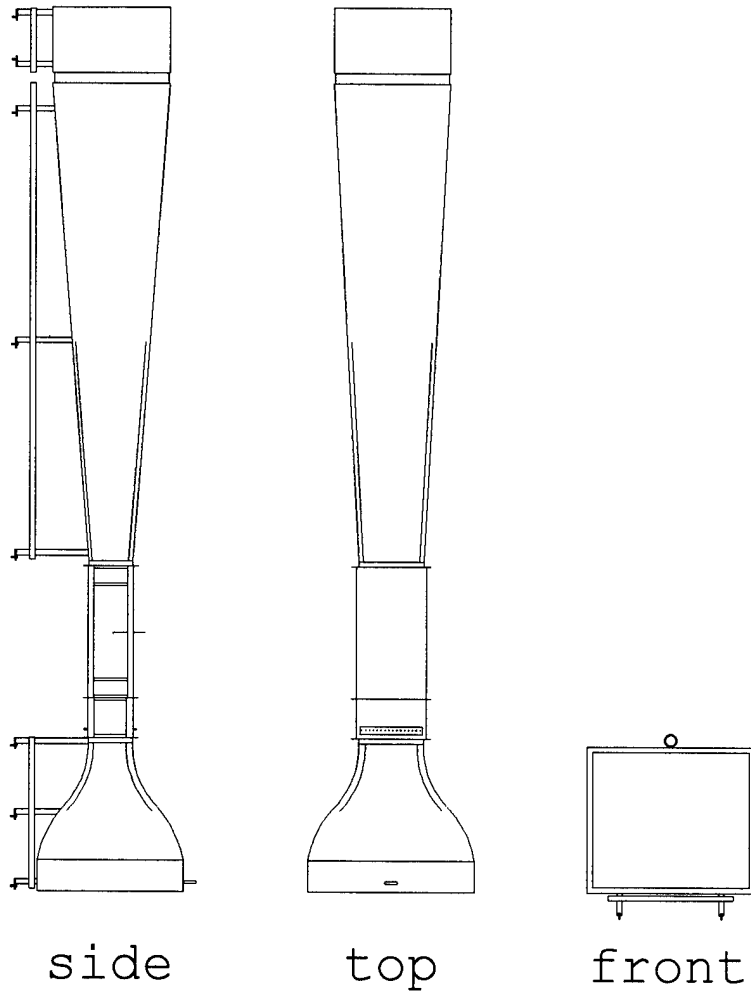


Figure 132. Turbulence generator placement upstream of straight test section.

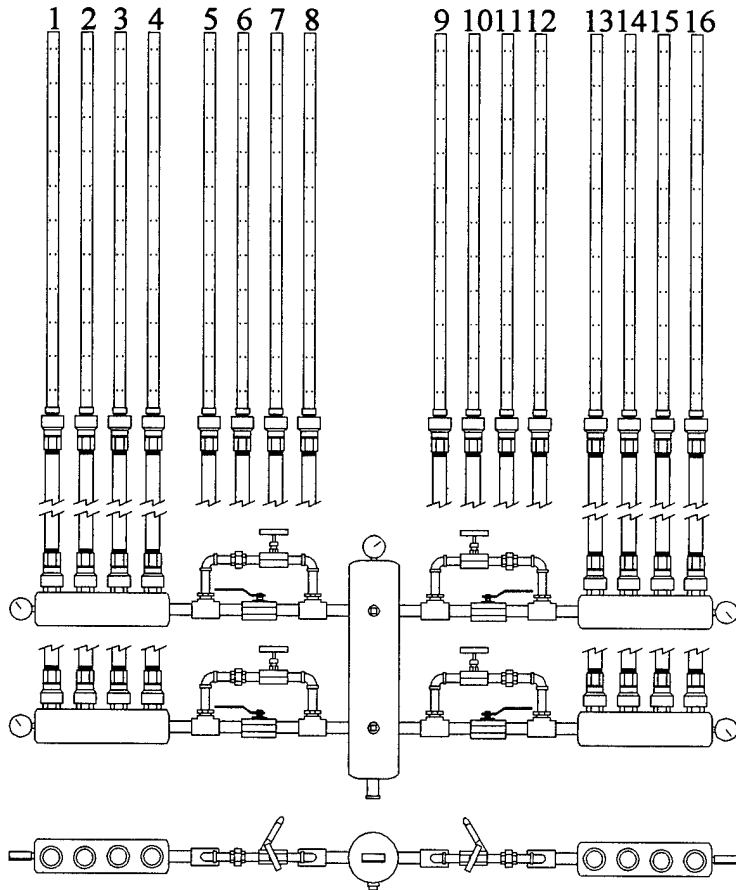


Figure 133. Front and top views of the pressure control system for active turbulence generation using blown air.

have axial chord lengths of 17.8 cm (7 inches). The axial chord to spacing ratio (solidity,  $\frac{c}{s}$ ) of the blade passage is 1.129. The blade spacing is 15.75 cm (6.2 inches) blade to blade. Each blade is molded from Ultralloy 108 white resin and is seven times engine scale in the axial direction. To further enhance the approximately 2-D flowfield of the midspan of the actual blades, each test blade is stretched in the z-axis to 78.63 cm (34.5 inches) high for an aspect ratio of 4.92 to 1. The inner and outer walls of the test section where the test blades are located were shaped to approximate the suction and pressure sides of a blade, respectively. The tunnel was set for the on-design specifications of the Pak-B blade with an air inlet angle of  $35^\circ$  relative to the engine x-axis (normal to the blade inlet plane) and an air exit angle of  $60^\circ$ .

The test section contains a central pivot joint which allows adjustment of the inlet and outlet channels separately. The inlet and outlet channels have the same cross-sectional area as the turbulence generator, and are connected at the pivot joint. Both the inlet and exit channel may be turned through a range of  $0^\circ$  to  $65^\circ$  independently of one another. The maximum total possible flow turning angle is  $130^\circ$  if both channels were fully rotated. This new test section will be used with other blade types in future experiments requiring a change in inlet and exit angle. To facilitate test section adjustments, the top, bottom, and outer walls of the test section were built using clear plexiglass.

The top of the new test section was constructed from two sheets of 2.54 cm (1 inch) thick clear plexiglass. These two large plexiglass pieces are attached to the top with a groove 6.4 mm ( $\frac{1}{4}$  inch) deep cut around the edge. This groove allows the plexiglass to hang into the test section and create a flush inner surface. The good visibility within the test section allows for easy adjustment of probes and tailboards when necessary. The plexiglass bottom of the new test section was similarly constructed.

Traverse slots were cut into the plexiglass sheets, arranged parallel to the leading and trailing edge of the blade row. The center of the 1.27 cm (0.5 inches) wide slots are spaced  $\frac{1}{2}$  and 1 axial

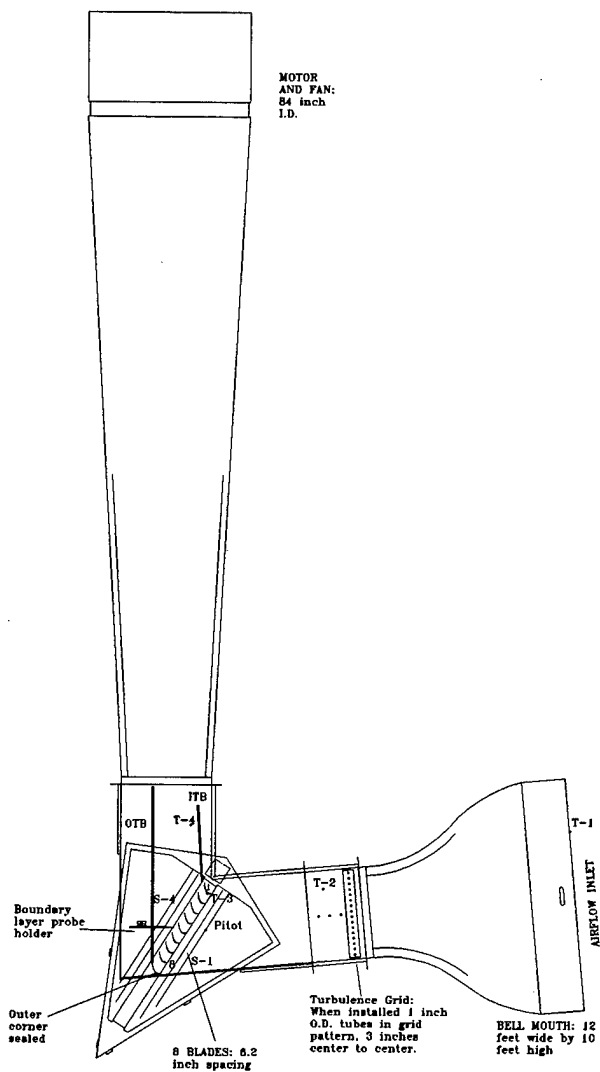


Figure 134. New linear cascade test section with independently adjustable inlet and exit angle capability.

chord length away from the blades. The slots allowed for easy measurement of the inlet and exit profiles of the blade cassette to verify periodicity, a requirement suggested by Gostelow [50]. Once periodicity had been acquired within the test section through adjustment of the tailboards testing was started on the Pak-B airfoils. The same procedure will be conducted to verify periodicity for other airfoil shapes when the Pak-B airfoils are replaced.

#### C.4 Removable Blade Cassette

The blade cassette which held the Pak-B airfoil cascade during testing. Seen in Figure 135, the blade cassette can be removed from the test section. The blade cassette was also constructed from clear plexiglass which allowed for improved visibility when inserting boundary layer probes into the test section. The ease with which the cassette can be installed and removed facilitates the testing of a variety of blade types with different inlet and exit flow angles.

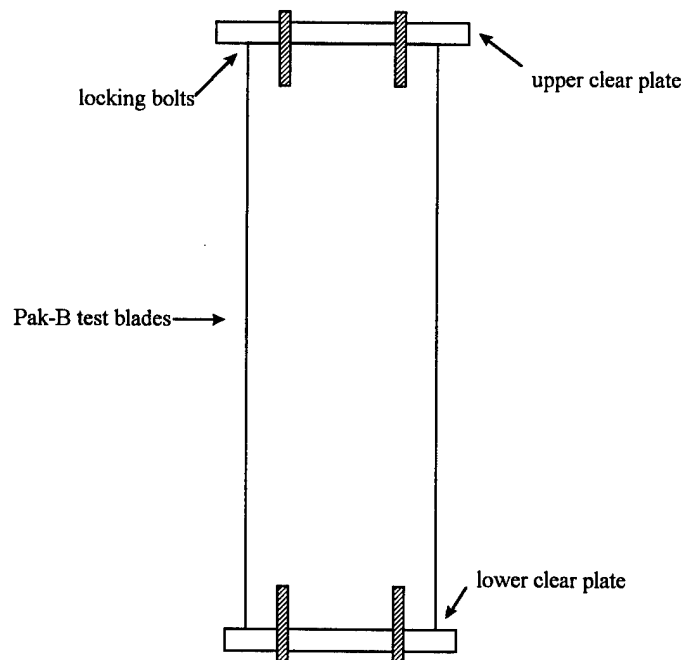


Figure 135. Side view of blade cassette

The blade cassette consists of the eight Pak-B blades and clear plexiglass top and bottom plates. To support the weight of the blade cassette steel channels fixed to the adjustable test section support the leading and trailing edge of the cassette plexiglass top and bottom plates. The blade cassette design is compatible with any other low pressure turbine blade shape.

#### **C.4.1 Testing Other Blade Shapes**

Once a new cassette is created with the new blades to be tested, the current blade cassette is removed by first removing the tailboards from the test section. Then the current cassette is lifted out using a crane and the new cassette lowered into place. The test section is then rotated to provide the correct exit angle for the blades with the tail boards inserted accordingly. The bell-mouth inlet is then lifted slightly ( $\sim 10$  mm) using a crane and rotated to provide the desired inlet angle. Rotating the bell-mouth inlet also rotates the turbulence generator and the inlet channel of the new test section. Since the bell-mouth is not bolted to the floor, it can remain attached to the test section during this procedure.

## APPENDIX D - Experimental Data Collection Software

### D.1 Overview of Software and Equipment

Control and data collection for the wind tunnel was managed through an IBM-compatible pc using an Intel 200 MHz pentium processor with a 2.0 Gb hard drive. The operating software was written in G, a visual programming language used by the LabView 5.0 software package. This software package included pre-written procedures and the ability to use them with operator created software. Each operator created program is called a "VI" (Virtual Instrument) and has a display on the monitor which presents both the entered and collected data.

### D.2 Hot Wire Calibration

The Hot Wire Calibration VI allowed calibration of the hot wire to be performed within the new test section of the tunnel. With the hot wire in place, measurement of the probe resistance was made using the TSI IFA 100 Intelligent Flow Analyzer. This resistance was entered in the hot wire settings frame on the left hand side of the screen (Figure 136) along with the factory measured internal resistance of the hot wire probe. The current atmospheric pressure was read from a Wallace and Tiernan FA 129 pressure gauge and entered into the program, while the temperatures were measured using J-type thermocouples. To calibrate the probe, a pitot-static probe was inserted into the tunnel 1 axial chord upstream of Blade #5. This pitot probe provided the  $P_{total} - P_{static}$  measurement necessary for the calibration. With the pitot and hot wire probes in place, the tunnel was run at a high velocity (higher than that used during data collection) and the resulting pressure from the pitot probe and voltage from the hot wire entered into the program.

The pressure and voltage entry procedure was repeated for several different decreasing velocities. When sufficient data was collected, the "Done Do Fit" button was pressed on the screen. This button activated a sub-routine to perform a curve of the hot wire data with the pressure data using

a method described by Bruun [31]. The resulting hot wire calibration curve was a nondimensional fit between the Nusselt number and Reynolds number of the form:

$$Nu = C_{INT} + D_{SLO} Re^{0.45} \quad (26)$$

where  $C_{INT}$  and  $D_{SLO}$  were the intercept and slope, respectively, for the curve. The exponent used for the hot wire equations was 0.45 since this provided better agreement with the low velocities used in this research (Giese [51]). The resulting intercept and slope were then entered into the Current Tunnel Conditions and other VI's where hot wire velocity information was collected.

### D.3 Current Tunnel Conditions

The initial environmental conditions were determined before every data collection. This was done by reading the atmospheric pressure from a Wallace and Tiernan FA-129 pressure gauge and obtaining the current humidity using an Omega Engineering, Inc. RH71 Digital Hygro-Thermometer. These values were then entered into the Current Tunnel Conditions VI which calculated and displayed the current tunnel velocity, air density, and temperatures throughout the tunnel using the hot wire, pressure gauge, and thermocouples, respectively. The desired Reynolds number for the test was then dialed in by increasing the tunnel motor speed control according to Figure 137. Velocity data was collected using a TSI model 1210-T1.5 hot wire described previously in Section 4.1. Each data point for the hot wire was graphed on the computer screen to allow easy determination of AC noise interference. For velocity data collected behind the blades, a pitot probe was used to determine the inlet velocity and Reynolds number. Figure 138 illustrates the Current Tunnel Conditions program.

The lower left part of Figure 138 shows the inlet Reynolds number based upon the pitot probe measurement. The tunnel pitot probe was located in a fixed position 1 axial chord length upstream of the blade cassette and outside of the boundary layer. The hot wire calibration information is just

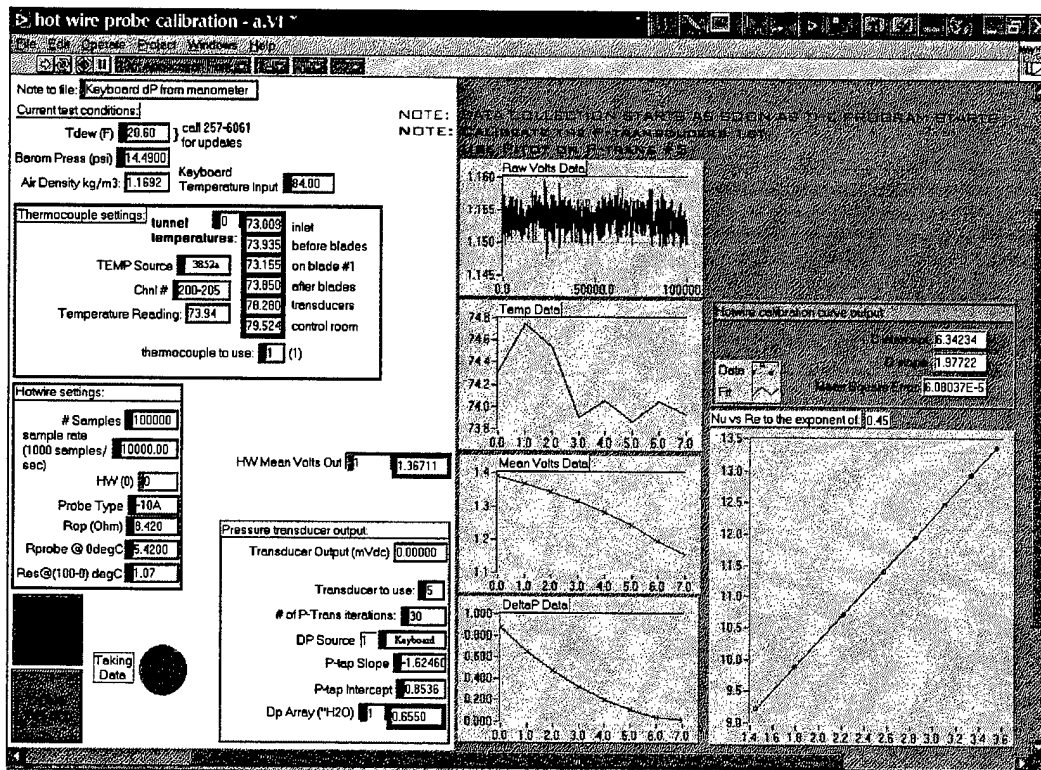


Figure 136. Software used for calibration of the hot wire.

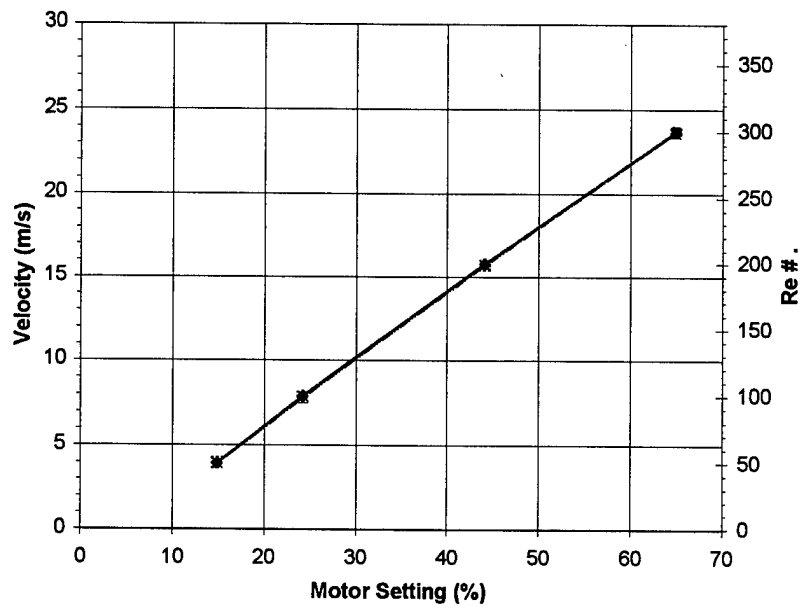


Figure 137. Relationship between tunnel inlet velocity, Reynolds number, and drive motor setting.

above the pitot probe data. The data seen in Figure 138 was taken with the hot wire downstream of the blade cassette and an appropriate velocity increase is shown between the upstream pitot velocity and the downstream hot wire velocity. All Reynolds number information presented in this document was based on inlet velocity and an axial chord length of 17.78 cm (7.0 inches). The calculated mean velocity and turbulence intensity are also displayed on the lower right portion of the screen. Turbulence intensity was based upon fluctuations in the hot wire velocity readings. Temperature measurements were recorded at four locations within the tunnel test section.

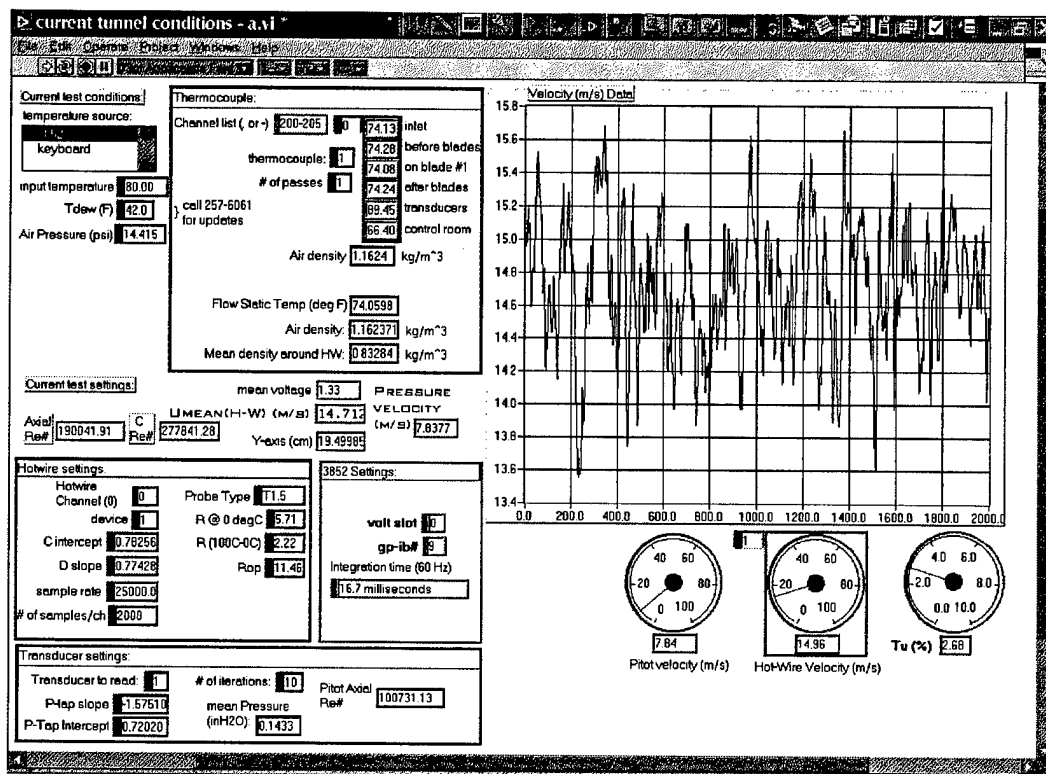


Figure 138. Current tunnel conditions determination program.

Thermocouples were used to measure the temperatures for the tunnel inlet, 1.45 m (57 inches) upstream of blade #1 (45.7 cm downstream of the turbulence grid), on blade #1 at the 40% axial chord position, 76.2 cm downstream of blade #1, and the insulated pressure transducer box. These

temperatures were displayed in the upper left box. The calculated air density was also displayed within this box. Thermocouple temperature data was collected with J-type thermocouples using a Kaye Instruments thermocouple 0°C (32°F) Ice Point Reference and the HP 3852A Data Acquisition/Control Unit. The thermocouples provided the current temperature for the other data collection programs, including the Grid Traverse Data Acquisition VI.

#### **D.4 Velocity Profiles Across The Blade Cassette Inlet and Exit**

The Grid Traverse Data Acquisition VI was used to verify periodicity and uniformity of the blade cassette inlet and exit flowfield. The velocity and turbulence intensity of the air was measured with a TSI 1210-T1.5 hot wire. The VI operated the Dantec 3-axis traverse to move the hot wire across the blade row inlet or exit plane. The coordinate system for the traverse is shown in Figure 139. In Figure 139 each of the traverse slots is numbered 1 through 4, where the first two are for measuring the inlet flow one and one-half axial chord lengths upstream of the blade row. The centerline position of these 1.27 cm (0.5 inches) wide slots relative to the blades is 17.78 cm (7 inches)  $\pm$  0.0127 cm (0.005 inches) and 8.89 cm (3.5 inches)  $\pm$  0.0127 cm (0.005 inches) upstream of the blades for slots #1 and #2 respectively. The downstream slots #3 and #4 are the same distance away from the blades as #2 and #1, respectively. The hot wire (symbolized as (b) in Figure 139) was moved upstream of the blades (a) while suspended through the traverse slot moving along the y-axis. The span covered by the hot wire was 61 cm (24 inches) which included the passages between blades #3 through #7. The hot wire was moved up and down using the z-axis to get velocity and turbulence intensity profiles for different heights along the blades. The particular slot the hot wire was in was changed by moving the z-axis up and thus lifting the probe out of the tunnel and then moving the x-axis forward or back to the next desired traverse slot. The velocity and turbulence intensity profiles in sections 3.3 and 3.4 were taken for all four traverse slots at Reynolds numbers

of 50k, 100k, and 200k. The Grid Traverse Data Acquisition program was divided into two sections, the left portion was for calibration and control inputs, while the grey right-hand portion displayed the velocity and turbulence outputs.

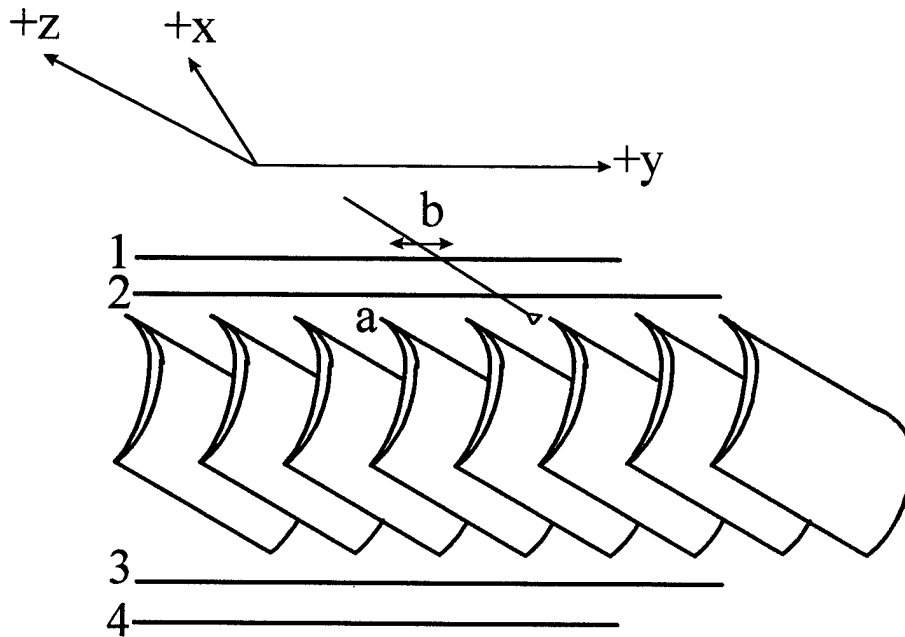


Figure 139. Tunnel test section 3-axis coordinate system used with the Dantec traverse.

#### D.4.1 Blade Cassette Velocity Profile Inputs

The program required the atmospheric pressure and dew point to be entered into the upper left frame seen in Figure 140. Other atmospheric conditions such as temperature and density were calculated using thermocouples and internal calculations based upon room pressure. The hot wire calibration information was located in the frame below the atmospheric data. It was necessary to enter the updated hot wire calibration information in this frame. The number of data samples and the frequency of their collection at each traverse location was also entered here. The 3-axis traverse was controlled through the lower left frame seen in Figure 140. The number of steps and spacing

between each collected data point across the pitch axis of the blades was entered here. The same control over the z-axis was maintained through this frame. Every averaged data point recorded for each y,z location was displayed on the right hand of the computer screen in two forms.

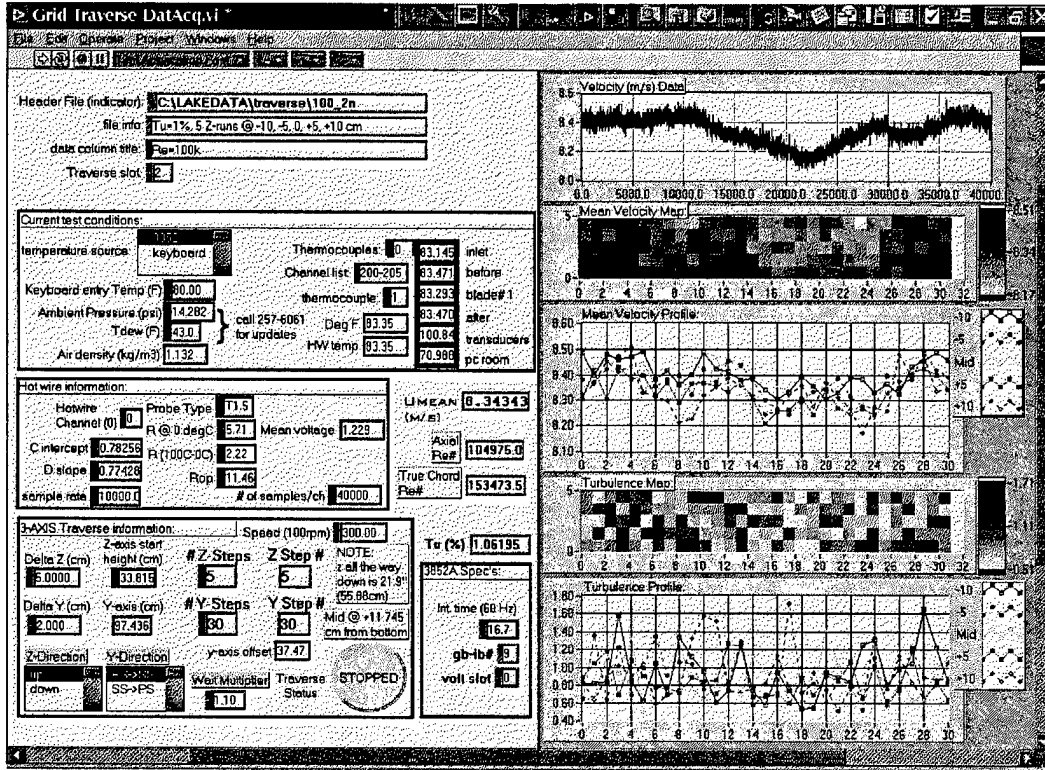


Figure 140. Velocity and turbulence measurements made using 3-axis traverse and hot wire probe program.

#### D.4.2 Blade Cassette Velocity Profile Outputs

The outputs of the Grid Traverse Data Acquisition VI were presented in color to the user, but are printed here in a grayscale format. The actual velocity data taken at each traverse location was displayed in near real time in the upper right-hand corner of Figure 140. Presentation of the complete raw data collection allowed for inspection of AC noise interference or unexpected velocity fluctuations. The velocity information for the particular x,y,z location was averaged and added to the collection for the particular pass in the y-axis direction. Each y-axis pass was run at a different height

with Figure 140 illustrating 5 passes, each 5 cm (1.97 inches) apart in the z-axis. The average values were presented in two different forms. The first average velocity graph was a color-scale contour map. Each averaged point was assigned a block of the appropriate color depending on its average velocity. The pitch of the blades spreads across the x-axis of the graph (traverse y-axis) and the different passes in the z-axis move up the maps y-axis. This contour mapping eased determination of improper periodicity and the effects of height within the tunnel during data collection. The velocity data was also graphed on a regular line chart just below the velocity contour map as seen in Figure 140. Each pass along the pitch axis of the blades was given a different symbol and line style to ease in differentiation. For example, the pass along the center of the blades was a simple line with no symbols, while the pass 5 cm (1.97 inches) above the center was marked by solid-filled squares. The same symbols were given to the turbulence intensity line chart located in the lower right-hand corner of Figure 140. A color contour map of the turbulence intensity data was also presented. The Reynolds number was also calculated each time the velocity measured.

The center of the display shows the calculated Reynolds number. Reynolds number was based upon axial chord length and inlet velocity. Also displayed is the Reynolds number based upon true chord length and exit velocity. Conversion of the Reynolds number to other standards is shown in Table 3. As with the Grid Traverse Data Acquisition VI the Pressure Transducer Calibration VI was visually divided into two separate areas for the data entry and output.

Table 3. Reynolds number conversion

Axial Chord, Inlet Velocity	True Chord, Exit Velocity	True Chord, Inlet Velocity	Axial Chord, Exit Velocity
50,000	119,157	73,102	81,500
100,000	238,315	146,205	163,000
200,000	476,630	292,411	326,000
500,000	1,191,574	731,027	815,000
1,000,000	2,383,147	1,462,054	1,630,000

## D.5 Pressure Transducer Calibration

Two pressure transducers were calibrated simultaneously using the Pressure Transducer Calibration VI with the Druck DPI-600 Digital Pressure Indicator calibrator and pressure source. The DPI-600 was connected to the total pressure side of the differential transducers with the static side open to room air. The DPI-600 provided the pressure to the transducer as well as the resulting reference pressure. Using the HP 3852A Data Acquisition/Control Unit, the millivolt outputs were read from the transducers. Each transducer output was read 30 times and then result averaged. Each calibration was done for the appropriate range to be measured in the next experiment, with pressures ranging from 0 to  $1.016 \times 10^{-2}$  kg/cm<sup>2</sup> (4 in-H<sub>2</sub>O). The resulting calibration curve coefficients were displayed in the right hand side of Figure 141. These coefficients were then entered into the Wake Traverse Data Acquisition VI and other programs that required the use of the pressure transducers.

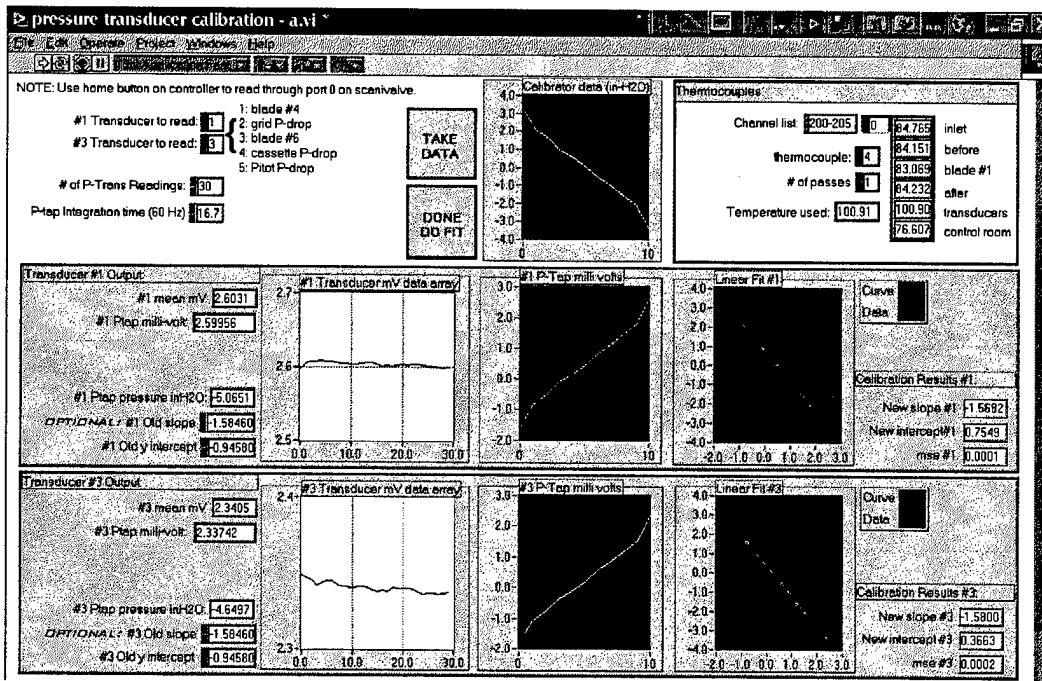


Figure 141. Pressure transducer calibration software.

## D.6 Wake Traverse Velocity and Pressure Data Collection

To measure the exit total pressure and velocity downstream of the test blade, the Wake Traverse Data Acquisition VI was created by modifying the existing Grid Traverse Data Acquisition VI. The modifications to the Grid Traverse Data Acquisition VI included removal of the color contour plots and addition of current sample and mean total pressure sample plots. The program inputs were still placed on the left (white) portion of the screen with the outputs on the right hand side of Figure 142.

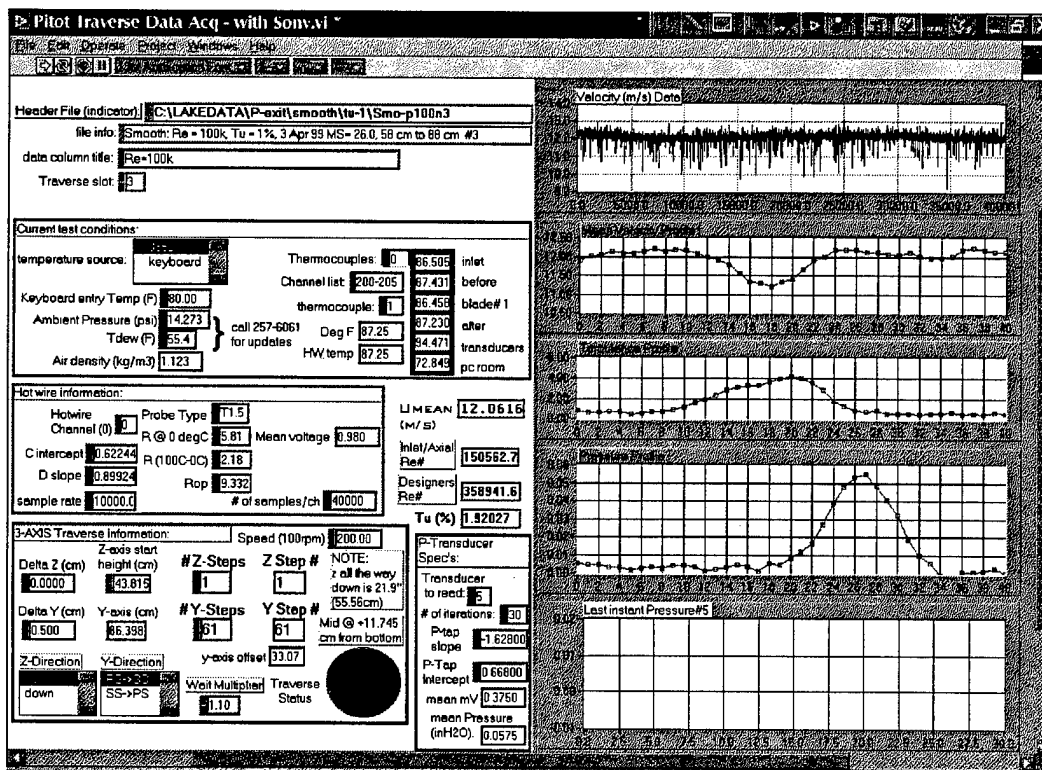


Figure 142. Exit wake total pressure and velocity measurement program.

### D.6.1 Wake Traverse Data Collection Inputs

In addition to the atmospheric conditions and hot wire calibration information, this VI also required the pressure transducer calibration information. The pressure transducer calibration infor-

mation was entered in the bottom center frame of Figure 142. Control of the probe movements was maintained in the lower left frame where the spacing between subsequent measurements was entered. The location of the probes was recorded to the output along with the pressure and velocity data.

#### **D.6.2 Wake Traverse Data Collection Outputs**

The pressure, velocity and turbulence intensity for each location were recorded and displayed on the screen. The last sample of velocity data was displayed in the upper right portion while the total pressure sample was displayed in the bottom right of the screen. The average values for each location for the velocity, turbulence intensity, and total pressure were also displayed. The entire data collection was also saved to a file, allowing calculation of the loss coefficient. The transducers were also used in gathering surface pressure coefficient information for the baseline Pak-b blades.

### **D.7 Surface Pressure Coefficient Determination**

Pressure coefficient profiles for the blades were obtained for both blade #4 and #6 simultaneously using the Scanivalve Data Collector VI shown in Figure 143. This VI operates the 48-channel scanivalves and records the pressure results from two pressure transducers. The results from the transducers were then converted and plotted to display both the actual pressure readings and the normalized coefficients. Tunnel velocity was determined using a hot wire and a pitot-static probe both located one axial chord length upstream of blade #5. Temperatures were obtained using J-type thermocouples within the test section. This VI was divided into two categories; inputs on the upper and left white sides, outputs on the lower and right grey sides.

#### **D.7.1 Surface Pressure Coefficient Inputs**

Atmospheric data including dew point and barometric pressure was entered in the upper left portion while temperatures from the thermocouples were displayed in the frame just below. The

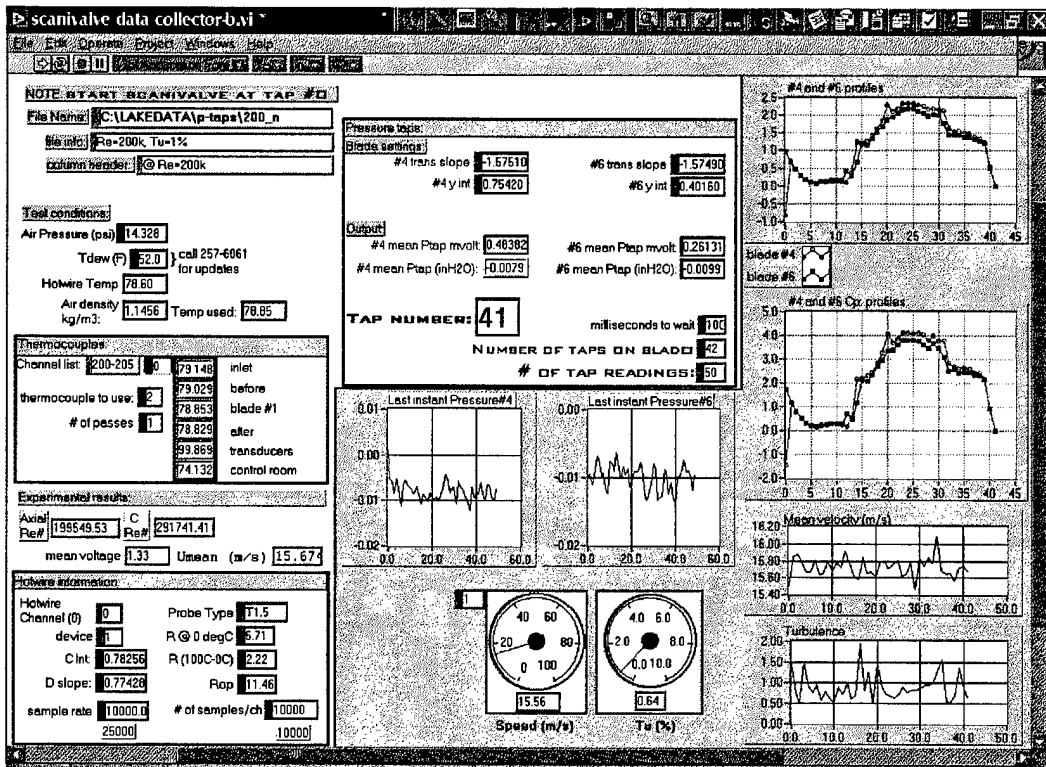


Figure 143. Blade surface pressure coefficient data collection program.

hot wire calibration information was entered in the lower left frame. This information was used to convert the hot wire voltage into a velocity and Reynolds number. The resulting Reynolds number and velocity were displayed just above the hot wire information frame. The pressure transducer information was entered in the upper center frame. Transducer information required for operation includes the number of surface taps to collect data from as well as the number of data points to take from each surface port for a good mean value. The slope and offset for each transducer from the pressure transducer calibrator VI was also entered in this frame.

#### **D.7.2 Surface Pressure Coefficient Outputs**

The software records a series of data points from zero to 43. Points zero through 39 are pressure tap locations on blade #4 and #6. The 40th data point measures  $P_{total} - P_{static}$  from the pitot static probe which was then used to calculate the tunnel velocity and serves as a double check with the hot wire. The 41st data point records the pressure shift due to thermal changes around the transducers by recording the difference between  $P_{total}$  readings on both the total and static side of the transducer. While the difference was zero, any thermal shift in the zero offset was recorded. This value was then subtracted from all of the previous data points to minimize the temperature shift error. Two additional measurements were taken including  $P_0 - P_{wall}$  (point #42) and  $P_0 - P_A$  (point #43). Point #42 provides the difference between the pitot probe static pressure and the tunnel test section static pressure. Point #43 was the difference in pressure between in the test section inlet total pressure and atmospheric pressure which gave the operator enough information to calculate the actual total pressure within the tunnel when room atmospheric pressure was considered. When data collection was complete, the operator was asked if the data was good enough to save to disk. The output file consists of surface port number and pressure information for both blades #4 and #6. Pressure

information for the blades includes the recorded values in inches-H<sub>2</sub>O, and Cp based upon hot wire velocity:

$$C_p = \frac{P_{total} - P_{surface,x}}{\frac{1}{2}\rho\bar{U}_{inlet}^2} \quad (27)$$

where  $\rho$  is determined from atmospheric pressure and tunnel temperature. No compressibility corrections were used for the density due to the very low Mach numbers of the test section airflow. The inlet velocity used in equation 27 was sampled immediately before each pressure tap. The inlet velocity was sampled 10,000 times for each surface port and then averaged. The recorded mean velocity and turbulence intensity for each measurement were displayed in the graphs on the lower right of the screen shown in Figure 143.

The grey portion of Figure 143 contains the outputs for this VI. In the center of the display are the most recent data samples for each blade in units of inches of water. Inspection of these values allows determination of unacceptable pressure fluctuations and so the quality of the data can be determined for each data point. The mean of these values were plotted for each pressure port in the upper right of the display. Temporary dimensionless Cp values were also plotted on the screen using equation 27.

## D.8 Boundary Layer Velocity and Turbulence Measurements

The Boundary Layer Traverse VI operated the 5.08 cm (2 inch) micro traverse which held a TSI 1279S-10A subminiature hot film probe. The built in accuracy of the micro traverse allowed highly detailed measurements within the boundary layer, down to within 0.0254 mm (0.001 inches) of the wall. This VI also used the color coded division of inputs and outputs to ease operation.

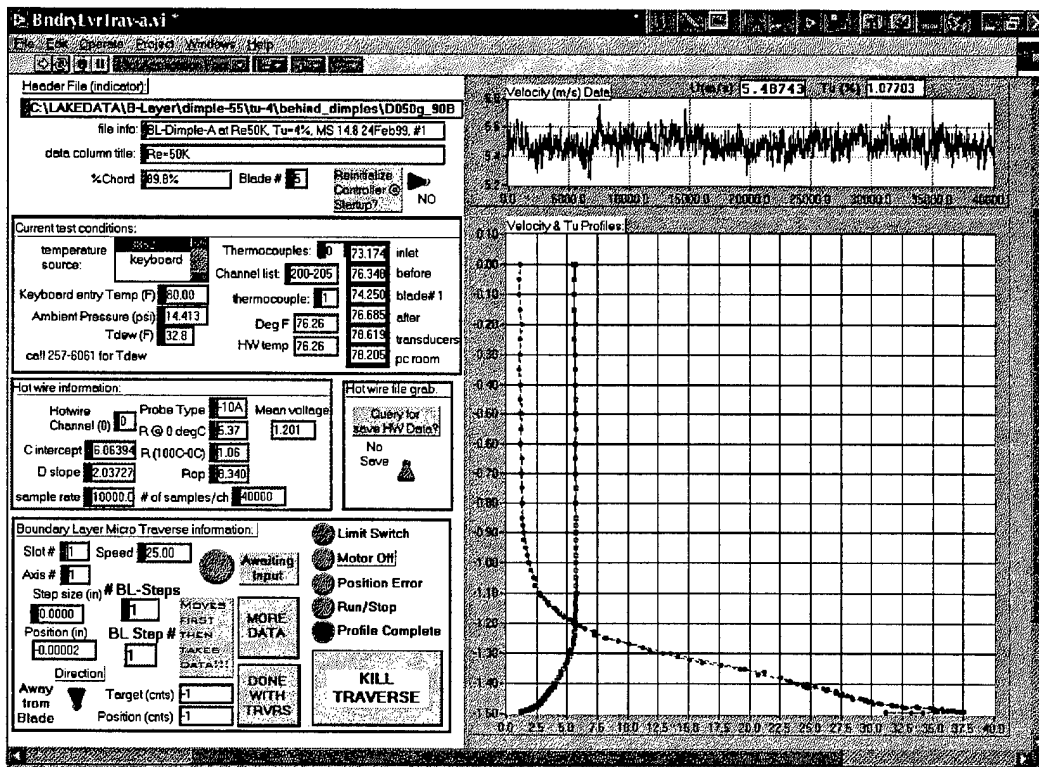


Figure 144. Boundary layer traverse software.

### D.8.1 Boundary Layer Traverse Inputs

The inputs for the Boundary Layer Traverse VI are on the left, or white, side of Figure 144. The inputs included the traverse movement controls in the bottom left of the screen, as well as the hot film calibration information in the frame just above it. The traverse controls allowed the user to specify a step distance and number of steps to complete. Velocity, turbulence, and temperature data were collected at every step. When the boundary layer profile was complete, the "Done With Traverse" button was pressed and the output file examined using a spreadsheet program.

### D.8.2 Boundary Layer Traverse Outputs

The velocity and turbulence data collected was displayed in the right hand side of the screen (Figure 144). The last velocity sample collected was shown at the top right of the screen, while the running survey was displayed in the large box below it. Both the velocity and turbulence intensity profiles were put on the same graph where the y-axis of the graph was height above the blade surface and the x-axis was shared by the velocity (m/s) and the turbulence intensity. The displayed turbulence intensity was the actual local value for each height, defined as:

$$Tu\% = \left( \frac{\sigma}{\bar{U}_y} \right) \cdot 100 \quad (28)$$

where  $\sigma$  is the rms of the mean velocity  $\bar{U}$  at height  $y$  above the surface. In addition to the turbulence intensity, the length scales of the turbulence were also calculated for the inlet and exit flow from the blade cassette.

## D.9 Turbulent Length Scale Determination Using Hot Wire

Turbulent integral length scales were determined for the Reynolds numbers and turbulence intensities under which the Pak-B blades have been tested. This was done using the Auto-Correlation VI and the single hot wire. The relative humidity and atmospheric pressure were entered into this program, while the hot wire takes 100 complete sets of data samples. The 100 sets of data were

averaged to provide power spectrum curve data in addition to the determined turbulence length scale.

#### **D.9.1 Required Data Inputs for Length Scale Software**

The software package developed by Wright Laboratory for the calculation of turbulent length scales records 65536 velocity data points at a rate of 20,000 Hz (Giese [51]) from a single hot wire placed in the wind tunnel. The user controlled software settings allowed the maximum frequency monitored to be 10,000 Hz. The high sampling rate was required to ensure all the turbulent frequencies present within the flowfield were captured by the hot wire sensor and not masked by a low sampling rate (Halstead and Solomon [24]). Most flowfield frequency fluctuations taper off around 5,000 Hz (Hinze [52]). The energy of the various frequencies present in the tunnel flowfield were presented to the user on the computer monitor. The control screen of the Auto-Correlation VI is presented in Figure 145, where the control inputs are in the upper left white sections and the outputs in the right-hand side grey sections. Inputs for the software included hot wire calibration information and the atmospheric properties of pressure and relative humidity. The outputs included the power spectrum of the measured flowfield, the auto-correlation of the power spectrum, as well as running strip charts of velocity, turbulence level, and temperature. The hot wire velocity values were used further in the calculation of the turbulent length scale.

#### **D.9.2 Calculation Process of Length Scale Software**

The Auto-Correlation VI used the recorded velocity data to find the root-mean-square velocity and average velocity  $\bar{U}$ . Other parameters used were the time step ( $\Delta t = \frac{1}{SR}$ ) equal to the inverse of the sampling rate ( $SR$ ) and the frequency resolution equal to the sampling rate divided by the number of data points ( $n$ ) taken in a single collection ( $\Delta f = \frac{SR}{n}$ ). The energy power spectrum curve was then created using a Fourier transform of the rms velocity data. The power spectrum

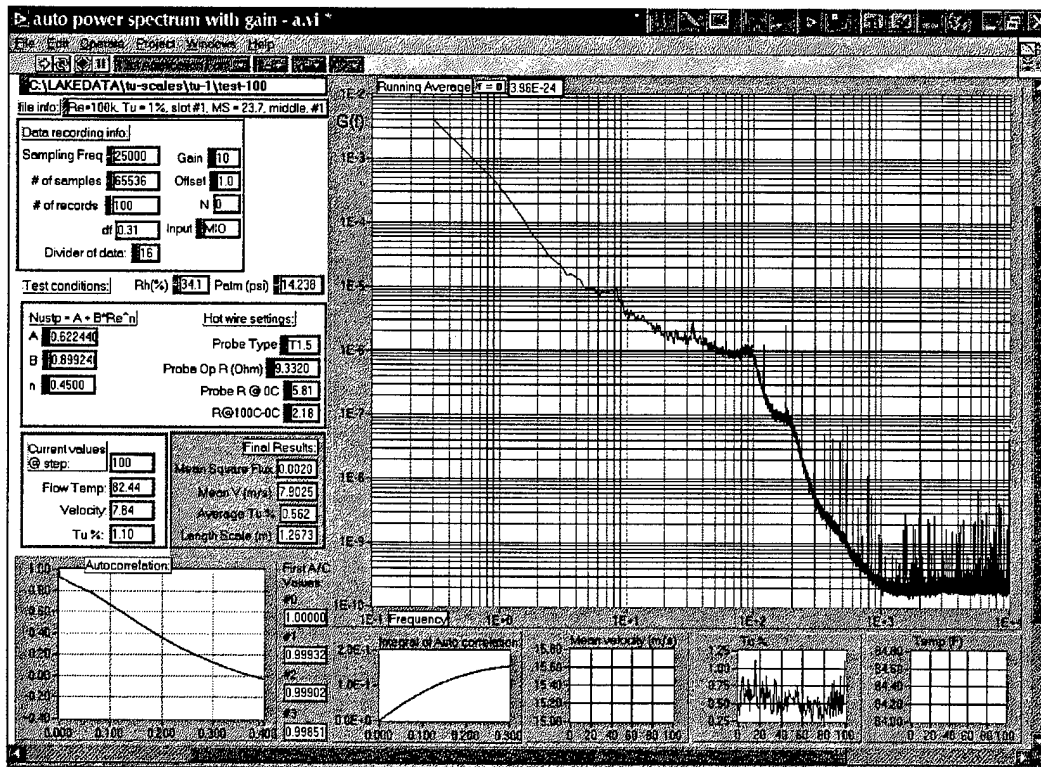


Figure 145. Turbulent length scale determination software.

curve was a single-sided auto spectrum plot of  $G(f)$  against frequency ( $f$ ). A single set of data contains unsteady fluctuations which could result in a jagged curve with high error. To reduce the error in the energy power spectrum curve calculation, several data collections were required using an averaging process. The averaging process may be done in real time by dividing the values in the next data set by the total number of data sets collected so far plus one (Bendat and Piersol [53]):

$$[\text{running average}] \frac{n}{n+1} + \frac{1}{n+1} [\text{new data set}] \quad (29)$$

and adding this to the current average multiplied by the ratio  $\frac{n}{n+1}$ . A typical resulting power spectrum is presented in Figure 146.

### D.9.3 Turbulence Intensity Verification Using Power Spectrum Curve

A verification was performed to ensure accuracy of the obtained spectral curve. First the normalized velocity was calculated by integrating the power spectrum curve (Bruun [31]):

$$\overline{u_n'^2} = \frac{\overline{U}}{2\pi} \int_0^\infty G(f) df \quad (30)$$

which gives a result in units of  $\frac{m^2}{s^2}$ . Assuming the  $u'$  and  $v'$  velocity components are of the same magnitude, the x-component of the velocity fluctuation is calculated from:

$$\overline{u_x'^2} = \frac{\overline{u_n'^2}}{\sqrt{2}} \quad (31)$$

so that the resulting turbulence intensity percentage is:

$$Tu(\%) = \frac{\sqrt{\overline{u_x'^2}}}{\overline{U}} \quad (32)$$

The resulting turbulence intensity should agree with previously calculated turbulence intensities using other methods.

### D.9.4 Integral Length Scale Determination and Program Outputs

The auto-correlation curve ( $\rho_x(\tau)$  versus  $\tau$ ) was created using an inverse Fourier transform on the power spectrum curve. This required the time step,  $\Delta t$ , and the frequency resolution,  $\Delta f$ . Normalization of the resulting auto-correlation curve was obtained by dividing the data set by the

maximum value within it. The integral time scale,  $T_I$ , was determined by locating the zero crossing of the curve ( $\tau^*$  - see Figure 147). The length scale was calculated by first integrating the auto-correlation curve (Bruun [31]):

$$T_I = \int_0^{\tau^*} \rho_x(\tau) d\tau \quad (33)$$

and then multiplying it by the mean velocity:

$$L = T_I \bar{U} \quad (34)$$

which resulted in the desired integral length scale ( $L$ ). Graphs of the power spectrum and auto-correlation curves may be produced on any spreadsheet program using the output data file.

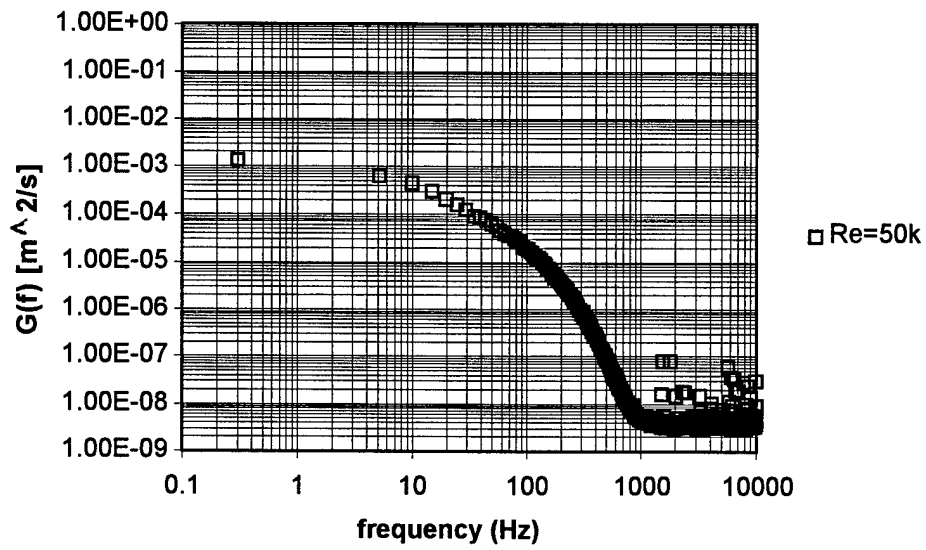


Figure 146. Power spectrum for inlet conditions of Re = 50k and Tu = 4%.

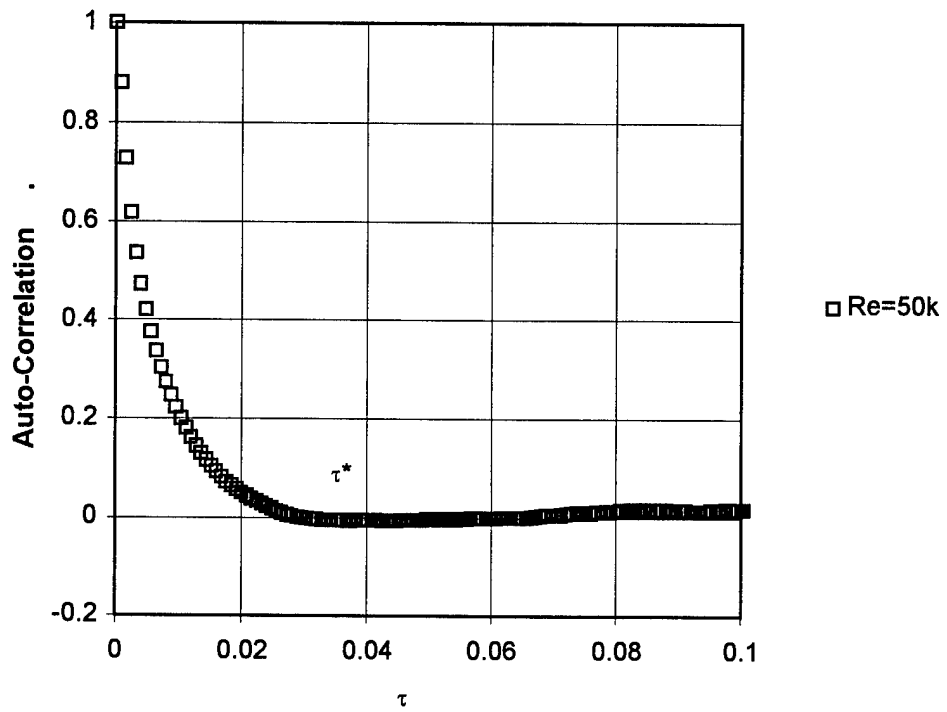


Figure 147. Normalized auto-correlation function for inlet conditions of  $Re = 50k$  and  $Tu = 4\%$ .

## APPENDIX E - 2-D Vane Blade Interaction Code

### E.1 VBI Software Inputs

The VBI 2-D code was capable of modeling a complete turbine stage consisting of both rotors and stators. While the capability to model a moving blade row and the associated wakes was not used, the inputs for both sets of blades are shown in Table 4. The required units for the program are also given in the table. Values for user defined parameters such as inlet relative Mach number and inlet total pressure were determined using the 17.8 cm (7 inch) axial chord length Pak-B blades and the environmental conditions of the experimental facility. All of the initial conditions were applied to both the airfoil wrapping O grid and the passage filling H grid.

Table 4. 2-D VBI code aerodynamic inputs

Parameter	Stator	Rotor
Rotor speed		rpm
Stage equivalent work		Btu/lb
stage expansion ratio		ratio
Inlet relative Mach number	user defined	user defined
Exit relative Mach number	user defined	user defined
Inlet relative flow angle	degrees	degrees
Exit relative flow angle	degrees	degrees
Inlet total temperature	°R	°R
Inlet total pressure	psi	
Corrected flow	lb/s	
Reynolds number	user defined	
Inlet turbulence intensity	%	
Reduced frequency	user defined	user defined
Vane setting angle	degrees	
Vane-Blade spacing	inches	

### E.2 The $k - \mathfrak{R}$ Two-Equation Model for Turbulent Viscosity

The overlapping nature of the O and H grids used in the VBI code presented a problem for typical turbulence models (e.g., Baldwin-Barth) where calculation of the dimensionless wall distance  $y^+$  was required. The turbulent viscosity  $\mu_t$  for the VBI code was modeled without the calculation

of  $y^+$  by using the  $k - \mathfrak{R}$  two-equation model (Kelecy and Delaney [54]). The turbulent viscosity  $\mu_t$  was calculated by a multistep process. The first step was solving for the transport variable  $\mathfrak{R}$ :

$$\mathfrak{R} = \frac{k^2}{\epsilon \nu} \quad (35)$$

and then using this to find the turbulent Reynolds number:

$$\text{Re}_T = \frac{\bar{\rho} \mathfrak{R}}{\mu}. \quad (36)$$

Once  $\mathfrak{R}$  and  $\text{Re}_T$  were calculated, the turbulent viscosity was solved for using:

$$\mu_t = C_\mu f_\mu \bar{\rho} \mathfrak{R} \quad (37)$$

where

$$f_\mu = \frac{1 - \exp(-A_\mu \text{Re}_T^{2/3})}{1 - \exp(-A_\epsilon \text{Re}_T^{2/3})}. \quad (38)$$

The constants involved with equation 37 and 38 were  $C_\mu = 0.09$ ,  $A_\mu = 2.5 \times 10^{-6}$ , and  $A_\epsilon = 0.2$ .

## APPENDIX F - Baseline Performance Loss Coefficient Estimation

The loss coefficient has been measured extensively by several researchers with an effort to create a universal curve fit for various blade shapes with different turning angles. The original experimental work of Ainley [35] has been expanded upon and re-iterated through the texts of Horlock [39] and Mattingly [20,55].

### F1 Extrapolation of Losses from Previous Experiments

Ainley [35] first published experimental loss coefficient data for turbine blades in 1948. Measurements of 2-D profile loss and total loss were made for variations of the T.6 turbine blade profile. The blade shape was tested at different inlet angles, axial chord to pitch ratios (solidity,  $\sigma$ ), Reynolds numbers, and thickness to chord ratios provide experimental data for a wide range of practical conditions. Ainley's measurements were made using a modified T.6 airfoil base profile. The T.6 was placed in a cascade and tested at a range of camber angles and spacings. Measurement of the loss coefficient ( $\gamma$ ) for the T.6 turbine blade in a reaction blade configuration was  $\gamma = 0.04$  and  $0.03$  for attached flow and inlet Reynolds numbers of 50k and 100k, respectively, and for an incidence of  $0^\circ$  (Ainley [35]). The reaction blade results of Ainley [35] agree very well with the measured Pak-B loss coefficient of  $\gamma = 0.038$  for an inlet Reynolds number of 100k.

### F2 Estimation of Losses Using Curve Fits

Ainley and Mathieson [36] continued to experiment with turbine blades providing a series of loss coefficient estimation curves for a range of solidities and gas flow exit angles. For the Pak-B design exit angle of  $60^\circ$ , the loss coefficient was 0.115 for impulse blade relations (inlet angle,  $\beta_1 = -\text{exit angle}$ ,  $\alpha_2$ ) and 0.023 for nozzle blade relations ( $\beta_1 = 0^\circ$ ). The experiments for these curves were completed at an approximate inlet Reynolds number of 123k with an incidence of  $0^\circ$ . Ainley and Mathieson [36] also provided a curve fit for their data so the profile loss coefficient other blade

shapes could be estimated:

$$\gamma = \left\{ \gamma_{(\beta_1=0)} + \left( \frac{\beta_1}{\alpha_2} \right)^2 \left[ \gamma_{(\beta_1=-\alpha_2)} - \gamma_{(\beta_1=0)} \right] \right\} \left( \frac{t/c}{0.2} \right)^{-\beta_1/\alpha_2} \quad (39)$$

where  $t/c$  is the thickness to chord ratio. Using equation 39 for the Pak-B design angles and thickness to chord ratio, the loss coefficient was estimated to be 0.069. The loss coefficient can be adjusted to account for changes in Reynolds number using a curve fit. The Reynolds number corrected loss coefficients are 0.07 and 0.12 at 50k and 100k, respectively. The difference in the estimation of loss coefficient using equation 39 and experiment can be attributed to the advised restriction that the equation only be used for  $0.15 < t/c < 0.25$  (Ainley and Mathieson [36]) where the Pak-B has a  $t/c = 0.134$  and the inability to account for differences in aspect ratio.

Horlock [37, 38] added to the work of Ainley [35] and Ainley and Mathieson [36] by incorporating the unpublished data of C. R. Soderberg. Horlock [37] presented the previously unpublished data next to the work of the published available data. Soderberg's data had loss coefficients of 0.082, 0.07 and 0.059 for Reynolds numbers of 50k, 100k and 200k, respectively, using blades with a higher thickness to chord ratio. Horlock [39] also presented a curve fit for Soderberg's data:

$$\gamma = 0.025 \left[ 1 + \left( \frac{\epsilon}{90} \right)^2 \right] \quad (40)$$

where  $\epsilon$  is the deflection angle in degrees. Using the Pak-B total turning (deflection) angle of  $95^\circ$ , the loss coefficient was predicted to be 0.053 with equation 40.

Craig and Cox [40] published a series of curve fits to account for several aspects of blade geometry. Flow angles, blade spacing, contraction ratio, and trailing edge thickness were accounted for in the figures published by Craig and Cox [40]. Using the figures with the geometry data for the Pak-B blade, loss coefficients were estimated to be 0.052, 0.043 and 0.034 for Reynolds numbers of 50k, 100k, and 200k. These values match the experimental data obtained for the Pak-B blade

when flow exits the blade passage attached to the suction surface. For example, for small separation zones at a freestream turbulence level of 4%, the estimated losses are only 10.3%, 10.3%, and 8.1% off from the experimental losses for Reynolds numbers of 50k, 100k, and 200k, respectively.

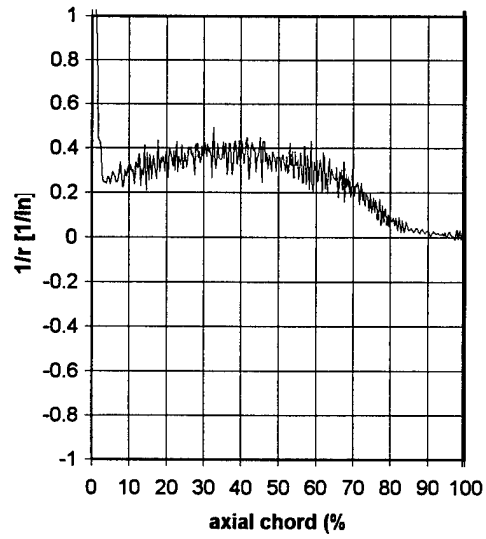
## APPENDIX G - Blade Surface Curvature Distribution

Wilson and Korkianitis [56] have shown that the boundary layer is directly affected by the continuity of the slopes that make up the surface of the blade. The continuity of the blade surface slope can be examined using the radius of surface curvature and the slope of the radius of curvature.

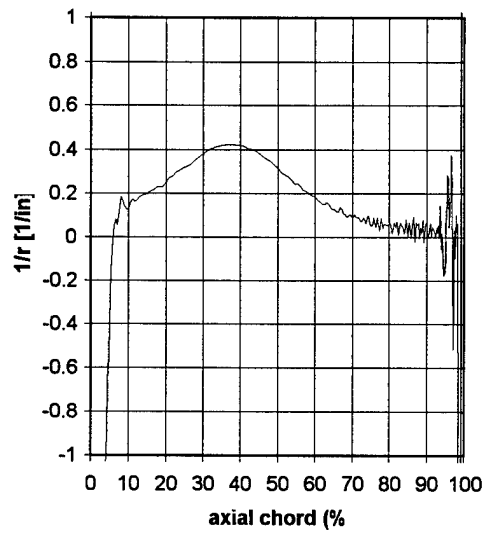
The radius of surface curvature can be determined using (Wilson and Korkianitis [56]):

$$\frac{1}{r} = \frac{(d^2y/dx^2)}{(1 + (dy/dx)^2)^{3/2}} \quad (41)$$

where  $dy$  and  $dx$  are the differences between sequential  $y$  and  $x$  coordinates, respectively, using a three point differencing scheme. The resulting values of  $1/r$  for the suction and pressure surfaces are shown in Figure 148. The curves in Figure 148 show several discontinuities due to limitations in the original coordinate data. These limitations prevented useful insight into what effects surface curvature may have had on the baseline separation position. The slope of the radius of curvature could not be calculated due to the same limitations.



a) Suction side



b) Pressure side

Figure 148. Radius of curvature plots for Pak-B blade.

## APPENDIX H - Hot Wire Control Equations

### H.1 Hot Wire Physical Characteristics

The hot wire used in freestream velocity and turbulence measurements was a single wire TSI 1210-T1.5. The wire element had a diameter of  $3.87 \times 10^{-3}$  mm ( $1.52 \times 10^{-4}$  inches) and a length of 1.27 mm (0.05 inches). The hot wire was powered by an IFA-100 Intelligent Flow Analyzer which also provided a voltage output which was calibrated to provide the flow velocity.

### H.2 Velocity Determination Equations

The velocity was calculated through a series of equations which accounted for changes in the flow condition including temperature, pressure, and humidity. The temperature within the tunnel was read through thermocouples while the current room pressure was entered into the computer through the keyboard. The humidity was obtained from an Omega Engineering, Inc. RH-71A Digital Hygro-thermometer and entered into the computer. The following equations were used for every data point taken by the hot wire. The control room computer processor speed was capable of providing all the velocity and turbulence level information in near real time. To calculate the air velocity, several factors were first calculated including viscosity, density, and the current molecular weight of air.

#### H.2.1 Atmospheric Molecular Weight

The humidity was entered into the computer in terms of its dew point in degrees Fahrenheit. This was quickly converted to Celsius and the following exponent calculated (Reid, et al. [57]):

$$Z = a_0 + T_D \cdot [a_1 + T_D \cdot [a_2 + T_D \cdot (a_3 + T_D \cdot a_4)]] \quad (42)$$

where  $T_D$  is the dewpoint in Celsius and  $a_0$  through  $a_4$  are constants. The humidity mass fraction is defined as:

$$m_f = 10^Z. \quad (43)$$

The humidity corrected molecular weight of air is therefore:

$$M_w = \frac{1}{\left[ \frac{(1-m_f)}{Mw_{air}} + \frac{m_f}{Mw_{H2O}} \right]} \quad (44)$$

where  $Mw_{air}$  is the molecular weight of dry air and  $Mw_{H2O}$  is the molecular weight of water.

## H.2.2 Atmospheric Constants

The mole fraction of water in the atmosphere was calculated with:

$$X_v = \left( \frac{Mw_{air}}{Mw_{H2O}} \right) \cdot \frac{m_f}{\left[ 1 + \left( \frac{Mw_{H2O}}{Mw_{air}} \right) \cdot m_f \right]} \quad (45)$$

where  $m_f$  is the previously calculated mass fraction. The mole fraction of air is simply:

$$X_a = 1 - X_v. \quad (46)$$

The gas constant was computed using the corrected molecular weight as:

$$R = \frac{8314.3}{M_w} \quad (47)$$

which is in units of  $J/(kg \cdot ^\circ K)$ .

To calculate the specific heat at constant pressure two initial variables were calculated:

$$c_{pa} = b_0 + T_K \cdot [b_1 + T_K \cdot (b_2 + T_K \cdot b_3)], \quad (48)$$

where  $T_K$  was the tunnel flow recovery temperature in Kelvin and  $b_0$  through  $b_3$  are constants. The other variable was:

$$c_{pv} = 1797.5 + 0.23 \cdot T_K. \quad (49)$$

The specific heat was then calculated using:

$$c_p = m_f \cdot c_{pv} + (1 - m_f) \cdot c_{pa} \quad (50)$$

The ratio of specific heats was determined from:

$$\gamma = \frac{c_p}{c_p - R} \quad (51)$$

and the speed of sound was calculated using:

$$a = \sqrt{\gamma \cdot R \cdot T_K}. \quad (52)$$

### H.2.3 Atmospheric Properties

To calculate the viscosity of the tunnel airflow, three coefficients were first computed. The first was:

$$\mu_{ua} = c_0 + T_K (c_1 + T_K \cdot c_2) \quad (53)$$

where  $c_0$  through  $c_2$  are constants and  $T_K$  is the tunnel temperature in degrees Kelvin. The second was (Reid, et al. [57]):

$$\phi_a = \left( 1 + \sqrt{\frac{\mu_{ua}}{\mu_{uv}}} \right) \cdot \frac{\left[ \left( \frac{MW_{H2O}}{MW_{air}} \right)^{0.25} \right]^2}{\sqrt{\left[ 8 \cdot \left[ 1 + \left( \frac{MW_{air}}{MW_{H2O}} \right) \right] \right]}} \quad (54)$$

where  $\mu_{uv}$  was a constant. The final coefficient was:

$$\phi_b = \phi_a \cdot \left( \frac{\mu_{uv}}{\mu_{ua}} \right) \cdot \left( \frac{MW_{air}}{MW_{H2O}} \right). \quad (55)$$

The viscosity was then computed using (Reid, et al. [57]):

$$\mu = \frac{X_a \cdot \mu_{ua}}{X_a + X_v \cdot \phi_a} + \frac{X_v \cdot \mu_{uv}}{X_v + X_a \cdot \phi_b} \quad (56)$$

where  $X_v$  and  $X_a$  were the mole fractions calculated previously.

The thermal conductivity was determined from four coefficients based upon the tunnel test section temperature in degrees Kelvin. The first coefficient was calculated using:

$$k_a = d_0 + T_K (d_1 + T_K \cdot d_2) \quad (57)$$

where  $d_0$  through  $d_2$  are constants. The second coefficient was:

$$k_v = e_0 + T_K (e_1 + T_K \cdot (e_2 + T_K \cdot e_3)) \quad (58)$$

where  $e_0$  through  $e_3$  are constants. The third and fourth coefficients were based upon  $k_a$  and  $k_v$ .

The third was (Reid, et al. [57]):

$$\psi_{12} = \frac{\left[ 1 + \left( \sqrt{\frac{k_a}{k_v}} \right) \cdot \left( \frac{MW_{air}}{MW_{H_2O}} \right)^{0.25} \right]^2}{\sqrt{8 \cdot \left[ 1 + \left( \frac{MW_{air}}{MW_{H_2O}} \right) \right]}} \quad (59)$$

The final coefficient was:

$$\psi_{21} = \frac{\left[ 1 + \left( \sqrt{\frac{k_v}{k_a}} \right) \cdot \left( \frac{MW_{H_2O}}{MW_{air}} \right)^{0.25} \right]^2}{\sqrt{8 \cdot \left[ 1 + \left( \frac{MW_{H_2O}}{MW_{air}} \right) \right]}} \quad (60)$$

The thermal conductivity was then calculated as (Reid, et al. [57]):

$$k = \frac{X_a \cdot k_a}{X_a + X_v \cdot \psi_{12}} + \frac{X_v \cdot k_v}{X_v + X_a \cdot \psi_{21}} \quad (61)$$

which allowed quick determination of the Prandtl number:

$$Pr = \frac{c_p \cdot \mu}{k} \quad (62)$$

which used the previously calculated specific heat at constant pressure.

The density of the air within the tunnel was simply calculated using:

$$\rho = \frac{P}{R \cdot T_k} \quad (63)$$

where  $P$  was the atmospheric pressure of the wind tunnel facility converted to metric units. No corrections were made for changes in density with increasing speed or blockage due to the low velocities used during testing.

#### H.2.4 Velocity Determination Using Atmospheric Properties and Hot Wire Voltage

The velocity of the air within the test section was calculated using the previously determined atmospheric properties of density, thermal conductivity, and Prandtl number. The calculated flow recovery and hot wire gas temperatures were also used along with some hot wire physical characteristics. The first of four coefficients calculated was:

$$F_1 = \frac{\rho \cdot d_w}{\mu} \quad (64)$$

where  $d_w$  is the hot wire diameter. The second coefficient was:

$$F_2 = \frac{V^2 \cdot \Omega_w}{(\Omega_w + 10)^2} \quad (65)$$

where  $\Omega_w$  was the hot wire probe operating resistance and  $V$  was the measured voltage. The third factor was:

$$F_3 = \left( \frac{T_m}{T_g} \right)^{T_R} \quad (66)$$

where  $T_m$  was the gas temperature determined as an average of the flow recovery temperature  $T_g$  and the probe temperature  $T_w$ . The exponent  $T_R$  was the temperature overheat ratio used by the IFA-100. The final coefficient was:

$$F_4 = \pi \cdot k \cdot l_w \cdot (T_w - T_g) \quad (67)$$

where  $l_w$  was the length of the hot wire and  $\pi$  is 3.14159. The temperature and humidity corrected velocity was then calculated first using:

$$F_5 = \frac{\left( \frac{F_2 \cdot F_3 \cdot Pr^{-\frac{1}{3}}}{F_4 - C_{int}} \right)}{D_{slo}} \quad (68)$$

which was then used in:

$$U = \frac{[F_5]^{Re_{exp}}}{F_1} \quad (69)$$

where  $Re_{exp}$  was the exponent used in the calibration of the hot wire. The intercept for the hot wire calibration is  $C_{int}$  and the slope is  $D_{slo}$ .

To determine the flow stagnation temperature the mean velocity  $\bar{U}$  was first calculated and then the following equation solved:

$$T_g = T_w - \frac{0.85 \cdot \bar{U}^2}{2 \cdot c_p} \quad (70)$$

which was then compared to the initially used  $T_g$ . These equations were all then recalculated to provide a more accurate velocity until the previously used and the current calculation for  $T_g$  were within 0.005 Kelvin.

### H.3 Turbulence Determination Equations

Turbulence intensity was determined after the velocity had been accurately resolved. The collection of velocity data involved sampling the voltage of the hot wire 40,000 times at a rate of 10,000 samples per second. The velocity was calculated for each of the 40,000 data points. With the 40,000

velocity values, a mean velocity was calculated as:

$$\bar{U} = \frac{\sum_1^n U_x}{n} \quad (71)$$

where  $U_x$  was the individual velocity data point stored in an array. Also calculated was the deviation,  $\sigma$ , from the mean and the division of these two provided the turbulence intensity. The turbulence intensity was multiplied by 100 to give the resulting value in terms of percent. The calculation of turbulence was:

$$Tu = \left( \frac{\sigma}{\bar{U}} \right) \cdot 100. \quad (72)$$

## APPENDIX I - Uncertainty Analysis

### I.1 Surface Static Pressure Cp Measurements

Using the method described by Kline and McClintok [33], the first step in determining the uncertainty is the calculation of the partial derivatives. The surface static pressure measurement was calculated using:

$$C_p = \frac{P_{0,inlet} - P_{s,x}}{\frac{1}{2}\rho\bar{U}_{inlet}^2} \quad (73)$$

where  $P_{0,inlet}$  and  $U_{inlet}$  were the total pressure and velocity, respectively, measured upstream of the blade cassette. This equation can be re-written to account for the calculation of density as:

$$C_p = \frac{2(\Delta P)RT}{P_A\bar{U}_{inlet}^2} \quad (74)$$

where  $\Delta P$  was the pressure difference measured across the transducer. The density term was broken into its components where  $P_A$  was the atmospheric pressure within the wind tunnel building,  $R$  is the gas constant and  $T$  was the tunnel test section temperature.

There are four partial derivatives that need to be calculated from equation 74, including measurements of  $\Delta P$ ,  $T$ ,  $P_A$ , and  $U_{inlet}$ . There is no need to calculate the partial derivative with respect to  $R$  since it is a constant. The four partial derivatives are:

$$\frac{\partial C_p}{\partial \Delta P} = \frac{2RT}{P_A\bar{U}_{inlet}^2} \quad (75)$$

$$\frac{\partial C_p}{\partial T} = \frac{2(\Delta P)R}{P_A\bar{U}_{inlet}^2} \quad (76)$$

$$\frac{\partial C_p}{\partial P_A} = \frac{-2(\Delta P)RT}{P_A^2\bar{U}_{inlet}^2} \quad (77)$$

$$\frac{\partial C_p}{\partial U} = \frac{-4(\Delta P)RT}{P_A\bar{U}_{inlet}^3} \quad (78)$$

The second step in determining the uncertainty is to calculate the square of each of the partial derivatives and divide each by the original expression squared (equation 73). Each of the partial derivatives after squaring and dividing becomes:

$$\frac{\left(\frac{\partial C_p}{\partial \Delta P}\right)^2}{C_p} = \frac{1}{\Delta P^2} \quad (79)$$

$$\frac{\left(\frac{\partial C_p}{\partial T}\right)^2}{C_p} = \frac{1}{T^2} \quad (80)$$

$$\frac{\left(\frac{\partial C_p}{\partial P_A}\right)^2}{C_p} = \frac{1}{P_A^2} \quad (81)$$

$$\frac{\left(\frac{\partial C_p}{\partial U}\right)^2}{C_p} = \frac{4}{U^2} \quad (82)$$

The uncertainty in the surface pressure coefficient equation can now be determined using:

$$\varpi_{C_p} = C_p \cdot \left[ \left(\frac{\varpi_{\Delta P}}{\Delta P}\right)^2 + \left(\frac{\varpi_T}{T}\right)^2 + \left(\frac{\varpi_{P_A}}{P_A}\right)^2 + \left(2 \cdot \frac{\varpi_U}{U}\right)^2 \right]^{1/2} \quad (83)$$

where  $\varpi$  was the uncertainty of each measurement made based upon the equipment used.

## I.2 Loss Coefficient Measurements

Since the loss coefficient and pressure coefficient use the same equation but with different symbols, the uncertainty analysis for the loss coefficient was determined using the method described previously for the surface pressure coefficient.

### I.3 Velocity Measurements

The velocity from the hot wire was calibrated using a water manometer. The velocity can be determined from the manometer through:

$$U = \sqrt{\frac{2(\Delta P) RT}{P_A}} \quad (84)$$

where  $\Delta P$  was the difference measured between the total and static ports of a pitot tube. Following the same steps as done with the surface pressure coefficient, the uncertainty for the velocity can be written as:

$$\varpi_U = U \cdot \left[ \left( \frac{\varpi_{\Delta P}}{2 \cdot \Delta P} \right)^2 + \left( \frac{\varpi_T}{2 \cdot T} \right)^2 + \left( \frac{\varpi_{P_A}}{2 \cdot P_A} \right)^2 \right]^{1/2} \quad (85)$$

### I.4 Wake Momentum Deficit Measurements

The uncertainty estimation for the wake momentum deficit was calculated using the same method described previously. The momentum deficit was defined as:

$$\Theta = \Sigma \left( \frac{U_w}{U_\infty} \right) \left( 1 - \frac{U_w}{U_\infty} \right) dy \quad (86)$$

where the three partial derivatives were:

$$\frac{\partial \Theta}{\partial U_w} = \frac{dy}{U_\infty} - 2 \frac{U_w dy}{U_\infty^2} \quad (87)$$

$$\frac{\partial \Theta}{\partial U_\infty} = \frac{-U_w dy}{U_\infty^2} + 2 \frac{U_w^2 dy}{U_\infty^3} \quad (88)$$

$$\frac{\partial \Theta}{\partial dy} = \frac{-U_w}{U_\infty} - \frac{U_w^2}{U_\infty^2} \quad (89)$$

The next steps were then completed using a spreadsheet program. Each of the partial derivatives were calculated and then squared. The square of the three uncertainties ( $\omega_{U_w}^2$ ,  $\omega_{U_\infty}^2$ ,  $\omega_{dy}^2$ ) was also calculated. The spreadsheet then multiplied the square of the partial derivative with its respec-

tive uncertainty squared. These products were then added and the square root taken. This can be written as:

$$\bar{\omega}_{\Theta} = \left[ \left( \omega_{U_w}^2 \cdot \left[ \frac{\partial \Theta}{\partial U_w} \right]^2 \right) + \left( \omega_{U_{\infty}}^2 \cdot \left[ \frac{\partial \Theta}{\partial U_{\infty}} \right]^2 \right) + \left( \omega_{dy}^2 \cdot \left[ \frac{\partial \Theta}{\partial dy} \right]^2 \right) \right]^{1/2} \quad (90)$$

## APPENDIX J - Rejected Separation Control Methods

### J.1 Separation Control Methods Unsuitable for LPT Use

Several methods initially considered for this project are presented in Figures 149 through 155. These methods have been documented in research for the reduction of separated flow and reduced drag. These methods were rejected; however, since the reported findings have shown various undesirable qualities.

#### J.1.1 Triangular Plow Vortex Generator Device

The plow is a submerged vortex generator (see Figure 149a) which has been suggested by many authors as a means for reducing separation. Chang [43] documents this design which was to be used in a compressor cascade to alleviate the shock-induced boundary layer separation (Austin [58]). Time constraints prevented Austin [58] from completing that testing and it was not until 1996 that Gernerding and Shreeve [59] managed to complete the work. The unexpected result for the Mach 1.4 flow indicated an improved turning angle of 0.94 degrees, but also an increase in flow losses by approximately 8%.

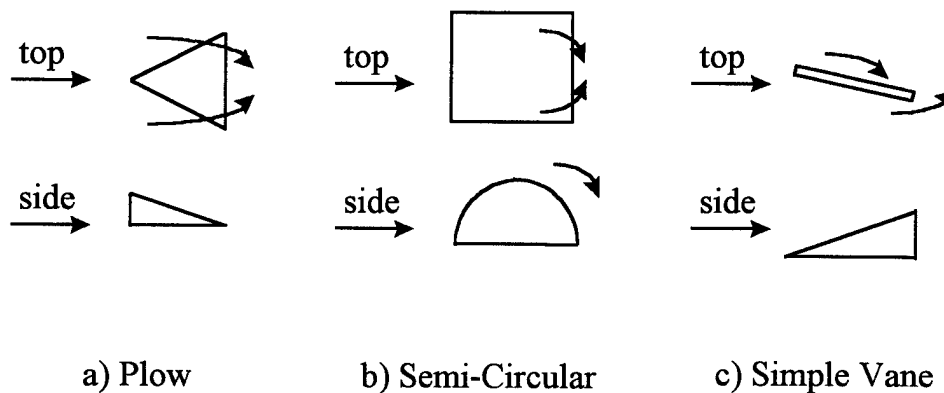


Figure 149. Plow, Semi-Circle and Vane concepts eliminated by available data.

### **J.1.2 Semi-Circle Vortex Generator Device**

The semi-circle is constructed from a solid rod cut in half longitudinally and attached flat side down to the surface which suffers separation problems (see Figure 149b). These cut rods were then placed in either a parallel or V pattern. Rao and Kariya [60] conducted semi-circle experiments with different device sweep angles, spacing and height on a flat plate but with results poorer than the other designs investigated by the same authors which included typical vane vortex generation devices. The unfavorable pressure recovery results found by Rao and Kariya [60] indicate this design was a poor candidate for the conditions found in a LPT.

### **J.1.3 Simple Vane Vortex Generator Device**

The simple vane was another concept considered by Rao and Kariya [60] that consisted of a simple vertical triangle with height equal to the boundary layer thickness. This design was considered as a baseline case for comparison and illustrated the capability for retaining attached flow over a flat plate (see Figure 149c). The vanes also showed a substantial reduction in the total pressure loss, but with a highly distorted profile for  $C_p$  over the baseline case. Sweep angles tested were  $60^\circ$  and  $70^\circ$  relative to the flow velocity. Considering the height of this design, a substantially higher drag penalty would result from its use compared to a submerged vortex generator design.

### **J.1.4 Passive Cavity Using Adverse Pressure Gradient**

McCormick [61] examined the passive cavity method on a flat plate as a means for reducing the large separation bubble due to shock interaction at speeds of Mach 1.56 to 1.65. The passive cavity utilizes the adverse pressure gradient behind the separation location to provide some flow through a cavity within the plate or airfoil and into the boundary layer ahead of the separation line. Results indicated the benefit of reducing the total pressure loss through the shock system, but significantly increasing the boundary layer losses downstream. Possible implementation of the passive cavity is

displayed in Figure 150a. This method was again attempted by Lin et al. [18] with a convex curved surface, simulating one side of an airfoil with turning. Results indicated that the passive porous surface increased the reattachment distance instead of reducing it. For the low Reynolds numbers of the LPT, this method was considered unsuitable.

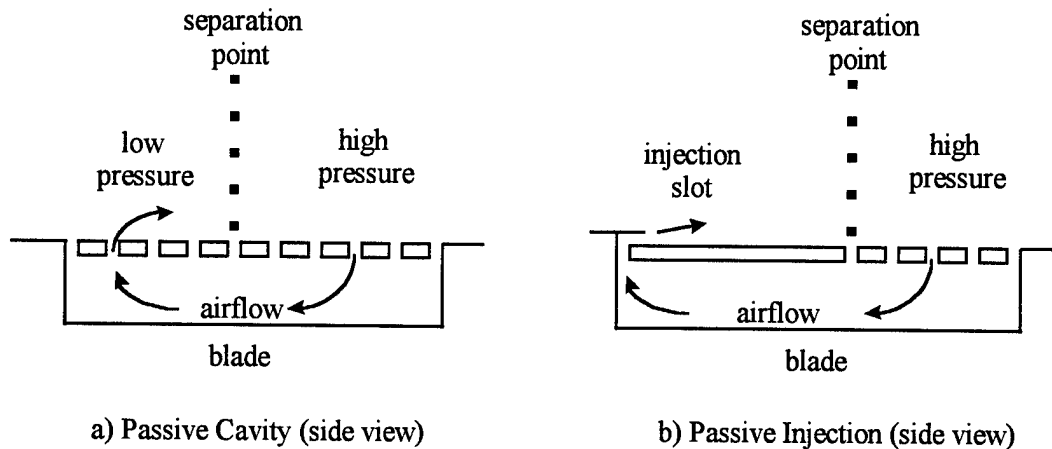


Figure 150. Porous suction surface methods.

### J.1.5 Passive Injection Using Adverse Pressure Gradient

The passive injection method uses a porous wall similar to the passive cavity method described by McCormick [61], but with the air now only allowed to flow through a narrow slot ahead of the separation line. This provides a powered jet effect in the downstream flow direction as seen in Figure 150b. This method was rejected because Lin et al. [18] discovered that passive injection does not provide any reduction in separation losses over the unmodified smooth surface.

### J.1.6 $\pm 45^\circ$ Small-Scale Riblets Located On the Suction Surface

The  $\pm 45^\circ$  riblet technique is similar to conventional riblets but with the ribs in a  $\pm 45^\circ$  pattern in the area where separation occurs. Attempted by Lin et al. [18] over a convex surface, the results for a variety of flow conditions always increased the reattachment distance. The reduced pressure

recovery of the model with this modified surface (see Figure 15 1a) indicated increased losses when compared to the baseline case.

#### **J.1.7 Leading Edge Vane Vortex Generators**

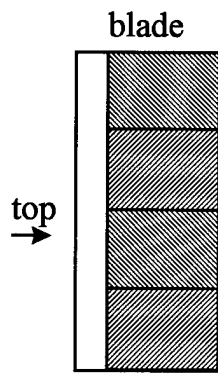
Chang [43] designed the leading edge vane vortex generators to extend into the freestream airflow at the front of the airfoil to provide trailing longitudinal vortices. Chang [43] theorized that the vortices generated would be of sufficient strength to maintain attached flow over the entire surface. The application of this design (see Figure 15 1b) would create several problems in turbine engine applications. Addition of the leading edge vane vortex generators would effectively decrease the spacing between the blade rows. In addition to the spacing and heat transfer problems involved, the lack of data on this concept means that implementation would have unpredictable results with the Pak-B blade.

#### **J.1.8 Wheeler Channel Groove Cut Into Surface**

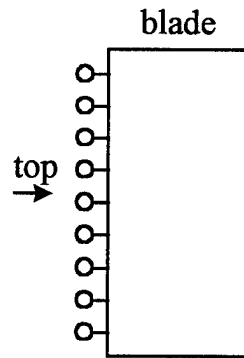
The Wheeler channel is a V-shaped groove cut into the surface (see Figure 15 1c). The air within the boundary layer spills into the channel and vortices are thus formed. Wheeler [62] suggests using multiple rows of these channels if necessary to maintain attached flow all the way to the trailing edge. Implementation of the complex Wheeler channel design involves cutting rows of channels into the turbine blade which presents a formidable machining cost. This design concept was eliminated due to the complexity and cost of machining the wheeler channels.

#### **J.1.9 Afterbody Groove Cut Into Surface**

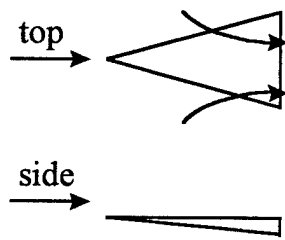
The afterbody groove is a cut-out V-shaped notch with a valley angle of  $90^\circ$  placed over the trailing portion of the surface where separation normally occurs. Tested by Howard et al. [63] on an axisymmetric bluff body for Reynolds numbers (based on diameter) from  $20 \times 10^3$  to  $200 \times 10^3$ , these grooves reduced drag by 16% to 33% by causing the flow within the grooves to remain



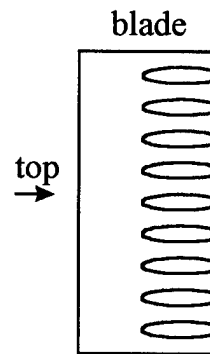
a) +/- 45 Riblets



b) Leading Edge Vanes



c) Wheeler Channel



d) Afterbody Groove

Figure 151. Rejected methods with difficult application.

attached. Howard et al. [63] speculated that the groove provides a pumping action for the three-dimensional separated flow regions similar to a fluid ejector. The lack of available documentation for this experiment does not support application to a LPT blade. The more extensively tested V-grooves of Lin et al. [18] discussed in Chapter 9 are similar to the afterbody groove and have been chosen for implementation on the Pak-B blade since they provide the same effect as the afterbody groove but had better documentation on the implementation of the technique.

#### J.1.10 Small-Scale V-Groove Riblets

Riblets are small scale V-grooves (see Figure 152a) which have been extensively investigated by Walsh [64–66] and by Bacher and Smith [67, 68]. The riblet sizes are determined by the non-dimensionalized height and spacing based upon law of the wall coordinates using the skin friction coefficient  $C_f$  and kinematic viscosity  $\nu$ . Nondimensional height of the riblets is defined as:

$$h^+ = \left( \frac{hu_\infty}{\nu} \right) \sqrt{\frac{C_f}{2}} \quad (91)$$

where  $h$  is the physical height. This allows easy graphing of results on a  $h^+$  vs.  $s^+$  plot for a variety of test cases. The nondimensional spacing between riblet peaks is similarly defined as:

$$s^+ = \left( \frac{su_\infty}{\nu} \right) \sqrt{\frac{C_f}{2}} \quad (92)$$

Walsh [64] has attained drag reductions for a flat plate with a turbulent boundary layer of up to 8% for  $h^+ \approx 10$  and  $s^+ \approx 15$  while Gallagher and Thomas [69] found no drag reduction and only a local 20% reduction in skin friction. The scope of possible drag reduction using riblets is narrowed by the results of Choi et al. [70] who found that for laminar flows no net drag reduction is possible with riblets.

Many attempts have been made to use the apparent drag reduction and flow attachment qualities of the riblets. These include the works of Wieck [71] on cylinders and airfoils, Reagan [72] on

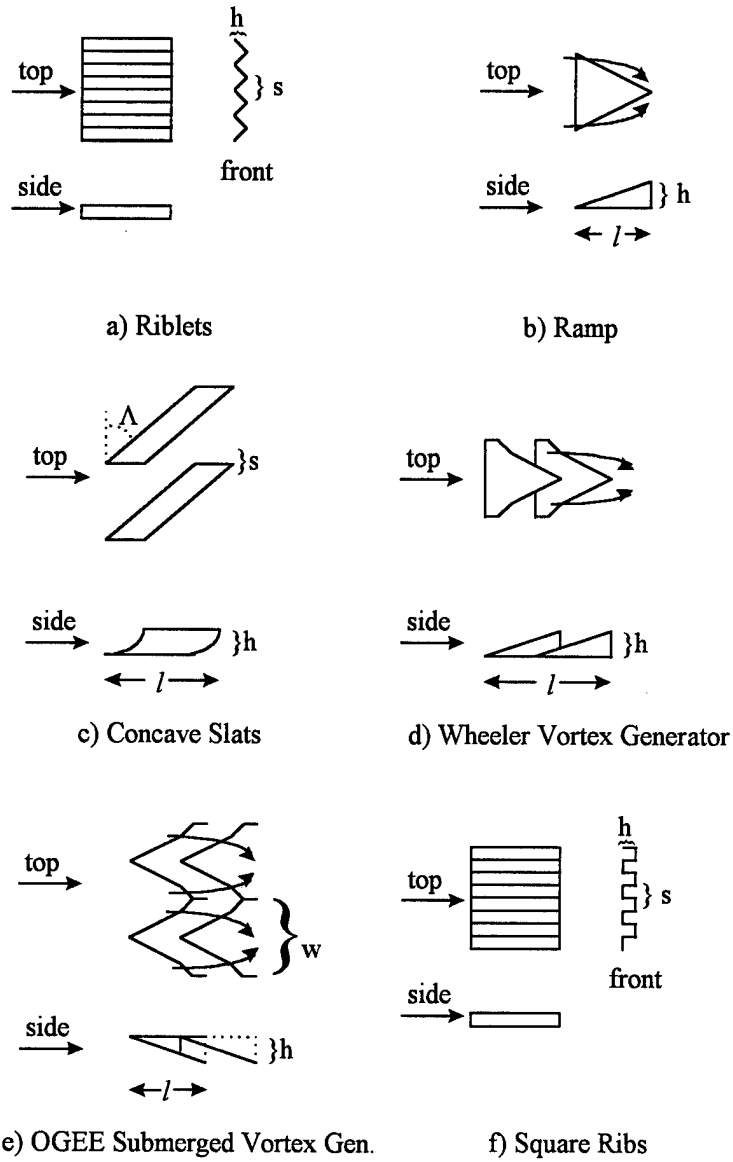


Figure 152. Other submerged design modifications considered and rejected.

diffusers and Rothenflue [73, 74] on concave surfaces. Wieck [71] demonstrated a separation delay from 2% to 11% with riblets for an airfoil in an adverse pressure gradient, depending on freestream velocity. Rothenflue [73] used riblets in a compressor cascade with the riblets giving the maximum benefit on the pressure surface. Suction surface riblet placement results were summarized as increasing the flow turning angle by 1%. Rothenflue [74, 75] also showed a delay in transitioning due to Görtler vortices forming above the riblets for a concave surface.

Application of the riblet concept to turbomachinery has been attempted by Chen et al. [14]. Using the ideal riblet parameters  $h^+ \leq 30$  and  $s^+ \leq 30$  as determined by Walsh [64], a 10% loss reduction benefit for a compressor cascade was found by Chen et al. [14] when the riblets were applied to the pressure surface and not the suction surface. When riblets were applied to the suction surface Chen et al. [14] found no drag reduction or delay in separation from the suction side. While small-scale riblets have shown reductions in drag for flat plate flows, the extreme turning and pressure gradients of the LPT require larger flow mixing devices if the technique is to be applied successfully. Considering the disappointing results of small-scale riblets they will not be applied to the Pratt and Whitney Pak-B blades.

#### **J.1.11 Triangular Ramp Vortex Generator**

Similar to the plow design (see Figure 152b), this device was found by Barber et al. [76] to have an optimal height of  $h \approx \frac{\delta_0}{3}$  with an ideal placement ahead of the original separation line. The optimal length to half-width to height ratio for the ramp was found to be 6:5:1. Flow spilling over the ramp produces trailing edge vortices which energize the lower momentum fluid near the surface, encouraging separation delay or prohibiting it entirely. Barber et al. [76] found that this submerged concept has one-tenth of the parasitic drag than larger devices which extend into the freestream. The

same author also found that the effective range downstream of the ramp was only  $\frac{10}{3}\delta_0$ , which for the turbine case is insufficient to manage the entire separation region.

#### **J.1.12 Parallel Concave Slat Vortex Generators**

Concave slats used by Rao and Kariya [60] were constructed from standard window venetian blinds and affixed to a flat plate surface. Depicted in Figure 152c, these slats were tested both in parallel and V-shaped configurations. The V-shaped test used the slats connected at their leading edges facing into the flow, with the trailing edges spreading apart at a  $30^\circ$  angle. The V configuration however produced a low-energy wake behind the attached devices, giving the parallel configuration better performance and a higher  $C_{p,max}$  recovery. The design and implementation of this device over the span of a curved turbine airfoil would prove difficult and perhaps retard performance at higher Reynolds numbers. The complexity of installing this device with the concerns of keeping the slats clean in an operable engine eliminate this concept.

#### **J.1.13 Wheeler Vortex Generators**

Designed as a low speed vortex generator, this device has an overall height of only  $h = 0.10\delta_0$ . Wheeler vortex generators are placed in an overlapping fashion on the surface (see Figure 152d), forming a "Wheeler Doublet." Optimum dimensions determined from subsonic testing with  $U_\infty = 40.23$  m/s (132 ft/s) by Lin et al. [18] showed placement should be  $2\delta_0$  ahead of the original, unmodified separation location with a length of  $1.28\delta_0$ . Wheeler Doublets tested by Lin, et al. [18] on a curved ramp simulating the suction surface of a blade showed a reduction in reattachment distance of up to 66% over the baseline case, with a delay in separation of 12.7 millimeters (0.5 inches). Drag for this device was estimated at  $1/44$  of the  $0.80\delta_0$  tall vane type vortex generator also tested by Lin, et al. [18]. McCormick [61] tested slightly taller Wheeler Doublets with an  $h = 0.36\delta_0$  for supersonic flow ( $M_\infty = 1.56-1.65$ ) with similar beneficial results. This good performance along

with the small height and less drag than many other devices makes this a desirable option for this study; however, implementation of such small devices over the highly curved surface of a turbine blade with a severe adverse pressure gradient would be very difficult and so this concept was not tested.

#### **J.1.14 Ogee Submerged Vortex Generators**

The Ogee (a reverse S-shaped curve) is a submerged vortex generator that is quite similar to the geometry of the Wheeler doublet described previously. The difference between the Ogee submerged vortex generator and the Wheeler vortex generator is that the Ogee is engraved into the surface rather than sticking out of it as the Wheeler vortex generator does (see Figure 152e). Also designed by Wheeler [62], the Ogee has a depth equal to 9% of the axial chord length and is doubled up by placing the apex of the next row of Ogee's at the 50% location of the current row. Optimum placement from the baseline separation location all the way to the end has maintained attached flow through turning angles of  $65^\circ$  on wind tunnel models of automobiles (Wheeler [62]). While quite capable of maintaining attached flow, the drastic modification necessary to the low-pressure turbine blades would be far too extensive for practical application. Implementation of this concept would be much more difficult than the simple, passive fix this investigation has found with the use of dimples.

#### **J.1.15 Small-Scale Square Ribs**

Simple inspection of Figure 152, parts a and f, shows the similarity of the square rib concept to those of riblets. While not tested as thoroughly as V-groove riblets, the same principles of nondimensional height ( $h^+$ ) and spacing ( $s^+$ ) have been applied. Maciejewski and Rivir [77] tested square ribs to see the effects on the heat transfer coefficient in a linear turbine cascade and found an average reduction of 7%. Their experiments were conducted for  $44,000 < Re < 410,000$  and freestream turbulence of  $0.8\% < Tu < 12.3\%$ ; however, no measurements were made concerning

the effect on separation. Maciejewski and Rivir [77] do provide the insight though that for application of such a device over an airfoil, the average value of  $h^+$  across the blade must be less than 5 in order for the local values of  $h^+$  to take on desirable values between 5 and 25. Since this research will focus only on concepts which will provide a profile drag reduction for Pak-B LPT blades, the lack of any drag data for this device eliminated this concept.

#### J.1.16 Large-Scale Vortex Generators

Based upon the early work of Taylor [45] the large-scale vortex generator is a small NACA 64-812 airfoil sticking through the boundary layer and into the freestream flow. While inherently having more drag than submerged designs, it is also much more effective. The design consists of a tapered airfoil of height  $h = 1.2\delta_0$ , with the quarter chord point unswept. The root chord is optimally  $3.84\delta_0$  while the tip chord is just  $1.92\delta_0$ . The airfoils are placed spanwise across the blade in an alternating fashion (to provide counter-rotating vortices) with a spacing of  $2.4\delta_0 \leq s \leq 6\delta_0$  between vortex generators, and ahead of the baseline separation a distance of  $10\delta_0$  to  $30\delta_0$ . Adjustments might have been necessary to find the correct angle of attack for Pak-B airfoils, but  $16^\circ$  was suggested as a starting point by Taylor [45] for any airfoil shape. Taylor [45] found through experiments with these large devices that drag reductions are obtained, but only when the initial conditions were quite poor. Considering the magnitude of the separation that was found over the Pak-B suction surface at  $Re = 50k$  and  $Tu = 1\%$ , these devices might have performed well. For example, testing by Taylor [45] of a NACA 16-325 airfoil at  $Re_c = 1.8 \times 10^6$  with the large-scale vortex generators (see Figure 153) showed a 33% increase in maximum lift coefficient ( $C_L$ ) and a general decrease in drag except when  $C_L$  dipped below 0.4 where flow was fully attached anyway. Drag increases for this benign flow of low  $C_L$  was approximately 72% from 0.018 to 0.031. Considering the drag increase for attached

flows at high Reynolds numbers in the LPT and the difficulty in implementing and maintaining the concept in a real engine, this idea was rejected.

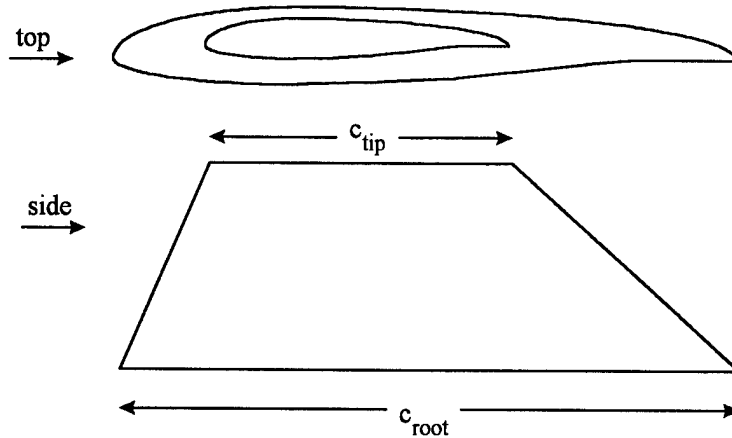


Figure 153. Large-Scale vortex generator using NACA airfoil.

#### J.1.17 Transverse Grooves Placed at Baseline Separation Point

As seen in Figure 154, the transverse groove concept includes square ribs engraved transversely to the flow direction along the span of the blade. The method by which this reduces the separation is described by Lin et al. [18] as a substitution of several smaller separation regions which provide a wall slip boundary condition. These smaller regions of separation replace the larger separated-flow region. Optimal placement of the grooves is one boundary layer thickness ( $\delta_0$ ) ahead of the baseline separation extending past the original separation point to one boundary layer thickness behind it, coinciding with the region of the greatest adverse pressure gradient. Experiments were conducted by Lin et al. [18] on a curved ramp with a turning of  $25^\circ$  and a radius of 20.3 cm (8 inches). The experiments were conducted at low velocities of  $U_\infty = 40.23$  m/s (132 ft/s) and showed these grooves reduced the reattachment distance by approximately 50%. To achieve this desirable result, the width of the groove valleys was  $b = 0.144\delta_0$ , the rib height was  $h = 0.385\delta_0$ , and the rib

thickness,  $t = 0.048\delta_0$  using the nomenclature of Figure 154. No other data concerning skin friction coefficient was given for this experiment.

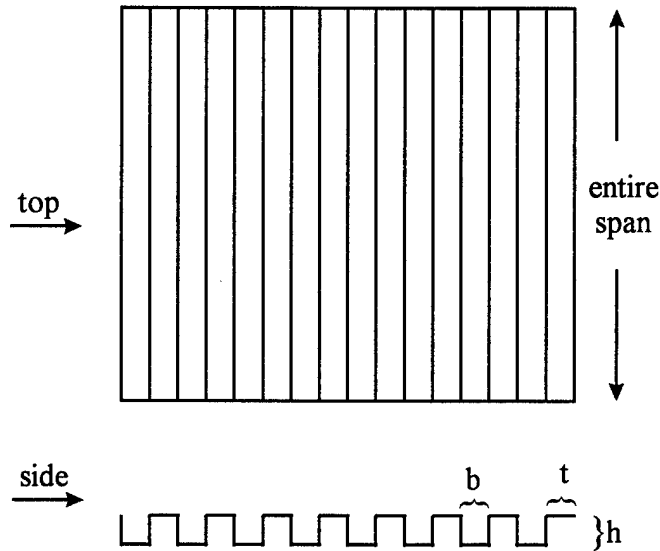


Figure 154. Transverse groove separation control device.

Upon further consideration this method was rejected due to the higher loss coefficients which may result from use at high Reynolds numbers. High Reynolds number flows such as take-off and sea-level operations do not require separation control and increasing the boundary layer thickness with a boundary layer trip would be detrimental to performance.

#### J.1.18 Increased Surface Roughness Over Surface of Pak-B Blade

The intentional roughing of the airfoil surface (see Figure 155) energizes the boundary layer into a turbulent state. Organized surface roughness as a means to reduce separation losses has been suggested by many authors including Radeztsky et al. [78], Mueller [28], and Yurchenko [30]. Previous experiments have placed roughness strips at two different locations: the leading edge, and the point of suction side peak curvature. Bloch and Mueller [79] conducted experiments for both the leading edge and suction peak cases. Bloch and Mueller's results indicated a prevention of trailing

edge separation with roughness applied to the suction peak of a Wortmann FX-63-137 airfoil for low Reynolds numbers. Minimum drag decreased slightly over the baseline smooth airfoil while maximum  $C_L$  decreased by 21% for a range of Reynolds numbers from  $100 \times 10^3$  to  $200 \times 10^3$ . Halstead and Solomon [24] recommended covering the entire airfoil with increased roughness which may prevent the loss in lift coefficient by tripping the flow into a turbulent state early on.

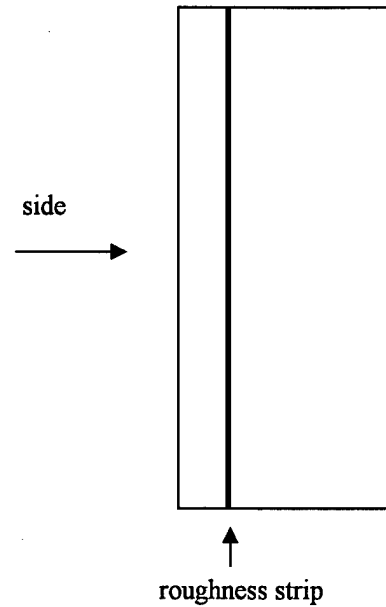


Figure 155. Surface roughness strip applied to Pak-B airfoil.

The moderate success of Bloch and Mueller's (Bloch and Mueller [79]) work may be increased by using a different roughness height for the given conditions. Williams [80] found a range of roughness values that least adversely affected the loss coefficient for his cascade. Roughness values below or above this range resulted in higher loss coefficients. An example of how grit roughness could have been used on the Pak-B LPT airfoil would be a 2 mm wide strip placed 5 mm downstream of the leading edge. The mean height of the roughness elements would be selected based on the optimal roughness Reynolds number:

$$\text{Re}_k = \frac{\rho u_k k}{\mu} \quad (93)$$

where  $k$  is the roughness height and  $u_k$  is the velocity at the top of the roughness element. Roughness studies by Braslow et al. [81] and Bragg et al. [82] on a NACA 0012 airfoil (for chord Reynolds number greater than  $3 \times 10^6$ ) have found an ideal value for  $\text{Re}_k$  of 600 was useful for tripping a laminar boundary layer. The associated increase in drag coefficient was 15% for adding the roughness strip. Achenbach [83] performed research with sand-roughened spheres and found a drag reduction for very narrow ranges of Reynolds numbers, but drag increases (compared to smooth spheres) for Reynolds numbers (based upon diameter) above  $3.8 \times 10^5$ . The intentional tripping of the boundary layer using a roughness strip was also rejected because of the hindered performance at high Reynolds numbers typical of take-off conditions.

## APPENDIX K - Limitations of LPT Computational Modelling

### K.1 Research Conducted by Halstead et al. [23]

Halstead et al. [23] studied different types of software codes that included comparisons to experimental values of displacement thickness,  $\delta^*$ , momentum thickness,  $\theta$ , momentum Reynolds number,  $Re_\theta$ , and shape factor,  $H = \frac{\delta^*}{\theta}$ . The software used by Halstead et al. [23] can be divided into three basic categories: steady boundary layer analyses, steady Navier-Stokes analyses, and unsteady boundary layer analysis. All of the codes failed to accurately predict transition location and length. Many of the codes predicted laminar separation where none existed. Results from all the codes used by Halstead et al. [23] gave reasonable answers for momentum and displacement thickness as well as momentum Reynolds number. One steady two-dimensional boundary layer analysis code used by Halstead et al. [23] was STANX, a variation of the STAN5 program developed by Crawford and Kays [84]. This program uses the compressible form of the boundary layer equations while incorporating a mixing length turbulence model adjusted for pressure gradients. The program must have a correlation supplied to estimate transition location, and cannot determine the length of transition. With this constraint, the flow is assumed to transition to turbulent flow at a single point. In addition to error in transition prediction, the STANX code results showed laminar separation prior to transition on a second-stage turbine nozzle, even though no separation was measured by Halstead [13] for the same environmental conditions. This is in part due to the inability of the code to include the unsteady calming effect of the passage of wakes through the boundary layer (Halstead et al. [23]). For the low Reynolds number cases, the STANX code overpredicted the profile loss coefficient by up to 56% (Halstead et al. [23]).

Halstead et al. [23] also examined a code similar to STANX, the two-dimensional KEP program for study of a low pressure turbine blade. KEP is a modified version of STANX which includes a k-

$\epsilon$  turbulence model for low Reynolds numbers. This program uses internal correlations to estimate transition onset, eliminating the need for user inputs. KEP estimated transition locations far too aft along the blade suction surface compared to the measurements. Predictions of loss coefficient by the KEP program were also overpredicted by 6.2% to 59.1% depending upon Reynolds number and turbulence intensity.

## Vita

Captain James Lake was born in Sauk City, Wisconsin, on 15 November 1968. Mr. Lake moved to Florida where he studied Aerospace Engineering at the Florida Institute of Technology. Being the first to graduate from F.I.T. with a B.S. degree in Aerospace Engineering helped in his decision to pursue an advanced degree at Georgia Tech. The graduate degree Mr. Lake worked on was funded by the United States Army, with the only stipulation that he study rotorcraft design. While at Georgia Tech Mr. Lake worked with the Autonomous Unmanned Aerial Vehicle System (AUAVS) competition as the team leader of the Subsystem Integration section. The helicopter modified for the study successfully performed autonomous hover and attitude corrections. Mr. Lake was also team leader of a vertical take-off and landing (VTOL) cargo aircraft design competition. The tilt-wing cargo plane design won third place in a national contest sponsored by Federal Express.

Mr. Lake entered the United States Air Force Officer Training School at Maxwell AFB on 25 Jan 1994. Completion of this training led to his first assignment at the 2nd Space Operations Squadron, Falcon AFB. While at 2SOPS 2Lt. Lake worked as a crew member for the Global Positioning System of navigational satellites, then the world's largest operational satellite constellation. Mr. Lake successfully performed many satellite station keeping maneuvers and assisted in the integration of the next generation of GPS satellites and operational software.

Immediately after his promotion to 1Lt., he began studies at the Air Force Institute of Technology under the Doctor of Philosophy program working with Dr. Paul King. Work at AFIT and AFRL using a newly designed and built linear cascade tunnel to find means of controlling separation flow losses from low pressure turbine blades was completed in June 1999.

REPORT DOCUMENTATION PAGE			Form Approved OMB No. 0704-0188		
Public reporting burden for this collection of information is estimated to average 1 hour per response, including the time for reviewing instructions, searching existing data sources, gathering and maintaining the data needed, and completing and reviewing the collection of information. Send comments regarding this burden estimate or any other aspect of this collection of information, including suggestions for reducing this burden, to Washington Headquarters Services, Directorate for Information Operations and Reports, 1215 Jefferson Davis Highway, Suite 1204, Arlington, VA 22202-4302, and to the Office of Management and Budget, Paperwork Reduction Project (0704-0188), Washington, DC 20503.					
1. AGENCY USE ONLY (Leave blank)		2. REPORT DATE June 1999	3. REPORT TYPE AND DATES COVERED PhD Dissertation		
4. TITLE AND SUBTITLE Flow Separation Prevention on a Turbine Blade in Cascade at Low Reynolds Number			5. FUNDING NUMBERS		
6. AUTHOR(S) James P. Lake					
7. PERFORMING ORGANIZATION NAME(S) AND ADDRESS(ES) Air Force Institute of Technology 2950 P. St. WPAFB, OH 45433			8. PERFORMING ORGANIZATION REPORT NUMBER		
9. SPONSORING/MONITORING AGENCY NAME(S) AND ADDRESS(ES) Dr. Richard Rivir AFRL/PRTT Bldg 18 1950 Fifth Street WPAFB, OH 45433 (937) 255-2744			10. SPONSORING/MONITORING AGENCY REPORT NUMBER  AFIT/DS/ENY/99-01		
11. SUPPLEMENTARY NOTES					
12a. DISTRIBUTION AVAILABILITY STATEMENT  Approved for public release; Distribution Unlimited			12b. DISTRIBUTION CODE		
13. ABSTRACT (Maximum 200 words)  The problem of flow separation from a low pressure turbine blade was investigated. The operating conditions under which the separation occurred were documented through measurement of surface pressure coefficients, boundary layer velocity and turbulence profiles, total pressure loss coefficient and wake velocity momentum deficit. Three different means for reducing the losses associated with the flow separation were also investigated. A boundary layer trip, dimples, and V-grooves were studied as passive means requiring no additional energy to reduce the separation losses. The boundary layer trip was only successful for an inlet and axial chord Reynolds number of 50k with a reduction in loss coefficient of 58.2%. Three sets of dimples were tested with the placement of each at axial chord locations of 50%, 55%, and 65%. The dimples provided reductions in the loss coefficient for Reynolds numbers of 50k, 100k, and 200k ranging from 5.1% (Re = 100k, freestream turbulence level of 4%) to 51.7% (Re = 50k, freestream turbulence level of 4%). Two sets of V-grooves were tested with axial chord start locations of 55% and 60%. The V-grooves provided smaller reductions in loss coefficient than the dimples. Boundary layer profiles, total pressure loss coefficients, and wake velocity momentum deficits are presented for the three passive modifications.					
14. SUBJECT TERMS			15. NUMBER OF PAGES 285		
			16. PRICE CODE		
17. SECURITY CLASSIFICATION OF REPORT UNCLASSIFIED		18. SECURITY CLASSIFICATION OF THIS PAGE UNCLASSIFIED	19. SECURITY CLASSIFICATION OF ABSTRACT UNCLASSIFIED	20. LIMITATION OF ABSTRACT UL	